

Unraveling the Electrocatalytic Activity of the 2D Transition Metal Dichalcogenides towards Hydrogen Evolution Reactions

Ph.D. Thesis

By

VIKASH KUMAR
(Roll Number: 2001151017)



DEPARTMENT OF PHYSICS

INDIAN INSTITUTE OF TECHNOLOGY INDORE

JUNE, 2025

Unraveling the Electrocatalytic Activity of the 2D Monolayer Transition Metal Dichalcogenides towards Hydrogen Evolution Reactions

A THESIS

*Submitted in partial fulfilment of the
Requirements for the award of the degree*

of

DOCTOR OF PHILOSOPHY

by

**VIKASH KUMAR
(Roll Number: 2001151017)**



**DEPARTMENT OF PHYSICS
INDIAN INSTITUTE OF TECHNOLOGY INDORE**

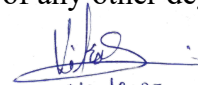
JUNE, 2025



INDIAN INSTITUTE OF TECHNOLOGY INDORE

I hereby certify that the work which is being presented in the thesis entitled **Unraveling the Electrocatalytic Activity of the 2D Monolayer Transition Metal Dichalcogenides towards Hydrogen Evolution Reactions**, in the partial fulfillment of the requirements for the award of the degree of **DOCTOR OF PHILOSOPHY** and submitted in the **Department of Physics, Indian Institute of Technology Indore**, is an authentic record of my own work carried out during the time period from August 2020 to June 2025 under the supervision of **Dr. Srimanta Pakhira, Associate Professor, Indian Institute of Technology, Indore**.

The matter presented in this thesis has not been submitted by me for the award of any other degree of this or any other institute.


09/10/2025

Signature of the student with date

(VIKASH KUMAR)

This is to certify that the above statement made by the candidate is correct to the best of my/our knowledge.



Dr. Srimanta Pakhira, Ph.D.
Associate Professor
Department of Physics and
Centre for Advanced Electronics
Indian Institute of Technology Indore, M.P., India

Signature of Thesis Supervisor with date

(DR. SRIMANTA PAKHIRA)

VIKASH KUMAR has successfully given his Ph.D. Oral Examination held on09.10.2025..



Dr. Srimanta Pakhira, Ph.D.
Associate Professor
Department of Physics and
Centre for Advanced Electronics
Indian Institute of Technology Indore, M.P., India

Signature of Thesis Supervisor #1

Date: 09.10.2025



Acknowledgements

*First and foremost, I praise the **Supreme Lord** for granting me this opportunity and blessing me with the capabilities to succeed. Without their divine guidance, this work would never have been accomplished. I am deeply grateful that they have listened to all my prayers and have supported me through my faith.*

*It is a great pleasure for me to acknowledge all the people who have helped and supported me to complete this Thesis. I express my deep and heartfelt gratitude to my supervisors **Dr. Srimanta Pakhira**. I have had the privilege of being associated with **Dr. Srimanta Pakhira** throughout this entire period of doctoral studies. I have been fortunate to have a supervisor who cared so much about my work, and who responded to my questions and queries so promptly. I have received continuous academic support, inspiration, and encouragement from him. This has not only enriched me academically but has also nourished my inner self and changed my perspective and attitude a lot. Through this association with him, I have been able to acquire, develop and sharpen the skills and the scientific methodologies which are invaluable for good independent research. His immense knowledge, guidance, observations, and comments helped me a lot to establish the overall direction of the research and to move forward with the investigation in depth. For all this, I will remain indebted and grateful to him for my entire life.*

*I gratefully extend my gratitude towards my PSPC members **Prof. Sudeshna Chattopadhyay**, Department of Physics, **Dr. Sumanta Samal**, Department of Metallurgical Engineering and Materials Science (MEMS), Indian Institute of Technology Indore for their valuable suggestions and comments to improve my work. I am grateful to the **Head, DPGC Convener**, all the faculty members, and staff of Department of PHYSICS, **IIT Indore**, for providing an encouraging environment to carry out research effectively.*

*I would like to acknowledge **Prof. Suhas S. Joshi**, Director IIT Indore for providing a conducive environment for research and the opportunity to explore my research capabilities at IIT Indore. I am also thankful to **The Dean of Academic Affairs**, **The Dean of Research and Development** and **The Dean***

of Student Affairs, IIT Indore.

I am indebted to my seniors, lab mates and colleague researchers, especially Dr. Nilima Sinha, Dr. Shrish Nath Upadhyay, Mr. Dikeshwar, Ms. Himani, Mr. Ashok, Mr. Lokesh, Ms. Kahkasha, Mr. Naveen, Mr. Anshuman, and Mr. Deepesh for their cooperation and stay so as to make my Ph.D. journey joyful and with whom I have spent so much time discussing both technical and non-technical stuff.

I am lucky to have good friends who have been constantly encouraging, motivating, and cheering me in all situations. There have been so many of you – it is impossible to name all of you.

This acknowledgment would not be complete without mentioning the pain staking efforts and patience of my family. I owe this thesis to my grandparents, my parents, my sister and other family members who always stood by me and provided me strength in pursuing this work. This achievement of my life would not be possible without their support and cooperation throughout this study.

Lastly, I express my hearty thanks to those whom I might have missed mentioning by name, who helped directly or indirectly and helped me a lot in completion of this Ph.D. research work.

-Vikash Kumar

Indian Institute of Technology Indore

Date: 09/10/2025

Dedicated To

My Beloved Family

Mother, Father and Sister for their love, care, and

Blessings

Unraveling the Electrocatalytic Activity of the 2D Monolayer Transition Metal Dichalcogenides towards Hydrogen Evolution Reactions

Synopsis of the Thesis

*Submitted in partial fulfillment of the
requirements for the award of the degree*

of

DOCTOR OF PHILOSOPHY

by

Vikash Kumar

(Roll Number:2001151017)

Under the supervision of

Dr. Srimanta Pakhira



**DEPARTMENT OF PHYSICS
INDIAN INSTITUTE OF TECHNOLOGY INDORE**

June 2025

Unraveling the Electrocatalytic Activity of the 2D Monolayer Transition Metal Dichalcogenides towards Hydrogen Evolution Reactions

1. Introduction

For a long time, energy production has mainly relied on fossil fuels which are non-renewable energy sources insufficient to meet the current energy requirements for our modern society. They also emit harmful greenhouse gases such as carbon dioxide (CO_2), carbon monoxide (CO), methane (CH_4) and other kinds of toxic gases. (Owusu and Asumadu-Sarkodie, 2016) This growing concern has galvanized the scientific community to pursue the development of sustainable, eco-friendly energy conversion and storage technologies. (Liu, 2015) The current energy infrastructure, heavily dependent on fossil fuels such as oil, coal, and natural gas, is unsustainable and detrimental to the environment, as shown in Figure 1. (International Energy Institute (IEI), 2023) Among various promising alternatives, electrochemical water splitting has garnered significant attention due to its capability to generate high-purity hydrogen, a clean and renewable energy resources with high energy density and zero-carbon emissions. (MacFarlane et al., 2016; Zhu et al., 2020)

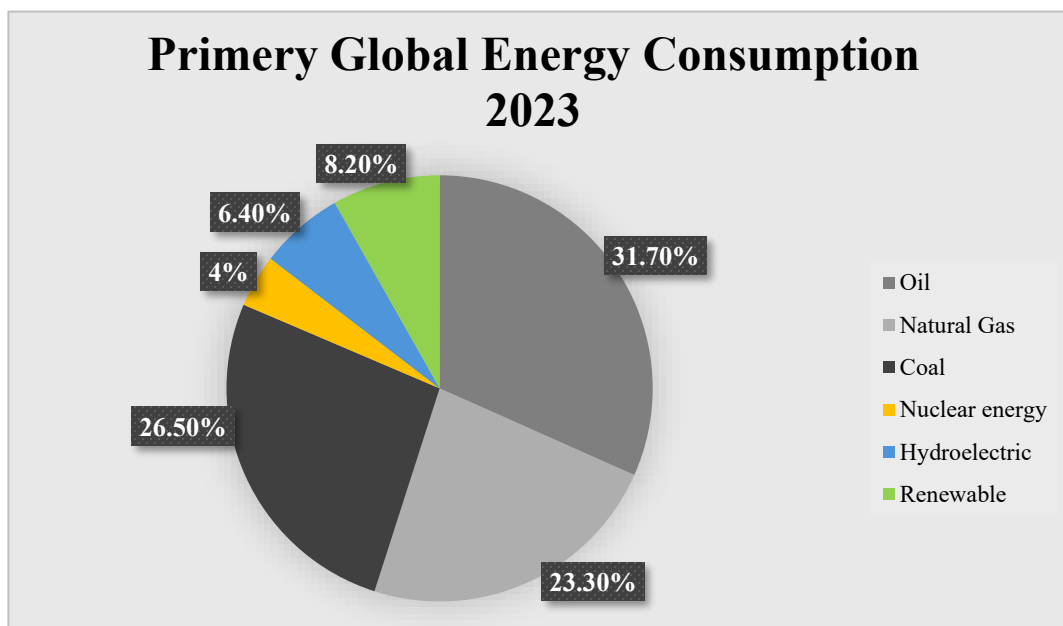


Figure 1: Global energy consumption in 2023. This chart is based on statistical data from the Energy Institute Statistical Review of World Energy. Fossil fuel consumption was 81.5% in 2023.

In the context of water electrolysis, the cathodic half-reaction in fuel cell is the Hydrogen Evolution Reaction (HER: $2\text{H}^+ + 2\text{e}^- \rightarrow \text{H}_2$) (Lasia, 2010; Lei et al., 2017, which plays a pivotal role in the generation of molecular hydrogen. A typical water electrolysis cell, depicted in Figure 2, comprises two electrodes: a cathode and an anode, both immersed in a conductive aqueous electrolyte. When a sufficient voltage is applied across the electrodes, an electric current is established. Electrons travel through the external circuit towards the cathode, while ions within the electrolyte facilitate the electrolysis process by moving between the electrodes. At the cathode, a reduction reaction known as HER occurs. During this process, water molecules gain electrons to form hydrogen gas (H_2) and hydroxide ions (OH^-). Conversely, at the anode, an oxidation reaction called the oxygen evolution reaction (OER) takes place. In this reaction, water molecules lose electrons to form oxygen gas (O_2) and hydrogen ions (H^+). This reaction is of particular interest as hydrogen is regarded as a potential replacement for fossil fuels in future energy infrastructure and technology. Nevertheless, HER suffers from sluggish kinetics, necessitating the use of electrocatalysts to lower the overpotential and accelerate the reaction rate.(Debe, 2012; Jaksic et al., 2013)

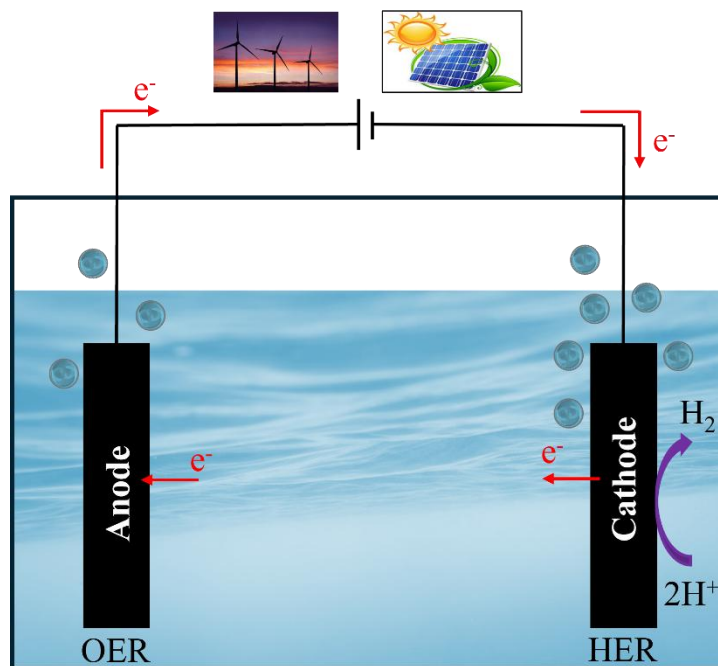


Figure 2: A schematic representation of a water electrolysis cell. The diagram illustrates the evolution of hydrogen gas at the cathode surface and oxygen gas at the anode surface.

The selection of an efficient HER electrocatalyst must account for multiple parameters, including catalytic activity, long-term stability, earth abundance, and economic viability.^(Debe, 2012; Jiao et al., 2015; Kongkanand and Mathias, 2016; Wang et al., 2019) Although noble metals such as Platinum (Pt), Ruthenium (Ru), and Palladium (Pd) exhibit outstanding HER performance due to their near-zero overpotentials and excellent catalytic efficiency^(Grigoriev et al., 2011; Shi and Zhang, 2016), but their scarcity and high costs hinder their scalability for commercial deployment and practical applications.^(Wang, Li and Heine, 2018)

Hence, the overarching challenge lies in the discovery of cost-effective, earth-abundant, and highly active electrocatalysts capable of facilitating HER at industrially relevant rates. In this work, two-dimensional (2D) materials, particularly Transition Metal Dichalcogenides (TMDs) and Janus TMDs have emerged as promising candidates. Their unique physicochemical attributes, including large specific surface area, tunable electronic properties, and abundant catalytically active sites, make them particularly attractive for

HER applications. The present investigation undertakes a comprehensive theoretical and computational study of 2D TMDs, with an emphasis on elucidating their hydrogen evolution capabilities. The structural and electronic properties of these materials are analyzed within a theoretical framework, while computational modeling provides insight into their intrinsic HER activity. This research aims to contribute to the rational design and identification of the next generation of HER electrocatalysts, thereby supporting the advancement of sustainable hydrogen production technologies.

The first chapter of this thesis introduces the background of the current study alongside a review of pertinent literature. It outlines the research motivation, central objective, and scope of the work focused exclusively on the HER.

2. Motivation and Objective of the Work

The central motivation of this research lies in the rational design of novel 2D TMDs with enhanced electrocatalytic activity for the HER, a key half-reaction in electrochemical water splitting. While conventional 2D TMDs typically exhibit catalytic activity at their edges, their basal planes remain inert. Activating these basal planes holds the potential to unlock a significantly higher density of active sites, thereby improving both the efficiency and scalability of HER processes.

Recent studies have demonstrated that engineered modifications, such as alloying, doping, or Janus configurations, can dramatically alter the electronic properties of 2D TMDs and enhance their HER activity and stability under operational conditions. Despite these advancements, a comprehensive understanding of the fundamental mechanisms driving such performance improvements, particularly those arising from basal plane activation, remains incomplete. Addressing this gap is critical for guiding the design of next-generation, earth-abundant, and cost-effective electrocatalysts for sustainable hydrogen production.

The objectives of the present work are:

1. Mechanistic Understanding of Efficient Electrocatalytic Hydrogen Evolution Reaction on 2D Monolayer WSe Janus Transition Metal Dichalcogenide.

- (Published: Kumar V. and Pakhira, S. (2023) *Molecular Systems Design & Engineering (MSDE)*, 8, pp. 1060–1074.)
2. Electrocatalytic Performance of 2D Monolayer WSeTe Janus Transition Metal Dichalcogenide for Highly Efficient H₂ Evolution Reaction.
(Published: Kumar V., Halba D., Upadhyay S.N. and Pakhira, S. (2024) *Langmuir*, 40, pp. 4872–4887.)
3. 2D Monolayer Molybdenum (IV) Telluride TMD: An Efficient Electrocatalyst for Hydrogen Evolution Reaction.
(Published: Kumar V. and Pakhira, S. (2025) *Materials Advances*, 6, pp. 2622–2635.)

3. Methodology of Work

3.1. The structural and electronic properties of the 2D Janus WSSe monolayer were investigated using first-principles DFT-D method as implemented in CRYSTAL17(Wang *et al.*, 2005; Yan *et al.*, 2018; Dovesi *et al.*, 2020), employing the B3LYP-D3(Becke, 1993; Pakhira *et al.*, 2012; Dovesi *et al.*, 2020) hybrid functional with Grimme's dispersion correction. The pob-TZVP basis set was used for S and Se atoms, and the HAYWSC 311(d31) basis set with Hay–Wadt ECPs was used for W atoms to account for relativistic effects. A $20 \times 20 \times 1$ Monkhorst–Pack k-point mesh was applied, and a 500 Å vacuum was included along the z-axis. Spin-polarized calculations used SPIN, SPINLOCK, and ATOMSPIN keywords. Geometry optimizations and electronic band structure calculations were performed in the present study.

A non-periodic finite molecular W₁₀S₁₂Se₉ cluster model system was computationally designed from the monolayer, capturing W and S/Se edges for HER mechanism studies. HER energetics and reaction barriers were computed using the M06-L(Zhao and Truhlar, 2006, 2008) functional implemented in Gaussian16(Frisch, 2016), employing 6-31+G** for light atoms and LANL2DZ ECP for W.(Pritchard *et al.*, 2019) Transition states (TS), adsorption energies, and free energies of the Volmer, Heyrovsky and Tafel steps were calculated.(Lei *et al.*, 2017; Laun, Vilela Oliveira and

Bredow, 2018; Pakhira and Mendoza-Cortes, 2018, 2019; Liang et al., 2019; Pakhira, 2019)

3.2. Periodic DFT calculations using the B3LYP-D3(*Becke, 1993; Pakhira et al., 2012; Dovesi et al., 2020*) hybrid functional were performed with CRYSTAL17(*Dovesi et al., 2018, 2020*) to study the equilibrium geometry and electronic properties of the 2D monolayer Janus WSeTe TMD. Triple- ζ valence with polarization (TZVP) Gaussian basis sets were used for W, Se, and Te. A vacuum of 500 Å along the z-axis was considered to avoid interlayer interactions. The phonon spectrum confirmed structural stability with no imaginary frequencies. Band structure and DOS were computed using a $15 \times 15 \times 1$ Monkhorst–Pack k-mesh.

For HER studies, a non-periodic finite molecular cluster model system $\text{W}_{10}\text{Se}_9\text{Te}_{12}$ was constructed, mimicking the edge terminations of the 2D monolayer. M06-L(*Zhao and Truhlar, 2006, 2008; Lei et al., 2017*) method with LANL2DZ (W, Se, Te) and 6-31+G** (H, O) basis sets was employed to investigate the reaction mechanisms by using Gaussian 16(*Frisch, 2016*). Transition states (TS) for HER steps were confirmed by harmonic vibrational analysis and intrinsic reaction coordinate (IRC) calculations(*Pakhira, Takayanagi and Nagaoka, 2015; Pakhira et al., 2016*). Solvation effects were considered by performing the polarizable continuum model (PCM) analysis with water as solvent.

Gibbs free energy changes (ΔG) were computed for HER pathways. Cluster model validation was confirmed by comparing H adsorption energies with periodic slab results under vacuum, showing consistent trends.

3.3. First-principles based quantum mechanical density functional theory (DFT) method was employed to investigate the structural, electronic, and catalytic properties of 2D MoTe_2 . Periodic slab models were constructed to simulate the monolayer MoTe_2 using the hybrid B3LYP-D3(*Becke, 1993; Pakhira et al., 2012; Dovesi et al., 2020*) functional with Grimme's D3 dispersion corrections, as implemented in CRYSTAL17(*Dovesi et al., 2018, 2020*). A triple- ζ valence polarized Gaussian basis set was used for Mo and Te atoms, and spin-polarized calculations were performed. The structure was optimized with stringent convergence criteria (10^{-7} a.u.), and a

vacuum of 500 Å along the z-axis was applied to eliminate interlayer interactions. A 20×20×1 Monkhorst-Pack k-mesh was used to compute the band structure and density of states.

A non-periodic Mo₁₀Te₂₁ molecular cluster model system representing both the Mo- and Te-terminated edges was computationally established to study the HER mechanism. The M06-L(*Zhao and Truhlar, 2006, 2008*) functional implemented in Gaussian16(*Frisch, 2016*) was employed for geometry optimization, reaction barrier, and frequency calculations. LANL2DZ basis sets with effective core potentials were used for Mo and Te, and 6-31+G** for H and O atoms.(*Pritchard et al., 2019*) Solvation effects were included by considering the PCM analysis with water as the solvent ($\epsilon = 80.13$) of the electrochemical reaction. All transition states were confirmed by a single imaginary frequency and validated through the IRC calculations.(*Pakhira, Takayanagi and Nagaoka, 2015; Pakhira et al., 2016*)

4. Summary of the Present Work

4.1. Mechanistic Understanding of Efficient Electrocatalytic Hydrogen Evolution Reaction on 2D Monolayer WSSe Janus Transition Metal Dichalcogenide

A first principles-based quantum mechanical (QM) hybrid periodic DFT method has been employed to examine the equilibrium structure, geometry, and electronic properties (such as the electronic band structure, band gap, and total density of states (DOS)) of a 2D monolayer WSSe JTMD. We have performed non-periodic quantum mechanical DFT computations to find out the most favorable HER pathway on both the W-edges (10 $\bar{1}$ 0) and S-/Se-edges ($\bar{1}$ 010) of the 2D Janus WSSe material. The present research shows that the 2D monolayer Janus WSSe TMD follows the Volmer–Heyrovsky (V-H) reaction mechanism with very low H*-migration and Heyrovsky reaction energy barriers about 2.33–7.52 kcal mol⁻¹ during the H₂ evolution. It was found that the 2D Janus WSSe has a high value of turnover frequency (TOF) of $\sim 1.91 \times 10^7$ s⁻¹ and a very low Tafel slope ($m = 29.54$ mV dec⁻¹ at $T = 298.15$ K) due to better overlapping of the *d*-orbital electron cloud of the W atom and the *s*-orbital electron cloud of the H₂ appearing in the HOMO–LUMO structure of the Heyrovsky TS. The present study demonstrates the extraordinary HER activity and performance of the 2D monolayer WSSe JTMD. Our research exhibits how to

computationally devise a highly active electrocatalyst from 2D JTMDs utilizing their active edges, and the current investigation will boost the further development of superior 2D electrocatalysts for efficient HER. *(Kumar and Pakhira, 2023)*

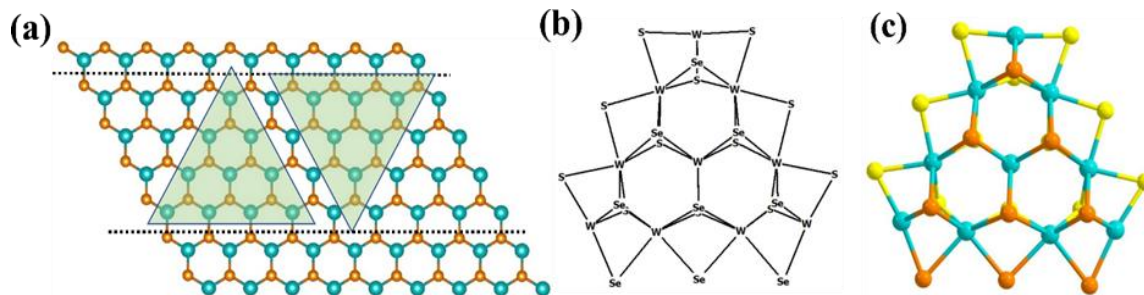


Figure 3: (a) Top view of a 2D Janus WSSe monolayer. The two up and down horizontal dashed lines represent the end points along the (10 $\bar{1}$ 0) W edge and ($\bar{1}$ 010) S-/Se-edge. These two triangles represent the W-edge and S-/Se-edge clusters; (b) schematic diagram of the W-edge cluster; (c) equilibrium geometry of the triangular W-edge cluster with W₁₀S₁₂Se₉ stoichiometry.

4.2. Electrocatalytic Performance of 2D Monolayer WSeTe Janus Transition Metal Dichalcogenide for Highly Efficient H₂ Evolution Reaction

We report a 2D monolayer WSeTe JTMD, which is highly effective toward HER. We have studied the electronic properties of 2D monolayer WSeTe JTMD using the periodic hybrid DFT-D method, and a direct electronic band gap of 2.39 eV has been obtained. We have explored the HER pathways, mechanisms, and intermediates, including various TS structures (Volmer TS, i.e., H*-migration TS, Heyrovsky TS, and Tafel TS) using a molecular cluster model of the subject JTMD noted as W₁₀Se₉Te₁₂. The present calculations reveal that the 2D monolayer WSeTe JTMD is a potential electrocatalyst for HER. It has the lowest energy barriers for all the TSs, among other TMDs. It has been shown that the Heyrovsky energy barrier (= 8.72 kcal mol⁻¹) in the case of the Volmer–Heyrovsky (V-H) mechanism is larger than the Tafel energy barrier (= 3.27 kcal mol⁻¹) in the V-T mechanism. Hence, our present study suggests that the formation of H₂ is energetically more favorable via the V-T mechanism. This study helps to shed light on the rational design of 2D single-layer JTMD, which is highly effective toward HER, and we expect that the present work can be further extended to other JTMDs to find out the improved electrocatalytic performance. *(Kumar et al., 2024)*

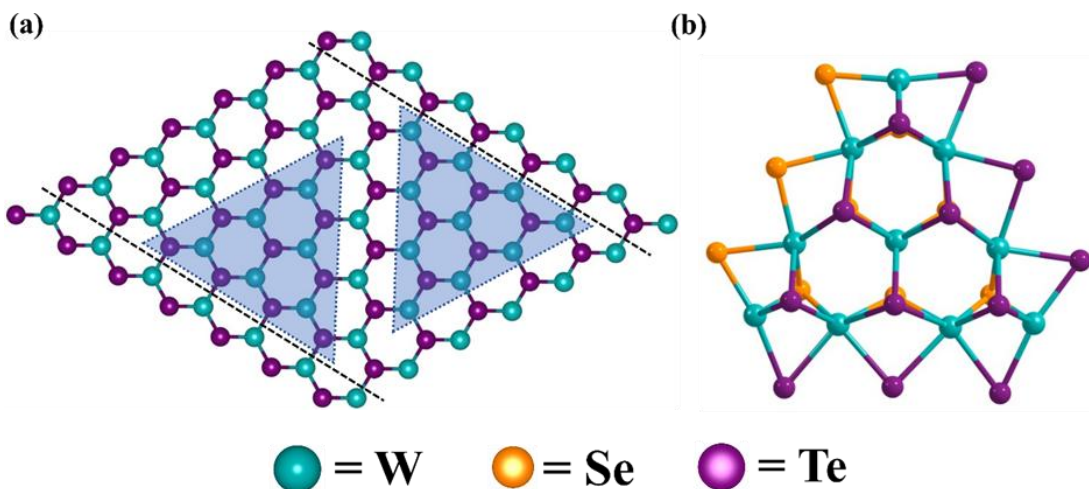


Figure 4: (a) Schematic presentation of the periodic 2D monolayer Janus WSeTe TMD material. Two black dotted lines show the $(\bar{1}010)$ Se-/Te-edges and $(10\bar{1}0)$ W-edges of the 2D monolayer Janus WSeTe TMD. Two triangles show the W-edges and Se-/Te-edges cluster model of the 2D monolayer WSeTe JTMD. (b) The W-edge finite molecular cluster model system ($W_{10}Se_9Te_{12}$) of the 2D WSeTe JTMD is presented here for studying HER.

4.3. 2D Monolayer Molybdenum (IV) Telluride TMD: An Efficient Electrocatalyst for Hydrogen Evolution Reaction

An electrocatalyst is needed to efficiently lower the reaction barriers to produce hydrogen through the HER. Recently, 2D TMDs, such as the pure 2D monolayer $MoTe_2$, MoS_2 , WS_2 , etc. have become attractive materials for HER. Using the first principles-based hybrid DFT method, we have computationally designed a pure 2D monolayer $MoTe_2$ TMD and examined its structural and electronic properties with electrocatalytic efficacy towards the HER. A non-periodic finite molecular cluster model $Mo_{10}Te_{21}$ system has been employed to explore the feasibility of both the V–H and V–T reaction mechanisms for the HER. The solvent-phase calculations demonstrate that this material can effectively undergo either V–H or V–T reaction pathways. This conclusion is supported by our determination of low reaction barriers for the H^* -migration, Heyrovsky, and Tafel TSs, which were found to be approximately 9.80, 12.55, and 5.29 kcal mol⁻¹, respectively. These results highlight the potential utility of 2D monolayer $MoTe_2$ TMD as a promising electrocatalyst for the HER.

The unusual electrocatalytic activity of the pristine 2D monolayer MoTe_2 TMD is evidenced by its ability to significantly reduce reaction barriers, achieving impressive TOF values of 3.91×10^3 and $8.22 \times 10^8 \text{ s}^{-1}$ during the Heyrovsky and Tafel reaction steps, respectively. Additionally, it demonstrates a remarkably low Tafel slope of $29.58 \text{ mV dec}^{-1}$. These outstanding performance metrics indicate that the pure 2D monolayer MoTe_2 TMD is a highly efficient electrocatalyst for the HER, surpassing the capabilities of traditional platinum group metal-based alternatives. Further exploration of its potential applications in electrocatalysis is warranted. The present work provides valuable insights into the atomic modulation of active sites for enhanced electrocatalytic performance towards the HER, paving the way for designing advanced non-noble metal-free electrocatalysts. (Kumar and Pakhira, 2025)

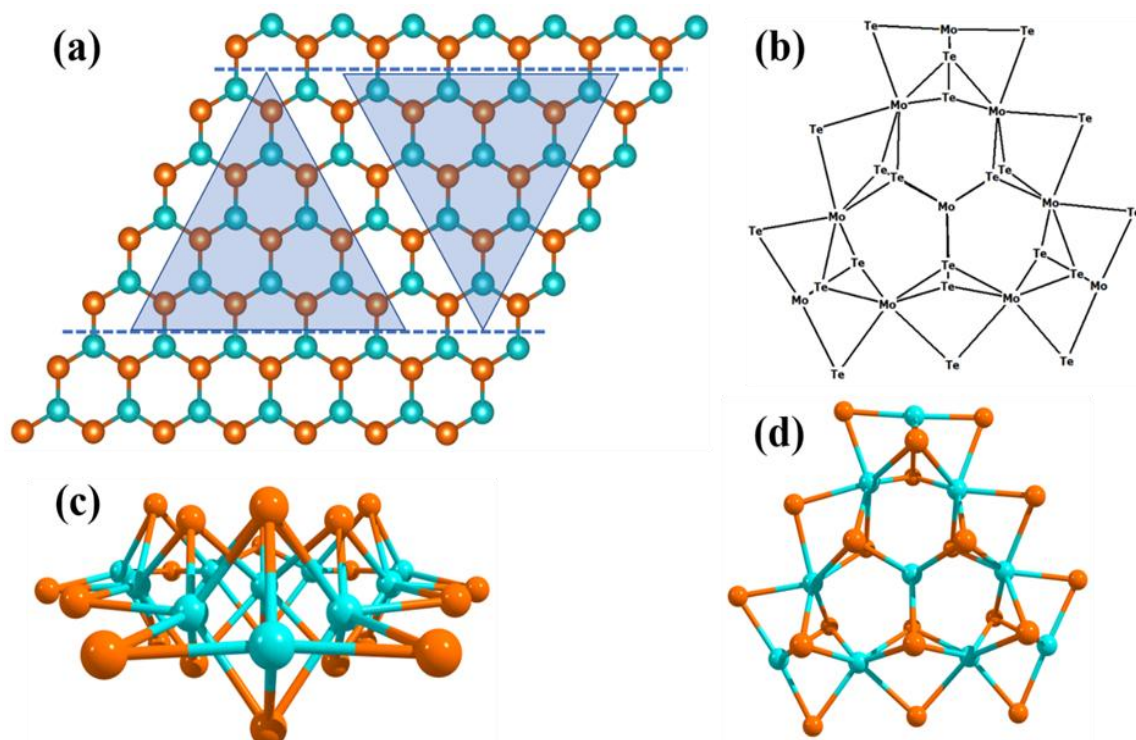


Figure 5: (a) shows the equilibrium 2D monolayer MoTe_2 TMD with a Te-Mo-Te tri-layer structure. The two horizontal blue color dashed lines indicate terminations along the $(10\bar{1}0)$ Mo-edge and $(\bar{1}010)$ Te-edge. The two triangles represent the terminations for Mo-edge and Te-edge clusters. It includes a non-periodic molecular cluster with an active Te-edge and a non-periodic molecular cluster with an active Mo-edge. (b) The molecular cluster model system of the 2D

monolayer MoTe₂ TMD is represented schematically. (c) A side view of the chosen Mo₁₀Te₂₁ non-periodic triangular molecular cluster is also shown. (d) A top view of the MoTe₂ TMD Mo-edge cluster.

5. Conclusion

In conclusion, our comprehensive computational investigation into the HER on the surface of 2D monolayer TMDs, specifically Janus WSSe, Janus WSeTe, and pristine MoTe₂ has yielded valuable insights into their structural, electronic, and catalytic behaviors. We have employed a combination of periodic hybrid DFT methods and non-periodic cluster modeling to accurately capture the equilibrium geometries, band structures, active sites, and detailed mechanistic pathways involved in HER.

The 2D Janus WSSe monolayer demonstrated exceptional electrocatalytic activity with low activation barriers (2.33–7.52 kcal mol⁻¹) for the V-H mechanism. Our calculations revealed highly favorable H*-migration and Heyrovsky steps at the W- and S/Se-terminated edges, leading to a remarkably high TOF of $\sim 1.91 \times 10^7$ s⁻¹ and a low Tafel slope of 29.54 mV dec⁻¹. The enhanced performance is attributed to the effective orbital overlap between the W *d*-orbitals and H₂ *s*-orbitals at the transition state, facilitating smooth H₂ evolution.

Similarly, Janus WSeTe TMD has been found to be a highly efficient HER catalyst. It exhibits a direct band gap of 2.39 eV and low transition state barriers, with the V-T mechanism emerging as more favorable (Tafel barrier = 3.27 kcal mol⁻¹) than the V-H pathway (Heyrovsky barrier = 8.72 kcal mol⁻¹). The study of the W₁₀Se₉Te₁₂ cluster model provides insight into the energetics of various HER intermediates and highlights the catalytic advantage of asymmetric Janus structures in optimizing the active edge states for efficient hydrogen evolution.

The pristine 2D MoTe₂ monolayer also exhibits noteworthy HER activity, despite lacking Janus asymmetry. Through hybrid DFT analysis of the Mo₁₀Te₂₁ cluster, we have observed that both V-H and V-T mechanisms are kinetically accessible, with transition state energy barriers of 9.80, 12.55, and 5.29 kcal mol⁻¹ for H*-migration, Heyrovsky, and Tafel steps, respectively. MoTe₂ has shows extremely high TOF values (up to 8.22×10^8 s⁻¹) and

a Tafel slope of $29.58 \text{ mV dec}^{-1}$, confirming its potential as a metal-free alternative to noble metal catalysts.

These studies demonstrate that both the 2D Janus and pristine TMDs, when properly engineered, can serve as high-performance HER electrocatalysts. Our research not only expands the fundamental understanding of the electronic properties of these catalysts but also provides a foundation for future endeavors in developing efficient electrocatalysts for renewable energy applications.

List of Publications

Related to Ph.D. Thesis:

- 1) **Kumar, V.** and Pakhira, S.* (2023) ‘Mechanistic Understanding of Efficient Electrocatalytic Hydrogen Evolution Reaction on 2D Monolayer WSSe Janus Transition Metal Dichalcogenide’, *Molecular Systems Design & Engineering (MSDE)*, 8, pp 1060-1074.
- 2) **Kumar, V.**, Halba, D., Upadhyay, S.N., and Pakhira, S.* (2024) ‘Electrocatalytic Performance of 2D Monolayer WSeTe Janus Transition Metal Dichalcogenide for Highly Efficient H₂ Evolution Reaction’, *Langmuir*, 40, pp 4872–14887.
- 3) **Kumar, V.** and Pakhira, S.* (2025) ‘2D Monolayer Molybdenum (IV) Telluride TMD: An Efficient Electrocatalyst for Hydrogen Evolution Reaction’, *Materials Advances*, 6, 2622 - 2635.

Other than Ph.D. Thesis:

- 1) Upadhyay, S. N., **Kumar, V.**, Sharma, N., and Pakhira, S.* (2025) ‘Enhanced Catalytic Performance of Vanadium-Doped MoS₂ as a Multifunctional Electrocatalyst towards ORR, OER, and HER Applications’, *ACS Applied Energy Materials*.(Just accepted)
- 2) **Kumar, V.**, Joshi, H., Sharma, N., and Pakhira, S.* (2025) Electrocatalytic Activity of Post Nb-doped 2D MoSe₂ TMD Towards Highly Effective H₂ Evolution Reaction, *ChemCatChem*.
- 3) Wagh, L., Singh, D., **Kumar, V.**, Upadhyay, S.N., Pakhira, S. and Das, A.K.* (2024) ‘Sonication Induced Boladipeptide-based Metallogel as Efficient Electrocatalyst for Oxygen Evolution Reaction’, *ACS Applied Materials & Interfaces*, 16, pp 28307–28318
- 4) Pakhira, S.*, **Kumar, V.**, and Ghosh, S. (2023) ‘Revealing the Superior Electrocatalytic Performance of 2D Monolayer WSe₂ Transition Metal Dichalcogenide for Efficient H₂ Evolution Reaction’, *Advanced Materials Interfaces*, 10, pp 2202075.

- 5) Upadhyay, S.N., Sardar, V.B., Singh, A., **Kumar, V.** and Pakhira, S.*, (2022) ‘Elucidating the Oxygen Reduction Reaction Mechanism on the Surfaces of 2D Monolayer CsPbBr₃ Perovskite’, *Physical Chemistry Chemical Physics*, 24, pp 28283-28294.
- 6) Patel, C., Singh, R., Dubey, M., Pandey, S.K., Upadhyay, S.N., **Kumar, V.** Sriram, S., Htay, M.T., Pakhira, S., Atuchin, V.V. and Mukherjee, S.* (2022) ‘A synergistic recipe to produce uniform, large-sized single crystal of MoS₂ monolayer via CVD for ppb-level NO₂ sensing’, *ACS Applied Nano Materials*, 7, pp 9415–9426.

*** Corresponding Author**

Table of Contents

List of Figures	XVII
List of Tables	XXIII
List of Abbreviations	XXV
Abstract	XXIX
1. Introduction and Literature Review	1-26
1.1 <u>The Hydrogen Economy</u>	Error! Bookmark not defined.
1.2 <u>Methods of Hydrogen Production</u>	4
1.2.1 <u>Steam Reforming of Natural Gas</u>	Error! Bookmark not defined.
1.2.2 <u>Water electrolysis</u>	5
1.3 <u>Hydrogen Evolution Reaction (HER) Mechanism</u>	9
1.4 <u>HER Activity Parameters</u>	12
1.5 <u>Electrocatalyst for HER</u>	16
1.5.1 <u>Metal-Based HER Electrocatalyst</u>	16
1.5.2 <u>Non-Noble Metal Compound-Based HER Electrocatalysts</u>	18
1.6 <u>Research Gap and Motivation</u>	Error! Bookmark not defined.
1.7 <u>Contributions from the Present Thesis</u>	22
1.8 <u>Organization of the Thesis</u>	26
2. Theory, Methodology and Computational Details	27-52
2.1 <u>Schrödinger equation</u>	28
2.2 <u>The Many-Body System and Born-Oppenheimer (BO) Approximation</u>	Error! Bookmark not defined.
2.3 <u>The Hartree-Fock Approximation</u>	30
2.4 <u>The Density Functional Theory</u>	32
2.4.1 <u>The Hohenberg-Kohn Theorems</u>	32
2.4.2 <u>The Kohn-Sham Equations</u>	34
2.4.2 <u>Exchange-Correlation Approximations</u>	36
2.5 <u>Software</u>	43
2.5.1 <u>CRYSTAL 17</u>	43
2.5.2 <u>Gaussian 16</u>	45

2.5	<u>Basis set</u>	47
-----	------------------------	----

3. Mechanistic understanding of efficient electrocatalytic hydrogen evolution reaction on a 2D monolayer WSe Janus transition metal dichalcogenide..... 53-94

3.1	<u>Introduction</u>	54
3.2	<u>Computational details</u>	56
	3.2.1 <i>2D periodic slab development and electronic property calculations</i>	57
	3.2.2 <i>Non-periodic finite molecular cluster model system and HER mechanism</i> .	60
	3.2.3 <i>Cluster Model Validation</i>	64
	3.2.4 <i>Theoretical Calculations and equations</i>	65
3.3	<u>Results and Discussions</u>	66
	3.3.1 <i>Equilibrium structural properties of the 2D monolayer WSe JTMD</i>	66
	3.3.2 <i>Electronic properties</i>	68
	3.3.3 <i>HER mechanism and electrocatalytic activity</i>	71
	3.3.3.1 <i>Volmer-Heyrovsky mechanism</i>	73
	3.3.3.2 <i>Tafel mechanism and S-terminal W-edge of 2D monolayer WSe JTMD material for HER</i>	82
	3.3.3.3 <i>Turnover Frequency (TOF) and Tafel Slope calculations</i>	87
	3.3.3.4 <i>HOMO and LUMO calculations</i>	89
3.4	<u>Summary</u>	92

4. Electrocatalytic Performance of 2D Monolayer WSeTe Janus Transition Metal Dichalcogenide for Highly Efficient H₂ Evolution Reaction 95-134

4.1	<u>Introduction</u>	95
4.2	<u>Methods and Computational Details</u>	98
	4.2.1 <i>Periodic DFT Calculations for the 2D Monolayer Janus WSeTe</i>	98
	4.2.2 <i>Finite Molecular Cluster Modeling</i>	100
	4.2.3 <i>Theoretical Calculations and Equations</i>	103
	4.2.4 <i>Validation of the cluster model</i>	103
4.3	<u>Results and discussion</u>	104
	4.3.1 <i>Structural and Electronic Properties of the 2D Monolayer WSeTe JTMD</i> 104	
	4.3.2 <i>Her Mechanisms</i>	110
	4.3.3 <i>Volmer–Heyrovsky Mechanism</i>	114

4.3.4	<i>Volmer–Tafel Reaction Mechanism</i>	122
4.3.5	<i>Other Thermodynamic Properties of the HER Mechanism</i>	127
4.3.5.1	<i>HOMO and LUMO Calculations</i>	127
4.3.5.2	<i>Turnover Frequency (TOF) and Tafel Slope Calculation</i>	130
4.4	<i>Summary</i>	133
5.	2D Monolayer Molybdenum(IV) Telluride TMD: an Efficient Electrocatalyst for H₂ Evolution	135-172
5.1	<i>Introduction</i>	136
5.2	<i>Computational Details</i>	138
5.2.1	<i>Periodic structure DFT calculations</i>	139
5.2.2	<i>Finite non-periodic molecular cluster modelling</i>	141
5.3	<i>Results and Discussion</i>	146
5.3.1	<i>Structural and electronic properties</i>	146
5.3.2	<i>HER Pathway</i>	149
5.3.2.1	<i>Volmer–Heyrovsky reaction mechanism</i>	154
5.3.2.2	<i>Volmer–Tafel reaction mechanism</i>	160
5.3.2.3	<i>Turnover Frequencies and Tafel slope calculations</i>	165
5.3.2.4	<i>HOMO-LUMO Calculations</i>	168
5.4	<i>Summary</i>	Error! Bookmark not defined.
6.	Conclusions and Future Perspectives	Error! Bookmark not defined.-176
6.1	<i>Major Conclusion</i>	173
6.2	<i>Future Perspective</i>	175

List of Figures

Figure No.	Figure Captions	Page No.
Figure 1.1	Global energy consumption in 2023. This chart is based on statistical data from the Energy Institute Statistical Review of World Energy. Fossil fuel consumption was 81.5% in 2023.	3
Figure 1.2	A schematic representation of a water electrolysis cell. The diagram illustrates the evolution of hydrogen gas at the cathode surface and oxygen gas at the anode surface.	6
Figure 1.3	H ₂ evolution reaction (HER) mechanism on the surface of a conducting electrode.	11
Figure 3.1	(a) Top view of a 2D Janus WSSe monolayer. The two up and down horizontal dashed lines represent the end points along the (10 $\bar{1}$ 0) W edge and ($\bar{1}$ 010) S-/Se-edge. These two triangles represent the W-edge and S-/Se-edge clusters; (b) schematic diagram of the W-edge cluster; (c) equilibrium geometry of the triangular W-edge cluster with W ₁₀ S ₁₂ Se ₉ stoichiometry.	61
Figure 3.2	Hydrogen adsorption energy at the W-edge of 2D monolayer WSSe JTMD. E _{Cluster} represents the relative electron energy during hydrogen adsorption considering the molecular cluster model system, and E _{Periodic} is the relative electron energy obtained from periodic 2D layer calculations.	65
Figure 3.3	(a) The top view and the side view representation of 2D monolayer WS ₂ with the band structure and total density of states (DOS). (b) The top view and the side view of 2D monolayer WSe ₂ with the band structure and total density of states. (c) The top view and the side view of 2D monolayer Janus WSSe with the band structure and the total density of states are shown here.	70
Figure 3.4	The HER mechanism occurs on the surface of the 2D monolayer WSSe JTMD as the electrocatalyst; the migration of H ⁺ indicates the first TS, highlighted by the blue dashed ellipse. The formation of H ₂ in the Heyrovsky step gives the second TS, highlighted by the red dashed ellipse.	75
Figure 3.5	Equilibrium geometries and change of free energies in the gas phase of (a) [WSSe], (b) [WSSe] ⁻ , (c) [WSSe]H _{Se} , (d) [WSSe]H _{Se} ⁻ , (e) H [*] -migration TS1, (f) [WSSe]H _W ⁻ , (g) [WSSe]H _{Se} H _W , (h) [WSSe]H _{Se} H _W + 3H ₂ O + H ₃ O ⁺ , (i) Heyrovsky TS2, and (j) [WSSe]H _{Se} ⁺ computed by the M06-L DFT method considering a molecular cluster model system W ₁₀ S ₁₂ Se ₉ to represent the 2D monolayer WSSe JTMD are shown here.	80

Figure 3.6	Free energy diagram <i>i.e.</i> , potential energy surface (PES) of the H ₂ evolution reaction followed by the Volmer–Heyrovsky reaction mechanism on the active surface of Janus WSSe in the gas phase is shown here.	82
Figure 3.7	Equilibrium geometries of the [WSSe]H _{Se} H _W and Tafel transition state TS3 occurred during the Volmer-Tafel reaction step with the change in the free energy (<i>i.e.</i> relative free energy or reaction barrier ΔG) about 10.02 kcal.mol ⁻¹ computed in the gas phase are depicted here.	83
Figure 3.8	The equilibrium geometry of the S-edge: [WSSe]H _S ⁻ and TS4 (H*-migration transition states) have been calculated by the M06-L DFT method. The HER occurs at the S-terminal W-edge of the 2D monolayer WSSe JTMD surface.	84
Figure 3.9	The H*-migration or Volmer and Heyrovsky reaction barriers (in the solvent phase) of previous reported 2D monolayer MoS ₂ , WS ₂ , W _{0.4} Mo _{0.6} S ₂ and Mn-MoS ₂ TMDs along with the 2D monolayer pristine WSSe JTMD material are shown here for comparison.	87
Figure 3.10	The equilibrium structure of (a) the HOMO of H*-migration or Volmer TS; (b) The LUMO of H* -migration TS; (c) The HOMO of Heyrovsky TS2; (d) The LUMO of Heyrovsky TS is shown here. The positions of molecular orbitals and hydrogen participating in the subject reaction have been highlighted with dotted circles are shown here.	91
Figure 4.1	(a) Schematic presentation of the periodic 2D monolayer Janus WSeTe TMD material. Two black dotted lines show the ($\bar{1}010$) Se-/Te-edges and ($10\bar{1}0$) W-edges of the 2D monolayer Janus WSeTe TMD. Two triangles show the W-edges and Se-/Te-edges cluster model of the 2D monolayer WSeTe JTMD. (b) The W-edge finite molecular cluster model system (W ₁₀ Se ₉ Te ₁₂) of the 2D WSeTe JTMD is presented here for studying HER.	98
Figure 4.2	Hydrogen adsorption energies on the 2D monolayer WSeTe JTMD. E _{cluster} represents the relative electronic energy during hydrogen adsorption considering the molecular cluster model system and E _{periodic} is the relative electronic energy obtained from the periodic 2D layer calculations.	104
Figure 4.3	(a) Top and side views of the equilibrium structure of the 2D monolayer WSeTe Janus TMD. (b) Band structure and (c) the total density of states (DOS) of the 2D monolayer WSeTe Janus TMD.	108
Figure 4.4	(a) The 2D WSe ₂ TMD monolayer achieves its equilibrium geometry when hydrogen is adsorbed, with an adsorption energy of -2.59 eV; (b) The 2D WTe ₂ TMD monolayer achieves its equilibrium geometry when hydrogen is adsorbed, with an adsorption energy of -3.79 eV; (c) The 2D WSeTe JTMD monolayer achieves its equilibrium geometry when hydrogen is adsorbed, with an adsorption energy of -2.13 eV.	109
Figure 4.5	Volmer-Heyrovsky hydrogen evolution reaction (HER) mechanism pathway on the 2D monolayer Janus WSeTe TMD surface.	112
Figure 4.6	Volmer-Tafel hydrogen evolution reaction (HER) mechanism pathway on the 2D monolayer Janus WSeTe TMD surface.	113

Figure 4.7	Equilibrium structures of various systems appeared during the HER process on the surface of the subject material: (a) [WSeTe], (b) [WSeTe] ⁻ , (c) [WSeTe]H _{Te} , (d) [WSeTe]H _{Te} ⁻ , (e) H*-Migration TS1, (f) [WSeTe]H _W ⁻ , (g) [WSeTe]H _{Te} H _W , (h) [WSeTe]H _{Te} H _W + 3H ₂ O + H ₃ O ⁺ , (i) Heyrovsky TS2, and (j) [WSeTe]H _{Te} ⁺ computed by the M06-L DFT method considering a nonperiodic finite molecular cluster model system W ₁₀ Se ₉ Te ₁₂ to represent the 2D monolayer WSeTe JTMD are displayed here.	116
Figure 4.8	Reaction energy diagram or PES of the Volmer–Heyrovsky reaction mechanism during HER on the surface of the 2D monolayer Janus WSeTe material is presented here. Changes in free energy (ΔG) (in the gas phase) are expressed in kcal mol ⁻¹ .	120
Figure 4.9	Volmer–Tafel reaction mechanism equilibrium geometries of the [WSeTe]H _W H _{Te} and TS3 are shown here.	123
Figure 4.10	Reaction energy diagram or PES of the Volmer–Tafel reaction mechanism during HER on the surface of 2D Janus WSeTe material is depicted here. Changes in the free energy (ΔG) diagram are expressed in kcal mol ⁻¹ .	125
Figure 4.11	(a) HOMO of TS1 during the H*-migration, (b) LUMO of TS1 during the H*-migration, (c) HOMO of TS2 during the Heyrovsky reaction step during H ₂ formation, (d) LUMO of TS2 during the Heyrovsky reaction step during H ₂ formation, (e) HOMO of TS3 during the Tafel reaction step during H ₂ formation, and (f) LUMO of TS3 during the Tafel reaction step during H ₂ formation are shown here.	129
Figure 5.1	(a) The equilibrium 2D monolayer MoTe ₂ TMD with a Te–Mo–Te tri-layer structure. The two horizontal blue color dashed lines indicate terminations along the (10 $\bar{1}$ 0) Mo-edge and ($\bar{1}$ 010) Te-edge. The two triangles represent the terminations for Mo-edge and Te-edge clusters. It includes a non-periodic molecular cluster with an active Te-edge and a non-periodic molecular cluster with an active Mo-edge. (b) The molecular cluster model system of the 2D monolayer MoTe ₂ TMD represented schematically. (c) A side view of the chosen Mo ₁₀ Te ₂₁ non-periodic triangular molecular cluster. (d) A top view of the MoTe ₂ TMD Mo-edge cluster.	138
Figure 5.2	Hydrogen adsorption energies on the 2D monolayer MoTe ₂ TMD. E _{cluster} represents the relative electronic energy during hydrogen adsorption considering the molecular cluster model system and E _{periodic} is the relative electronic energy obtained from the periodic 2D layer calculations.	146
Figure 5.3	(a) The top view and side view of the 2D monolayer MoTe ₂ TMD; (b) electronic band structure and (c) total density of states (DOSs) of the 2D monolayer MoTe ₂ TMD, obtained by the B3LYP-D3 DFT method.	148
Figure 5.4	Volmer–Heyrovsky HER mechanism of the detailed two electron transfer reaction pathways on the surface of the 2D MoTe ₂ material	153
Figure 5.5	The equilibrium geometry of important reaction intermediates and TSs: (a) [MoTe ₂], (b) [MoTe ₂] ⁻¹ , (c) [MoTe ₂]H _{Te} , (d) [MoTe ₂]H _{Te} ⁻¹ , (e) H*-	155

	Migration TS (TS1), (f) $[\text{MoTe}_2]\text{H}_{\text{Mo}}^{-1}$, (g) $[\text{MoTe}_2]\text{H}_{\text{Te}}\text{H}_{\text{Mo}}$, (h) $[\text{MoTe}_2]\text{HTeHMo}+3\text{H}_2\text{O}+\text{H}_3\text{O}^+$, (i) Heyrovsky TS (TS2) and (j) $[\text{MoTe}_2]\text{H}_{\text{Te}}^{+1}$ by M06-L calculation shows the DFT method considering the molecular cluster model system $\text{Mo}_{10}\text{Te}_{21}$ to represent the 2D monolayer of MoTe_2 .	
Figure 5.6	The HER pathway followed by the Volmer–Heyrovsky reaction mechanism is shown here as it occurs during the HER process at the surface of the 2D monolayer MoTe_2 material.	159
Figure 5.7	Volmer–Tafel HER mechanism with the detailed two-electron transfer reaction pathway on the surface of the 2D MoTe_2 material.	161
Figure 5.8	The Volmer–Tafel reaction mechanism equilibrium geometries of $[\text{MoTe}_2]\text{H}_{\text{Mo}}\text{H}_{\text{Te}}$ and TS3 are shown here.	163
Figure 5.9	The PES of the Volmer–Tafel reaction mechanism is shown here as it occurs during the HER process at the surface of the MoTe_2 material.	164
Figure 5.10	The equilibrium structure of MoTe_2 (a) The HOMO of Volmer TS; (b) The LUMO of Volmer TS; (c) The HOMO of Heyrovsky TS; (d) The LUMO of Heyrovsky TS; (e) The HOMO of Tafel TS; (f) The LUMO of Tafel TS is shown here.	169

List of Tables

Table No.	Table Caption	Page No.
Table 3.1	The equilibrium lattice parameter (a), bond distance (d), bond angles, and Band gap (E_g) of the 2D monolayer pristine WS_2 , WSe_2 and Janus $WSSe$ are summarized here.	67
Table 3.2	The changes of electronic energy, enthalpy and Gibbs free energy of the various intermediates in the HER mechanism computed in gas phase are shown here. The HER happens at the Se-terminated W-edges on the surfaces of 2D monolayer $WSSe$ JTMD	81
Table 3.3	The change of free energy (ΔG), enthalpy (ΔH) and electronic energy (ΔE) of the H^* -migration and Heyrovsky reaction steps on the 2D single-layer $WSSe$ JTMD surface during the HER process are listed here.	85
Table 3.4	Comparison of the energy barriers of the H^* -migration and Heyrovsky reaction during HER in the solvent phase with different reported 2D catalysts along with our system of interest are shown here.	86
Table 3.5	The Heyrovsky reaction barriers and TOF for the 2D monolayer MoS_2 , WS_2 , $W_{0.4}Mo_{0.6}S_2$ alloy, $Mn-MoS_2$ and Janus $WSSe$ material calculated at the theoretical level of DFT method in the solvent phase are shown here.	88
Table 4.1	The calculated lattice parameters, bond angle, bond distance, and band gap of the 2D monolayer Janus $WSeTe$ TMD at the equilibrium position.	106
Table 4.2	Energy changes (ΔE , ΔH , and ΔG) of various reaction intermediates and transition state structures (TSs) during the Volmer-Heyrovsky reaction mechanism computed by the M06-L DFT method in gas phase calculations are listed here.	118
Table 4.3	Energy changes (ΔE , ΔH , and ΔG) of the transition states (TS) during the Volmer-Heyrovsky reaction mechanism by computed M06-L DFT method in solvent phase calculations are listed here.	121
Table 4.4	Energy changes (ΔE , ΔH , and ΔG) of different intermediates and transition states (TS) during the Volmer-Tafel reaction mechanism computed by the M06-L DFT method in gas phase are listed here.	123
Table 4.5	Energy (E), Enthalpy (H) and Gibbs free energy (G) for different steps and transition states (TSs) during HER mechanism in the gas phase calculations are tabulated here.	126
Table 4.6	Charge distribution and imaginary frequency count across intermediates and TSs in the HER mechanism.	127
Table 4.7	HOMO and LUMO energy and HOMO-LUMO energy gaps (E_g) of all Transition states (TSs).	130

Table 4.8	Reaction barriers in both gas and solvent phases for various 2D TMDs.	133
Table 5.1	The average equilibrium bond length of the 2D monolayer MoTe ₂ with optimal equilibrium lattice parameters obtained by the DFT-D method.	148
Table 5.2	Relative electronic energy (ΔE), enthalpy (ΔH), and free energy (ΔG) for various intermediates and transition states (TSs) during the HER process followed by the Volmer–Heyrovsky reaction mechanism are computed in the gas phase	157
Table 5.3	Below are tabulated energy changes (ΔE , ΔH , and ΔG) for various intermediates and transition states (TSs) during calculations of the Volmer-Tafel reaction mechanism in the gas phase.	163
Table 5.4	Reaction barriers in both gas and solvent phases for various 2D TMDs.	165
Table 5.5	The Heyrovsky reaction barrier (ΔG) and turnover frequency (TOF) of the 2D monolayer MoS ₂ , WS ₂ , W _{0.4} Mo _{0.6} S ₂ , Mn-MoS ₂ , and MoTe ₂ TMD in the solvent phase are listed here.	167

List of Abbreviations and Symbols

Abbreviations

0D	Zero Dimension
1D	One Dimension
2D	Two Dimension
3D	Three Dimension
AO	Atomic Orbitals
CB	Conduction Bands
CGF	Contracted Gaussian Functions
CO	Crystalline Orbital
DFT	Density Functional Theory
DOS	Density of States
GGA	Generalized Gradient Approximation
GTO	Gaussian-Type Orbitals
GTF	Gaussian Type Functions
HF	Hartree-Fock
HK	Hohenberg-Kohn
HER	Hydrogen Evolution reaction
HOMO	Highest Occupied Molecular Orbital
IRC	Intrinsic Reaction Coordinate
LCAO	Linear Combination of Atomic Orbital
LDA	Local Density Approximation
LSDA	Local Spin-Density Approximation
LUMO	Lowest Unoccupied Molecular Orbital
MO	Molecular Orbitals
NAO	Natural Atomic Orbitals
NHO	Natural Hybrid Orbitals
NBO	Natural Bonding Orbitals
OER	Oxygen Evolution Reaction
VB	Valence Bond Theory
PCM	Polarizable Continuum Model
PES	Potential Energy Surface

PECs	Potential Energy Curves
PDOS	Partial Density of States
RHF	Restricted Hartree-Fock Theory
STO	Slater-Type Orbitals
SCF	Self-Consistent Field
TD-DFT	Time Dependent Density Functional Theory
TM	Transition Metal
TMD	Transition Metal Dichalcogenide
TZVP	Triple-Zeta (Z) Valence with Polarization
UB3LYP-D3	Dispersion Corrected Unrestricted B3LYP Method
vdW	Van Der Waals
VB	Valence Bond Theory
VB	valance bands

Symbols

Ψ	Wavefunction
H	Molecular Hamiltonian operator
E_t	Total energy of the system in the quantum state
\hbar	Reduced Planck constant
M_i	Nuclear masses
e	Elementary charge of electron
m_e	Electron mass
ϵ_0	Dielectric constant in free space
Z	Atomic number of the element
Ha	Hartree
$\Delta p,$	Momentum
Δx	Position
\hat{H}_0	Single-electron Hamiltonian
$\Phi_i(\mathbf{r}_i)$	Product of all the wave function
$\alpha(\xi)$	Spin function
$J_1\Phi(\vec{r})$	Coulomb operator
$K_1\Phi(\vec{r})$	Exchange operator
$c_{\mu i}$	Molecular orbital expansion coefficients

φ_{μ}	Basis functions
ψ_i	Individual molecular orbital
$n(\vec{r})$	Particle density
$n_0(\vec{r})$	Ground state density
$\Psi_0(\vec{r}_1, \dots, \vec{r}_N)$	Ground state wave function
ϵ_i	One-electron energy of a molecular orbital ψ_i
T_s	Non-interacting kinetic energy
V_s	External effective potential
V_{XC}	Exchange correlation potential
E^{XC}	Exchange correlation
E_{XC}^{GGA}	Appropriate GGA functional
E_{XC}	Functionals for exchange and correlation
E_{B3LYP}^{XC}	Becke three parameter exchange and Lee–Yang–Parr correlation functional
E_{hybrid}^{XC}	Hybrid functional
E_{HF}^X	HF exchange functional
E_{LDA}^X	Local density approximation (LDA) exchange functional
η^{STO}	Slater-type orbitals (sto)
η^{GTO}	Gaussian-type orbitals (gto)
β	The orbital exponent
E_{DFT}^{XC}	DFT exchange with correlation functional
E_X^{KS}	KS energy
H	Enthalpy of the systems
E_{elec}	Electronic energy
E_{vib}	Vibrational energy
(ΔH)	Change in enthalpy
(ΔG)	Change in free energy
(ΔE)	Change in electronic energy
ZPE is the	Zero-point vibration energies of the systems
E_{elec}	Electronic energy
E_{vib}	Vibrational energy
$E_{(\text{total})}$	Total energy of per unit cell of intercalated COF

ΔE	Internal energy/ Binding energy
V_{avg}	Working voltage or open circuit voltage
E_g	Electronic band gap
E_F	Fermi energy level
a, b, c	Lattice constants

Abstract

This thesis presents a comprehensive computational investigation into the hydrogen evolution reaction (HER) on the surfaces of two-dimensional (2D) monolayer transition metal dichalcogenides (TMDs) and Janus TMDs. The work aims to understand the structural properties, electronic properties, and electrocatalytic performance toward sustainable hydrogen production.

The first chapter introduces the fundamental principles of electrocatalysis, emphasizing the significance of HER in the context of clean energy technologies. Special attention is given to 2D single layer TMDs as emerging non-noble metal electrocatalysts. The chapter highlights their unique structural and electronic features, such as tunable band gaps and active edge sites, that make them highly promising candidates for HER catalysis.

The second chapter details the computational methodologies employed in the study. A detailed discussion is provided on both the periodic and non-periodic quantum mechanical (QM) approaches based on hybrid density functional theory (DFT) methods. The chapter also covers the theoretical foundations of DFT.

The third chapter focuses on the design and analysis of a 2D Janus WSSe monolayer. Using a periodic hybrid DFT approach, we examined the electronic properties, including band structure and density of states (DOSs). To gain deeper insight into HER activity, we computationally designed a non-periodic molecular cluster model system ($\text{W}_{10}\text{S}_9\text{Se}_{12}$) to simulate the local active edge environments. The HER is a fundamental electrochemical process involving the transfer of two electrons, typically proceeding through three key steps: Volmer, Heyrovsky, and Tafel. This study examined each of these HER steps using transition state (TS) analysis to determine the reaction pathways, energy barriers, and mechanistic insights at the atomic level. The results of this work indicate a preference for the Volmer–Heyrovsky (V-H) mechanism over the Volmer–Tafel (V-T) pathway, with lower associated energy barriers. The change in Gibbs free energy during the reaction process have been computed to determine the energetically preferred reaction pathway, revealing that the 2D monolayer WSSe Janus TMD exhibits excellent HER performance due to its asymmetric surface chemistry and active edge sites.

The fourth chapter extends this approach to a 2D monolayer Janus WSeTe TMD . A molecular cluster model system ($\text{W}_{10}\text{Se}_9\text{Te}_{12}$) has been used to explore the full HER mechanism. Electronic structure and TS calculations have been performed to map the entire reaction energy profile. The results indicate a preference for the Volmer–Tafel (V-T) mechanism over the Volmer–Heyrovsky (V-H) pathway, with lower associated energy barriers, further establishing 2D monolayer WSeTe Janus TMD as a potential HER catalyst.

In the fifth chapter, a pristine 2D MoTe_2 monolayer has been studied using both the periodic and non-periodic DFT techniques. A non-periodic molecular cluster model system ($\text{Mo}_{10}\text{Te}_{21}$) has been computationally designed to simulate HER mechanisms in explicit edge environments. Comprehensive electronic structure analysis, transition state calculations, and Gibbs free energy evaluations have been confirmed the capability of the pristine 2D monolayer MoTe_2 TMD to serve as an efficient HER electrocatalyst. Its remarkable performance arises from favorable electronic interactions and low kinetic barriers across both V-H and V-T pathways.

This thesis provides a systematic and comparative understanding of the HER across Janus and pristine 2D TMDs monolayers. By integrating periodic and non-periodic hybrid DFT approaches, the study thoroughly investigates the electronic structures, TSs, and reaction energetics of key HER mechanisms-Volmer, Heyrovsky, and Tafel on specifically designed non-periodic molecular cluster model systems. Overall, this work advances the computational study of electrocatalysis and establishes a fundamental strategy for designing the next generation of efficient and cost-effective HER electrocatalysts based on non-noble metal 2D TMD materials.

Chapter 1

Introduction and Literature Review

This chapter provides an in-depth exploration of electrocatalysts with a specific focus on the Hydrogen Evolution Reaction (HER) facilitated by two-dimensional Transition Metal Dichalcogenides (2D TMDs). It begins with a comprehensive introduction, offering an overview of 2D TMDs and their relevance in the field of electrochemistry. This section also underscores the importance of HER in energy conversion technologies, setting the stage for the detailed discussions to follow. The chapter proceeds with an extensive literature review, meticulously examining current research, methodologies, and recent advancements in the electrocatalytic applications of 2D TMDs. This review aims to provide a thorough understanding of the state-of-the-art developments in the field highlighting the various approaches and techniques employed by researchers. Furthermore, the chapter delineates the unique contributions of this thesis, emphasizing its novel insights and potential impact on the scientific discourse surrounding HER and 2D TMDs. It aims to position the thesis within the broader context of ongoing research, illustrating how it advances the field and addresses existing gaps. In essence, the abstract sets a comprehensive foundation for the subsequent chapters, preparing the reader for an in-depth exploration and critical analysis of HER on 2D TMDs. This foundational overview ensures that readers are well-equipped to understand the intricate details and implications of the research presented in the following sections of the thesis.

1. Introduction

Modern society is advancing faster than ever. Just over a century ago, we lived without electricity. Now, we rely on many technologies, like laptops, computers, internet, and chemical production, which require constant electricity with power. We currently use 13 TW of energy per year, and this demand is expected to more than triple by the end of the century due to the ever-increasing worldwide population and societal developments with novel technologies. (Armaroli and Balzani, 2007) To meet this growing demand, energy production must be significantly increased. (Owusu and Asumadu-Sarkodie, 2016)

However, with the looming threat of climate change, this expansion must occur without further reliance on fossil fuels. The current energy infrastructure, heavily dependent on fossil fuels such as oil, coal, and natural gas, is unsustainable and detrimental to the environment, as shown in Figure 1.1. (*International Energy Institute (IEI), 2023*) Fossil fuels, such as coal, oil, and natural gas, release harmful greenhouse gases, including carbon dioxide (CO₂), carbon monoxide (CO), and methane (CH₄), which contribute to the environment causing global warming and air pollution. (*Debe, 2012; Kumar and Pakhira, 2023*) Overusing these non-renewable resources has led to severe environmental degradation, exemplified by the ongoing climate crisis. In addition, reserves of fossil fuels are continuously depleted every year. Transitioning to renewable energy sources, such as wind and solar power, is crucial. These sources offer cleaner alternatives to fossil fuels, yet their intermittent nature poses reliability challenges. Thus, significant advancements in clean energy generation processes and storage technologies are essential. (*Krstajic, 2014*) Developing efficient, reliable, and scalable energy solutions will not only help mitigate the adverse impacts of climate change but also ensure a sustainable energy future for the growing demands of modern society. In summary, the rapid growth of modern society necessitates a substantial increase in energy production. A shift towards renewable energy and innovative clean energy technologies is imperative to achieve this without exacerbating climate change. Addressing these challenges will be pivotal in meeting the escalating energy needs while protecting our environment for future generations. (*Krstajic, 2014; Liu, 2015; Khan et al., 2019*)

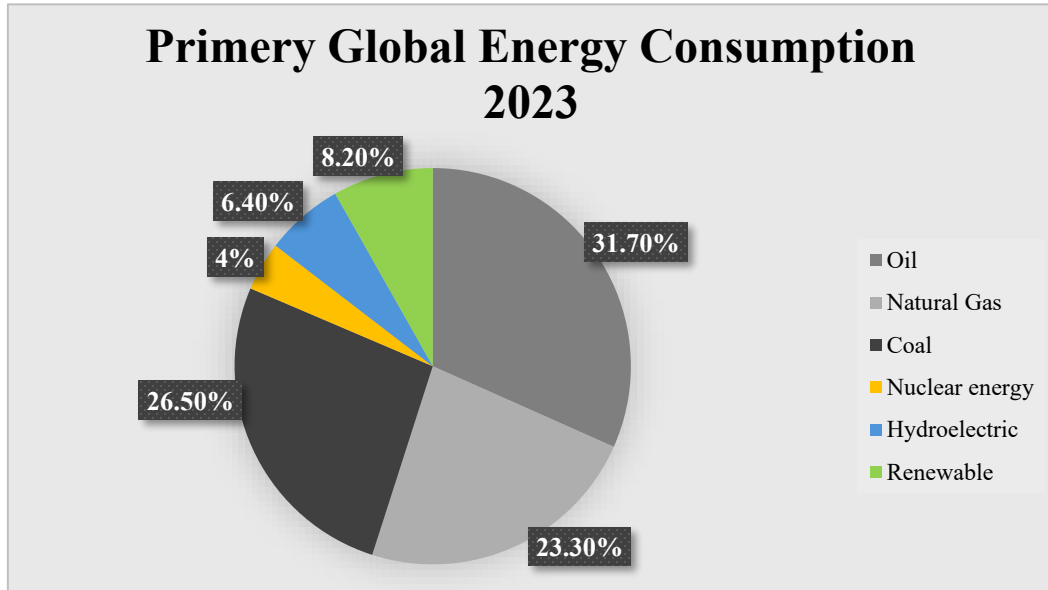


Figure 1.1: Global energy consumption in 2023. This chart is based on statistical data from the Energy Institute Statistical Review of World Energy. Fossil fuel consumption was 81.5% in 2023.

1.1. The Hydrogen Economy

One of the most promising alternatives to fossil fuels, particularly for a mobile society, is utilizing molecular hydrogen as an energy carrier. The "Hydrogen Economy" concept, introduced by John Bockris in 1972, envisions hydrogen as the primary energy source powering homes, transportation, and industrial processes. (Bockris, 2013; Krstajic, 2014) This transition offers a compelling solution to today's energy and environmental challenges by significantly reducing greenhouse gas emissions and decreasing reliance on non-renewable energy sources, paving the way for a sustainable future in energy production and consumption. (Katsounaros and Koper, 2017) Central to this vision is hydrogen as a primary energy carrier, replacing fossil fuels across various applications. Beyond energy production, hydrogen can be used in fuel cells to generate electricity for numerous applications, from powering vehicles to providing backup power for buildings and industries. (Capurso et al., 2022) Fuel cells offer high efficiency and zero carbon emissions, converting hydrogen and oxygen into electricity, water, and heat. Additionally, the potential of hydrogen for efficient storage and transportation addresses the

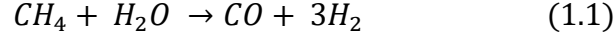
intermittency issues associated with renewable energy sources like solar and wind power.(Bockris, 2013; Staffell et al., 2019; Capurso et al., 2022) Realizing the Hydrogen Economy requires significant technological, infrastructure, and policy advancements. Investment in research and development is essential to enhance efficiency and reduce the costs of hydrogen production, storage, and distribution. Developing a robust hydrogen infrastructure, including pipelines, refueling stations, and storage facilities, is critical for widespread adoption. Supportive policies and regulations are also necessary to create a favorable market environment for hydrogen technologies.(Lei, Pakhira, Fujisawa, Wang, Iyiola, Perea López, et al., 2017; Kumar and Pakhira, 2023; Shilpa et al., 2023)

However, the current status of hydrogen production seriously hinders the realization of this goal. The natural gas steam reforming process emits large amounts of carbon dioxide and other greenhouse gases into the environment, yet it produces about 95% of hydrogen.(Upadhyay and Pakhira, 2021a; Kumar and Pakhira, 2023; Shilpa et al., 2023) The remaining hydrogen is produced by electrolysis of water, a cleaner process, but only a small fraction of it is produced globally. For the hydrogen economy to be truly sustainable and ecologically sound, hydrogen production must shift to renewable energy sources. This involves using renewable energy such as solar, wind, and hydroelectric power to fuel the electrolysis process to produce hydrogen. These technologies can significantly reduce the carbon footprint by producing hydrogen without releasing greenhouse gases.(Nasser et al., 2022) Furthermore, innovative technologies for producing green hydrogen, such as biomass gasification and electrochemical water splitting, offer promising avenues for development. A sustainable hydrogen economy can benefit significantly from investment and increased use of these cutting-edge technologies.

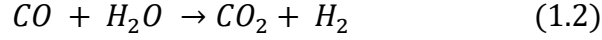
1.2. Methods of Hydrogen Production

1.2.1. Steam Reforming of Natural Gas:

At present, the most common method for producing commercial hydrogen is through the steam reforming of natural gas, as depicted in Equations 1.1 and 1.2.(LeValley, Richard and Fan, 2014) This process involves a high-temperature reaction where methane reacts with steam, yielding a mixture of carbon monoxide and hydrogen, also known as syngas:



To further enhance the hydrogen yield, the carbon monoxide in the syngas can undergo the Water-Gas Shift Reaction with water vapor, which converts it into carbon dioxide and additional hydrogen:



These processes not only produce hydrogen but also release large amounts of CO and CO₂, causing serious damage to the environment. This approach is unsustainable and harmful to the environment. Therefore, the long-term viability of steam reforming is highly questionable. Nevertheless, despite the adverse effects, producing hydrogen from carbon sources is still more cost-effective than renewable alternatives. (*Kumar et al., 2024; Vesborg, Seger and Chorkendorff, 2015; Eftekhari, 2017*)

1.2.2. Water Electrolysis:

Water electrolysis is a process that uses electrical energy to split water (H₂O) into its constituent gases, hydrogen (H₂) and oxygen (O₂). This method is highly promising for producing green hydrogen, particularly when the electricity used is derived from renewable sources such as solar, wind or hydroelectric power. Water electrolysis offers a clean and sustainable pathway for hydrogen production, which is crucial for the development of a hydrogen economy. A typical water electrolysis cell, depicted in Figure 1.2, comprises two electrodes: a cathode and an anode, both immersed in a conductive aqueous electrolyte. When a sufficient voltage is applied across the electrodes, an electric current is established. Electrons travel through the external circuit towards the cathode, while ions within the electrolyte facilitate the electrolysis process by moving between the electrodes. At the cathode, a reduction reaction known as the hydrogen evolution reaction (HER) occurs. During this process, water molecules gain electrons to form hydrogen gas (H₂) and hydroxide ions (OH⁻). Conversely, at the anode, an oxidation reaction called the oxygen evolution reaction (OER) takes place. In this reaction, water molecules lose electrons to form oxygen gas (O₂) and hydrogen ions (H⁺). (*Kumar and Pakhira, 2023, 2025; Pakhira, Kumar and Ghosh, 2023; Shilpa et al., 2023*)

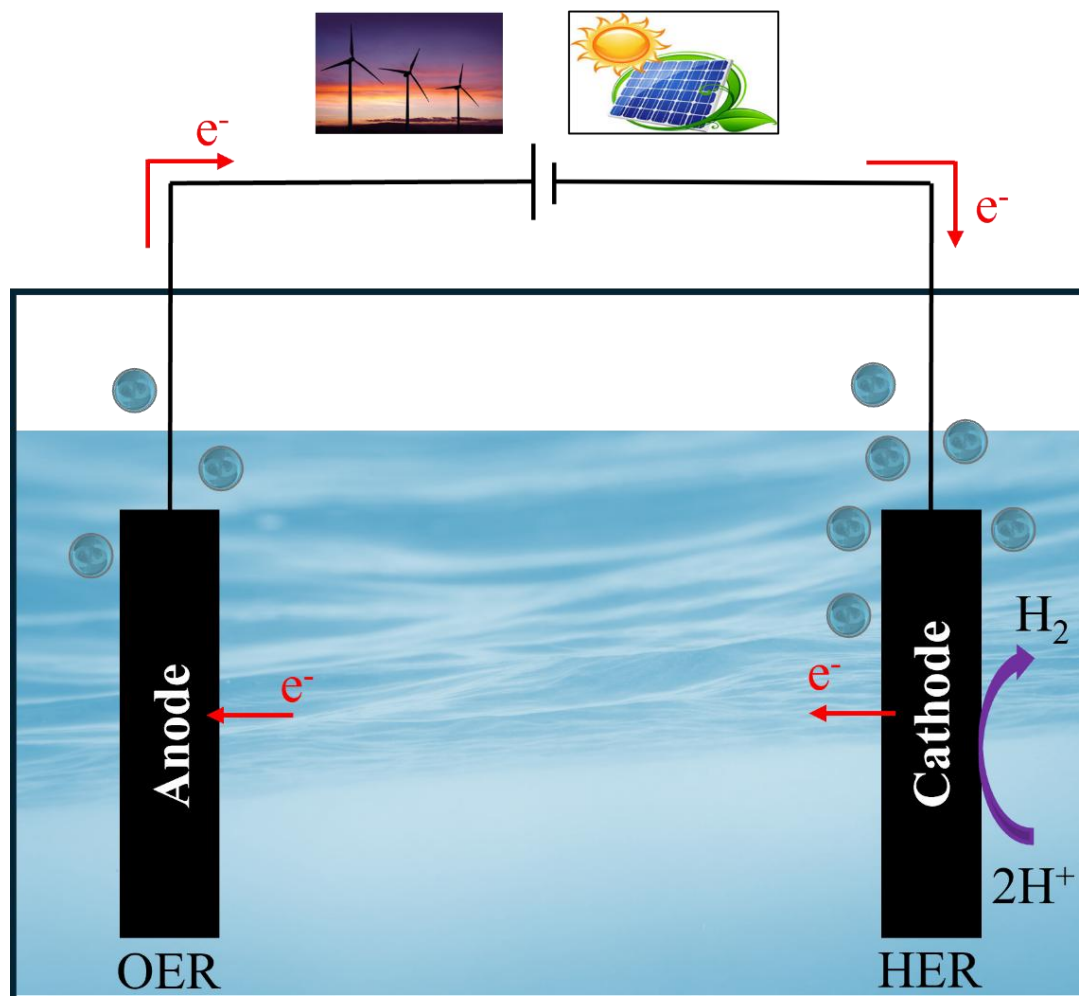
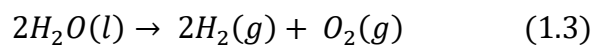


Figure 1.2: A schematic representation of a water electrolysis cell. The diagram illustrates the evolution of hydrogen gas at the cathode surface and oxygen gas at the anode surface.

Basic Principles of Water Electrolysis:

The basic principle of water electrolysis involves passing an electric current through water to cause a chemical reaction that splits water molecules into hydrogen and oxygen gases. (Ekka *et al.*, 2022; Kumar and Pakhira, 2023) The overall reaction for water electrolysis can be represented as:



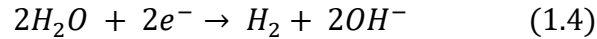
This process occurs in an electrolyzer with two electrodes (an anode and a cathode) submerged in an electrolyte solution. The electrolyte facilitates the movement of ions within the solution, enhancing the efficiency of the electrolysis process.

Types of Electrolyzers:

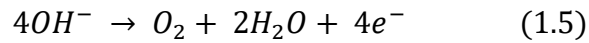
There are three main types of electrolyzers used for water electrolysis: *(Mohammadi and Mehrpooya, 2018)*

1. **Alkaline Electrolyzers:** Alkaline electrolyzers use a liquid alkaline solution (usually potassium hydroxide (KOH) or sodium hydroxide (NaOH)) as the electrolyte. This type of electrolyzer has been used for many years and is known for its durability and relatively low cost. The reactions at the electrodes in an alkaline electrolyzer are as follows:

- **Cathode (reduction):**

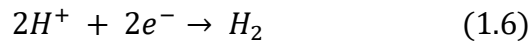


- **Anode (oxidation):**

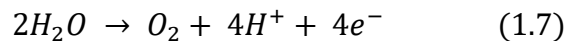


2. **Proton Exchange Membrane (PEM) Electrolyzers:** PEM electrolyzers use a solid polymer electrolyte (a proton exchange membrane) to conduct protons from the anode to the cathode and to separate the product gases. This type of electrolyzer offers several advantages, including higher efficiency, higher hydrogen purity, and quicker response times. The reactions at the electrodes in a PEM electrolyzer are:

- **Cathode (reduction):**

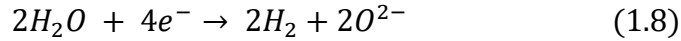


- **Anode (oxidation):**



3. **Solid Oxide Electrolyzers (SOE):** Solid oxide electrolyzers operate at high temperatures (typically between 700°C and 1000°C) and use a solid oxide or ceramic material as the electrolyte. This high-temperature operation allows for higher electrical efficiency and the possibility of utilizing waste heat from other processes. The reactions at the electrodes in a solid oxide electrolyzer are:

- **Cathode (reduction):**



- **Anode (oxidation):**



Advantages of Water Electrolysis:

1. **Environmental Benefits:** Water electrolysis produces hydrogen without emitting greenhouse gases if powered by renewable energy sources. This makes it a key technology for reducing carbon emissions and combating climate change.
2. **High-Purity Hydrogen:** The hydrogen produced by electrolysis is of high purity, which is essential for applications in fuel cells and other advanced technologies.
3. **Scalability:** Electrolyzers can be scaled to match the size and capacity required for different applications, from small-scale distributed hydrogen production to large industrial plants.
4. **Integration with Renewable Energy:** Electrolyzers can be integrated with renewable energy systems, utilizing excess electricity generated by solar and wind farms. This not only provides a method for storing renewable energy but also enhances the overall efficiency of renewable energy utilization.

Challenges and Developments:

1. **Cost:** One of the primary challenges of water electrolysis is the high cost associated with the electrolyzers and the electricity is required for the process. Reducing these

costs through technological advancements and economies of scale is crucial for making electrolysis a commercially viable option.

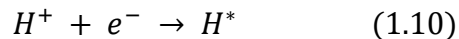
2. **Efficiency:** Improving the efficiency of electrolyzers is an ongoing area of research. Advances in materials science and electrochemical engineering are aimed at developing more efficient and durable electrolyzers.
3. **Infrastructure:** Developing the infrastructure for hydrogen production, H₂-storage, and distribution is essential for the widespread adoption of hydrogen as an energy carrier. This includes building refueling stations, pipelines, and storage facilities.
4. **Policy and Regulation:** Supportive policies and regulations are needed to create a favorable market environment for hydrogen technologies. This includes incentives for renewable energy integration, research and development funding, and hydrogen production and usage standards.

1.3. Hydrogen Evolution Reaction (HER) Mechanism:

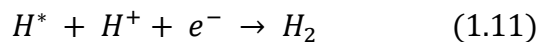
HER is a critical electrochemical process that takes place at the cathode during water electrolysis. The reaction mechanism can be described in several steps, involving adsorption, electron transfer, and desorption processes. For hydrogen to evolve, it must first adsorb onto the surface of the electrocatalyst where the reaction occurs, and then desorb to release the hydrogen gas. There are two possible mechanisms for hydrogen evolution, each involving three steps: the Volmer-Tafel (V-T) and the Volmer-Heyrovsky (V-H) mechanisms. *(Kumar and Pakhira, 2023; Pakhira, Kumar and Ghosh, 2023; Kumar et al., 2024)*

1. Volmer Step (Adsorption): In the initial step of the HER, a water molecule adsorbed on the cathode surface dissociates into a proton (H⁺) and a hydroxide ion (OH⁻). The proton migrates to the electrocatalyst surface, where it is adsorbed and subsequently reduced by an electron supplied from the external circuit, resulting in the formation of an adsorbed hydrogen atom (H*) bonded to the electrocatalyst surface, as illustrated in Figure 1.3. The Volmer step plays a crucial role in determining the overall reaction kinetics and is highly

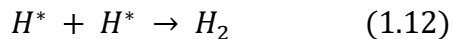
sensitive to the surface properties of the electrocatalyst, including active site availability, electronic structure, and hydrogen adsorption energetics.



2. Heyrovsky Step (Electrochemical Desorption): In the Heyrovsky step, an adsorbed hydrogen atom (H^*) reacts with a proton (H^+) from the solution (here only water) and an electron from the cathode to form a hydrogen molecule (H_2), subsequently desorbs from the electrocatalyst surface, as illustrated in Figure 1.3. The reaction rate of this step and the initial Volmer step critically govern the overall hydrogen evolution efficiency. The ability of the electrocatalyst to facilitate both proton-electron transfer and H_2 desorption significantly impacts the reaction kinetics.



3. Tafel Step (Chemical Desorption): In this alternative pathway for H_2 evolution, two adsorbed hydrogen atoms (H^*) recombine on the electrocatalyst surface to form a hydrogen molecule (H_2), which then desorbs from the cathode surface, as shown in Figure 1.3. This purely chemical step does not involve electron transfer and typically occurs on surfaces where the coverage of H^* is sufficiently high to enable recombination. The efficiency of the Tafel step depends on the mobility and binding strength of H^* on the surface, as well as the ability of the electrocatalyst to facilitate H-H bond formation, all of which are critical factors influencing the overall rate of the hydrogen evolution reaction.



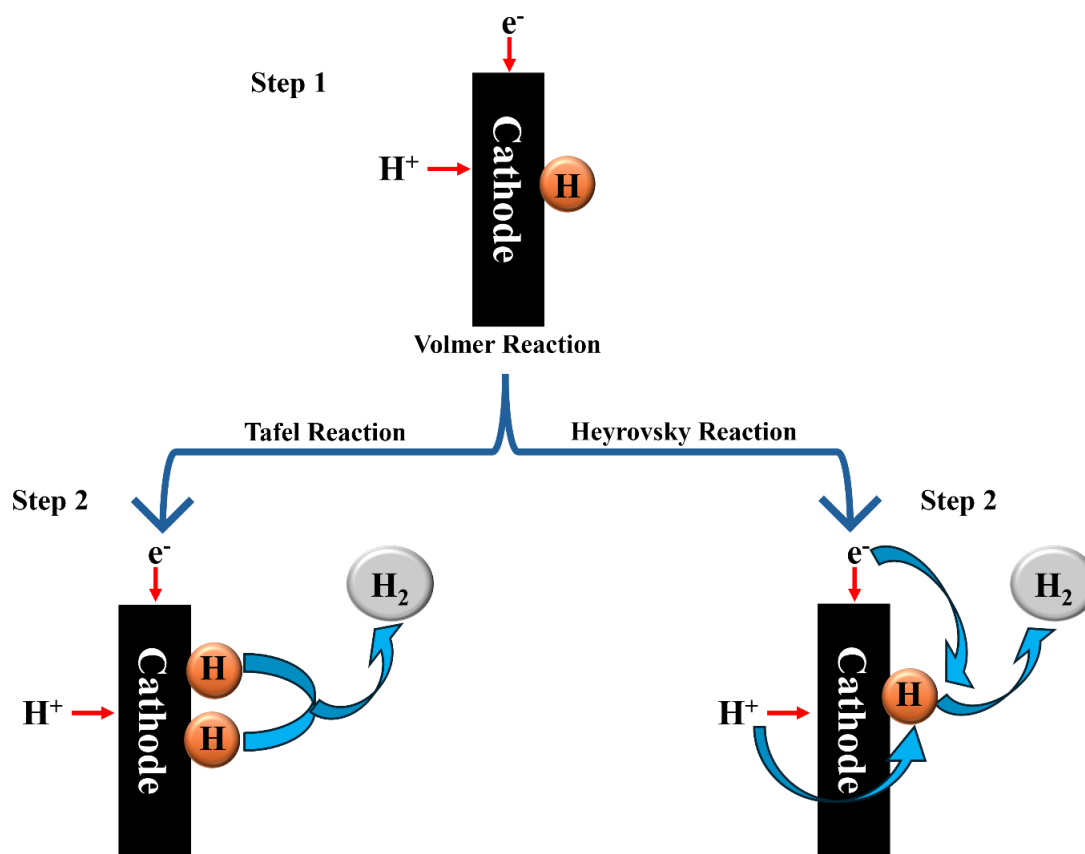


Figure 1.3: H_2 evolution reaction (HER) mechanism on the surface of a conducting electrode.

In summary, the HER involves the adsorption of water molecules, the transfer of electrons to form adsorbed hydrogen atoms, and the eventual desorption of hydrogen gas molecules. The efficiency of this reaction is influenced by the nature of the electrode material. Understanding and optimizing these factors are crucial for enhancing the performance of water electrolysis systems.^(Krstajic, 2014; Shilpa et al., 2023) To evaluate and improve HER performance, it is essential to analyze specific activity parameters that reflect the catalytic behavior of electrode materials under reaction conditions. These metrics provide fundamental insights into the catalytic process while enabling direct comparison between different materials.

1.4. HER Activity Parameters

Several key parameters influence the performance of an electrocatalyst for the HER. Understanding these parameters helps optimize the efficiency of the HER and improve the overall performance of electrolysis systems. Here are the critical parameters for the HER mechanism:

1. Overpotential (η): Overpotential refers to the additional voltage required beyond the thermodynamic equilibrium potential to drive the HER at a given rate. Since the equilibrium potential for HER is typically 0 V versus the reversible hydrogen electrode (RHE), any extra voltage applied represents the energy needed to overcome kinetic barriers.[\(Anantharaj et al., 2018\)](#) A lower overpotential is highly desirable, as it indicates superior catalytic efficiency, reducing the additional energy required to sustain the reaction and thereby improving overall energy efficiency. It also plays a crucial role in determining catalyst performance, as catalysts with lower overpotentials can achieve higher current densities at lower applied potentials, making them more suitable for practical electrolysis applications. Moreover, overpotential serves as a key indicator of reaction kinetics, providing insights into the energy barriers that must be overcome for HER to proceed effectively. By minimizing overpotential, researchers can develop advanced electrocatalysts that enhance hydrogen production while significantly reducing energy consumption, paving the way for more efficient and sustainable hydrogen generation technologies.[\(Nazari and Ghaemmaghami, 2023\)](#)

2. Tafel Slope: The Tafel slope is a fundamental parameter in electrochemical kinetics that can be theoretically determined based on the number of electrons transferred during the HER. Assuming that the reaction rate is not limited by direct electron transfer from the support to the catalyst, the Tafel slope is given by the equation $m = 2.303 \left(\frac{RT}{nF} \right)$, where R is the universal gas constant, T is the room temperature (considered constant for calculations), F is the Faraday constant (96485 C mol^{-1}), and n is the number of electrons involved in the process. The Tafel slope is crucial for understanding the HER mechanism, as it provides insights into the rate-determining step. Additionally, the Tafel slope is instrumental in kinetic analysis, helping to determine whether the HER is controlled by

electron transfer or by hydrogen adsorption and desorption processes. By analyzing the Tafel slope, researchers can optimize electrocatalysts for improved efficiency and faster reaction rates in hydrogen production. (Kumar and Pakhira, 2023; Pakhira, Kumar and Ghosh, 2023; Kumar et al., 2024)

3. Gibbs Free Energy (ΔG): The change of Gibbs free energy (ΔG) for the HER represents the change in free energy associated with the formation of hydrogen gas (H_2) from protons and electrons under standard conditions. It is a crucial thermodynamic parameter that determines whether the reaction will proceed spontaneously. (Lei, Pakhira, Fujisawa, Wang, Iyiola, Perea López, et al., 2017; Ekka et al., 2022) For HER, ΔG should be negative, indicating that the process is thermodynamically favorable. The magnitude of ΔG also plays a significant role in catalyst design, particularly in understanding the hydrogen adsorption-free energy (ΔG_{H^*}) on the catalyst surface. An ideal catalyst should have a ΔG_{H^*} value close to zero, ensuring a balance between hydrogen adsorption and desorption, which optimizes reaction efficiency. Moreover, a lower (more negative) ΔG value for the overall process signifies reduced energy loss.

4. Electrode Surface Area: The electrode surface area refers to the total available surface on the electrode where the HER can take place. It plays a critical role in determining the efficiency and performance of electrocatalysts. A larger surface area provides more active sites for the reaction, thereby enhancing catalytic activity and improving hydrogen production rates. The structural properties of electrode materials significantly influence surface area; for instance, porous materials or nanostructured catalysts are often employed to maximize active site availability. These high-surface-area materials facilitate greater interaction between the electrode and reactants, leading to improved reaction kinetics and overall efficiency. By optimizing the electrode surface area, researchers can enhance HER performance, making electrolysis systems more effective for large-scale hydrogen production. (Lei, Pakhira, Fujisawa, Wang, Iyiola, Perea López, et al., 2017; Ekka et al., 2022; Upadhyay and Pakhira, 2022; Pakhira, Kumar and Ghosh, 2023)

5. Catalyst Stability: Catalyst stability refers to the ability of an electrocatalyst to maintain its structural integrity and performance over extended periods under operating conditions.

Stability is a crucial factor in determining the long-term efficiency and reliability of HER catalysts. A highly stable catalyst ensures durability, allowing it to function efficiently without significant degradation, loss of activity, or structural changes over time. This is particularly important for large-scale hydrogen production, where consistent performance is essential. Additionally, catalyst stability directly impacts economic viability, as more stable materials reduce the need for frequent replacement, thereby lowering operational costs and improving the overall sustainability of electrolysis systems. Enhancing catalyst stability through material optimization and protective strategies is essential for developing cost-effective and long-lasting HER technologies. (Lei, Pakhira, Fujisawa, Wang, Iyiola, Perea López, et al., 2017; Ekka et al., 2022; Upadhyay and Pakhira, 2022; Pakhira, Kumar and Ghosh, 2023)

6. pH of the Electrolyte: The pH of the electrolyte is a measure of its acidity or alkalinity and plays a crucial role in the HER by influencing both catalyst selection and reaction pathways. Different electrocatalysts exhibit varying performance depending on the pH of the medium. For instance, platinum is highly effective in acidic conditions, whereas non-precious metals like nickel (Ni) perform better in alkaline environments. The pH also affects the reaction mechanism, dictating whether the HER follows the Volmer-Heyrovsky (V-H) or Volmer-Tafel (V-T) reaction pathway. Additionally, it impacts the stability of intermediate species formed during the reaction, which in turn affects overall reaction kinetics and efficiency. Optimizing the pH of the electrolyte is essential for ensuring maximum catalytic activity, stability, and efficiency in electrolysis systems designed for H₂ production. (Lei, Pakhira, Fujisawa, Wang, Iyiola, Perea López, et al., 2017; Ekka et al., 2022; Upadhyay and Pakhira, 2022; Pakhira, Kumar and Ghosh, 2023)

7. Conductivity of the Electrode Material: The conductivity of the electrode material refers to its ability to efficiently transport electrical current, which is a critical factor in determining the performance of the HER. High electrical conductivity facilitates efficient electron transfer during the reaction, reducing resistive losses and enhancing overall catalytic efficiency. Conversely, lower conductivity can lead to increased resistance, limiting the reaction rate and reducing energy efficiency. Therefore, selecting materials with excellent conductivity is essential for optimizing HER performance. Metals such as

platinum, gold, and nickel, as well as certain carbon-based materials like graphene and carbon nanotubes, are commonly used as electrode materials due to their superior conductivity. By choosing highly conductive materials, researchers can improve charge transfer processes, minimize energy losses, and enhance the overall efficiency of electrolysis systems for hydrogen production. *(Krstajic, 2014; Lei, Pakhira, Fujisawa, Wang, Iyiola, Perea López, et al., 2017; Ekka et al., 2022; Pakhira, Kumar and Ghosh, 2023; Kumar et al., 2024; Kumar and Pakhira, 2025)*

8. Turnover Frequency (TOF): Turnover Frequency (TOF) is a critical parameter used to evaluate the catalytic activity of electrocatalysts in the HER. It represents the number of hydrogen molecules produced per active site per unit time, providing a direct measure of catalyst efficiency. The formula gives the theoretical determination of TOF:

$$rate = \frac{(k_B T)}{h} \times \exp\left(-\frac{\Delta G}{RT}\right)$$

Where the symbol k_B represents the Boltzmann constant ($1.381 \times 10^{-23} \text{ J K}^{-1}$), T is the temperature in the absolute scale (here it is kept as a constant with an absolute scale value of 298.15 K throughout the non-periodic cluster model calculation), R is the universal gas constant ($8.314 \text{ J mol}^{-1} \text{ K}^{-1}$), h is the Planck's constant ($6.623 \times 10^{-34} \text{ J s}^{-1}$), and ΔG corresponds to the energy barriers. A higher value of TOF signifies a more efficient catalyst, as it indicates that each active site is capable of producing hydrogen at a faster rate. This parameter serves as a valuable comparison metric for assessing the relative activities of different catalysts on a per-active site basis, offering a more accurate evaluation than bulk current measurements. Understanding the TOF also aids in elucidating reaction kinetics and identifying highly active catalytic sites. Furthermore, optimizing TOF values is essential for designing and synthesizing highly efficient electrocatalysts, as it highlights the importance of maximizing active site utilization to enhance hydrogen production. *(Krstajic, 2014; Lei, Pakhira, Fujisawa, Wang, Iyiola, Perea López, et al., 2017; Ekka et al., 2022; Nazari and Ghaemmaghami, 2023; Pakhira, Kumar and Ghosh, 2023; Kumar et al., 2024; Kumar and Pakhira, 2025)*

1.5. Electrocatalyst for HER

1.5.1. Metal-Based HER Electrocatalysts: Metal-based electrocatalysts are among the most studied materials for the HER due to their diverse properties and ability to catalyze the reaction efficiently. These catalysts can be broadly categorized into noble metals, transition metals, and metal alloys.

1.5.1.1. Noble Metals in HER Electrocatalysis

1. Platinum (Pt): Platinum (Pt) is widely regarded as the benchmark for HER electrocatalysts due to its near-optimal hydrogen adsorption energy, which enables exceptional catalytic activity. Its stability across both acidic and alkaline environments makes it ideal for long-term use in various electrochemical applications. However, the primary limitation of Pt is its scarcity and high cost, which restricts its practicality for large-scale applications. *(Greeley et al., 2006; Zhu et al., 2019)*

2. Palladium (Pd): Palladium (Pd) shares similar electronic properties with platinum, resulting in good HER activity. It is stable in acidic environments, although it exhibits reduced stability in alkaline conditions. While slightly more abundant than platinum, palladium remains expensive, limiting its widespread use in large-scale applications. *(Bhowmik, Kundu and Barman, 2016; Zhu et al., 2019)*

3. Rhodium (Rh) and Iridium (Ir): Rhodium (Rh) and Iridium (Ir) are highly effective electrocatalysts for the HER, demonstrating excellent activity, especially in acidic media. Their high stability under harsh electrochemical conditions further enhances their suitability for demanding applications. However, Rh and Ir are even rarer and more expensive than platinum, significantly limiting their practicality for large-scale hydrogen production despite their superior performance. *(Zhu et al., 2019)*

1.5.1.2. Non-Noble Metals in HER Electrocatalysis: Non-noble metals, such as nickel (Ni), cobalt (Co), and iron (Fe), have gained significant attention as alternatives to noble metals for HER electrocatalysis. These metals offer a more cost-effective and abundant option while still delivering promising catalytic performance.

1. Nickel (Ni): Ni is one of the most widely used non-noble metals in HER, particularly in alkaline media. It exhibits good catalytic activity and relatively low overpotentials, making it a practical choice for industrial applications. Additionally, nickel's abundance and low cost make it an attractive option for large-scale hydrogen production. However, its stability in acidic environments is less robust, which has led to the development of nickel-based alloys and composites to enhance its performance and durability across different pH levels. *(Miles and Thomason, 1976; Zhu et al., 2019)*

2. Cobalt (Co): Co is another non-noble metal with strong potential as an HER catalyst, especially in alkaline solutions. Cobalt-based materials, including oxides, sulfides, and phosphides, have demonstrated good activity and stability. While cobalt is more expensive than nickel, it is still significantly cheaper than noble metals, and its catalytic properties can be further enhanced through alloying and surface modifications. *(Miles and Thomason, 1976; Zhu et al., 2019)*

3. Iron (Fe): Fe is the most abundant and inexpensive of the non-noble metals, making it a highly attractive candidate for sustainable HER electrocatalysis. Although pure iron is not as active as nickel or cobalt, it can be combined with other elements to form alloys or compounds that exhibit improved catalytic properties. For example, iron-nickel alloys and iron-based phosphides have shown promising results in HER performance. *(Pan et al., 2016; Zhu et al., 2019)*

Overall, Non-noble metals offer a promising and scalable alternative to noble metals for HER electrocatalysis. Although they may not achieve the same level of activity as platinum and other noble metals, their abundance, cost-effectiveness, and potential for enhanced performance through alloying and composite formation position them as essential materials in the quest for affordable and sustainable hydrogen production. Through strategic approaches such as doping, alloying, and composite formation, the catalytic performance of non-noble metals can be significantly enhanced, improving their stability, conductivity, and adsorption kinetics for hydrogen intermediates. These advancements position non-noble metal-based catalysts as viable candidates for replacing expensive noble metals,

contributing to the development of cost-effective and sustainable electrocatalytic systems for clean energy applications.

1.5.2. Non-Noble Metal Compound-Based HER Electrocatalysts: Non-noble metal compounds have emerged as promising alternatives for HER electrocatalysts due to their cost-effectiveness, abundance, and potential for high catalytic activity. Transition metal compounds such as oxides, nitrides, carbides, dichalcogenides, phosphides, and borides, particularly those based on molybdenum (Mo) and tungsten (W), have shown significant promise in replacing noble metals in HER applications due to their favorable catalytic properties and potential for structural and electronic modulation.[\(Zhu et al., 2019\)](#) Here's an overview of some notable non-noble metal compound-based HER electrocatalysts:

1. Oxides: Transition metal oxides, such as MoO_3 and WO_3 , have been explored for HER due to their stability and tunable electronic properties. These oxides can be modified through doping or defect engineering to enhance their catalytic activity, making them competitive alternatives to noble metal catalysts.[\(Ghosh and Basu, 2018\)](#)

2. Nitrides: Metal nitrides, including MoN and VN , exhibit excellent electrical conductivity and strong bonding with hydrogen, which are critical for efficient HER. Their robust structure and high catalytic efficiency make them promising candidates for sustainable hydrogen production.[\(Zhang et al., 2022\)](#)

3. Carbides: Transition metal carbides like Mo_2C and WC are known for their high hardness, chemical stability, and catalytic activity like that of platinum. These materials can be synthesized with various morphologies to optimize their surface area and catalytic performance.[\(Michalsky, Zhang and Peterson, 2014\)](#)

4. Dichalcogenides: Molybdenum disulfide (MoS_2) and tungsten diselenide (WSe_2) are prime examples of dichalcogenides which have attracted much attention for HER. Their layered structure and the presence of active edge sites contribute to their high catalytic activity, especially when combined with techniques like exfoliation or phase engineering.[\(Morales-Guio, Stern and Hu, 2014; Jin et al., 2018\)](#)

5. Phosphides: Metal phosphides, such as Ni₂P and CoP, are highly active HER catalysts due to their excellent electrical conductivity and strong metal-phosphorus bonds, which facilitate efficient H₂ evolution. These materials can be further optimized by alloying or incorporating other elements.*(Ghosh and Basu, 2018)*

6. Borides: Transition metal borides, including MoB and WB, are recognized for their mechanical strength and high conductivity. Their unique electronic structure enables efficient hydrogen adsorption and desorption, making them valuable for HER applications.*(Gupta et al., 2020)*

1.6. Research Gap and Motivation:

The pressing need for renewable and green energy sources to replace conventional fossil fuels has become a major focus for researchers across various fields of science and technology. Currently, the majority of our energy demands is met by traditional sources such as coal, petroleum, and natural gas, which are notorious for emitting greenhouse gases and contributing to environmental pollution. The widespread use of these fossil fuels has exacerbated global climate change, highlighting the urgent need for alternative energy solutions. Clean energy generation, along with high-capacity energy storage devices and efficient manufacturing processes, are critical in addressing these challenges. Among the promising technologies for sustainable energy are fuel cells, electrochemical water splitting, and metal-air batteries (MABs). Electrochemical water splitting, in particular, is a potential candidate for hydrogen production, offering high energy density and environmental friendliness. However, an efficient electrocatalyst is crucial for enhancing the kinetics of the HER, a key process in water splitting. Currently, platinum group metals (PGMs), particularly platinum (Pt), dominate the field as the most effective electrocatalysts for HER. Despite their superior catalytic activity, PGMs suffer from significant drawbacks such as high cost, poor stability, low durability, and susceptibility to poisoning, which severely limit their scalability and commercial viability.*(Katsounaros and Koper, 2017; Pakhira and Upadhyay, 2022; Kumar and Pakhira, 2025)*

Recently, it has been found that the 2D transition metal dichalcogenides (TMDs) can be adopted as efficient electrocatalytic materials, which can be used as an ideal alternative to Pt noble metal-based electrocatalyst for HER. 2D monolayered TMDs have several advantages, especially low cost, high abundance, and high efficiency in electrocatalytic activity for HER. 2D TMDs have a large surface area, and tuning their electronic structures and properties is possible. (Loo *et al.*, 2015; Katsounaros and Koper, 2017; Lei, Pakhira, Fujisawa, Wang, Iyiola, Perea López, *et al.*, 2017; Ekka *et al.*, 2022; Pakhira and Upadhyay, 2022; Kumar and Pakhira, 2025) TMDs usually have MX_2 chemical formula where M represents a transition metal (TM) from group IV-VII like Mo, W, etc. and X represents a chalcogen (S, Se, and Te). Their structural unit consists of a transition metal atomic plane sandwiched between two chalcogen planes and weak van der Waals (vdW) forces holding two successive MX_2 layers. These weak vdW interactions and forces significantly determine their structural phases, properties, equilibrium structures, and spectroscopic properties. However, with the exploitation of graphene and other 2D materials with unusual properties different from their bulk system, these TMD materials, especially 2D monolayer molybdenum disulfide (MoS_2) and tungsten disulfide (WS_2) have begun to gain attention as efficient HER catalysts. In the recent few decades, the discovery of chemical, electronic, and structural properties of 2D TMDs has significantly improved the basic understanding of the electrocatalysis process in HER. However, compared with the inert basal sites, the entire catalytic execution of the pristine TMDs rooted catalysts is constrained due to the relatively small proportion of active edge, and the carrier mobility of the charge carriers in TMDs is relatively low resulting in a lower electrolysis activity and also hinders its many other applications. Due to the lack of metal edge sites and electron transport efficiency in multilayer TMDs, the hydrogen production research efficiency of these catalytic materials has been hindered. As the scarcity of active edge sites on these catalysts is one of the main obstacles to H_2 production, the main challenge is to activate the surface of these substrates through enhancement of the number of substrate surface sites and, hence the catalytic activity. Several attempts have been made to activate the basal planes (001) of the pristine 2D TMDs by phase engineering, applying strain, doping, and vacancy creation. (Katsounaros and Koper, 2017; Lei, Pakhira, Fujisawa, Wang, Iyiola, Perea López, *et al.*, 2017)

Recently, Janus TMDs, such as 2D monolayer MoSSe and WSSe, have emerged as promising candidates for electrocatalysis in HER. These Janus structures possess an inherent asymmetry due to the different chalcogen atoms on each side of the transition metal layer, leading to unique electronic properties, built-in dipole moments, and enhanced catalytic activity. The broken symmetry in Janus TMDs results in improved charge transfer and optimized hydrogen adsorption energy, making them highly attractive for HER applications. By further exploring the activation of basal planes and the intrinsic properties of Janus TMDs, this study aims to develop the next generation electrocatalysts with superior performance and stability for efficient hydrogen production. *(Pakhira and Upadhyay, 2022; Kumar et al., 2024)*

2D TMDs have garnered considerable attention in materials science and engineering due to their unique structural, electronic, and catalytic properties, particularly for the HER. Their hexagonal symmetry, tunable electronic characteristics, and high surface-to-volume ratio make them promising alternatives to conventional platinum-based catalysts. *(Lei, Pakhira, Fujisawa, Wang, Iyiola, Perea López, et al., 2017)* Among various TMDs, 2D monolayer MoS₂ has emerged as a standout candidate, demonstrating exceptional HER performance in acidic media with an overpotential as low as 0.1-0.2 V, comparable to Pt-based systems. *(Hinnemann et al., 2005)* This catalytic efficiency is attributed to its near-thermoneutral hydrogen adsorption energy, which ensures optimal binding and release of hydrogen intermediates. Further investigations using first-principles density functional theory (DFT) method by Huang et al. have elucidated the HER reaction pathways and energy barriers on MoS₂ surfaces, providing deeper mechanistic insights. Beyond conventional TMDs, Janus-structured MoSSe, an asymmetric monolayer with S and Se on opposite faces, has recently gained attention due to its enhanced catalytic properties. As demonstrated in recent studies, the intrinsic dipole moment and strain-induced electronic modifications in Janus MoSSe further optimize hydrogen adsorption, leading to superior HER performance. *(Pakhira and Upadhyay, 2022)* A novel hybrid heterostructure was developed via a wet chemical method by synthesizing W_xMo_{1-x}S₂ alloy nanosheets supported on reduced graphene oxide (rGO). This composite material exhibited superior HER activity compared to pristine WS₂ and MoS₂, with the W_{0.4}Mo_{0.6}S₂/rGO heterostructure showing the highest catalytic efficiency. *(Lei, Pakhira, Fujisawa, Wang,*

Iyiola, Perea López, et al., 2017) Lei et al. employed DFT method using the M06-L functional to complement their experimental results to explore the underlying mechanisms. *(Lei, Pakhira, Fujisawa, Wang, Iyiola, Perea López, et al., 2017)* Their computational analysis revealed the enhanced HER performance from synergistic electronic interactions between the TMD alloys and rGO, optimizing hydrogen adsorption and charge transfer kinetics. This work underscores the potential of engineered TMD-based structures as high-performance, cost-effective electrocatalysts for sustainable hydrogen production.

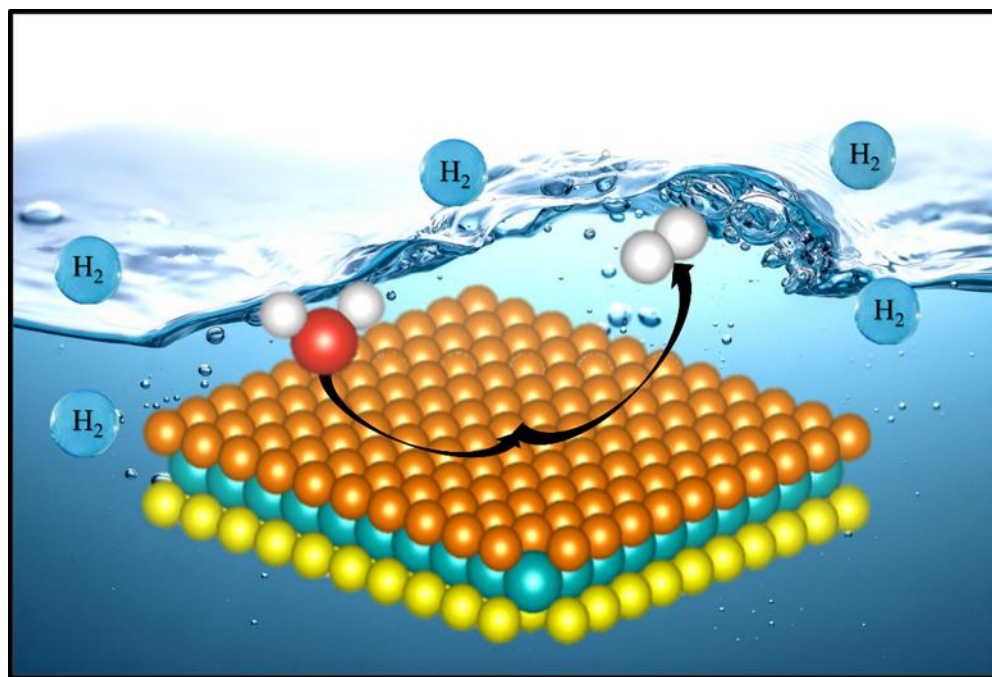
This research aims to design novel 2D TMDs with activated basal planes to enhance their catalytic performance during HER. These materials hold the potential to revolutionize electrocatalysis by offering improved efficiency and stability for hydrogen production. However, much remains to be explored in understanding how basal plane activation can be optimized for better performance. This study aims to contribute to the advancement of sustainable energy technologies by addressing these challenges and unlocking the full potential of 2D TMDs for HER applications.

1.7. Contributions from the Present Thesis

The following advancements in the field of 2D TMD materials for efficient electrocatalytic applications have been achieved in the course of preparing this dissertation:

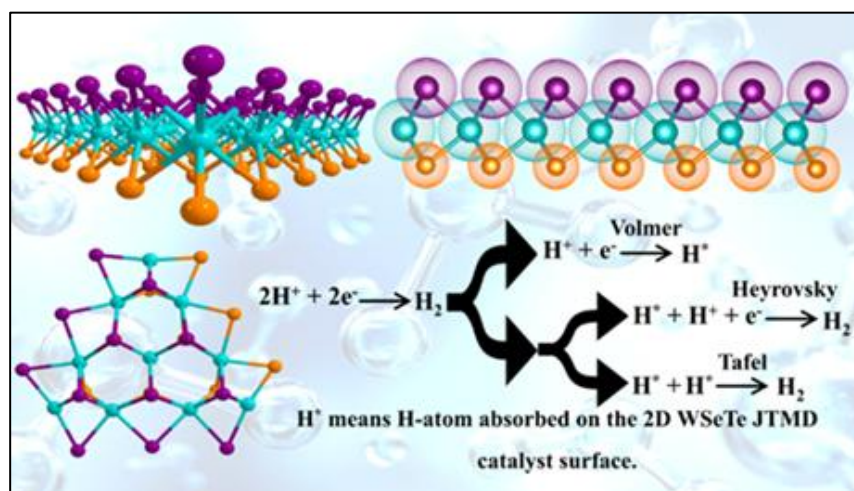
1. Ultrathin two-dimensional Janus transition metal dichalcogenides (2D JTMDs) have attracted much attention due to their potential applications in electrocatalysis, sensors, and other electromechanical devices. In the present work, a first principles-based quantum mechanical (QM) hybrid periodic DFT method has been employed to examine the equilibrium structure, geometry and electronic properties (such as the electronic band structure, band gap (E_g) and total density of states (DOS)) of a 2D monolayer WSSe JTMD. We have performed non-periodic quantum mechanical DFT computations to find out the most favorable HER pathway on the W-edges ($10\bar{1}0$) and S-/Se-edges ($\bar{1}010$) of the 2D Janus WSSe material. The present research shows that the 2D monolayer Janus WSSe TMD follows the

Volmer–Heyrovsky (V-H) reaction mechanism with very low H^{*}-migration and Heyrovsky reaction energy barriers about 2.33–7.52 kcal mol^{−1} during the H₂ evolution. It was found that the 2D Janus WSe has a high value of turnover frequency (TOF) of $\sim 1.91 \times 10^7 \text{ s}^{-1}$ and a very low Tafel slope ($m = 29.54 \text{ mV dec}^{-1}$ at $T = 298.15 \text{ K}$) due to better overlapping of the *d*-orbital electron cloud of the W atom and the *s*-orbital electron cloud of the H₂ appearing in the highest occupied molecular orbital and lowest unoccupied molecular orbital (HOMO–LUMO) structure of the Heyrovsky TS. The present study demonstrates the extraordinary HER activity and performance of the 2D monolayer WSe JTMD. Our research exhibits how to computationally design a highly active electrocatalyst from 2D JTMDs utilizing their active edges, and the current investigation will boost the further development of superior 2D electrocatalysts for efficient HER.



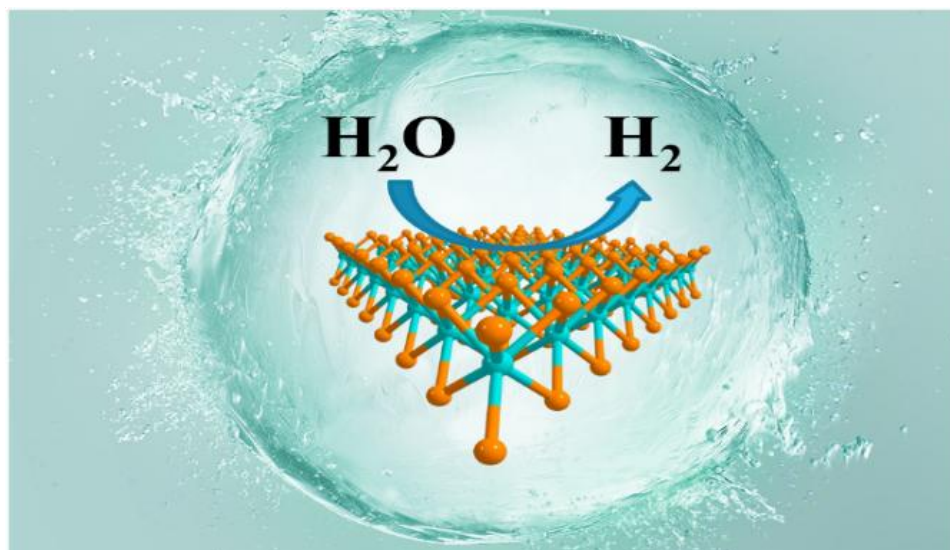
2. We report a 2D monolayer WSeTe JTMD, which is highly effective toward HER. We have studied the electronic properties of 2D monolayer WSeTe JTMD using the periodic hybrid DFT-D method, and a direct electronic band gap of 2.39 eV was obtained. We have explored the HER pathways, mechanisms, and intermediates, including various transition state (TS) structures (Volmer TS, i.e., H^{*}-migration

TS, Heyrovsky TS, and Tafel TS) using a molecular cluster model of the subject JTMD noted as $W_{10}Se_9Te_{12}$. The present calculations reveal that the 2D monolayer WSeTe JTMD is a potential electrocatalyst for HER. It has the lowest energy barriers for all the TSs among other TMDs. It has been shown that the Heyrovsky energy barrier ($= 8.72 \text{ kcal mol}^{-1}$) in the case of the Volmer–Heyrovsky (V-H) mechanism is larger than the Tafel energy barrier ($= 3.27 \text{ kcal mol}^{-1}$) in the Volmer–Tafel (V-T) mechanism. Hence, our present study suggests that the formation of H_2 is energetically more favorable via the Volmer–Tafel mechanism. This study helps to shed light on the rational design of 2D single-layer JTMD, which is highly effective toward HER, and we expect that the present work can be further extended to other JTMDs to find out the improved electrocatalytic performance.



3. An electrocatalyst is needed to efficiently lower the reaction barriers to produce hydrogen through the H_2 evolution reaction. Recently, 2D TMDs, such as the pure 2D monolayer $MoTe_2$ TMD, have become attractive materials for HER. Using the first principle-based hybrid DFT method, we have computationally designed a pure 2D monolayer $MoTe_2$ TMD and examined its structural and electronic properties and electrocatalytic efficacy towards HER. A non-periodic finite molecular cluster model $Mo_{10}Te_{21}$ system was employed to explore the feasibility of both the Volmer-Heyrovsky and Volmer-Tafel reaction mechanisms for the HER. The

solvent-phase calculations of the HER on the 2D monolayer MoTe₂ TMD demonstrate that this material can effectively undergo either Volmer-Heyrovsky or Volmer-Tafel reaction pathways. This conclusion is supported by our determination of low reaction barriers for the H*-migration, Heyrovsky, and Tafel transition states (TSs), which were found to be approximately 9.80, 12.55, and 5.29 kcal.mol⁻¹, respectively. These results highlight the potential utility of MoTe₂ TMD as a promising electrocatalyst for HER. The unusual electrocatalytic activity of the pure 2D monolayer MoTe₂ TMD is evidenced by its ability to significantly reduce reaction barriers, achieving impressive turnover frequency (TOF) values of 3.91×10^3 and 8.22×10^8 sec⁻¹ during the Heyrovsky and Tafel reaction steps, respectively. Additionally, it demonstrates a remarkably low Tafel slope of 29.58 mV.dec⁻¹. These outstanding performance metrics indicate that pure 2D monolayer MoTe₂ TMD is a highly efficient electrocatalyst for HER, surpassing the capabilities of traditional platinum group metal-based alternatives. Further exploration of its potential applications in electrocatalysis is warranted. The present work provides valuable insights into the atomic modulation of active sites for enhanced electrocatalytic performance towards HER, paving the way for designing advanced non-noble metal-free electrocatalysts.



1.8 Organization of the Thesis

The remaining sections of the ***Thesis*** are structured as follows:

- **Chapter 2:** The second chapter presents the methodology utilized in this research. It offers a thorough investigation of computational science, detailing the methods, theories, and the integration of computational materials science with chemistry.
- **Chapter 3:** This chapter builds upon the previous one by focusing on the design of a molecular cluster model system based on the 2D monolayer Janus WSe crystal structure. The molecular cluster model ($\text{W}_{10}\text{S}_9\text{Se}_{12}$) system of the 2D monolayer WSe Janus TMD material is used to investigate its HER activity. A detailed exploration of all the reaction steps, including transition state (TS) calculations and thermochemistry analysis, is conducted to provide insights into the HER mechanism.
- **Chapter 4:** In this chapter a 2D monolayer Janus TMD, WSeTe has been studied. We have investigated the electronic properties and designed a molecular cluster model to study the whole HER mechanism.
- **Chapter 5:** In this chapter a 2D monolayer TMD, MoTe_2 has been investigated towards HER studies. We have computed the electronic properties of the material and designed a molecular cluster model system to learn the HER mechanisms.

Chapter 2

Theory, Methodology and Computational Details

An overview of the theoretical and computational techniques used in the current study is given in this chapter. The first half of the course covers the fundamental ideas of theoretical physics, quantum mechanics/physics, materials science, and engineering, emphasizing the solutions to Schrödinger's equation for systems with many particles. A succinct but thorough overview of Density Functional Theory (DFT) method is provided, emphasizing the functionals employed and the most recent developments in contemporary science and engineering. The chapter also addresses the software and computational tools used to carry out quantum computations, as well as the usage of basis sets for ab initio approaches.

Over the past few decades, Density Functional Theory (DFT) method has emerged as a dominant computational method in the quantum mechanical simulation of periodic systems and molecular energy surfaces. Quantum mechanics (QM), which originated in the early 20th century through the pioneering work of physicists like Erwin Schrödinger and Werner Heisenberg, laid the foundation for understanding electron behavior in atoms and molecules. Early quantum calculations were performed manually, but the development of digital computers in the 1950s transformed the field, with methods like Hartree-Fock (HF) gaining prominence in the 1960s for *ab initio* quantum chemical calculations. However, HF methods struggled to account for strong electron-electron interactions, requiring the development of post-HF methods that incorporated additional determinants to improve accuracy, albeit with higher computational costs. The 1970s and 1980s marked a revolutionary shift with the formulation of DFT by Pierre Hohenberg and Walter Kohn, which introduced electron density as a central variable. This innovation has greatly enhanced computational efficiency, making DFT widely applicable to larger systems including many-electron materials.[\(Jones, 2015\)](#)

Recent advancements in computational power have made the advanced quantum physics and chemistry an accessible and efficient tool for predicting material properties and guiding the design of molecules for diverse applications. Grounded in the Schrödinger equation and variational principles, methods like Hartree-Fock (HF) and Kohn-Sham (KS) DFT methods are now the standard approaches for determining electronic ground states of various systems in modern physics and materials science. Although the efficiency of the DFT has driven its widespread adoption, recent developments in exchange-correlation functionals continue to refine its accuracy, ensuring more reliable predictions across various chemical and material systems.

2.1. Schrödinger equation

The Schrödinger Equation (SE) is a fundamental equation in quantum mechanics that describes the wave function (Ψ) of a quantum system. First proposed by Erwin Schrödinger in 1925 and published in 1926, it plays a crucial role in determining the electronic structure of atoms and molecules. The time-independent Schrödinger Equation is expressed as:

$$\hat{H}\Psi = E\Psi \quad \dots (2.1)$$

where \hat{H} is the Hamiltonian operator, Ψ is the wave function of the system, and E is the corresponding eigenvalue, representing the system's total energy. The Hamiltonian operator \hat{H} consists of two main components: kinetic energy and potential energy. Mathematically, it can be written as:

$$\hat{H} = -\frac{\hbar^2}{2m}\nabla^2 + V \quad \dots (2.2)$$

where \hbar is the reduced Planck's constant, m is the particle mass, V is the potential energy, and ∇^2 represents the Laplacian operator, which in three-dimensional Cartesian coordinates is given by:

$$\nabla^2 = \frac{\partial^2}{\partial x^2} + \frac{\partial^2}{\partial y^2} + \frac{\partial^2}{\partial z^2} \quad \dots (2.3)$$

While the SE can be solved analytically for simple systems like hydrogen-like atoms, more complex systems require numerical methods to approximate solutions. These approaches have become essential for studying the electronic structure of larger, multi-electron systems in both chemistry and materials science. *(Berezin and Shubin, 2012)*

2.2. The Many-Body System and Born-Oppenheimer (BO) Approximation

The many-body SE is fundamental in describing the behavior of systems with multiple interacting particles, such as atoms, molecules, and solids. However, solving the Schrödinger Equation for such systems is extremely complex due to the interactions between all particles. The Hamiltonian operator for a system of nuclei and electrons consists of terms representing the kinetic energy of the electrons and nuclei, the electron-nucleus Coulomb attraction, and the repulsion between electrons and between nuclei. The general many-body SE is given as:

$$\hat{H}\Psi(\mathbf{r}, \mathbf{R}) = E\Psi(\mathbf{r}, \mathbf{R}) \quad \dots (2.4)$$

where \mathbf{r} represents the positions of the electrons, \mathbf{R} represents the positions of the nuclei, \hat{H} is the Hamiltonian operator, and E is the total energy of the system.

The Hamiltonian for a many-body system can be written as:

$$\begin{aligned} \hat{H} = & -\sum_i \frac{\hbar^2}{2m_e} \nabla_i^2 - \sum_A \frac{\hbar^2}{2M_A} \nabla_A^2 - \sum_{\{i,A\}} \frac{Z_A e^2}{|\mathbf{r}_i - \mathbf{R}_A|} + \sum_{\{i < j\}} \frac{e^2}{|\mathbf{r}_i - \mathbf{r}_j|} \\ & + \sum_{\{A < B\}} \frac{Z_A Z_B}{|\mathbf{R}_A - \mathbf{R}_B|} \quad \dots (2.5) \end{aligned}$$

In this expression:

- The first term represents the kinetic energy of the electrons (\hat{T}_e).
- The second term represents the kinetic energy of the nuclei (\hat{T}_N).
- The third term accounts for the Coulomb attraction between electrons and nuclei (\hat{V}_{eN}).
- The fourth term describes electron-electron repulsion (\hat{V}_{ee}).

- The fifth term corresponds to the nucleus-nucleus repulsion (\hat{V}_{NN}).

Since the motion of nuclei is much slower than that of electrons due to their greater mass, the Born-Oppenheimer (BO) approximation is introduced to simplify the many-body SE. This approximation assumes that the electronic wave function $\Psi_{elec}(r; R)$ can be separated from the nuclear wave function $\Psi_{nuc}(R)$, as the nuclei are considered fixed while solving the electronic part. The total wave function can be approximated as:

$$\Psi(r, R) = \Psi_{elec}(r; R)\Psi_{nuc}(R) \quad \dots (2.6)$$

This leads to a two-step solution process: first, solving the electronic SE for fixed nuclear positions and then solving the nuclear motion, typically treated using classical or semi-classical methods. The electronic SE under the BO approximation is:

$$\hat{H}_{elec}\Psi_{elec}(r; R) = E_{elec}(R)\Psi_{elec}(r; R) \quad \dots (2.7)$$

where $E_{elec}(R)$ is the electronic energy that depends parametrically on the nuclear positions. This approximation significantly reduces the computational complexity of solving the many-body SE and is widely used in quantum chemistry and molecular dynamics simulations.

2.3. The Hartree-Fock Approximation

Although the Born-Oppenheimer approximation simplifies the separation of nuclear and electronic wavefunctions, solving the Schrödinger equation for systems with many electrons remains challenging due to the complexity of electron-electron interactions. To address this, Douglas Hartree proposed the Hartree method in 1928, also known as the self-consistent field (SCF) method, to simplify the wavefunction description and energy calculation for atoms and ions. In the Hartree method, electron motions are considered approximately independent, with each electron moving in the average field created by the nucleus and other electrons. A single-electron wavefunction can describe the state of each electron, and the total wavefunction of an n -electron system is the product of these single-electron wavefunctions:

$$\Psi(r) = \Psi_1(r_1) \cdot \Psi_2(r_2) \cdot \dots \cdot \Psi_n(r_n) \quad \dots (2.8)$$

However, in 1930, Slater and Fock pointed out that the Hartree method did not fully obey the wavefunction anti-symmetry principle and ignored electron spin. They introduced the Hartree-Fock (HF) method to improve the description of electronic wavefunctions by treating electrons as fermions. According to the Pauli exclusion principle, Fermions cannot occupy the same quantum state. The HF method uses the Slater determinant to represent the wavefunction of an N -electron system, ensuring anti-symmetry and correct fermionic behavior:

$$\Psi_{HF} = \frac{1}{\sqrt{N!}} \begin{bmatrix} \psi_{1\alpha}(1) & \psi_{1\beta}(1) & \dots & \psi_{N\alpha}(1) \\ \psi_{1\alpha}(2) & \psi_{1\beta}(2) & \dots & \psi_{N\alpha}(2) \\ \vdots & \vdots & \ddots & \vdots \\ \psi_{1\alpha}(N) & \psi_{1\beta}(N) & \dots & \psi_{N\alpha}(N) \end{bmatrix} \quad \dots (2.9)$$

In this equation, the columns represent individual wavefunctions for each electron, while the rows correspond to electron coordinates. Exchanging any two rows or columns results in a sign change, ensuring the anti-symmetry of the wavefunction. Additionally, the determinant structure guarantees that no two electrons can occupy the same state, as identical rows or columns would lead to a zero determinant.

The Hartree-Fock method relies on five key approximations:

1. The Born-Oppenheimer approximation assumes that the nuclei are stationary relative to the electrons.
2. Relativistic effects are neglected, and the operators are non-relativistic.
3. The solution is expressed as a linear combination of orthogonal basis functions.
4. The energy eigenfunction is represented by a single Slater determinant, ensuring the anti-symmetric nature of the wavefunction.
5. Electron correlation effects are neglected, as the method assumes a mean-field environment.

Neglecting electron correlation is a significant limitation of the HF method, leading to discrepancies between experimental and calculated results. The difference between the exact energy and the HF energy is defined as the correlation energy:

$$E_{\text{correlation}} = E_{\text{exact}} - E_{\text{HF}} \quad \dots (2.10)$$

In some cases, the HF method can be replaced by density functional theory (DFT), which accounts for both exchange and correlation energies, providing a more accurate description of electronic systems. *(Echenique and Alonso, 2007)*

2.4. The Density Functional Theory

Density Functional Theory (DFT) emerged in the 1960s as a computationally efficient alternative to the HF method for determining the properties of many-electron systems. Instead of relying on complex many-body wavefunctions, DFT utilizes functionals of the electron density, which varies with spatial coordinates. This approach significantly reduces computational costs while maintaining accuracy. The roots of DFT can be traced back to the Thomas-Fermi model of 1927, which assumed a uniform distribution of electrons within an atom, though it had notable errors related to exchange energy and electron correlation. The foundation of modern DFT was firmly established with the publication of the Hohenberg-Kohn (HK) theorems in 1964, which demonstrated that the ground-state energy of a system is uniquely determined by its electron density. Together with the Kohn-Sham (KS) equations (1965), these theorems provide the framework for solving the Schrödinger equation in a more efficient way, making DFT the most widely used method for solid-state simulations today. *(Engel, 2011; Giustino, 2014)*

2.4.1 The Hohenberg-Kohn Theorems

The Hohenberg-Kohn (HK) theorems, formulated in 1964, provide the theoretical foundation for DFT by demonstrating that the electron density, rather than the many-body wavefunction, can be used to determine the properties of a quantum system. The theorems are based on two fundamental principles.

Theorem 1: Uniqueness of the Electron Density

The first HK theorem states that the external potential $V_{\text{ext}}(r)$, and thus, all properties of a many-electron system are uniquely determined by the ground-state electron density $\rho(r)$. This implies that the total energy and the wavefunction of the system can be expressed as functionals of the electron density. In other words, for a given electron density, there is a unique external potential and ground-state wavefunction.

Mathematically, this can be expressed as:

$$E[\rho] = T[\rho] + V_{\text{ee}}[\rho] + \int V_{\text{ext}}(r)\rho(r) dr \quad \dots (2.11)$$

Where:

- $E[\rho]$ is the total energy as a functional of the electron density.
- $T[\rho]$ represents the kinetic energy of the electrons.
- $V_{\text{ee}}[\rho]$ is the electron-electron interaction energy.
- $\int V_{\text{ext}}(r)\rho(r) dr$ represents the interaction between the electron density and the external potential, such as the potential due to nuclei.

Theorem 2: Variational Principle

The second HK theorem asserts that the ground-state electron density minimizes the energy functional. Any trial electron density ρ' that is not the actual ground-state density will yield higher energy than the actual ground-state energy. This theorem is analogous to the variational principle used in quantum mechanics.

Mathematically, the variational principle is given by:

$$E[\rho'] \geq E[\rho_{\text{GS}}] \quad \dots (2.12)$$

Where:

- $E[\rho']$ is the energy functional evaluated with a trial density ρ' .
- $E[\rho_{\text{GS}}]$ is the actual ground-state energy, and ρ_{GS} is the ground-state electron density.

Thus, the ground-state energy E_{GS} can be obtained by minimizing the energy functional $E[\rho]$ with respect to ρ , leading to:

$$E_{\text{GS}} = \min_{\rho} E[\rho] \quad \dots (2.13)$$

Reformulation of the Schrödinger Equation

In light of these theorems, the Schrödinger equation can be reformulated in terms of the electron density. The total energy functional becomes:

$$E[\rho] = T[\rho] + V_{\text{ee}}[\rho] + \int V_{\text{ext}}(r)\rho(r) dr \quad \dots (2.14)$$

Where:

- $T[\rho]$ represents the kinetic energy functional.
- $V_{\text{ee}}[\rho]$ accounts for electron-electron interactions, including Coulombic repulsion and exchange-correlation effects.
- $\int V_{\text{ext}}(r)\rho(r) dr$ is the potential energy due to the external potential.

Although the HK theorems provide a way to describe the total energy in terms of electron density, the exact form of the electron-electron interaction energy $V_{\text{ee}}[\rho]$ is generally unknown. This complexity is addressed through approximations, which later led to the development of the Kohn-Sham equations.

2.4.2 The Kohn-Sham Equations

While the HK theorems establish that the ground-state energy is a unique functional of the electron density, they do not provide an explicit form for the kinetic energy $T[\rho]$ or the electron-electron interaction energy $V_{\text{ee}}[\rho]$. To overcome this, Kohn and Sham (1965) proposed an auxiliary system of non-interacting electrons that yield the same ground-state density as the real interacting system. This led to a set of self-consistent equations known as the Kohn-Sham (KS) equations.

In this approach, the total energy functional is expressed as:

$$E[\rho] = T_s[\rho] + E_{\text{ext}}[\rho] + E_H[\rho] + E_{\text{XC}}[\rho] \quad \dots (2.15)$$

Where:

- $T_s[\rho]$ is the kinetic energy of the non-interacting reference system.

- $E_{\text{ext}}[\rho] = \int V_{\text{ext}}(r)\rho(r)dr$ is the energy due to the external potential.
- $E_H[\rho] = \frac{1}{2} \int \int \frac{\rho(r)\rho(r')}{|r-r'|} dr dr'$ is the classical Hartree electrostatic interaction.
- $E_{XC}[\rho]$ is the exchange-correlation energy, accounting for all many-body effects including exchange, correlation, and the difference between $T[\rho]$ and $T_s[\rho]$.

The KS equations are derived by minimizing this total energy functional with respect to the electron density, leading to the following single-particle Schrödinger-like equation for the KS orbitals $\varphi_i(r)$:

$$\left[-\frac{\hbar^2}{2m} \nabla^2 + V_{\text{eff}}(r) \right] \varphi_i(r) = \varepsilon_i \varphi_i(r) \quad \dots (2.16)$$

Here:

- $V_{\text{eff}}(r) = V_{\text{ext}}(r) + V_H(r) + V_{XC}(r)$ is the effective potential,
- $V_H(r) = \int \frac{\rho(r')}{|r-r'|} dr'$ is the Hartree potential,
- $V_{XC}(r) = \frac{\delta E_{XC}[\rho]}{\delta \rho(r)}$ is the exchange-correlation potential.

The total electron density is reconstructed from the KS orbitals:

$$\rho(r) = \sum_{i=1}^N |\varphi_i(r)|^2 \quad \dots (2.17)$$

where N is the total number of electrons.

The KS method reduces the many-electron problem to a set of single-particle equations that are solved self-consistently. However, the exact form of the exchange-correlation functional $E_{XC}[\rho]$ remains unknown, and various approximations like the Local Density Approximation (LDA) and Generalized Gradient Approximation (GGA) are commonly used in practical calculations. (*Bickelhaupt and Baerends, 2000*)

2.4.3 Exchange-Correlation Approximations

In DFT, the exchange-correlation energy functional $E_{XC}[\rho]$ accounts for the complex many-body interactions between electrons, including exchange effects (arising from the anti-symmetric of the wavefunction) and correlation effects (due to electron-electron repulsion beyond the mean-field approximation). However, the exact analytical form of $E_{XC}[\rho]$ is unknown for real systems, necessitating the development of practical approximations. The choice of an exchange-correlation functional greatly influences the accuracy and predictive power of DFT calculations. (*Perdew, Burke and Wang, 1996*)

Several widely used approximations to $E_{XC}[\rho]$ are described below:

(a) Local Density Approximation (LDA)

The LDA is the earliest and one of the most widely adopted approximations in DFT for treating the exchange-correlation energy. It is based on the assumption that the exchange-correlation energy at any point in a real, inhomogeneous system can be locally approximated by that of a homogeneous electron gas (HEG) with the same electron density $\rho(\mathbf{r})$ at that point.

The total exchange-correlation energy functional in LDA is expressed as:

$$E_{XC}^{LDA}[\rho] = \int \rho(\mathbf{r}) \epsilon_{XC}^{HEG}(\rho(\mathbf{r})) d\mathbf{r} \quad \dots (2.18)$$

Here:

- $\epsilon_{XC}^{HEG}(\rho(\mathbf{r}))$ is the exchange-correlation energy per electron for a uniform electron gas of density ρ ,
- $\rho(\mathbf{r})$ is the local electron density at position \mathbf{r} .

Despite being a local approximation, the LDA has shown remarkable success in predicting the ground-state properties of a wide range of materials, particularly for systems with nearly homogeneous electron densities. It performs well in describing the structural and cohesive properties of simple metals and semiconductors, making it a foundational tool in solid-state physics. However, the LDA does have some important limitations, especially

when applied to systems where the electron density changes rapidly or involves strong electron interactions. Since it is based on the assumption of a slowly varying electron density, it becomes increasingly inaccurate for systems where the electron density varies rapidly in space, such as in molecules, surfaces, or low-dimensional systems. In these cases, LDA tends to over bind atoms, leading to systematic errors in the prediction of bond lengths, binding energies, and reaction energetics. Moreover, LDA struggles to capture the correct energetics of chemical bonds, including underestimation of reaction barriers, heat of formation, and activation energies. It also fails to provide a proper description of strongly correlated systems, such as transition metal oxides and compounds containing **d**- and **f**-electrons, where electron localization and strong correlation effects are significant.

In summary, while LDA provides a computationally efficient framework and is surprisingly effective for many bulk systems, its inherent local nature limits its accuracy for complex and inhomogeneous systems, prompting the development of more advanced approximations such as the Generalized Gradient Approximation (GGA) and hybrid functionals.

(b) Generalized Gradient Approximation (GGA)

The GGA is a significant improvement over the LDA, especially for systems with rapidly varying electron densities. While LDA considers only the local electron density $\rho(r)$, GGA incorporates the gradient (spatial variation) of the density, $\nabla\rho(r)$, allowing for a more accurate and flexible representation of the exchange-correlation (XC) energy functional.

In GGA, the exchange-correlation energy is generally written as:

$$E_{\text{XC}}^{\text{GGA}}[\rho] = \int \rho(r) \epsilon_{\text{XC}}^{\text{GGA}}[\rho(r), \nabla\rho(r)] dr \quad \dots (2.19)$$

Here, $\epsilon_{\text{XC}}^{\text{GGA}}$ is the exchange-correlation energy density, which is a function of both the electron density and its gradient at each point in space. This dependence allows GGA to capture the non-uniformity in electronic systems more accurately than LDA.

GGA functionals extend beyond LDA by incorporating the gradient of electron density, allowing better treatment of systems with non-uniform densities. Prominent examples include Perdew–Wang (PW86, PW91), Becke88, Perdew–Burke–Ernzerhof (PBE), and

Becke–Lee–Yang–Parr (BLYP). While functionals like B88 and W96 are based on exact scaling relations and theoretical constraints, others like PBE use empirical fitting to match experimental molecular properties. BLYP, in particular, combines Becke’s exchange (1988) with the Lee–Yang–Parr correlation (1988). GGA functionals generally provide accurate results for most bonding types-covalent, ionic, metallic, and hydrogen bonds—but perform poorly for van der Waals (vdW) interactions. Additionally, both LDA and GGA tend to underestimate semiconductor band gaps and struggle with strongly correlated materials. To address these limitations, meta-GGA functionals have been developed, incorporating terms like kinetic energy density or the Laplacian of electron density for improved accuracy.

(c) Hybrid Functionals

Hybrid functionals improve upon GGA by incorporating a portion of exact exchange energy from the Hartree-Fock (HF) theory with DFT exchange-correlation functionals. This blending helps overcome some of the key deficiencies of LDA and GGA, especially in systems where electron self-interaction errors and delocalization effects are significant. A general form of a hybrid functional is:

$$E_{XC}^{\text{Hybrid}} = aE_X^{\text{HF}} + (1 - a)E_X^{\text{DFT}} + E_C^{\text{DFT}} \quad \dots (2.20)$$

where E_X^{HF} is the exact Hartree–Fock exchange, E_X^{DFT} and E_C^{DFT} are the exchange and correlation energies from a GGA-type functional, and a is a mixing parameter (typically between 0.2 and 0.25).

Popular examples include B3LYP and PBE0, which offer significantly improved accuracy in thermochemistry, reaction barriers, and electronic structures, particularly for molecules, semiconductors, and insulators. However, hybrid functionals are computationally more expensive, especially for large systems and periodic solids, due to the evaluation of non-local HF exchange. The best example of the hybrid functionals is Becke 3 Lee Yang Parr (B3LYP) hybrid functional, which has the form:

B3LYP Functional

B3LYP (Becke, 3-parameter, Lee–Yang–Parr) is a hybrid exchange-correlation functional that combines Hartree-Fock exact exchange with gradient-corrected DFT functionals. It was introduced to improve the accuracy of molecular property predictions, especially for thermochemistry, reaction energies, and vibrational frequencies.

The general form of the B3LYP functional is:

$$E_{\text{XC}}^{\text{B3LYP}} = E_{\text{XC}}^{\text{LSDA}} + a_0(E_X^{\text{HF}} - E_X^{\text{LSDA}}) + a_X\Delta E_X^{\text{B88}} + a_C\Delta E_C^{\text{LYP}} \quad \dots (2.21)$$

Where:

- $E_{\text{XC}}^{\text{LSDA}}$: Exchange-correlation energy from the Local Spin Density Approximation.
- E_X^{HF} : Exact Hartree–Fock exchange energy.
- ΔE_X^{B88} : Gradient correction to exchange energy by Becke (1988).
- ΔE_C^{LYP} : Gradient correction to correlation energy by Lee–Yang–Parr.
- $a_0 = 0.20$, $a_X = 0.72$, and $a_C = 0.81$ are empirical fitting parameters optimized against experimental data.

The B3LYP functional, introduced by Becke, is a well-known three-parameter hybrid functional that incorporates 20% exact exchange from Hartree–Fock theory. It combines the Becke88 exchange functional and the Lee–Yang–Parr (LYP) correlation functional, with empirical parameters fitted to experimental thermochemical data. B3LYP has become one of the most widely used functionals in quantum chemistry due to its excellent balance between accuracy and computational efficiency. Other prominent functionals in the hybrid functional family include PBE0, Heyd-Scuseria-Ernzerhof (HSE), and B3PW91. These functionals incorporate a portion of exact exchange and often demonstrate improved performance over generalized gradient approximation (GGA) functionals, particularly in calculating atomization energies, geometries, and vibrational frequencies. An advanced category of functionals, known as hybrid meta-GGA functionals, extends the GGA formalism by including the kinetic energy density or Laplacian of the electron density. Examples include the Minnesota functionals (e.g., M05, M06-L), which are specifically designed to account for non-covalent interactions such as dispersion forces.

In this thesis, the B3LYP hybrid functional has been employed due to its robust performance in capturing the electronic structure, bonding characteristics, and energetics of materials. It has proven ability to provide a more accurate description of band gaps, reaction energetics, and intermolecular forces makes it an excellent choice for the systems studied herein. Additionally, the M06-L meta-GGA functional has also been utilized for its strong capabilities in dealing with transition metal systems, noncovalent interactions, and solid-state properties, without the need for exact exchange. The combined use of B3LYP and M06-L ensures a balanced and reliable computational approach, enabling a comprehensive and accurate understanding of the studied material systems. *(Tirado-Rives and Jorgensen, 2008)*

(d) van der Waals (vdW) Corrections

van der Waals (vdW) interactions, named after Johannes Diderik van der Waals, are distance-dependent forces acting between atoms, molecules, and surfaces. These interactions stem from fluctuations in electron density, which induce transient multipoles and give rise to weak, long-range attractive forces. In simpler terms, vdW forces arise from temporary shifts in electron density within atoms or molecules, creating momentary dipoles that can attract or repel neighboring particles. vdW interactions include forces between permanent dipoles (dipole-dipole), between a permanent dipole and an induced dipole (dipole-induced dipole), and between two instantaneous dipoles (London dispersion forces). Although these are the weakest force among intermolecular forces, they play a significant role in various systems, such as biomolecular structures, molecular adsorption on surfaces, polymer behavior, and the stacking of layered materials. In the context of this work, where layered structure two dimensional (2D) transition metal dichalcogenides (TMDs) and adsorption of molecules such as HER species on slab surfaces are studied, therefore, accurately capturing the vdW interactions is crucial. However, conventional DFT functionals, including the LDA and GGA, inherently fail to account for such long-range dispersion interactions. This limitation arises because vdW forces are non-local in nature, whereas standard exchange-correlation functionals are typically local or semi-local. *(Ortmann, Bechstedt and Schmidt, 2006)*

To address this, Grimme proposed the DFT-D method, where a semi-empirical dispersion correction is added to the conventional DFT energy. The total energy in the DFT-D approach is expressed as:

$$E_{\text{total}} = E_{\text{KS-DFT}} + E_{\text{disp}} \quad \dots (2.22)$$

Here, $E_{\text{KS-DFT}}$ is the standard DFT energy obtained from Kohn–Sham calculations, and E_{disp} is the empirical dispersion correction term. At long distances, the dispersion interaction behaves as $-\frac{C_6}{R^6}$, where C_6 is a dispersion coefficient and R is the interatomic distance. To prevent unphysical contributions at short distances-where conventional DFT is reliable damping function is applied to smoothly reduce the correction in this region.

The general expression for the dispersion term is:

$$E_{\text{disp}} = -\frac{1}{2} \sum_{A \neq B}^{\text{atoms}} \sum_{n=6,8} S_n \frac{C_n^{AB}}{R_{AB}^n} f_{\text{damp},6}(R_{AB}) \quad \dots (2.23)$$

Where:

- C_n^{AB} are the dispersion coefficients specific to atom pairs A and B ,
- R_{AB}^n is the distance between atoms A and B ,
- S_n are global scaling factors that depend on the exchange-correlation functional used,
- $f_{\text{damp},6}(R_{AB})$ is the damping function to correct for short-range effects.

DFT-D3 Dispersion Corrections

In the DFT-D3 approach developed by Grimme, the total dispersion energy correction includes both two-body and three-body interactions. The dispersion energy in DFT-D3 is expressed as:

$$E_{\text{disp}}^{\text{D3}} = E^{(2)} + E^{(3)} \quad \dots (2.24)$$

The **two-body** energy term incorporates both the C_6 and C_8 coefficients, accounting for dipole-dipole and dipole-quadrupole interactions, respectively:

$$E^{(2)} = -\frac{1}{2} \sum_A^{\text{atoms}} \sum_{B < A}^{\text{atoms}} \left[\left(\frac{C_6^{AB}}{R_{AB}^6} \right) f_{\text{dmp},6}(R_{AB}) + \left(\frac{C_8^{AB}}{R_{AB}^8} \right) f_{\text{dmp},8}(R_{AB}) \right] \quad \dots (2.25)$$

The **three-body** energy term captures non-additive effects via the Axilrod–Teller–Muto (ATM) interaction:

$$E^{(3)} = - \sum_A^{\text{atoms}} \sum_{B < A}^{\text{atoms}} \sum_{C < B}^{\text{atoms}} 16 \cdot C_9^{ABC} \cdot R_{ABC}^{-9} \cdot f_9^d(R_{ABC}, \theta_{ABC}) \quad \dots (2.26)$$

Where:

- R_{AB} is the interatomic distance between atoms A and B,
- C_6^{AB} and C_8^{AB} are dispersion coefficients,
- $C_9^{ABC} = -\sqrt{C_6^{AB} C_6^{AC} C_6^{BC}}$,
- R_{ABC} is the geometric mean of the triangle sides R_{AB} , R_{BC} , and R_{CA} ,
- θ_A , θ_B , θ_C are the internal angles of the triangle formed by atoms A, B, and C.

The damping functions used to avoid overestimation of dispersion effects at short distances are defined as:

$$f_{\text{dmp},n}(R_{AB}) = \frac{S_n}{1 + 6 \left(\frac{R_{AB}}{S_{r,n} R_{0,AB}} \right)^{-\alpha_n}} \quad \dots (2.27)$$

$$f_9^d(R_{ABC}, \theta_{ABC}) = \frac{3 \cos \theta_A \cos \theta_B \cos \theta_C + 1}{1 + 6 \left(\frac{R_{ABC}}{S_{r,n} R_{0,AB}} \right)^{-\alpha_n}} \quad \dots (2.28)$$

These damping functions effectively reduce the empirical contributions where the local DFT already describes interactions adequately.

The DFT-D3 method, with its combination of semi-empirical accuracy and computational efficiency, has proven to be a powerful tool for including vdW effects in DFT simulations. In this thesis, “-D3” corrections with the DFT method are applied to ensure accurate modeling of adsorption processes and interlayer interactions in layered TMD systems.

In this thesis, structural and electronic properties related to the hydrogen evolution reaction (HER) were investigated by using CRYSTAL17 suite code with the B3LYP-D3 functional. For the evaluation of energy barriers and identification of transition states along the reaction pathway, Gaussian 16 with the M06-L functional was employed due to its reliable performance in modeling reaction kinetics and transition state geometries for the HER mechanism.

To ensure the reliability and accuracy of the computational results in this study, a systematic validation of the exchange-correlation (XC) functional was performed. Benchmark calculations were carried out for key structural and electronic properties specifically, the lattice parameters and band gaps using several widely adopted XC functionals, including PBE, HSE06, B3LYP-D3, and, where available, many-body perturbation methods such as G_0W_0 and their spin-orbit-coupled variants. The results were compared directly with experimental data and high-level theoretical values reported in the literature. This benchmarking process is summarized in Table 2.1, which provides a side-by-side comparison of calculated and reference values for WSSe, WSeTe, and MoTe₂. The close agreement between the results obtained with the chosen functional (B3LYP-D3) and the reference data supports its suitability for accurately describing both the structural and electronic properties of the studied materials. This approach follows best practices in computational materials science, where method validation through comparison with experimental or high-level theoretical benchmarks is essential for establishing the credibility of the computational methodology and the robustness of the conclusions drawn from the study.

Table 2.1. Benchmarking of Exchange-Correlation Functionals for Lattice Parameters and Band Gaps of WSSe, WSeTe, and MoTe₂.

Material	XC Functional	Lattice Parameter (Å)	Band Gap (eV)	References
WSSe	B3LYP-D3	3.20	2.64	This work
	PBE	3.25	1.77	ACS Appl. Energy Mater. 2024, 7, 9986–9995.

	HSE06	3.25	2.27	ACS Appl. Energy Mater. 2024, 7, 9986–9995.
	G ₀ W ₀	3.26	2.68	ACS Appl. Mater. Interfaces 2020, 12, 26, 29335–29343.
	G ₀ W ₀ +SOC	3.24	2.59	J. Phys. Chem. Lett. 2017, 8, 5959–5965.
WSeTe	B3LYP-D3	3.37	2.39	This work
	PBE	3.40	1.42	Surfaces and Interfaces 37 (2023) 102572.
	HSE06	3.43	1.98	J. Phys. Chem. C 2024, 128, 12511–12524.
	HSE06+SOC	3.42	1.73	International Journal of Hydrogen Energy 170 (2025) 151246
MoTe₂	B3LYP-D3	3.40	1.65	This work
	PBE	3.50	1.19	Nanoscale Adv.,2024,6, 3624
	HSE06	3.50	1.65	Nanoscale Adv.,2024,6, 3624
	PBE+U	3.48	1.40	Journal of Nepal Chemical Society, July, 2025, Vol. 45, No.2

2.5 Software

This thesis relies on several pivotal software programs and packages to execute the tasks integral to its objectives. These tools can be categorized as:

2.5.1 CRYSTAL 17

The CRYSTAL package, as outlined by Dovesi et al. in 2018 (*Dovesi et al., 2018*), facilitates *ab initio* computations for various properties of periodic systems. These calculations encompass ground state energy, energy gradients, electronic wave functions, and diverse properties. The software accommodates both the Hartree-Fock and Kohn-Sham Hamiltonians within the framework of DFT, incorporating an Exchange-Correlation potential.

CRYSTAL17 suite code is used to design the systems with different dimensionalities in a cohesive manner. It seamlessly addresses molecules (0D), polymers

(1D), slabs (2D), and crystals (3D). A fundamental aspect of CRYSTAL involves the expansion of single-particle wave functions, known as Crystalline Orbitals (COs). These COs are expressed as linear combinations of Bloch functions (BF), which, in turn, are defined using local functions termed Atomic Orbitals (AOs). These AOs are constructed as linear combinations of Gaussian-type functions (GTF). The input parameters of the software permit the selection of symmetry-adapted functions, encompassing s, p, d, and f orbitals for the atoms.

CRYSTAL17 incorporates an automatic handling system for space symmetry, granting users access to 230 space groups, 80-layer groups, 99-rod groups, and 45-point groups. In the context of polymers, the software adeptly manages helical structures achieved through translation and rotation around the periodic axis. Support for free molecules is provided, aligning with point symmetries compatible with translation symmetry. The software's input capabilities enable the generation of 2D slabs, 1D nanorods, and 0D clusters derived from 3D crystalline structures. Additionally, CRYSTAL offers a range of options, including lattice distortion, the creation of supercells with defects, and diverse structure editing capabilities. The software also includes specific input options for generating special structures, such as 1D nanotubes and 0D fullerenes from 2D structures. These features enhance the flexibility and applicability of CRYSTAL in studying a wide range of periodic systems.

The input file of CRYSTAL17: Here we are taking an example input file structure of 2D monolayer WSe₂

Monolayer WSe ₂ SLAB	#Title Line
SLAB	#Dimensionality of the system
78	#Layer Group (p-6m; 278)
3.21635989 3.21635989 120.0	#Lattice Parameters
2	#Number of Atoms in the System
274 0.66667 0.33333 0.000000	} #Atomic number and coordinates
34 0.33333 0.66667 1.670544	
OPTGEOM	}
FULLOPTG	

MAXCYCLE

800

ENDOPT

END

#Keywords Related to Geometry
Optimization

274 4

#Basis Sets for non-equivalent atoms

INPUT

6. 6 6 5 6 0 0

329.3529656 -0.1457448 -2

113.6102932 -43.8187612 -1

39.9308141 -229.4536668 0

11.0046548 -101.4253295 0

3.3099176 -24.2972893 0

1.0597874 -3.8771269 0

120.7193610 2.7625960 -2

40.4863153 90.9432757 -1

12.2414413 212.5686798 0

3.3536130 54.6162565 0

0.7254557 20.7664520 0

0.5842076 -7.5448433 0

97.7263572 1.8994679 -2

32.0030370 53.3500287 -1

10.3044815 131.0179317 0

2.8403761 30.9930029 0

0.5753263 8.8195349 0

80.9725549 2.9410060 -2

29.8854425 52.8348829 -1

10.7716934 132.5222840 0

2.7612542 50.2360265 0

2.0639584 -14.2411625 0

0.3408971 -0.2994311 0

0 1 1 2. 1.

0.6000 1.00000 1.00000

0 1 1 0. 1.

0.200 1. 1.

0 3 3 4. 1.

1.2230 0.09700

0.9630 0.24100

0.3770 0.53000

0 3 1 0. 1.

```
0.2600    1.00000
99 0
#Optional keywords

END                                #End of basis set input section

SHRINK                             #Reciprocal space integration parameters.

SHRINK

0 8

4 4 1 #Optional keywords

END                                #End of SCF input section
```

2.5.2 Gaussian 16

Gaussian 16 stands as the latest advancement in the Gaussian series of electronic structure quantum chemistry programs, widely embraced by a global community of scientists, including chemists, chemical engineers, biochemists, physicists, and material scientists. Gaussian 16 provides a comprehensive suite of sophisticated modeling capabilities especially molecular modelling (*Frisch et al., 2016*).

Drawing upon the foundational principles of quantum mechanics, this program facilitates the accurate prediction of energies, molecular structures, vibrational frequencies, and molecular properties across a diverse array of compounds and reactions within varied chemical environments. The models studied by Gaussian16 suite code extend their applicability to stable species as well as compounds that pose challenges they are impossible to observe experimentally due to factors such as combustibility, toxicity, radioactivity, or their inherently transient nature, including short-lived intermediates and transition state (TS) structures.

Gaussian16 enables in-depth investigations into chemical problems by swiftly and reliably minimizing molecular structures and predicting the structures of transition states. Moreover, it validates whether the anticipated stationary points represent minima or transition structures. The Intrinsic Reaction Coordinate (IRC) calculation feature in Gaussian 16 facilitates the computation of the reaction route, identifying the reactants and

products connected by a specific transition structure. This capability allows for a comprehensive depiction of the potential energy surface (PES), enabling precise predictions of reaction energies and barriers.

Program Features and Calculation Capabilities of Gaussian16:

Gaussian16 stands as a comprehensive and robust program, offering numerous features and advanced calculation capabilities. Its primary goal is to provide accurate and reliable models without compromising quality. The software accommodates various chemical conditions showcasing high versatility. Gaussian16 excels in performance across diverse computing environments, including multiprocessor, single CPU, cluster/network, multicore, and GPU setups. An outstanding feature of Gaussian16 is its user-friendly interface, streamlining the calculation setup process.

The computed results generated by Gaussian16 are presented in a comprehensible graphical format through the GaussView software (*Frisch et al., 2009*). This feature enables users to visualize and interpret outcomes naturally and intuitively. Gaussian16 offers a broad array of methods for modeling compounds and chemical processes, with continuous updates incorporating the latest advancements in the field.

Example input file in Gaussian16

```
%chk=test.chk
# HF/6-31G(d) Opt
Title
0 1
0
H 1 0.96
H 1 0.96 2 104.5
```

Let's break down the structure of this Gaussian 16 input file:

%chk=test.chk: Specifies the checkpoint file name where the calculation's intermediate data will be saved.

HF/6-31G(d) Opt: Specifies the type of calculation. In this case, it's a Hartree-Fock (HF) calculation with the 6-31G(d) basis set, and the Opt keyword indicates geometry optimization.

Title: A title or description for the calculation.

0 1: Specifies the molecular charge (0 for neutral) and multiplicity (1 for a singlet).

Molecular geometry section: Defines the atomic coordinates of the molecule. In this example, it's a water molecule with oxygen (O) and two hydrogen (H) atoms.

2.6 Basis set:

In the DFT method and other quantum chemical methods, the solution of the KS equations requires an approximation of the molecular orbitals in terms of predefined mathematical functions known as basis functions. These functions form a basis set, which is used to construct molecular orbitals via linear combinations of atomic orbitals (LCAO). The accuracy and efficiency of electronic structure calculations strongly depend on the choice and quality of the basis set.

A basis function is designed to represent the shape and behavior of atomic orbitals (AOs). The general expression of a molecular orbital (Φ_i) as a linear combination of M atomic basis functions $\chi_a(r)$ is:

$$\Phi_i(r) = \sum_{\alpha}^M C_{\alpha i} \chi_{\alpha}(r) \quad \dots (2.29)$$

Where $\Phi_i(r)$, $\chi_{\alpha}(r)$, and $C_{\alpha i}$ represents the molecular orbital, basis function, and expansion coefficient. If $M \rightarrow \infty$, then $\Phi_i(r)$ reaches the complete basis set limit and represents the exact expression of a molecular orbital, not the approximations. Unfortunately, complete basis sets tend to have an infinite number of functions and, therefore, are not practical for calculations. In practice, a finite basis set is used to represent a molecular orbital in electronic structure calculations. However, the smaller the basis set, the poorer the representation of the molecular orbitals. (Davidson, 1988; Jensen, 2013; Nagy and Jensen, 2017)

Types of basis functions: There are two types of basis functions commonly used for the representation of molecular orbital in electronic structure calculations. One is called Slater type orbital (STO), and the other is Gaussian type orbital (GTO).

Slater-type orbitals (STOs): The STOs have the mathematical function form as:

$$S_{\xi nlm}(r, \theta, \phi) = N Y_{l,m}(\theta, \phi) r^{n-1} e^{-\xi r} \quad \dots (2.30)$$

Where N is a normalization constant, $Y_{l,m}(\theta, \phi)$ represents the spherical harmonic functions, and n represents the principal quantum number. STOs do not contain radial nodes, and these nodes are introduced through linear combinations of STOs. These functions were originally used for atomic and diatomic systems that demand high accuracy, as well as in semi-empirical methods that neglect three- and four-center integrals. However, from a computational standpoint, STOs present challenges, as most of the necessary integrals for the SCF procedure need to be computed numerically, which considerably reduces the speed of the calculations.

Gaussian-type orbitals (GTOs): The GTOs can be written in terms of the cartesian and polar coordinates. The mathematical definition of GTOs can be written as:

$$G_{\xi, l_x, l_y, l_z} = NX^{l_x}Y^{l_y}Z^{l_z}e^{-\xi r^2} \quad \dots (2.31)$$

$$G_{\xi, n, l, m}(r, \theta, \phi) = NY_{l,m}(\theta, \phi)r^{2n-2-l}e^{-\xi r^2} \quad \dots (2.32)$$

In the cartesian coordinate, the angular dependence of the GTOs is computed from the l_x, l_y, l_z . For example, s-orbital ($l=0$), p-orbital ($l=1$), and so on. A comparison between the STOs and GTOs shows that there are some major differences in the behavior of these two functions. (1) the behavior at $r \rightarrow 0$: the derivative of GTOs at the nucleus is equal to zero due to r^2 dependence in the exponent of the function, hence has zero slope. In contrast to GTOs, STOs have discontinuous derive and, hence, have a cusp. Thus, GTOs represent an incorrect electronic behavior near the nucleus. (2) the behavior at $r \rightarrow \infty$: far from the nucleus, the GTOs decay rapidly as compared to the STOs. Thus, the tail of the Gaussian-type wavefunctions poorly represent electronic behavior. In principle, more GTOs are required in order to achieve a certain accuracy.

Properties of Basis Functions

- **Physical Significance:** The basis functions must closely resemble the actual atomic orbitals (AOs) and reflect the physical characteristics of electrons in atoms and molecules.

- **Variational Optimization:** Expansion coefficients in the linear combination of basis functions are determined through the variational principle, ensuring the lowest possible energy configuration for a given basis set.
- **Flexibility and Completeness:** A good basis set should be flexible enough to describe changes in the electron density during chemical bonding, ensuring accurate predictions of molecular properties.
- **Correct Near-Nucleus Behavior:** Basis functions should capture the correct cusp behavior near nuclei (especially for Slater-type orbitals) or approximate it well (e.g., via contracted Gaussians).
- **Proper Asymptotic Decay:** At large distances from the nucleus, basis functions should decay smoothly and accurately reflect electron delocalization, which is particularly important in weak interactions.
- **Computational Efficiency:** Basis functions should allow for fast and accurate evaluation of integrals required in quantum mechanical calculations, often favoring Gaussian-type orbitals for this reason.
- **Transferability:** A reliable basis set should perform consistently across a wide range of molecular systems without needing reparameterization.
- **Orthonormality (Ideal Case):** Ideally, basis functions should be orthogonal and normalized to simplify matrix operations and improve numerical stability.

Classification of Basis Sets

Basis sets are classified based on the number, type, and functions of Gaussian functions used to represent core and valence orbitals. The classification plays a significant role in determining the accuracy and computational cost of quantum chemical calculations. Below are the common classifications of basis sets: *(Nagy and Jensen, 2017)*

1. Minimal Basis Set: A minimal basis set uses only one basis function per atomic orbital (AO) in the electronic configuration of an atom. This set provides the simplest representation of atomic orbitals but may lack sufficient flexibility to describe complex bonding. Minimal basis sets are particularly useful in preliminary calculations or for systems where computational efficiency is paramount, and high accuracy is not essential.

- **Example: STO-3G** (This represents Slater-type orbitals (STOs) with a linear combination of three Gaussian functions to approximate the behavior of a single STO).

2. Split-Valence Basis Set: A split-valence basis set represents each valence orbital using multiple basis functions, offering more flexibility and allowing for a better description of molecular bonding. This classification is important for systems where the bonding and electron distribution are complex, such as in large organic molecules or transition metal complexes.

- **Example: 3-21G** (In this set, the core orbitals are described by a single Gaussian function, while the valence orbitals are split into two parts, one with three functions and the other with one).
- **Example: 6-31G, 6-311G** (These involve more Gaussian functions to describe the core and valence electrons, offering a balance between accuracy and computational cost).

3. Polarized Basis Set: A polarized basis set includes higher angular momentum functions, such as d or f functions, for atoms that are involved in bonding. These functions allow for the distortion of orbitals during bonding, which is crucial for more accurate representation of electronic structures in molecules with significant bonding effects. Polarized basis sets are commonly used for transition metal chemistry, reaction pathways, and systems where bond formation and orbital overlap are significant. Polarization functions are denoted by asterisks (*).

- **Example: 6-31G and 6-31G*:** The single asterisk (*) indicates the inclusion of polarization functions for the valence orbitals.
- **Example: 6-31G:** a double-zeta basis set with polarization functions added to improve the flexibility of the orbital description.

4. Diffuse Basis Set: A diffuse basis set incorporates functions with small exponents, which are essential for describing electron density in the outer regions of molecules, especially for systems like anions or weakly bound species where the electron density

extends over a larger spatial region. Diffuse functions are denoted by a plus sign (“+”). These basis sets improve the description of long-range interactions and are particularly important for accurate treatment of anions, electron affinities, and weak intermolecular forces.

- **Example:** *6-31+G, 6-31++G: The “+” indicates the addition of diffuse functions, and “++” further enhances the description with more diffuse functions, which are especially important for accurately modeling weak interactions or anionic species.

5. Double-Zeta (DZ) and Triple-Zeta (TZ) Basis Sets: DZ and TZ basis sets improve upon minimal sets by using two or three basis functions per valence orbital, respectively. This added flexibility allows for a more accurate representation of orbital shapes and electron distribution, especially important in chemical bonding and reactions. While they require more computational resources, they provide a good balance between accuracy and efficiency.

Example: pob-TZVP (used in CRYSTAL17) is a triple-zeta valence plus polarization basis set, well-suited for solid-state and periodic calculations.

6. Effective Core Potentials (ECPs) Basis Set: ECP basis sets are used to simplify quantum chemical calculations for heavy atoms by replacing their tightly bound inner-core electrons with an effective potential. This allows only the chemically relevant valence electrons to be treated explicitly, significantly reducing computational effort and incorporating relativistic effects where necessary.

Example: LANL2DZ-ECP (used in Gaussian 16) is commonly employed for transition metals and heavier elements, offering a good balance between accuracy and efficiency.

Chapter 3

Mechanistic understanding of efficient electrocatalytic hydrogen evolution reaction on a 2D monolayer WSSe Janus transition metal dichalcogenide

In this chapter, a first principles-based quantum mechanical (QM) hybrid periodic density functional theory (DFT) method has been employed to examine the equilibrium structure, geometry, and electronic properties (such as the electronic band structure, band gap, and total density of states (DOS)) of a 2D monolayer WSSe 2D Janus Transition Metal Dichalcogenide (JTMD or Janus TMD). We have performed non-periodic quantum mechanical DFT computations to find out the most favorable hydrogen evolution reaction (HER) pathway on the W-edges ($10\bar{1}0$) and S-/Se-edges ($\bar{1}010$) of the 2D Janus WSSe material. The present research shows that the 2D monolayer Janus WSSe TMD follows the Volmer–Heyrovsky reaction mechanism with very low H^ -migration and Heyrovsky reaction energy barriers about $2.33\text{--}7.52\text{ kcal mol}^{-1}$ during the H_2 evolution. It has found that the 2D Janus WSSe has a high value of turnover frequency (TOF) of $\sim 1.91 \times 10^7\text{ s}^{-1}$ and a very low Tafel slope ($m = 29.54\text{ mV dec}^{-1}$ at $T = 298.15\text{ K}$) due to better overlapping of the d -orbital electron cloud of the W atom and the s -orbital electron cloud of the H_2 appearing in the HOMO–LUMO structure of the Heyrovsky TS. The present study demonstrates the extraordinary HER activity and performance of the 2D monolayer WSSe JTMD. Our research exhibits how to computationally devise a highly active electrocatalyst from 2D JTMDs utilizing their active edges, and the current investigation will boost the further development of superior 2D electrocatalysts for efficient HER.*

3.1 Introduction

Recently, it has been found that 2D transition metal dichalcogenides (TMDs) can be adopted as efficient electrocatalytic materials, which can be used as an ideal alternative to Pt noble metal-based electrocatalysts for the HER. 2D monolayer TMDs have several advantages, especially in terms of low cost and high abundance. (Yang and Shin, 2014; Lei, Pakhira, Fujisawa, Wang, Iyiola, Perea López, et al., 2017; Ao et al., 2020; Upadhyay and Pakhira, 2021b; Xiao et al., 2021; Ekka et al., 2022) They have a large surface area, and it is possible to tune their electronic properties. (Lei, Pakhira, Fujisawa, Wang, Iyiola, Perea López, et al., 2017) Their structural unit consists of a transition metal atomic plane sandwiched between two chalcogen planes, and weak van der Waals (vdW) forces hold two successive MX_2 layers to form the 2D layer structure. (Shi and Wang, 2018; Cardoso, Piquini and Ahuja, 2021) These weak vdW interactions and forces significantly determine their structural phases, properties, equilibrium structures, and spectroscopic properties. These TMD materials, especially 2D monolayer molybdenum disulfide (MoS_2) and 2D monolayer tungsten disulfide (WS_2) nanosheets, have shown electrocatalytic activity for the HER. (Yang and Shin, 2014; Lei, Pakhira, Fujisawa, Wang, Iyiola, Perea López, et al., 2017) In the past few decades, the discovery of chemical, electronic and structural properties of these 2D TMDs has brought a significant improvement in the basic understanding of the electrocatalysis process during the HER. However, due to the lack of metal edge sites and electron transport efficiency in multilayer TMDs, the electrocatalytic efficiency of these materials for hydrogen production has been hindered. (Wang et al., 2015; Som, Mankad and Jha, 2018) In other words, the scarcity of active edge sites on these catalysts is one of the main obstacles to H_2 production. The main challenge is to activate the surface of these substrates by enhancing the number of substrate surface sites and hence the catalytic activity. Several attempts have been made to activate the basal planes (001) of the pristine 2D TMDs by phase engineering, applying strain, doping and vacancy creation. (Li et al., 2016; Er et al., 2018; Lee et al., 2018)

It is reported that the fabrication of the Janus structure of TMDs is also an effective method to enhance their chemical and physical properties, and they have gained a lot of interest in electrochemistry because of their excellent catalytic properties and performances. (Er et al., 2018; Ji et al., 2018) Generally, both layers of chalcogen atoms in

the pristine TMDs have identical chalcogen atoms, whereas a Janus 2D single-layer TMD is formed when both layers of chalcogen atoms are not identical atomic layers. (A. Y. Lu et al., 2017; Er et al., 2018; Shi and Wang, 2018) Janus single-layer TMDs have been synthesized through various experimental techniques in which JTMDs break the symmetry of the out-of-plane structure. (Yuan, Shan and Li, 2020) It has been studied that the JTMD layers (MXY, where M = transition metal atoms, W; X/Y = VI A group elements) have shown intensification of inactive sites at basal planes as well as edges in contrast to the pristine TMD (like MX₂) layers, which helps to increase the evolution of hydrogen. (Zhang et al., 2017; Er et al., 2018) Due to the different electronegativity of the X and Y layers of chalcogen atoms in the Janus MXY structure, an inherent dipole moment exists. This property distributes holes and electrons present in the structure resourcefully on the surface for upgrading electrocatalytic activity. (Ji et al., 2018) Recently, Lu et al. adopted hydrogen plasma treatment to change the top layer S atoms in the 2D monolayer MoS₂ with H atoms by CVD and then controlled the reaction conditions to change the top H atoms with Se atoms to synthesize a 2D monolayer of the Janus MoSSe TMD. (A. Y. Lu et al., 2017) In another method, Janus MoSSe was successfully fabricated via the vulcanization of single-layer MoSe₂ in which the top layer Se atoms were vulcanized with a controlled displacement reaction with a vaporized S-layer. (Zhang et al., 2017) Both methods generate a highly asymmetric monolayer Janus MoSSe with inherent strain as well as an electric field, thus providing an alternative method to enhance the activity in the HER as a JTMD catalyst. Another type of Janus monolayer WSSe also has a desired energy band arrangement; however, its electrocatalytic performance for the HER is still unclear. (Ju et al., 2020) A detailed investigation of the electronic properties, HER mechanism, activation barriers, reaction pathways on the surfaces of 2D WSSe JTMDs and reaction kinetics with thermodynamics has not been explored yet. We hypothesized that the 2D monolayer WSSe JTMDs could be used as an excellent electrocatalysts for the HER due to their reasonable design to trigger the “inert” in-plane Se-W-S.

Inspired by the unique properties of Janus single-layers, we computationally designed a 2D monolayer WSSe JTMD material and studied its electronic properties, i.e., the band structure, band gap and total density of states (DOSs) with its HER catalytic efficiency based on the first-principles density functional theory (DFT) method. To explain

the HER mechanism with the catalytic activity of the 2D WSSe JTMD, we developed a finite non-periodic molecular cluster model system $W_{10}S_{12}Se_9$ corresponding to the 2D monolayer Janus WSSe material and studied all the reaction intermediates with the transition states (TSs) by employing the DFT method.^(Huang *et al.*, 2015) The DFT method is very much helpful to derive thermodynamic quantities like free energy, reaction barriers, zero-point vibrational energy (ZPE), enthalpy, etc., by simulating the reaction intermediates that occurred during the HER process on the surface of the electrocatalyst. Therefore, in order to screen out the suitable candidate from the available options, it is important to calculate the relative free energy (ΔG) value during the hydrogen adsorption process and the H_2 molecule evolution process in both the gas and the solvent phases.^(Tang and Jiang, 2016)

In the present study, it was found that the exposed S-/Se-edge ($\bar{1}010$) and W-edge ($10\bar{1}0$) of the 2D monolayer JTMD WSSe are catalytically active for the HER, and the (001) basal planes of the S-W-Se tri-layer of the WSSe JTMD have exposed surfaces. It has more active sites for hydrogen adsorption on the catalytic surface due to the presence of a higher surface-to-volume ratio compared to the pristine 2D TMDs. The HER mechanism on the active surface of the 2D monolayer Janus WSSe material has been studied by exploring the reaction pathways with changes in free energy (ΔG) during the reaction process. The present DFT study shows that our 2D monolayer Janus WSSe catalyst follows the Volmer–Heyrovsky (V-H) reaction mechanism pathway with very low activation energy barriers. The low activation energy barriers, high TOF rate and low Tafel slope of the 2D Janus WSSe TMD have led us to report that it is an excellent HER electrocatalyst for the sustainable production of H_2 .

3.2 Computational Details

Computational methods play a significant role in studying transition metal-containing molecules or complexes compared to the other row elements/atoms in the modern periodic table.^(Chen, Menning and Zellner, 2008; Pakhira *et al.*, 2015, 2016; Pakhira, 2019) Recently developed plane-wave basis sets, Gaussian basis sets, Gaussian-type orbitals (GTOs), pseudopotentials and ultra-fast supercomputers make computations easier to explore the surface phenomenon of different catalysts for investigating various

surface mechanisms. (Sinha, Deshpande and Pakhira, 2019; Nagaraj et al., 2020; Pakhira and Mendoza-Cortes, 2020; Sinha and Pakhira, 2021) The theoretical and computational methods along with other parameters used in the calculations have a great importance in exploring the HER activity of the electrocatalyst. Reaction barriers play a prominent role in understanding the adsorption of an atom on the catalytic surface (adsorbent) to use it for various electrocatalytic applications. First-principles-based DFT (Frost and Musulin, 1953; Pakhira, et al., 2013; Nagaraj et al., 2020; Upadhyay and Pakhira, 2021b) methods are used to explore the electronic structure, properties, reaction pathways, kinetics, energetics, thermodynamics and mechanism for the H₂ evolution. (Baseden and Tye, 2014; Hui, Schorr, et al., 2018; Upadhyay and Pakhira, 2021b) The equilibrium geometry of the 2D periodic monolayer structure of the Janus WSSe with its electronic properties has been computed by employing the periodic hybrid DFT (Chen, Menning and Zellner, 2008) method in the present investigation. A non-periodic finite molecular cluster model system W₁₀S₁₂Se₉ of the 2D monolayer WSSe JTMD has been used here to explore the reaction kinetics, and the DFT method has been applied to study the HER mechanism on the active surface of the 2D Janus WSSe. The detailed description of the methods and computational techniques can be found below:

3.2.1 2D periodic slab development and electronic property calculations:

DFT is one of the most important theoretical and computational methods for assessing structural properties, equilibrium geometries, material properties and ground-state electronic property calculations of any kind of quantum mechanical system. (Frost and Musulin, 1953; Pakhira, et al., 2013; Nagaraj et al., 2020; Upadhyay and Pakhira, 2021b) This DFT computational method is based on the first-principles quantum mechanical approach to deal with the systems at the subatomic level where the electron density, electronic configuration and electronic energies play a vital role towards the overall structure, energy, reactivity and stability of the system of consideration. The equilibrium geometry of the 2D layer structure of the WSSe JTMD has been obtained by employing the B3LYP-D3 DFT-D (i.e., Becke, 3-parameter, Lee–Yang–Parr with Grimme's 3rd order dispersion-corrected hybrid density functional theory) method (Grimme et al., 2010; Pakhira, et al., 2013; Pakhira, Takayanagi and Nagaoka,

2015; Caldeweyher, Bannwarth and Grimme, 2017; Pakhira, Lucht and Mendoza-Cortes, 2017; Upadhyay et al., 2022) implemented in the CRYSTAL17(Dovesi et al., 2018; Patel et al., 2022) suite code, which has been proven to provide the reliable electronic structures and properties within the DFT frame. Compared to the Hartree–Fock (HF) method, the B3LYP-D3 method(Kellie and Kellie, 2013; Pakhira, Sahu, et al., 2013; Pakhira and Mendoza-Cortes, 2020; Patel et al., 2022) endures less or no spin contamination effect which helps to provide excellent geometry calculations, i.e., in other words, the present DFT-D method diminishes the spin contamination effects during the calculations. The semi-empirical Grimme's “-D3” dispersion correction has been added to the present calculations to consider all long-range weak vdW interactions.(Allouche, 2012; Pakhira, et al., 2013; Pakhira, Lucht and Mendoza-Cortes, 2016) By adding the Grimme semi-empirical dispersion correction parameters, the weak vdW interactions between the different layers of the material and atoms have been included in this B3LYP DFT calculation.(Grimme et al., 2010; Pakhira, Takayanagi and Nagaoka, 2015; Caldeweyher, Bannwarth and Grimme, 2017) Gaussian-type atomic basis sets have been taken into account in the present DFT method calculations and found to be more effective than other types of basis sets for DFT calculations of the periodic systems.(Lei, Pakhira, Fujisawa, Wang, Iyiola, Perea López, et al., 2017; Liang et al., 2019; Lei et al., 2021; Sinha and Pakhira, 2021; Upadhyay and Pakhira, 2021b; Upadhyay and Pakhira, 2021) It is important to note here that Gaussian-type orbitals (GTOs) are used in the CRYSTAL17 code, which have not been implemented in the Vienna Ab initio Simulation Package (VASP) code. This method is different from the plane wave-based codes like VASP, Wien2K, CP2K, CASTEP and Quantum Espresso. However, both approaches yield similar results, that is, the same results are obtained in both the VASP and CRYSTAL17 codes. Triple- ζ valence with polarization (TZVP) Gaussian-type atomic basis sets have been considered for both the S and Se atoms,(Peintinger, Oliveira and Bredow, 2013; Vilela Oliveira et al., 2019) and the HAYWSC 311(d31) Gaussian basis set with Hay–Wadt type effective core potentials (ECPs) has been used for the W atoms in the present calculations.(Corà et al., 1996) ECP is very useful for computations as it can replace the core electrons in a calculation with an effective potential, thereby eliminating the need for the core basis functions, which usually require a large set of Gaussians to describe

them.(Bergner *et al.*, 1993; Martin and Sundermann, 2001; Pakhira and Das, 2011, 2012; Pakhira, Bera and Das, 2011; Pakhira, Mondal and Das, 2011) In addition to replacing the core, they are used to represent relativistic effects, which are largely confined to the core. In this context, both the scalar (spin-free) relativistic effects and spin–orbit (spin-dependent) relativistic effects are included in effective potentials.(Pakhira, Mondal and Das, 2011; Pakhira *et al.*, 2012) The DFT-D method reduces the spin contamination effects in the structural and electronic property calculations of the 2D periodic layered materials which helps to provide a good elevated and equilibrium geometry.(Baker, Scheiner and Andzelm, 1993; Montoya, Truong and Sarofim, 2000; Pakhira, Takayanagi and Nagaoka, 2015; Pakhira and Mendoza-Cortes, 2020) Spin-polarized calculations have been performed to obtain the equilibrium structures and to study the electronic properties during periodic hybrid DFT-D calculations. A spin-polarized solution has been computed after the definition of the (α , up spin and β , down spin) electron occupancy. In other words, it may be here noted that spin-unrestricted wave functions are used in the present calculations to incorporate spin polarization by using the keywords “SPIN” and “SPINLOCK” in the *ab initio* CRYSTAL17 program. The “ATOMSPIN” keyword is also used to specify the single spin of the TM atoms in the material.(Pakhira, Lucht and Mendoza-Cortes, 2017; Salustro *et al.*, 2017) The threshold for the convergence of energy, force and electron density is set to 10^{-7} a.u. To develop the 2D monolayer Janus WS₂Se, we took a hexagonal symmetric 2D monolayer WS₂ structure with ABA layered stacking (where A is sulfur and B is tungsten) and replaced the top layer of S in the WS₂ with a Se atom layer to form a 2D WS₂Se structure with ABC layered stacking (A-sulfur, B-tungsten, and C-selenium). Furthermore, a vacuum slab of 500 Å is introduced in the Z direction to avoid the interaction between the two periodic units as implemented in CRYSTAL17.(Dovesi *et al.*, 2018; Pakhira, Kumar and Ghosh, 2023)

Contribution related to the DFT exchange is assessed through the numerical integration of the unit cell volume. All the integrations in the first Brillouin zone are sampled on a $20 \times 20 \times 1$ Monkhorst–Pack(Evarestov and Smirnov, 2004) k-mesh grids with a resolution $2\pi \times \frac{1}{60} \text{ Å}^{-1}$ for the 2D monolayer WS₂Se JTMD. Monkhorst k-mesh grids were used for computing the 2D electronic layer structure, geometry, density of states (DOS), and electronic band structure calculations. The k-vector path used to draw the band

structure is selected in the highly symmetric Γ - M - K - Γ direction according to the original 2D layer group symmetry of the Janus WSe TMDs. The atomic orbital electron densities of the S, Se and W atoms are used to calculate the DOSs. The total number of eight electronic bands were calculated around the Fermi level (E_F) in the first Brillouin zone along the highly symmetric Γ - M - K - Γ direction which is consistent with the symmetry of the 2D WSe JTMD. The VESTA(*Momma and Izumi, 2011*) visualization software has been used to analyze the crystal structures and to draw the graphics.

3.2.2 Non-periodic finite molecular cluster model system and HER mechanism:

A finite cluster model system $W_{10}S_{12}Se_9$ has been constructed by considering the periodic structure of the 2D monolayer WSe JTMD material, which is highlighted by a triangle as shown in Figure 3.1. This molecular cluster model consists of 10 W atoms, 12 S atoms and 9 Se atoms. From this finite molecular $W_{10}S_{12}Se_9$ cluster model system, 3-W periodicity can be understood by simple electronic counting parameters. Each W atom in the central basal plane (001) of the cluster model is bonded with 6 chalcogen atoms (3-S atoms in one plane and 3-Se atoms in the other plane) and each chalcogen atom (either S or Se atoms) in the basal plane is bonded with 3-W atoms in the middle plane of the inert basal plane. In Figure 3.1, the two horizontal dashed lines indicate the terminations along with the $(10\bar{1}0)$ W-edges and $(\bar{1}010)$ S-/Se-edges. The triangle represents the terminations for the W-edge and S-/Se-edge clusters and the dangling bonds in the finite cluster have been set by considering the same triangle as shown in Figure 3.1. Each W atom in the basal plane (001) of the finite molecular cluster model has an oxidation state of +4 and is bonded with the three Se atoms at the upper plane and the three S atoms at the lower plane, which gives a contribution of $4/6 = 2/3$ electrons towards each W-Se and W-S bonding resulting in a stabilized structure. The same can be understood with the oxidation state of the Se atoms in the basal plane. Each Se atom has a -2-oxidation state and it shares an electron to the W atom, which results in a contribution of $2/3$ electrons towards each W-Se bond. Similarly, the edges of the periodic molecular cluster $(00\bar{1}0)$ are stabilized with the 2 local electrons of the W-Se bonds (as well as W-S bonds) having a single electron contribution towards four W-Se bonds in the basal plane as shown in Figure 3.1. In the valence bond picture, this has been illustrated in terms of resonating structures. However, the surface

stabilizes the W–S/Se valence bond structures with local 2-electron bonds. This $14/3$ {i.e., $(2 \times 1) + [4 \times (2/3)]$ } contribution of electrons towards the W–Se bonds of the edge W atom is satisfied with the d^2 configuration of one W atom and d^1 configuration of two W atoms at the edges. This configuration leads to a molecular system with a periodicity of 3, which results in the achievement of a stabilized molecular cluster model having three edges without any unsatisfied valency. Thus, we considered a molecular cluster $W_{10}S_{12}Se_9$ model system (denoted as [WSSe]) to represent both the S- and Se-terminated W-edges on the surfaces of the 2D monolayer WSSe JTMD and this molecular model system is good enough to explain the HER process.

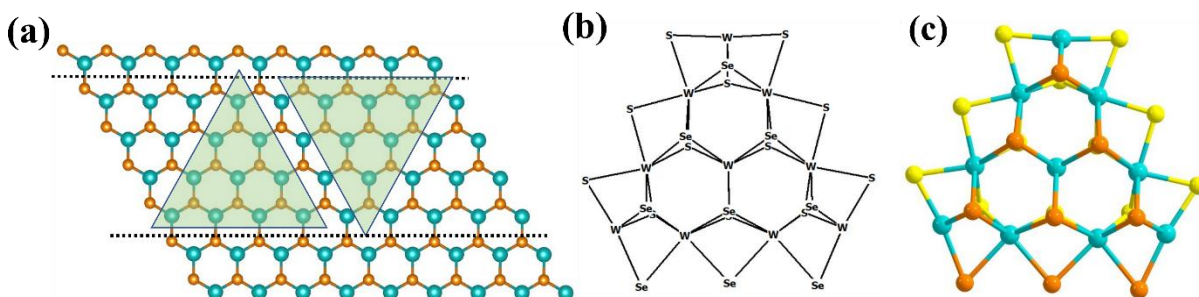


Figure 3.1 (a) Top view of a 2D Janus WSSe monolayer. The two up and down horizontal dashed lines represent the end points along the $(10\bar{1}0)$ W edge and $(\bar{1}010)$ S-/Se-edge. These two triangles represent the W-edge and S-/Se-edge clusters; (b) schematic diagram of the W-edge cluster; (c) equilibrium geometry of the triangular W-edge cluster with $W_{10}S_{12}Se_9$ stoichiometry.

We performed non-periodic quantum mechanical DFT calculations to determine the HER reaction mechanism pathway on both the W site and S-/Se- site of the 2D Janus WSSe. It should be mentioned here that the exposed surface is usually the (001) basal plane of the WSSe three-layer, W edge and S-/Se-edge. It was found that the exposed S-/Se-edge $(\bar{1}010)$ and W-edge $(10\bar{1}0)$ of the 2D monolayer JTMD WSSe are catalytically active for the HER, and the (001) basal planes of the S–W–Se tri-layer of the WSSe JTMD are exposed surfaces. Figure 3.1a shows how we have selected the triangular non-periodic molecular clusters from the periodic array to highlight the W edges and the X (chalcogen) edges to form the non-periodic finite molecular cluster $W_{10}S_{12}Se_9$ system. Figure 3.1b represents the schematic diagram of the finite W-edge cluster with the chalcogen active sites, and Figure 3.1c represents the equilibrium structure of the non-periodic molecular

cluster $W_{10}S_{12}Se_9$ obtained by the M06-L DFT computational method. It has been used to explore the HER mechanism with the reaction pathways on the active surface of the 2D monolayer WSSe JTMD by calculating the free energy changes of the different reaction intermediates and the energy barriers corresponding to the proton adsorption at the TM during the H^* -migration or Volmer reaction step with the H_2 evolution during the Heyrovsky reaction step of the HER process. (Phys, 2008; Zhao and Truhlar, 2008) It is found that the M06-L DFT method provides a reliable energy barrier for reaction mechanisms of the subject reaction of the material systems containing TMs such as Mo, W, etc., i.e., organometallic catalysts. (Ekka et al., 2022) These calculations include optimizing the reactants, products and transition states (TSs). The most important significance of using the M06-L local functional DFT method is that it helps to provide the accurate measurements of energies of the systems consisting of a large number of atoms and molecules, considering the Gaussian group density algorithms, which is the major advantage over the non-local functionals. Again this M06-L method is computationally cost-effective, helps to precisely calculate the energies of the systems having TMs and is also able to calculate the energy changes during the formation of transition states (TSs). (Phys, 2008; Zhao and Truhlar, 2008; Lei, Pakhira, Fujisawa, Wang, Iyiola, Perea López, et al., 2017; Niu et al., 2018; Liang et al., 2019) For this model, we used the 6-31+G** (double- ζ Pople-type) (W J Hehre, Ditchfield and Pople, 1972; Frisch, Pople and Binkley, 1984) Gaussian basis sets for the H, O and S atoms, and the LANL2DZ (Los Alamos National Laboratory 2 double- ζ) basis set with effective core potential (ECP) for the W atoms. (P Jeffrey Hay and Wadt, 1985; P. Jeffrey Hay and Wadt, 1985)

It is necessary to introduce individual electrons (e^-) and protons (H^+) to our molecular system separately to study the detailed HER mechanism on the active surface of the 2D Janus WSSe and to find out the energy changes during different intermediate formations. This requires calculating the energies for electrons and protons, so the free energy of electrons in a standard hydrogen electrode (SHE) is determined by taking the difference between half of the free energy of the hydrogen molecule $G(1/2 H_2)$ and the free energy of a proton $G(H^+)$. The free energy of the hydrogen at 1 atmospheric pressure and 298.15 K temperature is calculated in the same way as the above DFT M06-L method. The Gibbs free energy (G) of a proton at 1 M in the solvent is about $-270.3 \text{ kcal mol}^{-1}$. The

Gibbs free energy (G) value of a proton (H^+) at 1 M in water has been computed by considering its gas phase value $-6.3 \text{ kcal mol}^{-1}$ and it was taken as the sum of its gas-phase value and the empirical hydration energy $-264.0 \text{ kcal mol}^{-1}$.[\(Tissandier et al., 1998\)](#)

The polarizable continuum model (PCM) has been used to take into account the solvation effects in all calculations and to find out the energy barriers of the TSs during the HER process on the surfaces of the 2D WSSe JTMD. The HER involves the adsorbed hydrogen migration from the active chalcogen site to the metal site in the H^* -migration reaction and the recombination of adsorbed hydrogen (at the transition metal atom site in the 2D WSSe JTMD) with the solvated proton from the water cluster to evolve as H_2 . The water cluster (three water molecules and hydronium ion i.e., $3\text{H}_2\text{O} + \text{H}_3\text{O}^+$) acts as a source for an external proton which is explicitly brought to the vicinity of the molecular cluster model system.[\(Lipparini and Mennucci, 2016\)](#) We have modeled our reaction mechanism in water with a dielectric constant of 78.35. To get a better understanding of the HER mechanism on the active surface of the 2D monolayer WSSe JTMD, the highest occupied molecular orbital (HOMO) and lowest unoccupied molecular orbital (LUMO) calculations have been performed at the equilibrium geometries of both the TSs. This gives a better overview of the atomic orbitals in the MO which have been overlapped during the adsorbed hydrogen migration in the Volmer reaction step and the evolution of molecular H_2 during the Heyrovsky step for the proposed Volmer–Heyrovsky reaction mechanism of the HER.[\(Hu, Wu and Jiang, 2018\)](#) Harmonic vibrational frequency calculations at the equilibrium geometry have been performed to obtain the thermodynamic parameters such as entropy, Gibbs free energy, enthalpy and the zero-point vibrational energy (ZPE) at the same level of theory. To confirm the TSs appearing during the HER, intrinsic reaction coordinate (IRC) calculations have been performed.[\(Sahu et al., 2013; Pakhira et al., 2015, 2016\)](#) The Gaussian16 suite code has been employed to obtain the equilibrium structures (i.e., geometry) and TSs of the different intermediates obtained during the HER mechanism.[\(Frisch, Trucks, Schlegel, Scuseria, M. A. Robb, et al., 2016\)](#) The Gaussian16 code is the latest version of the Gaussian series of programs which has the capabilities of the most advanced electronic structure designing functions. ChemCraft visualization software has been used to visualize and analyze all the equilibrium geometries, intermediate structures and TSs during the HER process.[\(Andrienko, 2015\)](#)

3.2.3 Cluster Model Validation:

In order to verify the molecular cluster model system $W_{10}S_{12}Se_9$ which has the same chemical/electronic properties as the W-edge of the 2D monolayer WSSe JTMD, we calculated the hydrogen adsorption energies for both the molecular cluster model and periodic 2D monolayer WSSe JTMD. Figure 3.2 shows that the hydrogen binding energies determined by using the finite clusters and 2D periodic slabs differ by an amount 0.09 eV and 0.21 eV for the two different stoichiometries. This cluster model $W_{10}S_{12}Se_9$ has been developed to explore and investigate the electrochemical reaction mechanisms with the most favorable H_2 evolution reaction pathway, as it allows for more flexible use of the M06-L DFT method, which more precisely determines reaction barriers, reaction kinetics, intermediates and bond energies. It is difficult to use a cluster model with a net charge in the case of periodic systems, i.e., it is not possible to consider the charge of the system during the subject reaction in the 2D periodic model system of the WSSe JTMD. Furthermore, the cluster model allows us to incorporate electrons (e^-) and protons (H^+) simultaneously into various reaction steps and report free energy as a function of electrochemical potential and pH. Very recently, Pakhira et al. studied the electrocatalytic activities of the 2D single layer MoSSe JTMD where they used similar kinds of molecular cluster model system to investigate the electrocatalytic HER on the surfaces of MoSSe JTMD. *(Pakhira and Upadhyay, 2022)* The present $W_{10}S_{12}Se_9$ molecular cluster model has the same chemical properties as the periodic 2D Janus WSSe as depicted in Figure 3.2.

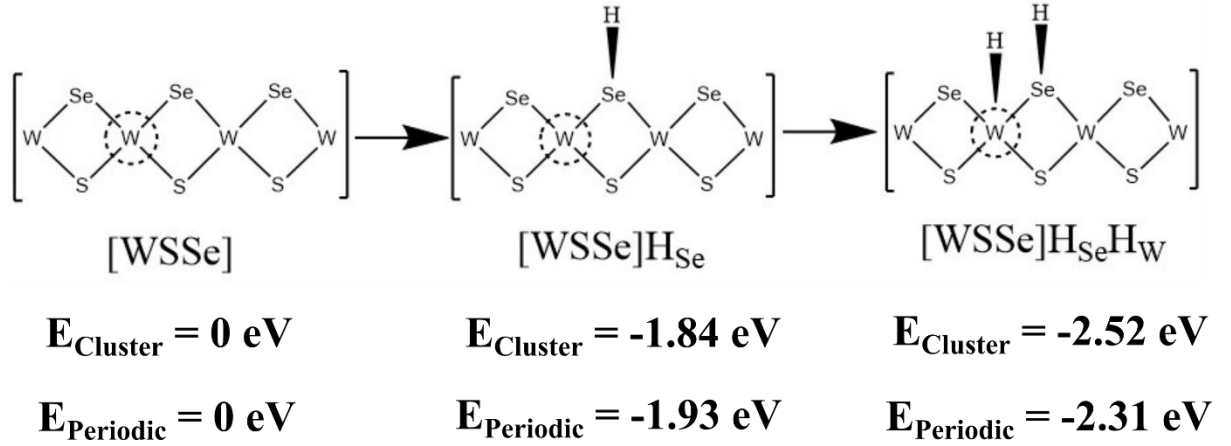


Figure 3.2. Hydrogen adsorption energy at the W-edge of 2D monolayer WSSe JTMD. $E_{Cluster}$ represents the relative electron energy during hydrogen adsorption considering the molecular cluster model system, and $E_{Periodic}$ is the relative electron energy obtained from periodic 2D layer calculations.

We calculated the hydrogen adsorption energies of 2D WS_2 and WSe_2 periodic structures for comparison with 2D monolayer WSSe JTMD. In pristine 2D monolayers, WS_2 and WSe_2 hydrogen adsorption energy have been found at -2.23 eV and -2.59 eV, respectively. However, in 2D monolayer Janus WSSe, hydrogen adsorption has been found at -1.93 eV. We need a catalyst for hydrogen production that has hydrogen adsorption energies approximately equal to zero. Therefore, the hydrogen adsorption energy of the catalyst should appear as close to zero as possible. So, here we show that the hydrogen adsorption energy of the 2D Janus WSSe is close to zero compared to other pristine materials (WS_2 and WSe_2). Then 2D Janus WSSe excellent electrocatalyst for hydrogen production because of its less hydrogen adsorption energy than pristine WS_2 and WSe_2 materials.

3.2.4 Theoretical Calculations and equations

Here, it is important to calculate the change in Gibbs free energy (ΔG) in between intermediates states for the HER mechanism. So, the Gibbs free energy (G) for each HER steps were calculated at 298.15 K by following equation:

$$G = E_{DFT} + E_{ZPE} + \int C_p dT - TS$$

Where E_{DFT} is the electronic energy, E_{ZPE} is the zero-point energy, $\int C_{\text{pdT}}$ is the enthalpic temperature correction, and TS is the entropic contribution. E_{ZPE} , C_{pdT} and TS are calculated from temperature, pressure and calculated vibrational energy using the standard DFT method. The catalytic performances of the 2D monolayer Janus WSSe was characterized by the calculations of the changes of free energy (ΔG), enthalpy (ΔH), and electronic energy (ΔE) for all the reactant, products, intermediates and TSs for the HER.

$$\text{Change of free energy:} \quad \Delta G = \sum G_{\text{Product}} - \sum G_{\text{Reactant}}$$

$$\text{Change of enthalpy:} \quad \Delta H = \sum H_{\text{Product}} - \sum H_{\text{Reactant}}$$

$$\text{Change of electronic energy:} \quad \Delta E = \sum E_{\text{Product}} - \sum E_{\text{Reactant}}$$

For all purposes, we considered standard hydrogen electrode (SHE) conditions, where electrons and protons ($\text{pH} = 0$) are in equilibrium with 1 atmosphere of H_2 . In other words, the energy of the H^+/e^- pair is equal to half of the gaseous hydrogen (i.e., 0.5H_2) at equilibrium potential.

3.3 Result and Discussions

3.3.1. Equilibrium structural properties of the 2D monolayer WSSe JTMD

The catalytic performance of any catalyst depends on its stability, geometry, and electronic properties. So, to develop a better electrocatalyst for effective HER, it is essential to study their structural as well as electronic properties. In the case of the 2D monolayer WSSe JTMD, the transition metal W is sandwiched between the layer of S in one side and Se in the other side as depicted in Figure 3.1. The WSSe single layer has a similar honeycomb structure to the original 2D monolayer WS_2 TMD as shown in Figure 3.1 and there are three types of atoms W, S and Se in the primitive unit cell of the 2D monolayer WSSe JTMD. The W atom is six-fold coordinated, and S and Se are three-fold coordinated. We have computationally developed a 2D monolayer structure of the WSSe JTMD symmetric slab through the (001) basal planes to study their equilibrium geometries and properties. It was found that the 2D Janus WSSe monolayer slab has $\overline{P3}m1$ symmetry with the layer group number 69 corresponding to the tetragonal 2D layer system.⁸³ Table 3.1

lists the equilibrium lattice parameters of the equilibrium structures of the pristine 2D monolayer Janus WSSe computed by the hybrid periodic B3LYP-D3 DFT-D method. The equilibrium lattice parameters of the 2D monolayer WSSe JTMD were found to be 3.19 Å, which is consistent with the previously reported findings.[\(Ju et al., 2020\)](#) The relaxation structural parameters with the lattice constants of the 2D WSSe JTMD are reported in Table 3.1. A comparison of the lattice parameters of the 2D WSSe JTMD with the pristine 2D monolayer WS₂ and WSe₂ materials can be found in Table 3.1. The lattice constants (a and b) of the 2D Janus WSSe monolayer with the identical chalcogen element almost remain the same after the optimization regardless of the metal element, which indicates that the chalcogen atom has a vital role in determining the structural properties.

Table 3.1: The equilibrium lattice parameter (a), bond distance (d), bond angles, and Band gap (E_g) of the 2D monolayer pristine WS₂, WSe₂ and Janus WSSe are summarized here.

Materials	Lattice parameter (in Å)	Bond distance (in Å)	Bond angle (in °)	Band gap (in eV)	References
WS ₂	3.14	W-S= 2.39	$\alpha =$ $\beta=90$ $\gamma = 120$	2.78	This work
WS ₂ (Previously reported)	3.16	W-S=2.45	$\alpha =$ $\beta=90$ $\gamma = 120$	2.88	(Ramasubramaniam, 2012; Deng, Li and Li, 2018)
WSe ₂	3.22	W-Se=2.50	$\alpha =$ $\beta=90$ $\gamma = 120$	2.39	This work
WSe ₂	3.29		$\alpha =$ $\beta=90$	2.42	

(Previously reported)		W-Se=2.53	$\gamma = 120$		(Ramasubramaniam, 2012; Deng, Li and Li, 2018)
WSSe	3.19	W-S=2.40, W-Se=2.49	$\alpha =$ $\beta=90$ $\gamma = 120$	2.64	This work
WSSe (Previously reported)	3.26	W-S=2.42, W-Se=2.54	$\alpha =$ $\beta=90$ $\gamma = 120$	2.68	(Ju et al., 2020)

The vertical distance between the top and bottom chalcogen atoms (S and Se layers) defines the thickness of the 2D monolayer Janus WSSe TMD, and the thickness, which is the vertical distance between S and Se atoms in the WSSe JTMD material, is about 3.21 Å obtained by the DFT-D method. The equilibrium slab structure of the 2D single layer WSSe JTMD is depicted in Figure 3.3. The lattice parameter increases when the atomic number of chalcogenide atoms increases, and when element X/Y (which represents the type of chalcogen atom in the JTMDs) changes from the element S to Se, the atomic radius increases. All types of dissimilarity can be resolved through the non-identical oxidation and atomic radius between S and Se atoms, where the Se atom has a higher radius and smaller oxidation. Stability is also a major parameter to compare the catalytic performance of the electrocatalysts for effective HER.

3.3.2. Electronic properties

Studying the electronic properties of the 2D Janus monolayer TMDs is also important for its potential applications in electrochemistry. According to the present B3LYP-D3 calculations, the 2D monolayer Janus WSSe TMD has a direct band gap (E_g) at the K point which is about 2.64 eV given in Table 3.1. An earlier report shows that the

band gap of the 2D monolayer WSSe JTMD is 2.68 eV, and the calculated value of the energy band gap in the present study is well harmonized (~ 0.04 eV) with the earlier reported result. (Ju *et al.*, 2020) The electronic band structures and total density of states (DOS) of the 2D monolayer Janus WSSe TMD are depicted in Figure 3.3. To compare the electronic properties of the WSSe JTMD, the electronic band structures and total density of states of both the 2D monolayer WSe₂ and WS₂ TMDs have been computed at the same level of theory, as shown in Figure 3.3. The direct band gap of the 2D single-layer WSSe lies between those of the 2D single-layer WSe₂ and WS₂, as shown in Figure 3.3. The present DFT-D calculations reveal that these three WSSe, WSe₂ and WS₂ 2D monolayer TMDs are direct band gap semiconductors as the maximum of the valence band (VB) and the minimum of the conduction band (CB) of these TMDs are at *K* point and there is no electron density at the Fermi level (E_F) as depicted in Figure 3.3.

In addition, the total density of states of the 2D monolayer Janus WSSe TMD is calculated which helps in further understanding the electronic properties of the JTMD as shown in Figure 3.3. The E_F was found at -5.60 eV which is close to the top of the valence band as shown in the band structure and DOS of the 2D Janus WSSe. Due to the electronic energy states at the top of the valence band, the electron density in the total DOS of the 2D monolayer Janus WSSe TMD is also close to the E_F level as depicted in Figure 3.3. The total electron density of states (DOS) calculation confirms that the electronic band gap of the 2D monolayer Janus WSSe TMD is about 2.64 eV. The electron density at the bottom of the conduction band is far away from the E_F level which is equal to the energy band gap. The electronic property calculation of the 2D Janus WSSe confirms that it can be a potential electrocatalyst for the electrocatalytic HER. It was computationally found that the Janus WSSe material exhibits good catalytic activity compared with its parent materials WS₂ and WSe₂. So, as per our findings, we continue our research towards the computational study of the HER mechanism on the surface of 2D Janus WSSe. A comparison of the electronic properties of the 2D WSSe JTMD with the pristine materials (WS₂ and WSe₂) can be found in Table 3.1. (Wang *et al.*, 2018)

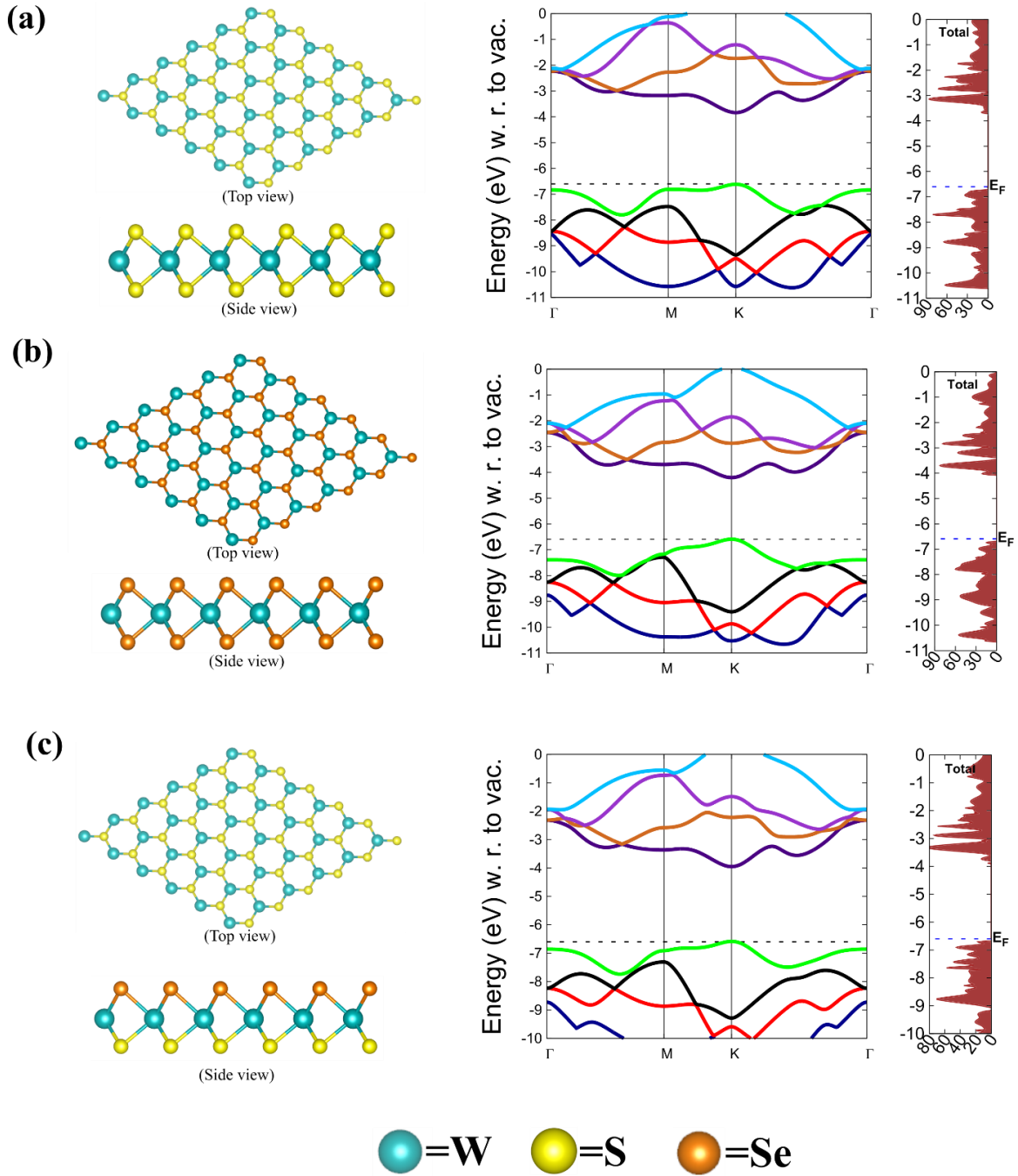


Figure 3.3. (a) The top view and the side view representation of 2D monolayer WS₂ with the band structure and total density of states (DOS). (b) The top view and the side view of 2D monolayer WSe₂ with the band structure and total density of states. (c) The top view and the side view of 2D monolayer Janus WSSe with the band structure and the total density of states are shown here.

3.3.3. HER mechanism and electrocatalytic activity

To investigate the HER performance of electrocatalysts, it is necessary to understand the HER mechanism with the chemical reaction process taking place on the surface of the catalysts. HER is a multi-step chemical reaction process for the production of molecular hydrogen (H_2), where both hydrogen adsorption and hydrogen molecule formation processes are of paramount importance to show the reactivity of electrocatalysts. Therefore, it is necessary to examine this 2D monolayer WSSe JTMD as a possible alternative to the Pt catalyst or Pt-based electrocatalysts for effective HER. The Pt electrode has nearly zero overpotential in acidic electrolytes, and that is why it has shown the best electrocatalytic HER activity to date. Though the Pt electrode is the best electrocatalyst, its commercial-scale application is impossible due to the metal scarcity and high cost. So, we computationally designed the 2D monolayer pristine WSSe JTMD to investigate the H_2 evolution reaction on the surface which can be useful for commercial application purposes alternative to Pt-based electrocatalysts. The HER reaction mechanism can be introduced by two reaction processes: (i) the Volmer reaction is the adsorption of hydrogen on the active edges of the 2D WSSe JTMD, which is represented by $H^+ + e^- \rightarrow H$, and (ii) in the other reaction, H_2 molecules are released by the catalyst after the Heyrovsky reaction ($H + H^+ + e^- \rightarrow H_2$) known as H_2 formation. Therefore, in the Volmer reaction process, the constant rate step is the resettling of hydrogen atoms, while in the Heyrovsky reaction process, the constant rate step requires imminent hydronium (H_3O^+), which is the source of protons (H^+) and reacts with adsorbed hydride to form H_2 .(Lei, Pakhira, Fujisawa, Wang, Iyiola, Perea López, et al., 2017; Mir et al., 2017; Wang et al., 2017) In the case of transition metal-based electrocatalysts, the Volmer-Heyrovsky reaction mechanism is more likely to dominate because they have a low value of relative free energy of the hydrogen adsorption during the HER process. An important fact that appears is the activity descriptor of the aforementioned HER mechanism and process.(Li et al., 2019) Therefore, for the analysis of the H_2 evolution reaction mechanisms and kinetics of the proposed 2D Janus WSSe catalyst, we have followed the mechanism discussed above. According to the Sabatier principle, a catalyst should create moderate bonds to the reagents and intermediates so that they are likely to adsorb to the surface, allowing the reaction to occur.(Laursen et al., 2012) The change of free energy (ΔG) during hydrogen adsorption

has been shown to be a successful descriptor of the HER activity, where the value of ΔG is close to thermal neutrality leading to the most active catalyst. In order to measure the efficiency of the catalyst for these reactions, it is necessary to calculate the change in free energy (ΔG) of the adsorption of hydrogen atoms at various positions on the electrode plane. The change in Gibbs free energy (ΔG_H) during the hydrogen adsorption is defined as:

$$\Delta G = \Delta E_H + \Delta E_{ZPE} - T\Delta S^H$$

where ΔE_H is the relative hydrogen adsorption electronic energy, ΔE_{ZPE} is the relative zero-point vibrational energy (ZPE) during the HER and ΔS^H is the relative adsorption entropy of $\frac{1}{2}H_2$, which has been expressed as $\Delta S^H = -\frac{1}{2}S_{H_2}^0$; $S_{H_2}^0$ is the entropy of H_2 under normal conditions and the value of $S_{H_2}^0 = 0.4$ eV. Taking $\Delta E_{ZPE} = 0.04$ eV, $\Delta G = \Delta E_H + 0.24$ eV, indicating that the binding energy of hydrogen atoms on the ideal catalyst surface must be equal to 0.24 eV. (Tang and Jiang, 2016; Mir et al., 2017; Som and Jha, 2020) Pt is the best HER catalyst because it possesses zero hydrogen adsorption energy ($\Delta G_H = 0$). So, we need a catalyst that has hydrogen adsorption energies (ΔG_H) approximately equal to zero. The change of Gibbs free energy should be neither too much negative nor too much positive because if there is a more negative value of ΔG , then hydrogen will bond more strongly to the surface of the catalyst, making the desorption step more difficult, and if there is a more positive value of ΔG , then the hydrogen bonded with the catalyst will be extremely weak, due to which the adsorption step will be difficult. Therefore, the change of Gibbs free energy of the catalyst should appear as close to zero as possible.

It has been described that the 2D monolayer WSe JTMD is a pure direct band semiconductor that might have potential applications in electrocatalysis because of its suitable band gap and thermal stability. However, the hydrogen adsorption energy is a useful descriptor for screening materials to identify the candidates for the HER. But the reaction barriers play an important role in determining the performance of the electrocatalyst, which determines the reaction rates for H_2 evolution. Thus, to design the most efficient HER catalysts, we must determine the reaction barriers for the various reaction sequences that can convert protons and electrons to H_2 . To enable the use of the most accurate DFT for reaction barriers while describing solvation effects, we used a

cluster model system of the 2D WSSe JTMD. This allows us to consider the introduction of protons (H^+) and electrons (e^-) separately and report free energies. Using a finite non-periodic molecular cluster model of a periodic system in determining reaction mechanisms with reaction barriers allows more flexibility in the accuracy of the methods (allowing us to use M06-L which is more accurate for reaction barriers and bond energies). Using the 2D non-periodic finite Janus WSSe cluster model, electrons and protons on the surfaces of the Janus WSSe TMD can be independently added or subtracted in separate phases during the HER process. We have used the $W_{10}S_{12}Se_9$ stoichiometric triangular W edge cluster, as shown in Figure 3.1c, and implemented it in non-periodic M06-L DFT theory. In order to verify that the molecular cluster model system $W_{10}S_{12}Se_9$ has the same chemical properties as the W-edge of the periodic 2D monolayer WSSe JTMD, we have calculated the hydrogen adsorption energies for both the molecular cluster model and periodic 2D monolayer WSSe JTMD systems.

3.3.3.1 Volmer-Heyrovsky (V-H) mechanism

The V–H reaction pathway at the active site of the 2D monolayer Janus WSSe is shown in Figure 3.4. It shows two steps of reactions, one is the Volmer reaction step, and the other is the Heyrovsky reaction step. The Volmer reaction refers to the initial adsorption of protons and electrons to form the adsorbed H^* . In the Heyrovsky reaction step, solvated protons from water (as a solvent) react with hydrogen adsorbed on a W-edge atom to form an H_2 molecule, i.e., in other words, the H_2 has been formed by adsorbing one solvated proton (H^+) from the solvent (here water) interacting with the adsorbed hydride H^- in the 2D WSSe JTMD during this Heyrovsky reaction. A source of hydronium (H_3O^+ ; i.e., protonation of water) that follows the proton reaction pathway is required during the Heyrovsky reaction. This process is a multi-step electrode reaction. As shown in Figure 3.4, in this reaction step, intermediate states and transition states (TS) appear during the HER process. The Heyrovsky reaction process is more complex than the Volmer reaction process because the source of protons H_3O^+ must be solvated in the reaction route. By using a set of 4 water molecules, we get actual results, one of them is a hydronium molecule (H_3O^+) that is protonated at first but is neutral at last. To facilitate the bonding between the adsorbed hydrogen atom and the proton, it is necessary to rearrange the protons within the

water cluster, thereby exposing the hydronium ion. We investigated the detailed reaction mechanism of the HER on the surfaces of the 2D monolayer WSSe JTMD, especially the active $(10\bar{1}0)$ W-edges and $(\bar{1}010)$ S-/Se-edges. Then, we examined the constraints of each reaction step to find the reaction rate-limiting step. The detailed scheme of the V-H reaction mechanism with the pathways is shown in Figure 3.4.

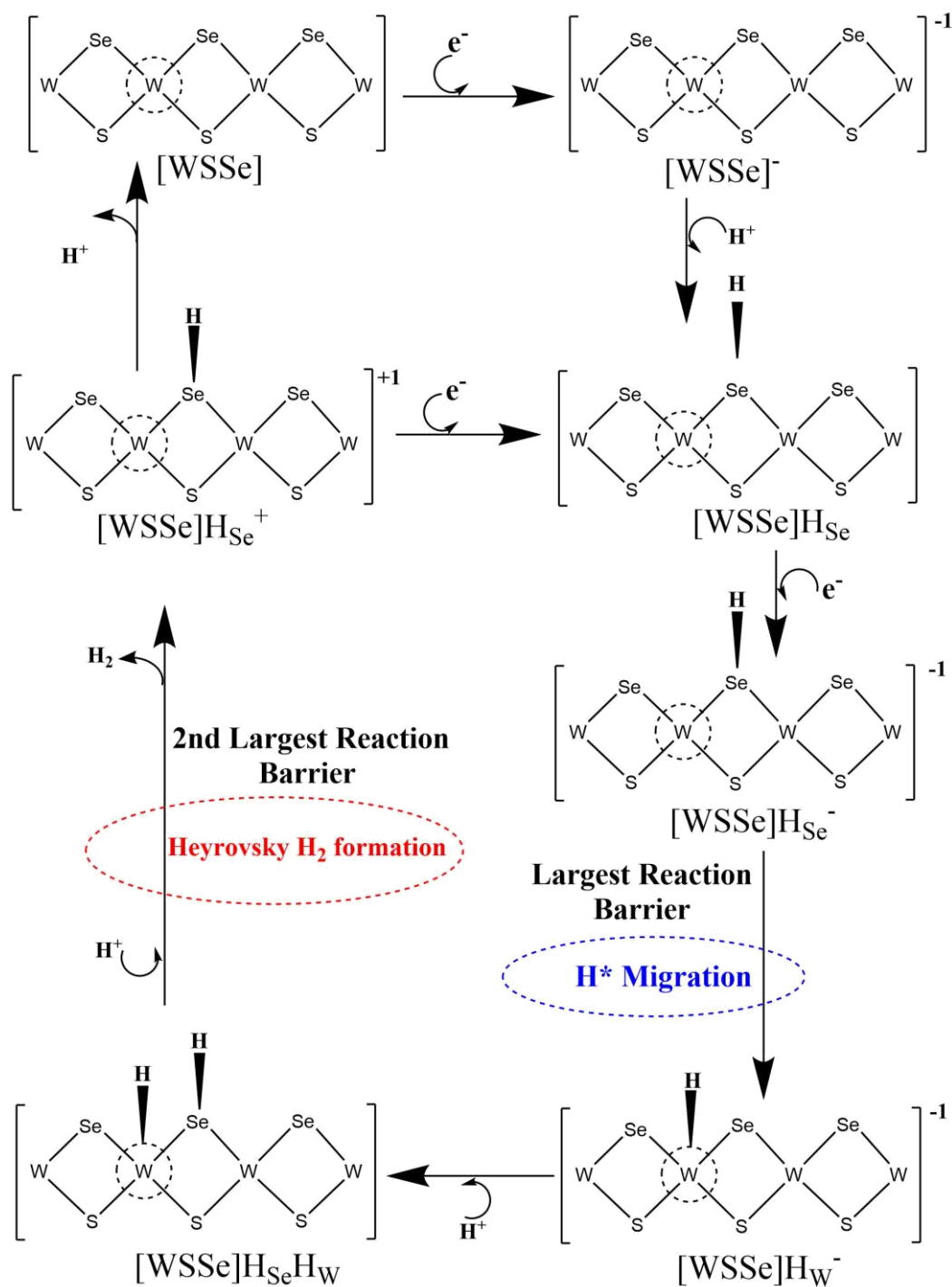


Figure 3.4: The HER mechanism occurs on the surface of the 2D monolayer WSSe JTMD as the electrocatalyst; the migration of H^+ indicates the first TS, highlighted by the blue dashed ellipse. The formation of H_2 in the Heyrovsky step gives the second TS, highlighted by the red dashed ellipse.

The equilibrium structure of the finite molecular $W_{10}S_{12}Se_9$ cluster model was obtained by the M06-L DFT method, and the electronic energy, free energy and enthalpy during the HER process have been successfully calculated at the same level of the DFT method. The detailed HER pathways are shown in Figure 3.4. A harmonic vibrational analysis has been performed at the equilibrium structures of the reactant, products, intermediates, and transition states (TSs) that appeared during the HER process. We observed that the equilibrium structure of the finite molecular $W_{10}S_{12}Se_9$ cluster model computed by the M06-L DFT method has positive frequencies, which confirms that the structure of the $W_{10}S_{12}Se_9$ cluster is thermodynamically stable.

The complete H_2 evolution process is accomplished with the introduction of individual electrons (e^-) and protons (H^+). It is necessary to inspect the most stable structure of the non-periodic finite molecular $W_{10}S_{12}Se_9$ cluster model system along with the other structures (products, intermediates, and TSs) resulting from the successive addition of each extra number of electrons and protons in order to understand the variation of changes of free energies between intermediates and eventually discover the possible lowest barrier pathway. Under the standard hydrogen electrode (SHE) conditions and $pH = 0$, the 2D monolayer [WSSe] JTMD material is in the most stable state with the bare neutral W-edge, which becomes the basis for our thermodynamic potential calculations. In the next step, an electron is adsorbed to the 2D WSSe JTMD, and then the Janus WSSe is negatively charged, $[WSSe]^{-1}$. The optimization was performed for the negatively charged Janus WSSe, and the electronic energy, free energy and enthalpy in the gas phase were successfully calculated. This equilibrium geometry $[WSSe]^{-1}$ is shown in Figure 3.5b. This step is performed under standard hydrogen electrode (SHE) conditions, which are the basis for the thermodynamic potential of oxidation and reduction processes. The energy cost ΔG from the [WSSe] state to the $[WSSe]^{-1}$ state computed in the gas phase is about 10.25 kcal mol^{-1} , listed in Table 3.2. The obtained reduction potential of $[WSSe]^{-1}$ is about -0.444 V, and in other words, we can say that the first reduction potential to obtain $[WSSe]^{-1}$ is about -444 mV, leading to a negatively charged cluster solvated in water. Here, the free energy of an electron in the SHE is laid down as the difference between half of the free energies of the hydrogen molecule and H^+ , (Tissandier *et al.*, 1998) and finally, we found that the free energy of an electron is about -0.1478 Hartree. The change of Gibbs free energy (ΔG)

of an electron under SHE conditions was computed by considering the difference between the free energy of an H^+ (proton) and half of the free energy of the H_2 molecule when $pH = 0$. After that, an H^+ is adsorbed on the Se-edge in the equilibrium structure of the 2D $[WSSe]^{-1}$. Here, we have considered adding a proton to the Se site of the W-triangle in the finite molecular system, i.e., it was found that the Se site is more favorable than the W-site for the proton adsorption considered in the present calculations. This is currently the most energetically favorable site. In the present study, we have chosen 50% Se/S coverage of the W-edge to study the HER mechanism. In 50% Se/S coverage of the W-edge cluster model system, the chalcogen atoms are more thermodynamically favorable sites for H^+ adsorption. After adsorbing the proton, $[WSSe]H_{Se}$ has been formed and the system becomes neutral and energetically stable again. To proceed further the HER, another electron (e^-) has been adsorbed by the $[WSSe]H_{Se}$, and the system becomes negatively charged denoted as $[WSSe]H_{Se}^{-1}$ with a reduction potential of -0.789 V. The changes of free energy (ΔG) due to the second electron reduction is about -18.65 kcal mol $^{-1}$ computed in the gas phase indicating that it is thermodynamically stable. Therefore, this HER follows a two-electron ($2e^-$) transfer reaction mechanism. In the next step of the HER process, the hydride ion (H^-) from the selenium (Se) site moves to the next adjacent reaction tungsten (W) site, this step is known as the H^* -migration reaction step or the Volmer reaction step. When the H^* migrates from the Se site to the nearest W site, a transition state (TS) has been formed, denoted as H^* -migration TS1. This step is the first reaction barrier, i.e., the H^* -migration reaction barrier or TS1. The optimized structure of the first transition state (TS1), i.e., TS1 is shown in Fig. 4e, and the position of the hydrogen during the formation of the TS1 is highlighted by a dotted red circle in Figure 3.5e. Here, we observed an imaginary negative frequency (-416.5 cm $^{-1}$) after optimization of this transition structure TS1. This negative frequency indicates that this is the correct geometry to be considered as a transition state structure formed during the HER process which has been verified by the IRC. The calculated H^* -migration barrier (computed in the gas phase) is about 2.33 kcal mol $^{-1}$, reported in Table 3.2. In the next step, the equilibrium structure of the $[WSSe]H_W^{-1}$ system is obtained by the same DFT method after hydrogen atom migration, and the optimized structure of the $[WSSe]H_W^{-1}$ is shown in Figure 3.5f. The free energy, electronic energy, and enthalpy have been calculated at the optimized geometry of

[WSSe]H_W⁻¹. Now, the H⁺ from the solvent medium attacks the Se site again and attaches to the Se on the surface of [WSSe]H_W⁻¹ to form the [WSSe]H_WH_{Se} which is also a thermodynamically stable intermediate. The equilibrium structure of the [WSSe]H_WH_{Se} is shown in Figure 3.5g. The equilibrium W–H and Se–H bond lengths were 1.72 Å and 1.478 Å, respectively, and the average W–Se equilibrium bond length at the reaction place was about 2.661 Å computed at the M06-L level of theory. The next step of the HER process is the formation of H₂ through the Heyrovsky mechanism, and this Heyrovsky reaction step is a very complicated reaction as H₂ evolves during this reaction. Three water molecules and one hydronium molecular cluster, i.e., 3H₂O + 1H₃O⁺ system, have been considered for exploring the Heyrovsky reaction mechanism to study the H₂ evolution process. In the Heyrovsky reaction step of the HER, the adsorbed H⁺ from hydronium (H₃O⁺) interacts with the solvated proton and H₂ is formed. First, we studied the reaction of hydronium (H₃O⁺) with the hydrogen atoms adsorbed on the edge of the Se atom. However, we found that the transition barrier, i.e., the reaction barrier (ΔG), was 33.24 kcal mol⁻¹ computed by the M06-L DFT method. This reaction barrier (i.e., transition state barrier) is quite high, so we have used a similar strategy to study further the reaction at the W edges where another hydrogen is already adsorbed by the H*-migration reaction. We found the optimized Heyrovsky transition state (TS2) and calculated the relative free energy (ΔG), electronic energy (ΔE), and enthalpy (ΔH) by employing the same M06-L DFT method. After the frequency calculations of TS2, we observed an imaginary negative frequency (about -263.31 cm⁻¹) in the system which confirms this structure to be a transition state structure. An IRC calculation has been performed at TS2 in both the forward and reverse directions to confirm the exact Heyrovsky TS in this H₂ evolution reaction step. The IRC can be defined as the minimum energy reaction path (MERP) in mass-weighted Cartesian coordinates between a reaction transition state and its reactants and products. It can be thought of as a path for molecules to move down the valley of products and reactants with zero kinetic energy. IRC methods have been widely used in quantum chemical analysis and prediction of chemical reaction mechanisms. IRC gives unique linkages from a given transition structure to local minima on the reactant and product sides. The equilibrium structure of this Heyrovsky transition state (TS2) is shown in Figure 3.5i. The Heyrovsky reaction barrier (ΔG) was calculated to be 5.05 kcal mol⁻¹ in the gas phase, as tabulated in

Table 3.2, and the values of ΔE and ΔH are 8.19 and 6.12 kcal mol⁻¹, respectively, found during H₂ formation in TS2. After the formation of Heyrovsky TS2, the molecular cluster becomes [WSSe]HSe⁺, and then we optimized this structure and calculated the changes of free energy, electronic energy and enthalpy. The equilibrium structure of the [WSSe]HSe⁺ is shown in Figure 3.5j.

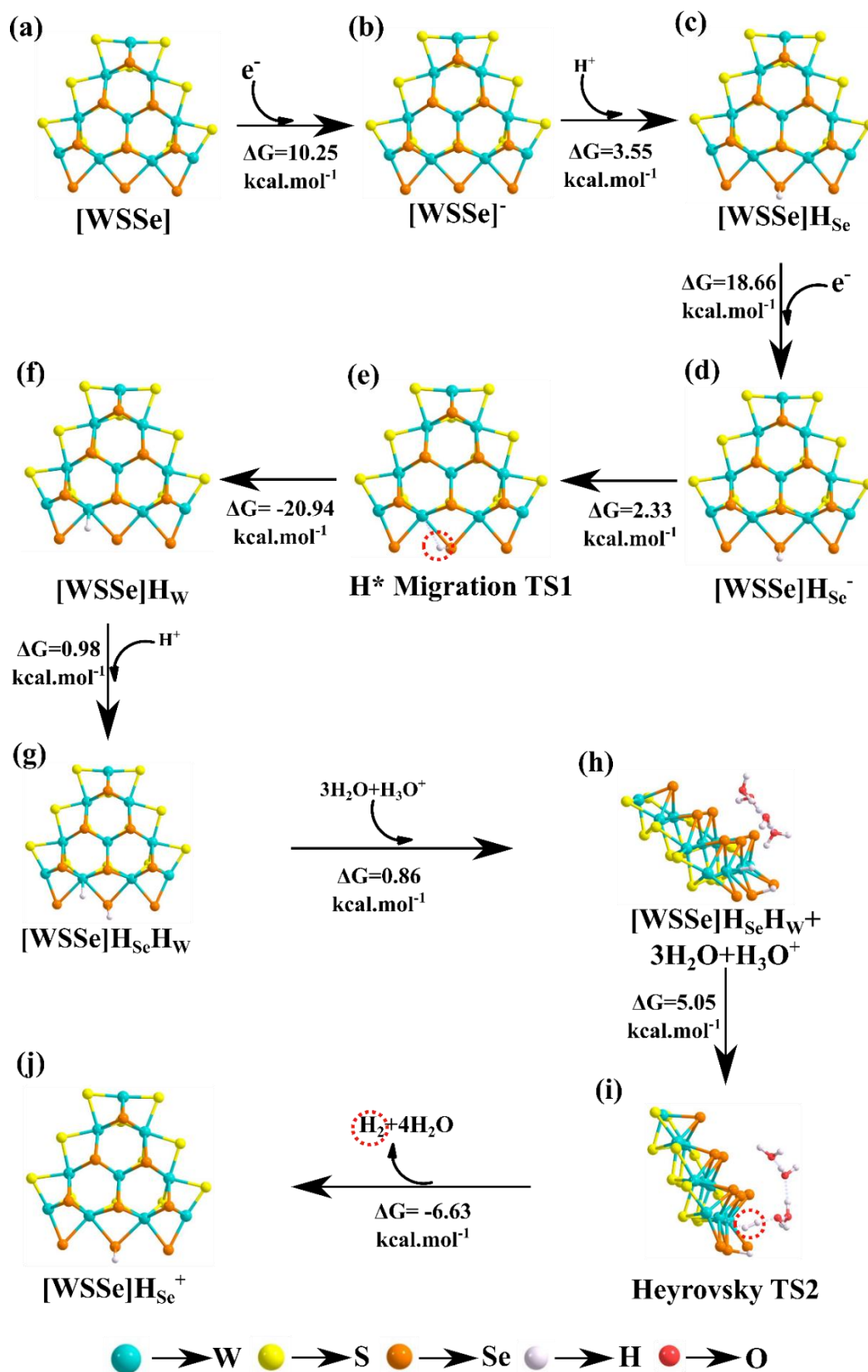


Figure 3.5: Equilibrium geometries and change of free energies in the gas phase of (a) [WSSe], (b) [WSSe]⁻, (c) [WSSe]H_{Se}, (d) [WSSe]H_{Se}⁻, (e) H^{*}-migration TS1, (f) [WSSe]H_W⁻, (g) [WSSe]H_{Se}H_W, (h) [WSSe]H_{Se}H_W + 3H₂O + H₃O⁺, (i) Heyrovsky TS2, and (j) [WSSe]H_{Se}⁺ computed by the M06-L DFT method considering a molecular cluster model system W₁₀S₁₂Se₉ to represent the 2D monolayer WSSe JTMD are shown here.

Table 3.2. The changes of electronic energy, enthalpy and Gibbs free energy of the various intermediates in the HER mechanism computed in gas phase are shown here. The HER happens at the Se-terminated W-edges on the surfaces of 2D monolayer WSSe JTMD

HER Reaction Intermediates	ΔE (kcal.mol ⁻¹) Gas Phase	ΔH (kcal.mol ⁻¹) Gas Phase	ΔG (kcal.mol ⁻¹) Gas Phase
[WSSe] → [WSSe] ⁻	11.24	11.08	10.25
[WSSe] ⁻ → [WSSe]H _{Se}	-0.99	4.08	3.55
[WSSe]H _{Se} → [WSSe]H _{Se} ⁻	18.23	18.02	18.65
[WSSe]H _{Se} ⁻ → Volmer TS1	2.59	1.65	2.33
Volmer TS → [WSSe]H _W ⁻	-22.14	-20.88	-20.94
[WSSe]H _W ⁻ → [WSSe]H _W H _{Se}	-4.11	1.23	0.98
[WSSe]H _W H _{Se} → [WSSe]H _W H _{Se} + 3H ₂ O + H ₃ O ⁺	-14.72	-13.49	0.86
[WSSe]H _W H _{Se} + 3H ₂ O + H ₃ O ⁺ → Heyrovsky TS2	8.19	6.12	5.05
Heyrovsky TS → [WSSe]H _{Se} ⁺	8.89	8.12	-6.63
[WSSe]H _W H _{Se} → Tafel TS3	11.74	10.09	10.02

We keenly follow different reaction pathways scheme as shown in Figure 3.6, but we have focused on two important saddle points, namely the H^{*}-migration TS (TS1), in which H^{*} atoms migrate from the Se to the transition metal atom site (W), and the other one is the Heyrovsky reaction step, where H⁺ from the adjacent water cluster combines with hydrated hydrogen and H^{*} from the W site to evolve as H₂, denoted as Heyrovsky TS2. It has been observed that the Heyrovsky TS2 reaction step is the rate-determining step

for the HER. The changes in free energy, enthalpy and electronic energy after each reaction step are listed in Table 3.2. According to our gas phase calculations, we observed that the activation barrier for the H*-migration step is about 2.33 kcal mol⁻¹ and the energy barrier of the Heyrovsky reaction step is about 5.05 kcal mol⁻¹ for the 2D Janus WSSe material as shown in Figure 3.6. The potential energy surface (PES) of the H₂ evolution reaction followed by the Volmer-Heyrovsky reaction mechanism on the active surface of the 2D monolayer WSSe JTMD material computed in the gas phase is depicted in Figure 3.6.

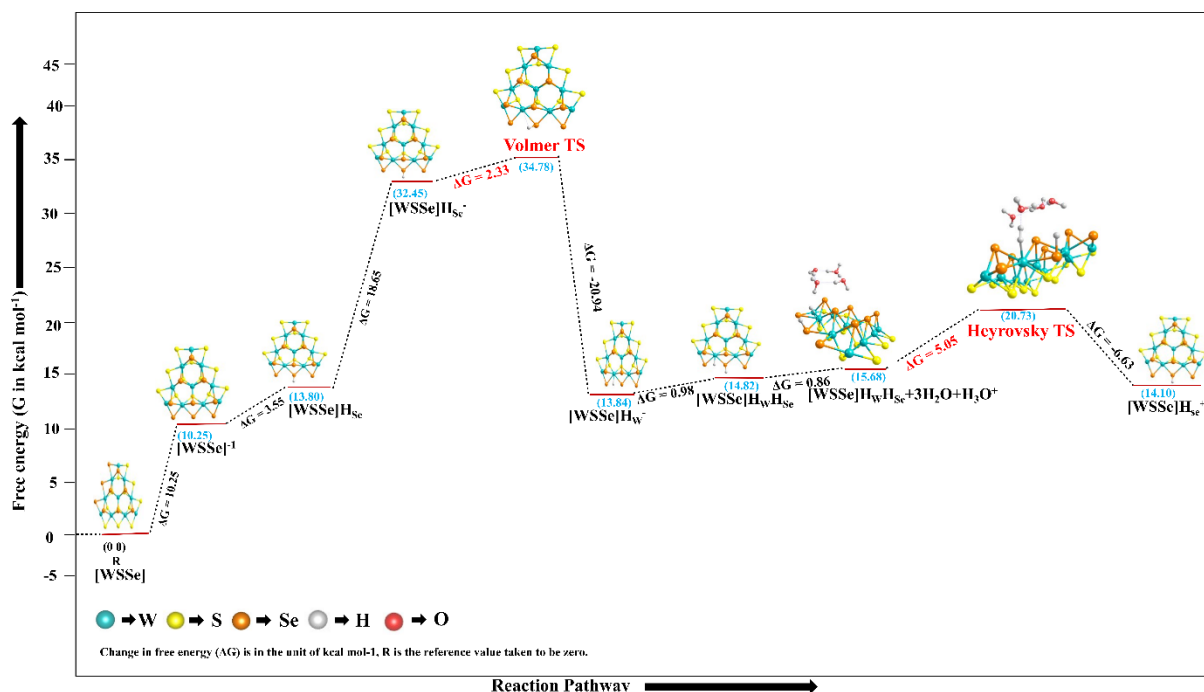


Figure 3.6: Free energy diagram *i.e.*, potential energy surface (PES) of the H₂ evolution reaction followed by the V-H reaction mechanism on the active surface of Janus WSSe in the gas phase is shown here.

3.3.3.2 Tafel mechanism and S-terminal W-edge of 2D monolayer WSSe JTMD material for HER

In this study, we have also investigated the Volmer-Tafel (V-T) reaction mechanism for HER to compare the reaction performances and thermodynamic stability with the V-H mechanism. The reaction pathway, reaction thermodynamics, kinetics, and reaction energy constraints of H₂ formation are examined considering the V-T HER mechanism considering the molecular cluster model system W₁₀S₁₂Se₉ of the 2D monolayer WSSe JTMD. The

equilibrium geometry, intermediate and transition state (TS) of the V-T mechanism have been calculated by the same M06-L DFT method and are shown in Figure 3.5a-g and Figure 3.7. However, to move the H atoms on the two neighboring Se and W atoms towards a potential transition state (TS3), known as the Tafel transition state (noted by TS3), is found in the present study, as depicted in Figure 3.7. In other words, $[\text{WSSe}]\text{H}_\text{W}\text{H}_\text{Se}$ has two H atoms which react with each other through a potential transition state called the Tafel TS3. Harmonic vibrational calculations indicate that TS3 has a single imaginary frequency about -485.27 cm^{-1} before forming H_2 during Tafel HER. The reaction barrier (ΔG) obtained by the M06-L DFT method was found to be $10.02\text{ kcal.mol}^{-1}$, which is higher than the previous intermediate $[\text{WSSe}]\text{H}_\text{Se}\text{H}_\text{W}$. The changes in the electronic energy (ΔE) and enthalpy (ΔH) of the Tafel TS3 in this Volmer-Tafel reaction phase are shown in Table 3.2. Therefore, these calculations suggest that the V-T reaction mechanism is thermodynamically less favorable for the evolution of H_2 than the V-H reaction mechanism.

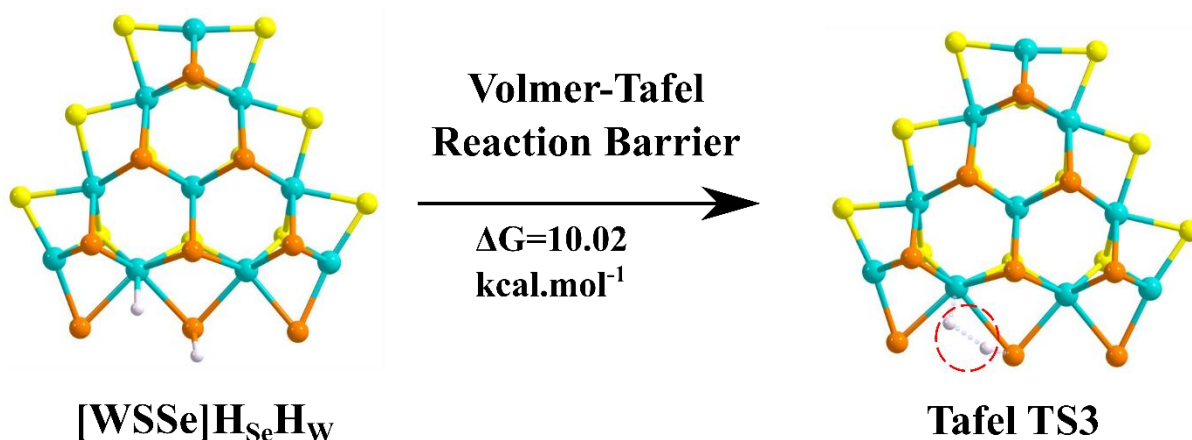


Figure 3.7: Equilibrium geometries of the $[\text{WSSe}]\text{H}_\text{Se}\text{H}_\text{W}$ and Tafel transition state TS3 occurred during the Volmer-Tafel reaction step with the change in the free energy (i.e. relative free energy or reaction barrier ΔG) about $10.02\text{ kcal.mol}^{-1}$ computed in the gas phase are depicted here.

Considering the same cluster model system $\text{W}_{10}\text{S}_{12}\text{Se}_9$, further examinations have been carried out to investigate the electrocatalytic activity of the S-terminal W-edge of 2D monolayer WSSe JTMD material for HER. By considering the S-terminal W-edge of the 2D monolayer WSSe material, the same H_2 evolution reaction pathway has been investigated (as shown in Figure 3.4) contemplating the similar finite clustering model system $\text{W}_{10}\text{S}_{12}\text{Se}_9$. Equilibrium geometries of the important intermediates and transition

states involved in the subject reaction, $[\text{WSSe}]\text{H}_\text{S}^-$ and TS4 (H^* -migration), are displayed in Figure 3.8, as they play an important role in determining the performance of electrocatalytic activity for efficient HER. The present DFT-D calculations found that the H^* -migration reaction barrier (ΔG) is approximately $2.94 \text{ kcal.mol}^{-1}$ when reacted at the S-terminated W-side of the 2D monolayer WSSe JTMD material. The reaction barrier of the TS4 was approximately $0.61 \text{ kcal.mol}^{-1}$ higher than that TS1 of the Se-terminated W-edge of the 2D WSSe JTMD material indicating that the S-terminated W-edges of the 2D monolayer WSSe JTMD are thermodynamically less favorable for HER compared to the Se-terminated W-edges during the HER process. It has been recently reported that the Se-terminated Metal-edges of the 2D monolayer JTMD are thermodynamically favorable than S-terminated Metal-edges during the HER process. (*Pakhira and Upadhyay, 2022*) The present investigation also shows that the HER process at the S-terminal W-edge of the 2D WSSe JTMD is less thermodynamically favorable than the Se-terminal W-edge.

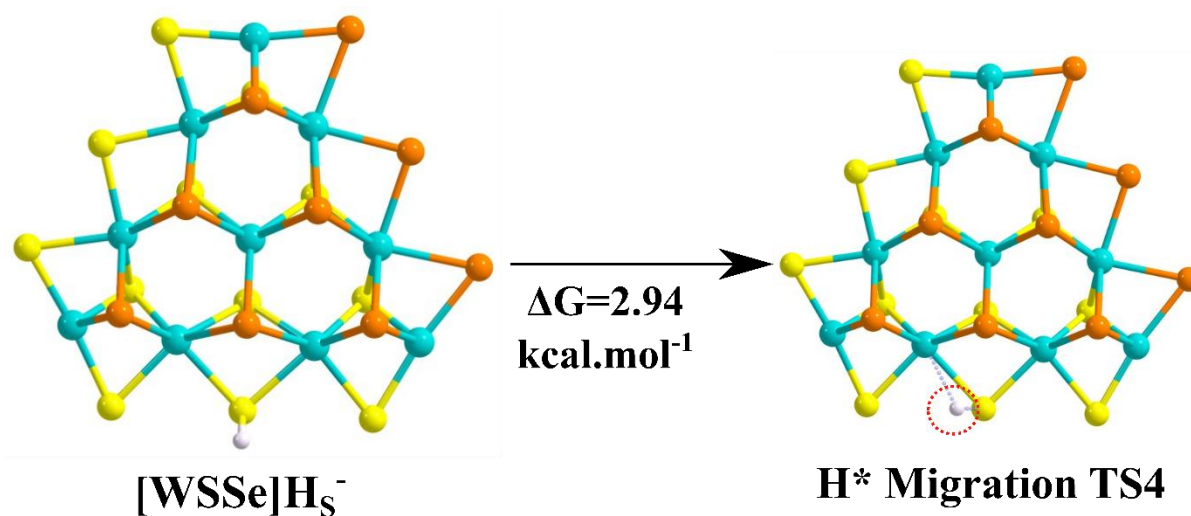


Figure 3.8. The equilibrium geometry of the S-edge: $[\text{WSSe}]\text{H}_\text{S}^-$ and TS4 (H^* -migration transition states) have been calculated by the M06-L DFT method. The HER occurs at the S-terminal W-edge of the 2D monolayer WSSe JTMD surface.

In this study, we have also explored the HER in the solvent phase by performing the PCM calculations at the same level of the DFT method. Here, water (H_2O) has been used as a solvent for PCM calculations, and the dielectric constant for water is considered to be 78.35, which contributes to the solvation effect in the HER mechanism of the 2D

monolayer WSSe JTMD material. In the present calculations, the activation energy barrier (ΔG) for the H*-migration TS step in the solvent phase is about 2.88 kcal mol⁻¹ and the second energy barrier (ΔG) of the solvent phase for the Heyrovsky TS is about 7.52 kcal mol⁻¹. The changes in the electronic energy (ΔE), enthalpy (ΔH) and Gibbs free energy (ΔG) of the H*-migration and Heyrovsky reaction barriers of the 2D Janus WSSe calculated by the M06-L DFT method in the solvent phase are listed in Table 3.3. The H*-migration and Heyrovsky reaction energy barriers computed in the solvent phase of the different materials are given in Figure 3.9 and Table 3.4. We report from our present DFT calculations that the proposed 2D monolayer Janus WSSe catalyst shows much lower reaction barriers (both the H*-migration and Heyrovsky reaction barriers) during the HER process, as shown in Figure 3.9.

Table 3.3: The change of free energy (ΔG), enthalpy (ΔH) and electronic energy (ΔE) of the H*-migration and Heyrovsky reaction steps on the 2D single-layer WSSe JTMD surface during the HER process are listed here.

Activation barrier	ΔG (kcal.mol ⁻¹) in gas phase	ΔE (kcal.mol ⁻¹) in solvent phase	ΔH (kcal.mol ⁻¹) in solvent phase	ΔG (kcal.mol ⁻¹) in solvent phase
H*-migration reaction barrier	2.33	3.15	2.20	2.88
Heyrovsky reaction barrier	5.05	10.66	8.58	7.52

Table 3.4. Comparison of the energy barriers of the H^{*}-migration and Heyrovsky reaction during HER in the solvent phase with different reported 2D catalysts along with our system of interest are shown here.

Materials	H[*]-migration Reaction Barrier (ΔG)(kcal.mol⁻¹)	Heyrovsky Reaction Barrier (ΔG) (kcal.mol⁻¹)	References
MoS₂	17.7	23.8	<i>(Lei, Pakhira, Fujisawa, Wang, Iyiola, Perea López, et al., 2017)</i>
WS₂	18.1	21.3	<i>(Lei, Pakhira, Fujisawa, Wang, Iyiola, Perea López, et al., 2017)</i>
W_{0.4}Mo_{0.6}S₂	11.9	13.3	<i>(Lei, Pakhira, Fujisawa, Wang, Iyiola, Perea López, et al., 2017)</i>
Mn-MoS₂	10.34	10.79	<i>(Ekka et al., 2022)</i>
WSSe	2.88	7.52	This work

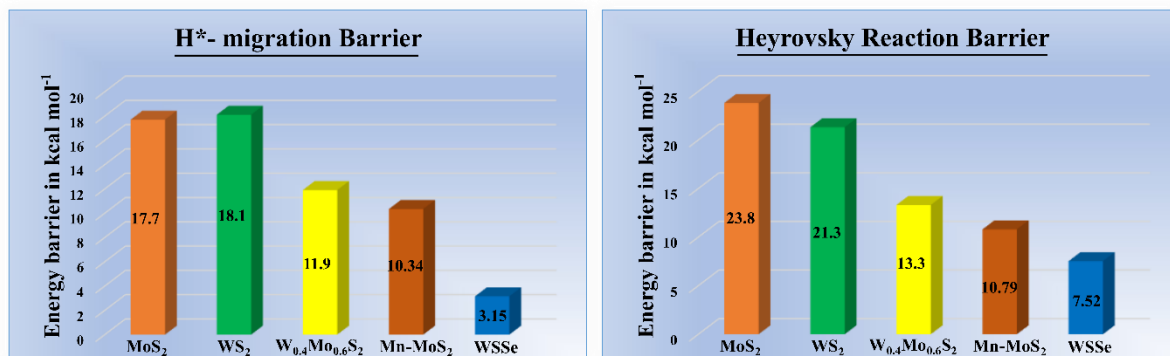


Figure 3.9. The H*-migration or Volmer and Heyrovsky reaction barriers (in the solvent phase) of previous reported 2D monolayer MoS₂, WS₂, W_{0.4}Mo_{0.6}S₂ and Mn-MoS₂ TMDs along with the 2D monolayer pristine WSSe JTMD material are shown here for comparison.

3.3.3.3 Turnover Frequency (TOF) and Tafel Slope calculations

To rank the electrocatalysts as per their catalytic activity, the turnover frequency (TOF) (Huang *et al.*, 2015) corresponding to the quantity of H₂ released from each active site per unit time is another key parameter. According to the transition state theory (TST) (Jordan, 2012) or activation recombination theory, we have determined the turnover frequency for the H₂ evolution at each edge of the W atom in the 2D WSSe JTMD catalyst. For the theoretical determination, we used the following formula:

$$rate = \frac{(k_B T)}{h} \times \exp\left(-\frac{\Delta G}{RT}\right)$$

Where the symbol k_B represents the Boltzmann constant (1.381×10^{-23} J K⁻¹), T is the temperature in the absolute scale (here it is kept as a constant with an absolute scale value of 298.15 K throughout the non-periodic cluster model calculation), R is the universal gas constant (8.314 J mol⁻¹ K⁻¹), h is the Planck's constant (6.623×10^{-34} J s⁻¹), and ΔG corresponds to the energy barriers. Our DFT-D study on the 2D single-layer Janus WSSe material found that the TOF at the edge of W is about 1.91×10^7 sec⁻¹, which corresponds to the activation energy barrier ($\Delta G \sim 7.52$ kcal mol⁻¹) during the Heyrovsky TS formation, i.e., TS2 at the Wedges. A higher TOF value is suitable for better H₂ production during the reaction. As shown in Table 3.5, the comparison of the activation energy and TOF of different TMD materials provides an understanding of their electrocatalytic activity and

performance for effective HER. We can observe that the 2D monolayer Janus WSSe material shows comparable results to the hybrid $W_{0.4}Mo_{0.6}S_2$ alloy material. However, the value of TOF is higher than the hybrid $W_{0.4}Mo_{0.6}S_2$ alloy material and other TMDs which indicates that the 2D monolayer Janus WSSe material is an excellent electrocatalyst for H_2 evolution. Therefore, what can be mentioned here is that the 2D monolayer WSSe material can prove to be a better and more practical alternative electrocatalyst to the catalytic performance of HER.

Table 3.5. The reaction barriers for the 2D monolayer TMD and other 2D material calculated at the theoretical level of DFT method are shown here.

Catalysts	H*-migration TS1 barrier		Heyrovsky TS2 barrier		Tafel TS3 barrier		References
	Gas phase (kcal.mol ⁻¹)	Solvent phase (kcal.mol ⁻¹)	Gas phase (kcal.mol ⁻¹)	Solvent phase (kcal.mol ⁻¹)	Gas phase (kcal. mol ⁻¹)	Solve nt phase (kcal. mol ⁻¹)	
MoS₂	11.90	17.70	16.0	23.8	-	-	<i>ACS Nano</i> 2017, 11, 5, 5103– 5112
WS₂	12.40	18.10	14.4	21.3	-	-	<i>ACS Nano</i> 2017, 11, 5, 5103– 5112
W_{0.4}Mo_{0.6}S₂	6.80	11.90	11.50	13.30	-	-	<i>ACS Nano</i> 2017, 11, 5, 5103– 5112
WSe₂	2.67	6.11	6.24	8.41	-	-	<i>Adv. Mater. Interfaces</i> 2023, 10, 2202075

Mechanistic understanding of efficient electrocatalytic hydrogen evolution reaction on a 2D monolayer WSSe Janus transition metal dichalcogenides

Mn-MoS₂	7.23	10.34	10.59	10.79	90.13	93.72	<i>Phys. Chem. Chem. Phys.</i> , 2022,24, 265-280.
MoSSe	3.93	7.10	5.61	4.72	8.52	-	<i>Sustainable Energy Fuels</i> , 2022,6, 1733-1752.
MoP	17.5	-	16.3	-	56	60	<i>ACS Catal.</i> 2019, 9, 1, 651–659
MoSP	12.90	14	9.2	12.90	34	-	<i>ACS Catal.</i> 2019, 9, 1, 651–659
Borophene	4.84	-	8.07	-	31.62	-	<i>ACS Appl. Energy Mater.</i> 2023, 6, 8941–8948.
NbCO₂	-	-	31.59	-	43.58		<i>J. Mater. Chem. A</i> , 2018,6, 4271-4278
Epitaxial Graphene	28.59	35.51	-	-	28.74	29.03	<i>ACS Omega</i> 2022, 7, 13221–13227
WSSe	2.33	2.88	5.05	7.52	10.02	-	This work

Another electrochemical parameter is the Tafel slope (*m*) which can be theoretically calculated based on the number of electrons transferred during the whole HER mechanism. Assuming that the rate of the catalyst is not confined by the electron directly transfer from the support to the desired catalyst, theoretically, the Tafel slope(*Huang et al., 2015*) (*m*) is

given as $m = 2.303 \left(\frac{RT}{nF} \right)$, where R = universal gas constant, T = absolute temperature which has constant value for our calculation, F = Faraday constant (96485 C mol^{-1}) and n is the number of electrons participating in the whole process. Tafel slope is an inverse measure of how strongly the reaction rate responds to changes in potential. It is used to evaluate the rate determining steps during the HER generally assume extreme coverage of the adsorbed species. The lower values of both the activation energy barriers (both the H*-migration and Heyrovsky's reaction barrier energies) lead to the establishment of a sophisticated number of active sites by shrinking the value of electrochemical properties like Tafel slope (m) and increasing the turnover frequency (TOF) (*Pakhira, Kumar and Ghosh, 2023*) for an excellent catalytic activity to generate molecular hydrogen. As mentioned earlier, the proposed reaction is a two-electron transfer mechanism for the evolution of H₂ molecules, and it has been found that the calculated Tafel slope of this reaction occurred at the active edges of the 2D monolayer WSSe JTMD is about 29.54 mV dec⁻¹ at T=298.15 K when n = 2.

3.3.3.4 HOMO and LUMO calculations

Through the visualization of the respective TS structures calculated by highest occupied molecular orbital (HOMO) and lowest unoccupied molecular orbital (LUMO), it is possible to more intuitively understand the electronic effects of H*-migration during the Volmer reaction mechanism i.e. when the H*-migrates from Se to W, and the bond formation mechanism produced by H₂ during the Heyrovsky reaction mechanism. Our current calculations are very beneficial for the low energy barriers in the H*-migration and Heyrovsky steps on the 2D monolayer Janus WSSe surface during HER, leading to 2D Janus monolayer WSSe as a promising electrocatalyst. To support our current computational research on HER for 2D monolayer WSSe, we have performed natural bond orbital (NBO), The Highest Occupied Molecular Orbitals and Lowest Unoccupied Molecular Orbitals (HOMO-LUMO) calculations at the equilibrium transition states (TS1 and TS2) using the same M06-L DFT method. These calculations are performed to show the proper standpoint of the formation of H₂ at the active site from the perspective of the overlap of the electron charge clouds and the molecular orbitals. The NBO study delivers the most probable 'natural Lewis structure' picture of the wave function (ϕ), such that total

information related to orbitals is selected mathematically to consider the maximum possible energy of electron density. The precise Lewis structure, that is the structure with the largest electron charge in the Lewis orbit, can be found by calculating NBO. An advantage of this orbital is that it gives information about the intra-molecular and inter-molecular interactions (i.e. connections between bonds of atoms of the molecule). Donor acceptor interactions in NBO calculations are known from second order Fock-matrix. The NBO study provides complete mathematical information about the bonding orbitals of the maximum possible energy of the electron density. The benefit of conducting this research is that it provides information about both the intermolecular and intramolecular interactions. The second order Fock-matrix participates in the evolution of the donor-accepting interaction. Solving a multi-electron atomic system requires an approximation called the linear combination of atomic orbitals (LCAO approximation). A qualitative image of a molecular orbital is analyzed by extending the molecular orbital to any absolute base of all atomic orbitals in the nucleus. Therefore, the multi-electron wave function of a molecule in a specific atomic configuration can be given by approximately extending the orbital to the molecule.

The wave function calculated from the NBO analysis is a linear combination of the W, S, Se and H atomic orbitals of H^{*}-migration TS1. The HOMO LUMO calculations have been performed at the optimized H^{*}-migration TS or Volmer transition structure (i.e. TS1) as shown in Figure 3.10 (a) and (b). Similarly, the wave function calculated from the NBO analysis is a linear combination of the W, S, Se, H, and O atomic orbitals in the case of the Heyrovsky TS i.e. TS2. The HOMO LUMO is obtained from at computed Heyrovsky transition structure as shown in Figure 3.10c and 3.10d. The red color indicates the in-phase bonding of the orbitals, and the blue color indicates the out-of-phase bonding. The ranges of isosurface value to predict the atomic orbital overlapping around the H₂-formation (from blue to red) are set to -0.1 to 0.1.

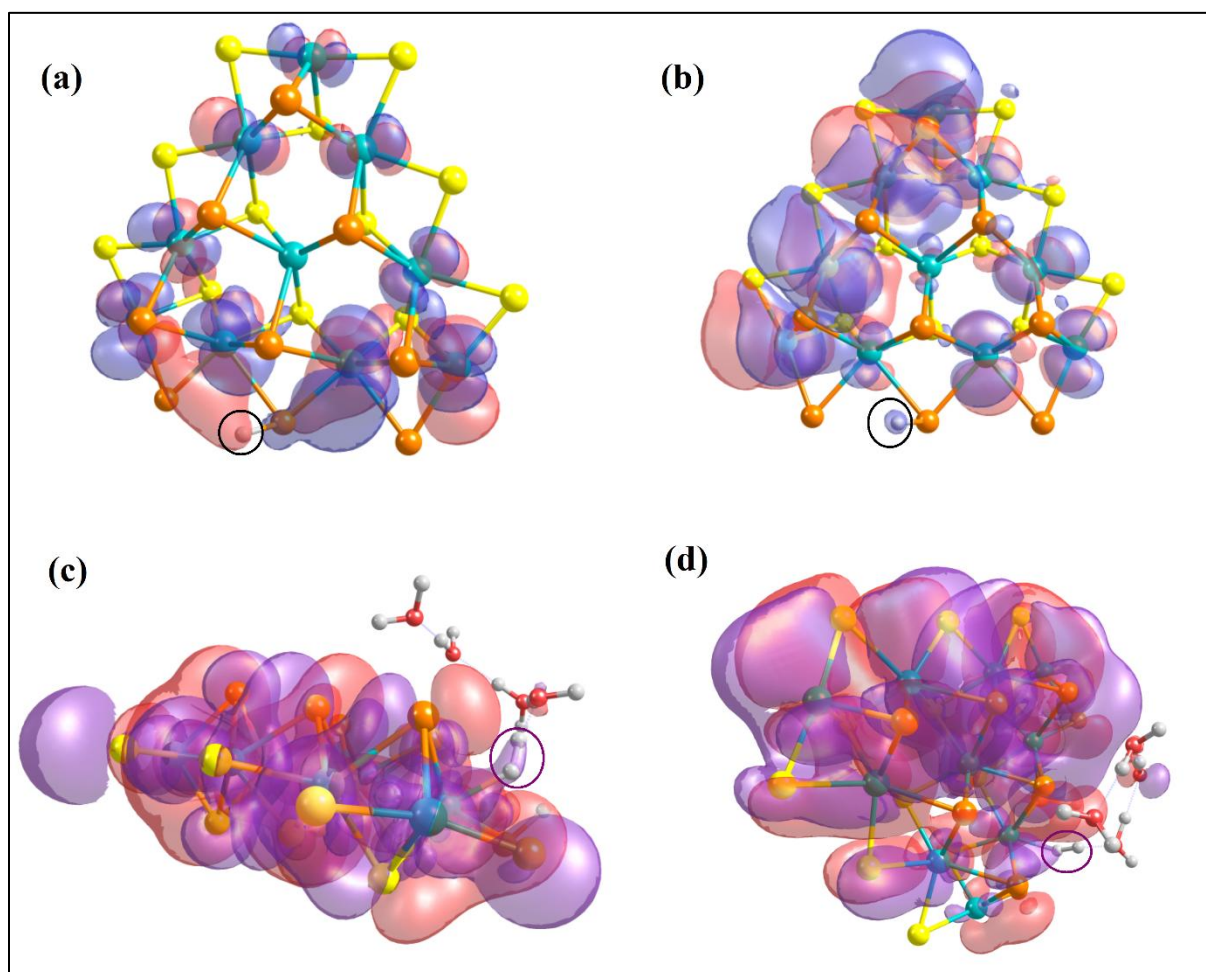


Figure 3.10. The equilibrium structure of (a) the HOMO of H^* -migration or Volmer TS; (b) The LUMO of H^* -migration TS; (c) The HOMO of Heyrovsky TS2; (d) The LUMO of Heyrovsky TS is shown here. The positions of molecular orbitals and hydrogen participating in the subject reaction have been highlighted with dotted circles are shown here.

In the case of H^* -migration TS, the HOMO-LUMO calculations indicate that the electronic wave function of the H^* moves from the Se atom site to the W transition metal atom site. The light red bubble indicates that the electron in the s -orbital of the H atom overlaps with the electron in the d -orbital of the W atom as the electron clouds have been found in the region where the orbitals are overlapped highlighted by a black circle. The role of the electronic structure in the HER mechanism can be understood from the HOMO-LUMO calculation of the Heyrovsky transition state as shown in Figure 3.10c-d. A better overlap of the s -orbitals of the hydrogen atom attached with the W and the water cluster ($H_3O^+ + 3H_2O$) seemed in the HOMO-LUMO Heyrovsky's transition state TS2 has found,

and this better overlap of the atomic orbitals during the H₂ formation in the Heyrovsky's TS2 reduces the reaction barrier. Therefore, it can be concluded that in the rate-limiting step of HER, that is, the Heyrovsky step, the stability of the atomic orbital is also one of the key features of reducing the reaction barrier. This strategy differs from well-known methods used to adjust the H₂ binding energies of TMDs or to control the acidity of the proton source. The electron cloud around the H atom in Heyrovsky TS2 is highlighted by a circle. When H₂ is precipitated, the overlap of the atomic orbitals of H and W atoms with H₃O⁺ ions support this step. This is one of the reasons why the 2D monolayer Janus WSSe exhibits excellent activity against HER. The energy difference between HOMO and LUMO, also known as the HOMO-LUMO gap is used to predict the stability of transition metal-based complexes because it is the lowest energy electron excitation possible in the molecule. The HOMO and LUMO energy values of the H*-migration TS1 or Volmer TS are found at $E_{\text{HOMO}} = -1.78 \text{ kcal.mol}^{-1}$ and $E_{\text{LUMO}} = -1.73 \text{ kcal.mol}^{-1}$, respectively. The energy required for an electron for the transition from HOMO to LUMO, $E_{\text{GAP}} = E_{\text{LUMO}} - E_{\text{HOMO}} = 0.05 \text{ kcal.mol}^{-1}$. The HOMO and LUMO energy values of Heyrovsky TS are $-6.83 \text{ kcal.mol}^{-1}$ and $-5.97 \text{ kcal.mol}^{-1}$, respectively. It is found that the HOMO-LUMO gap is about $-0.86 \text{ kcal.mol}^{-1}$, which is the energy of the electron transition from HOMO to LUMO. The gentle orbital overlaps of the molecular orbitals during the H migration in the H*-migration reaction step and the H₂ formation in the Heyrovsky reaction step reveal the excellent electrocatalytic activity of the 2D monolayer Janus WSSe for HER.

3.4 Summary

In summary, we have computationally designed a 2D single-layer WSSe JTMD through the first principles-based periodic hybrid B3LYP-D3 DFT-D method. The electronic structure, equilibrium geometry and properties (such as the electronic band structure, band gap, and total DOS) have been investigated by using the same DFT-D method. The present DFT-D calculations indicate that the 2D single-layer WSSe JTMD has a direct band gap of about 2.64 eV. It has been found that the exposed surfaces with the Se-/S-edges ($\bar{1}010$) and W-edges ($10\bar{1}0$) of the 2D monolayer JTMD material are electrocatalytically active for the HER. In order to explore the detailed reaction mechanism to evolve H₂ at the active sites of the 2D WSSe JTMD, we developed a molecular cluster

model system $\text{W}_{10}\text{S}_{12}\text{Se}_9$. The catalytic activity performance of the 2D monolayer Janus WSSe material was tested by using the non-periodic finite $\text{W}_{10}\text{S}_{12}\text{Se}_9$ molecular cluster model system at the W-edges of the WSSe JTMD. The detailed reaction mechanisms, pathways, intermediates, and transition states have been investigated by the M06-L DFT method. The HER mechanisms with the pathways have been investigated by following each reaction step considering the Volmer–Heyrovsky reaction mechanisms to produce molecular hydrogen through electrochemical water splitting. It has been observed that the overall chemical reaction of the HER has followed two-electron ($2e^-$) transfer mechanism steps (i.e., Volmer and Heyrovsky reactions). We calculated the changes of Gibbs free energy (ΔG) of each reaction step. The values of free energy changes suggest that all intermediate steps of the HER are thermodynamically favorable for the V–H reaction mechanism, rather than the V–T reaction mechanism during the H_2 evolution process. It was found that the energy barriers of both the H^* -migration and Heyrovsky transition structures in the gas phase are $2.33 \text{ kcal mol}^{-1}$ and $5.05 \text{ kcal mol}^{-1}$, respectively. We also conducted a HER mechanism study in the solvent phase considering water as the solvent and calculated the H^* -migration and Heyrovsky reaction barriers in the solvent phase to be $2.88 \text{ kcal mol}^{-1}$ and $7.52 \text{ kcal mol}^{-1}$, respectively. The TOF and a theoretically determined Tafel slope are $1.91 \times 10^7 \text{ sec}^{-1}$ and $29.54 \text{ mV dec}^{-1}$, respectively, which are attributed to the 2D monolayer WSSe JTMD as a promising and efficient HER electrocatalyst. The HOMO and LUMO calculations of TS-2 show that the molecular hydrogen is formed by orbital overlap, that is, in the Heyrovsky step, the d-orbital of the W atoms and the s-orbital of the H_2 molecule. Reducing the activation energy barrier is one of the key features of the catalyst, and the electron cloud overlap between the s-orbital of hydrogen and the d-orbital of the transition metal in the JTMD is suited to the formation of H_2 . In view of all these, the introduced Janus monolayer is expected to be a candidate for a highly sensitive electrocatalyst for the HER. Finally, the electrocatalytic activity of the 2D JTMD can be coordinated by activating the base surface. Therefore, great potential can be found in the layered heterostructure of HER electrocatalytic activity. This study will further trigger more fundamental research in developing new electrocatalysts for the HER.

Chapter 4

Electrocatalytic Performance of 2D Monolayer WSeTe Janus Transition Metal Dichalcogenide for Highly Efficient H₂ Evolution Reaction

In this chapter, we have reported a 2D monolayer WSeTe JTMD, which is highly effective toward HER. We have studied the electronic properties of 2D monolayer WSeTe JTMD using the periodic hybrid DFT-D method, and a direct electronic band gap of 2.39 eV has been obtained. We have explored the HER pathways, mechanisms, and intermediates, including various transition state (TS) structures (Volmer TS, i.e., H-migration TS, Heyrovsky TS, and Tafel TS) using a molecular cluster model of the subject JTMD noted as W₁₀Se₉Te₁₂. The present calculations reveal that the 2D monolayer WSeTe JTMD is a potential electrocatalyst for HER. It has the lowest energy barriers for all the TSs among other TMDs. It has been shown that the Heyrovsky energy barrier (= 8.72 kcal mol⁻¹) in the case of the Volmer–Heyrovsky mechanism is larger than the Tafel energy barrier (= 3.27 kcal mol⁻¹) in the V–T mechanism. Hence, our present study suggests that the formation of H₂ is energetically more favorable via the V–T mechanism. This study helps to shed light on the rational design of 2D single-layer JTMD, which can be highly effective toward HER, and we expect that the present work can be further extended to other JTMDs to find out the improved electrocatalytic performance.*

4.1 Introduction

2D materials have attracted a lot of research interest in recent years due to their excellent optical, electronic, and electrocatalytic properties with their potential applications in various fields. Among the different types of 2D materials, TMDs, such as MX₂ (where M = Mo or W; and X = S or Se), have attracted much attention due to their

excellent semiconducting, physical, and chemical properties.(*Lei, Pakhira, Fujisawa, Wang, Iyiola, Perea López, et al., 2017*) They are considered promising alternatives to noble metal catalysts for effective HER due to their unique 2D layer structure and electronic properties.(*Lei, Pakhira, Fujisawa, Wang, Iyiola, Perea López, et al., 2017*) However, TMDs materials are still less efficient for HER than Pt due to the limited density of active sites and inert basal planes. Although large-scale studies have been carried out to increase the density of active sites, it is still beneficial and necessary to develop new strategies to enhance the catalytic activity of TMDs.(*Lei, Pakhira, Fujisawa, Wang, Iyiola, Perea López, et al., 2017; Chia et al., 2018; Ju et al., 2020*) Due to several constraints of the TMDs, their overall electrocatalytic performance is limited, and the pristine TMDs have inert basal planes. The key challenge is to activate the basal plane of these TMDs by phase engineering, which includes doping of foreign atoms and creating defects. To overcome the limitations of pristine TMDs and to obtain excellent HER activity, new techniques are required to further improve the electrochemical performance toward HER potentially by tuning the electronic properties of the pristine TMDs. Recently, Ekka et al. computationally designed a 2D monolayer Mn-doped MoS₂ (Mn-MoS₂) TMD material and a nonperiodic finite molecular cluster model Mn₁Mo₉S₂₁ system of the same material to investigate the electrocatalytic activity toward H₂ evolution.(*Ekka et al., 2022*) They reported that the Mn-doping in the pristine TMD has enhanced the electrocatalytic activity of the 2D monolayer MoS₂ toward HER.(*Ekka et al., 2022*) Now-a-days, another class of 2D materials, Janus TMDs, has recently gained much interest toward electrochemical reactions, where they have shown excellent electrocatalytic performance for H₂ evolution. A few theoretical and experimental studies have been performed on 2D monolayer Janus TMDs. These materials have a structural configuration MXY, where M is a transition metal, and X and Y are different chalcogen elements (M = Mo or W, and X/Y = S, Se, and Te; X ≠ Y). The Janus TMDs show a lack of mirror symmetry and have vertical dipoles. The 2D Janus TMD (denoted as MXY) possesses a symmetry-broken structure with a C_{3v} point group compared with the 2D single layer MX₂ TMD structure, which has a higher symmetry than the D_{3h} point group.(*Dong, Lou and Shenoy, 2017; Li, Cheng and Huang, 2018*) An electronegativity difference between the X and Y layers of the Janus TMDs contributes to an inherent dipole moment. This property subtly distributes the holes and electrons in its

structure on its surface to enhance the electrocatalytic activity at room temperature. (A.-Y. Lu et al., 2017; Er et al., 2018; Chaurasiya, Gupta and Dixit, 2019; Som and Jha, 2020) Theoretically, the stability of group-VI chalcogenides MXY monolayers (such as MoSSe, WSSe, WSeTe, and WTe JTMDs) has been checked and determined through phonon dispersion calculation and molecular dynamics simulations. (Cheng et al., 2013; Maghirang et al., 2019) Recently, 2D Monolayer Janus MoSSe and WSSe materials have been broadly studied with their potential applications in sensors, electrochemistry, catalysis, and other devices. (Pakhira and Upadhyay, 2022; Kumar and Pakhira, 2023) Very recently, Pakhira et al. theoretically studied the electrocatalytic activity of the 2D monolayer MoSSe Janus TMD toward HER, and they reported that it has the lowest energy barriers among several TMDs such as MoS₂, WS₂, and W_xMo_{1-x}S₂. (Lei, Pakhira, Fujisawa, Wang, Iyiola, Perea López, et al., 2017; Pakhira and Upadhyay, 2022) Driven by this, in the present work, we have systematically investigated the stability and hydrogen evolution activity of the 2D monolayer WSeTe Janus TMD by using first-principles-based Density Functional Theory (DFT) methods. Here, we have employed first-principles-based periodic DFT method with van der Waals (vdW) corrections to compute the equilibrium geometry, electronic structure, band structure, electronic band gap, Fermi energy level (E_F), and total density of state (DOS) of the 2D single layer WSeTe Janus TMD. (Becke, 1993) Electronic property calculations of the 2D monolayer Janus WSeTe indicate that this material may be excellent for H₂ production with a high catalytic performance. Both the exposed Se-/Te-edges ($\bar{1}010$) and W-edges ($10\bar{1}0$) of the 2D monolayer Janus TMD WSeTe are found to be catalytically active for HER, while the Se–W–Te trilayer of the Janus WSeTe TMD was the uncovered surface. To examine the reaction pathway of the HER, we have computationally designed a nonperiodic finite molecular cluster model system (noted as W₁₀Se₉Te₁₂) of the 2D Janus WSeTe, as shown in Figure 4.1. The nonperiodic finite molecular cluster W₁₀Se₉Te₁₂ describes both the W-edge and Se/Te-edges of the 2D monolayer WSeTe Janus TMD, which are important for studying the HER mechanism. It is important to calculate the value of the free energy changes (ΔG) during hydrogen adsorption to screen suitable candidates among the available options, which is an important parameter for evaluating catalytic activity during the HER process. We found that the Janus 2D WSeTe has exceptional electrochemical performance toward the HER process and

reasonable electrochemical parameters, such as the small value of the Tafel slope, low activation energy barrier, and a large value of turnover frequency (TOF).

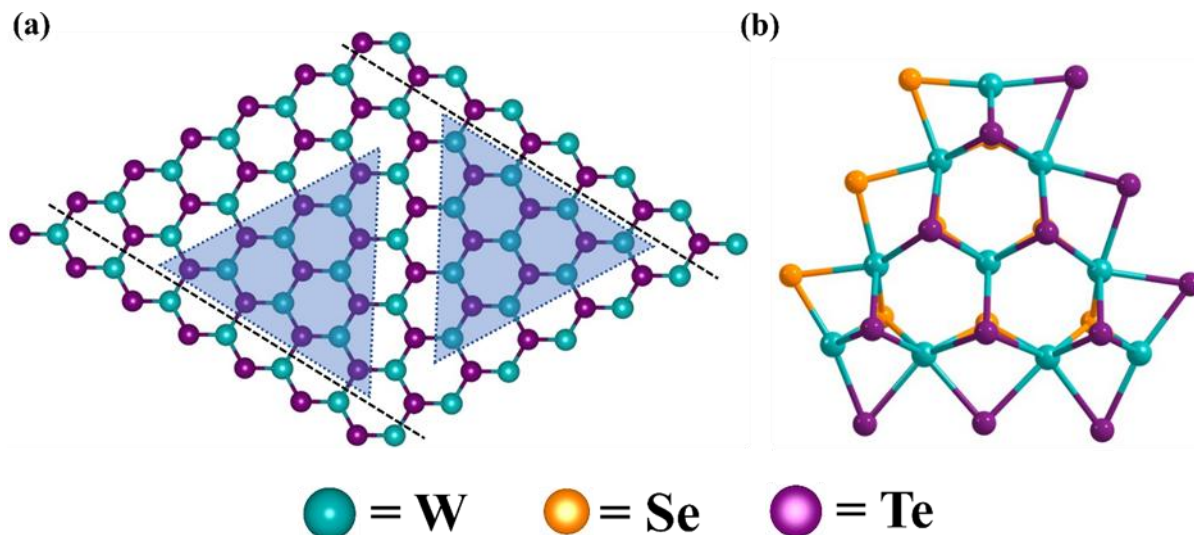


Figure 4.1: (a) Schematic presentation of the periodic 2D monolayer Janus WSeTe TMD material. Two black dotted lines show the $(\bar{1}010)$ Se-/Te-edges and $(10\bar{1}0)$ W-edges of the 2D monolayer Janus WSeTe TMD. Two triangles show the W-edges and Se-/Te-edges cluster model of the 2D monolayer WSeTe JTMD. (b) The W-edge finite molecular cluster model system ($W_{10}Se_9Te_{12}$) of the 2D WSeTe JTMD is presented here for studying HER.

4.2 Methods and Computational Details

4.2.1 Periodic DFT Calculations for the 2D Monolayer Janus WSeTe

It has been shown that the DFT-D methods are efficient for studying HER activity for H_2 production by electrochemical water splitting. (Pakhira, , *et al.*, 2013; Lei *et al.*, 2017; Li *et al.*, 2017; Er *et al.*, 2018) They are very useful for obtaining the electronic properties, equilibrium structure, thermochemistry, reaction kinetics, reaction barriers, and activation energy constraints of the individual active sites of TMDs. (Pakhira, *et al.*, 2013; Lei *et al.*, 2017; Li *et al.*, 2017; Er *et al.*, 2018) Therefore, we have performed periodic DFT calculations to study the 2D monolayer structure and electronic properties of the 2D monolayer WSeTe JTMD. The electronic properties were studied at the equilibrium geometry of the 2D monolayer WSeTe JTMD. Therefore, we first performed geometry optimization to get the equilibrium lattice constants by using the B3LYP-D3

method.(Becke, 2005; Puttaswamy et al., 2021; Ekka et al., 2022; Pakhira and Upadhyay, 2022) At the equilibrium geometry of the WSeTe JTMD, the electronic properties calculations were carried out by applying the same B3LYP-D3 DFT-D method.(Becke, 2005; Puttaswamy et al., 2021; Upadhyay and Pakhira, 2021a; Ekka et al., 2022; Pakhira and Upadhyay, 2022)

Ab initio-based CRYSTAL17(Dovesi et al., 2018; Patel et al., 2022; Upadhyay et al., 2022) suit code, which uses Gaussian-type of orbitals (GTOs), was used to obtain the equilibrium structure and electronic properties of the 2D WSeTe JTMD. The earlier reports in the literature show that the localized GTO kind of basis sets are more accurate in solving the Hartree–Fock (HF) part of the Schrödinger equations implemented in the hybrid density functional methods.(Hui, Pakhira, et al., 2018; Liang et al., 2018; Nagaraj et al., 2020) Grimme’s semiempirical dispersion corrections (-D3) were incorporated in the periodic B3LYP DFT method to consider the weak van der Waals (vdW) interactions between the layers and atoms of the 2D monolayer WSeTe JTMD material.(Grimme et al., 2010; Pakhira, Takayanagi and Nagaoka, 2015; Caldeweyher, Bannwarth and Grimme, 2017; Lei et al., 2021) Triple- ζ valence with polarization (TZVP) quality Gaussian types of atomic basis sets were applied for the W, Se, and Te atoms in the present calculations.(Peintinger, Oliveira and Bredow, 2013; Vilela Oliveira et al., 2019; Laun and Bredow, 2021) The DFT-D3 methods provide a good quality geometry of the 2D layered structure materials by reducing the spin contamination effects, and it does not affect the calculation of electronic and structural properties of the 2D WSeTe JTMD.(Baker, Scheiner and Andzelm, 1993; Montoya, Truong and Sarofim, 2000; Pakhira, Takayanagi and Nagaoka, 2015; Pakhira and Mendoza-Cortes, 2020) Spin-polarized calculations were performed to obtain the equilibrium structures and to study the electronic properties during periodic hybrid DFT-D3 calculations. A spin-polarized solution has been computed after the definition of the (α , up spin; β , down spin) electron occupancy. In other words, it may be here noted that spin-unrestricted wave functions are used in the present calculations to incorporate spin polarization by using the keywords SPIN and SPINLOCK in the *ab initio* CRYSTAL17 program. The ATOMSPIN keyword is also used to specify the single spin of the TM atoms in the material.(Pakhira, Lucht and Mendoza-Cortes, 2017; Salustro et al., 2017) A threshold value of 10^{-7} au has been used for the convergence of forces, energy,

and electron density for all cases. The periodicity in the z-direction of the crystal structure has been ignored by keeping the height of the unit cell around 500 Å, i.e., the vacuum region of approximately 500 Å has been considered in the present calculations to accommodate the vacuum environment. The vacuum region of 500 Å has been set to avoid the interlayer interaction between two consecutive layers in the z-direction. (Dovesi *et al.*, 2018) We have computed the frequency (phonon) spectrum to confirm stability using the CRYSTAL17 suite code. A harmonic vibrational analysis has been performed to understand the thermodynamic stability of the system. The frequency calculations showed that the structure is thermodynamically stable (as there was no imaginary frequency in the WSeTe JTMD), and the thermodynamical potentials (Gibbs free energy and enthalpy) have been computed at room temperature, which also confirms the thermodynamic stability of the WSeTe JTMD.

Electronic structure calculations have been performed on the equilibrium geometry of the 2D monolayer WSeTe JTMD material by employing the same level of theory. Monkhorst k-mesh grids of the size of $15 \times 15 \times 1$ have been used to compute the 2D electronic layer structure, geometry, band structure, electronic band gap (E_g), Fermi energy level (E_F), and total density of states (DOS). (Evarestov and Smirnov, 2004) In the first Brillouin zone, a total of eight electronic energy bands have been calculated around the Fermi energy level in a highly symmetric Γ -M-K- Γ direction. All the atomic orbitals of the W, Se, and Te atoms have been taken into account to calculate the total density of states of the 2D monolayer WSeTe JTMD. The electrostatic potential effects have been added in the present calculations, i.e., the electronic band structures and DOS have been calculated with respect to the vacuum, and the band alignment has been conducted. VESTA (Momma and Izumi, 2011), a visualization software, has been used to create graphics and visualize the equilibrium structure of the 2D monolayer WSeTe JTMD.

4.2.2. Finite Molecular Cluster Modeling

In the present study, we have computationally designed a finite nonperiodic molecular cluster model system (noted by $W_{10}Se_9Te_{12}$) of the 2D monolayer WSeTe JTMD to investigate the HER pathway and explore the chemical reaction mechanism toward H_2 evolution. A schematic representation of the finite molecular cluster model system

W₁₀Se₉Te₁₂ is shown in Figure 4.1b. This molecular cluster model of the 2D WSeTe JTMD has been designed by following our previous works on the 2D monolayer Janus WSSe JTMD. (Kumar and Pakhira, 2023) The finite cluster model system has been constructed by considering the periodic structure of the 2D monolayer WSeTe JTMD material, highlighted by a triangle, as shown in Figure 4.1. Two horizontal dashed lines indicate terminations along the (10 $\bar{1}$ 0) W-edges and ($\bar{1}$ 010) Se-/Te-edges. The triangle represents the terminations for both the W-edge and Se/Te-edge clusters, and the dangling bonds in the finite cluster have been set by considering the same triangle, as shown in Figure 4.1. Each W atom in the basal plane (001) of the finite molecular cluster model has an oxidation state of “+4” and is bonded with the three numbers of the Te atoms at the upper plane and three numbers of the Se atoms at the lower plane of W which gives a contribution of $4/6 = 2/3$ electrons toward each W–Se and W–Te bonding resulting a stabilized structure. The same can be understood for the oxidation state of the Te atoms in the basal plane. Tellurium (Te) has a “–2” oxidation state, and bonding with 3 W atoms results in a contribution of two-thirds electrons toward each W–Te bond. Similarly, the edges of the periodic molecular cluster (10 $\bar{1}$ 0) is being stabilized with the 2 local electron W–Se bonds (as well as W–Te bonds) having a single electron contribution toward 4 W–Te bonding in the basal plane, as shown in Figure 4.1. This $14/3$ {i.e., $(2 \times 1) + [4 \times (2/3)]$ } contribution of electrons toward the W–Se bonding of the edge W atom is satisfied with the *d2* configuration of one W atom and *d1* configuration of two W atoms at the edges. This configuration leads to the molecular system with a periodicity of 3 which results in the achievement of a stabilized molecular cluster model having three edges without any unsatisfied valency. Thus, we have considered a molecular cluster W₁₀Se₉Te₁₂ model system (noted by [WSeTe]) to represent both the Se-/Te-terminated W-edges, which are present on the surfaces of 2D monolayer WSeTe JTMD, and this molecular model system is good enough to explain the HER process. We have used the unequal numbers to just satisfy the dangling bonds, and we have also interchanged the numbers and it did not affect on the performance of electrocatalysis as the reaction happens on the active surface of the JTMD.

This molecular cluster model system allows us to investigate the unique properties and potential applications of the WSeTe JTMD. The development of the finite molecular

cluster model has been done in such a way that it has the same chemical properties as the periodic 2D slab of WSeTe JTMD as shown in Figure 4.1. We have used the M06-L DFT method to determine the reaction barriers, kinetics, and bond energies. This method provides more flexibility and accuracy while using molecular clusters and gives very precise results for the HER calculations. (Zhao and Truhlar, 2006, 2008) It is easy to use a cluster model with net charges, which is not possible to consider in the case of a periodic system. (Huang et al., 2015; Huang, Nielsen and Goddard III, 2018) Incorporation of simultaneous electrons (e^-) and protons (H^+) while performing the chemical reaction studies of various steps in HER becomes very easy when the molecular cluster model is used. All the nonperiodic calculations have been performed by using the GAUSSIAN16 (Frisch, M. J.; Trucks, G. W.; Schlegel, H. B.; Scuseria, G. E.; Robb, M. A.; Cheeseman, J. R.; Scalmani, G.; Barone, V.; Petersson, G. A.; Nakatsuji, 2016) suit code. We have focused on the energy barriers and changes in free energy during the reaction to explore the reaction pathways by employing the Minnesota Density Functional (M06-L) based on the meta-GGA approximation, which is intended to be good and fast for transition metal complexes. The LANL2DZ (P Jeffrey Hay and Wadt, 1985; P. Jeffrey Hay and Wadt, 1985) Gaussian type of atomic basis sets with the relativistic effective core potentials (ECPs) have been used for the W, Se, and Te atoms, and the 6-31+G** (double- ζ Pople-type) (Warren J Hehre, Ditchfield and Pople, 1972; Frisch, Pople and Binkley, 1984) Gaussian basis sets for the H and O atoms in the present computations. TS structures (transition state structures or saddle point) of H^+ -migration, Heyrovsky, and Tafel reaction steps have been obtained to study the reaction barriers, which has been confirmed by obtaining one imaginary frequency, modes of vibration, and intrinsic reaction coordinate (IRC) calculations. (Pakhira et al., 2016; Upadhyay and Pakhira, 2022; Pakhira, Kumar and Ghosh, 2023) ChemCraft software has been used to visualize them. (Andrienko, 2015)

Harmonic vibrational analysis with thermodynamic calculations has been performed to get the relative Gibbs free energy (ΔG) and enthalpy (ΔH). All the reaction intermediates involved in the subject reaction (HER) have been confirmed to be stable and feasible by obtaining all the positive frequencies (except in the case of TSs, where one imaginary frequency was obtained) during the frequency calculations. PCM (polarization continuum model) calculations have been performed to study the solvation effects on

reaction barriers. For the PCM calculations, water has been taken as a solvent with the dielectric constant $\epsilon = 78.54$ at 298.15 K. (Uematsu and Frank, 1980) PCM is one of the best models to consider the solvation effects, and it is a commonly used method in computational quantum chemistry to model solvation effects. (Lei, Pakhira, Fujisawa, Wang, Iyiola, Perea López, et al., 2017; Garza et al., 2018; Liang et al., 2018)

4.2.3 Theoretical Calculations and Equations

The electrocatalytic performances of the 2D monolayer WSeTe JTMD have been characterized by computing the changes of the Gibbs free energy (ΔG) for H₂ adsorption on the ($\bar{1}010$) Se-/Te edges and ($10\bar{1}0$) W-edges of the system. The change of various energies, such as a change in Gibbs free energy (ΔG), enthalpy (ΔH), and electronic energy (ΔE), have been calculated at pH = 0 using the following equation

$$\Delta G = \sum G_{\text{Products}} - \sum G_{\text{Reactants}}$$

$$\Delta H = \sum H_{\text{Products}} - \sum H_{\text{Reactants}}$$

$$\Delta E = \sum E_{\text{Products}} - \sum E_{\text{Reactants}}$$

Where G, H, and E values are Gibbs free energy, enthalpy, and electronic energy of the systems considered in the present study. Gibbs free energy of an electron (e^-) has been calculated at the standard hydrogen electrode (SHE) conditions where electron (e^-) and proton (H^+) (at pH=0) are in equilibrium with 1 atm H₂. The PCM analysis was employed for all of the theoretical calculations to describe the solvation effects by employing the M06-L DFT method, and three H₂O molecules with one H₃O⁺ (i.e., 3H₂O_H₃O⁺) have been combined unambiguously for the Heyrovsky reaction step.

4.2.4 Validation of the cluster model

For the validation of the molecular cluster model system W₁₀Se₉Te₁₂, which has the same chemical properties as the 2D monolayer periodic slab Se-/Te-/W-edges of the WSeTe JTMD, we have calculated the hydrogen adsorption energies for the molecular cluster model and the periodic 2D monolayer slab both under the vacuum conditions followed by previous works. (Ortmann, Bechstedt and Schmidt, 2006; Pakhira, et al., 2013; Wu et al., 2018; Bera, Betal and Sahu, 2020; Ekka et al., 2022; Pakhira, Kumar and

Ghosh, 2023) The calculated values of hydrogen adsorption energies for both systems are almost equal where the stoichiometry has been maintained during the study. Figure 4.2 shows that the hydrogen binding energies have been calculated by using the finite molecular cluster model system and the periodic 2D slab. Thus, it can be mentioned here that the molecular cluster model has the same chemical properties as the periodic 2D WSeTe JTMD.

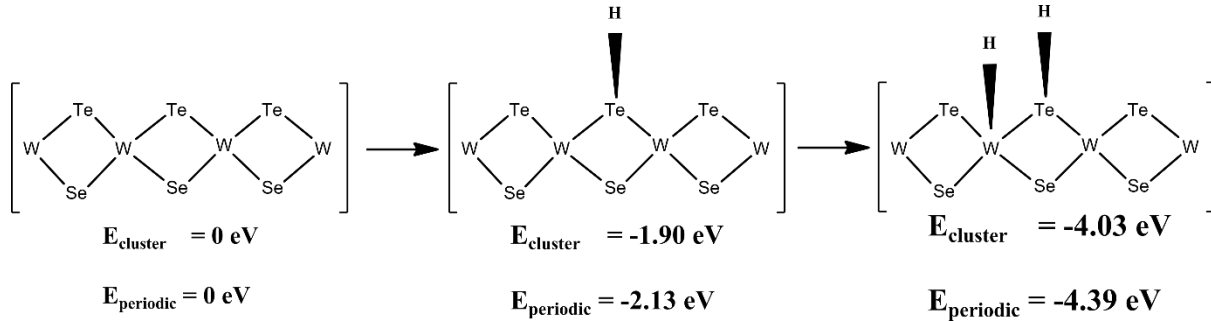


Figure 4.2: Hydrogen adsorption energies on the 2D monolayer WSeTe JTMD. E_{cluster} represents the relative electronic energy during hydrogen adsorption considering the molecular cluster model system and E_{periodic} is the relative electronic energy obtained from the periodic 2D layer calculations.

4.3 Results and Discussion

4.3.1 Structural and Electronic Properties of the 2D Monolayer WSeTe JTMD

The catalytic performance depends on the stability of the material and its electronic properties, so for the stability of the material, we first look at the structural and electronic properties of the 2D monolayer WSeTe JTMD. We have computationally designed a 2D monolayer structure of the Janus WSeTe TMD, which is a highly symmetric slab with a (001) basal plane, and the symmetrical unit structure of the 2D monolayer slab has been used for structural and electronic properties calculations. It has been computationally found that the Janus WSeTe monolayer slab has a $P\bar{3}m_1$ symmetry with symmetric interlayer group number 69 corresponding to the hexagonal 2D layer system. The top view and side view of equilibrium 2D single structures of the Janus WSeTe TMD are shown in Figure 4.3 In the present study, the equilibrium geometry of a periodic 2D monolayer of WSeTe Janus TMD has been obtained using the periodic hybrid B3LYP-D3 method. We included Grimme's third order (-D3) corrections to account for all long-range vdW interactions,

which are very crucial as there were weak interactions with the layers and atoms in the subject material WSeTe JTMD. Employing the DFT-D approach, particularly B3LYP-D3, proves advantageous as it not only provides precise geometric details for the 2D structure but also minimizes the influence of spin contaminations on energy and density in the present computations. The structure of 2D monolayer WSeTe Janus TMD has been optimized to locate the minimum energy value (negative value of total electronic energy (E), Enthalpy (H), and Gibbs free energy (G)) of the system, which results in thermodynamic stability. We have computed the frequency (phonon) spectrum to confirm the stability of the system using the CRYSTAL17 suite code. The frequency calculations showed that the structure is thermodynamically stable and the thermodynamical potentials (Gibbs free energy and enthalpy have been computed at room temperature) have been computed at the equilibrium geometry of the 2D monolayer WSeTe Janus TMD at room temperature $T = 298.15$ K, which also confirms the thermodynamical stability of the WSeTe JTMD.

It should be mentioned here that Tuan et al. performed the phonon dispersion calculations of the 2D monolayer WSeTe JTMD and found that the phonon dispersion curves of Janus WSeTe structure have no imaginary phonon modes, indicating its dynamical stability. They also calculated the imaginary part of the dielectric function of the Janus WSeTe monolayer and found that the imaginary part of the Janus WSeTe monolayer mainly consists of two peaks, peak A- and B-excitons. These peaks are the lowest energy transitions at the energy range of 1.65–2.20 eV. (*Vu et al., 2020*)

The Janus WSeTe monolayer slab structure loses out-of-plane symmetry compared to the 2D pristine monolayer MoS₂, WS₂, and WSe₂ TMDs. (*Lei, Pakhira, Fujisawa, Wang, Iyiola, Perea López, et al., 2017; Pakhira, Kumar and Ghosh, 2023*) 2D Janus WSeTe monolayer can be created by replacing one layer of Se atoms with Te atoms in the WSe₂ monolayer. We first consider the key properties of the 2D Janus WSeTe monolayer by examining its electronic equilibrium structure with its band structure, the position of the Fermi energy level (E_F), and the total density of states (DOS).

Table 4.1: The calculated lattice parameters, bond angle, bond distance, and band gap of the 2D monolayer Janus WSeTe TMD at the equilibrium position.

Materials	Lattice parameter (Å)	\angle SeWTe (in °)	Bond distance (in Å)		Band Gap (eV)	References
			W-Se (Å)	W-Te (Å)		
WSeTe	$a = b = 3.37$	83.29	2.52	2.69	2.39	This work
WSeTe (Previous Report)	$a = b = 3.45$	81.68	2.56	2.72	1.88	(Vu et al., 2020; Yu et al., 2023)

In contrast to ordinary TMDs (WSe₂ and WTe₂ monolayers), the dissimilarity in the electronegativity between Te (~2.10) and Se (~2.55) atoms in the WSeTe monolayer structure of the Janus TMD results in unequal bond lengths of the W–Se and W–Te bonds, as shown in Table 4.1. (Vu et al., 2020) It has been evident that the equilibrium W–Te bond length is slightly 0.17 Å longer than the W–Se bond. The equilibrium bond angle between W–Se and W–Te is about 83.29°. Equilibrium geometry, band structure, and total density of states (DOS) of the 2D monolayer WSeTe JTMD have been computed by the B3LYP-D3 DFT-D method, as displayed in Figure 4.3. The lattice parameters (a and b) of the WSeTe JTMD are equal and the values are $a = b = 3.37$ Å obtained by the same DFT-D (B3LYP-D3) method, which is consistent with the previous report (Xia et al., 2018) within 0.1 Å. The estimated value of the lattice parameters of the JTMD is 3.30 Å, obtained by the HSE06-D3 method in our present investigation. The deviation of the lattice parameters obtained by the HSE06-D3 and B3LYP-D3 methods is within the range of the DFT-D error bar. The electronic band structure of the 2D monolayer WSeTe is shown in Figure 4.3b, which indicates that it has semiconducting properties with a direct band gap of about (E_g) 2.39 eV at K point obtained by B3LYP-D3 method, which is in good agreement with the

earlier reported data.(*Er et al., 2018; Shi and Wang, 2018; Xia et al., 2018; Yang et al., 2019; Vu et al., 2020*) In other words, the present study reproduces the earlier reported results, and computed results are well harmonized with the previous experimental observation wherever available. In our study, we used the B3LYP-D3 method to obtain the electronic band gap, and the E_g was found to be 2.39 eV. This method, while widely used and computationally efficient, is known to sometimes overestimate band gaps, particularly for semiconductors and insulators. The HSE06-D3 method has been applied to obtain the value of E_g of the subject material, which is about 2.14 eV, and this value is about 0.25 eV lower than the electronic band gap computed by the B3LYP-D3 method. It should be mentioned here that the reported electronic band gap obtained by the B3LYP-D3 method overestimates the electronic band gap energy by 0.25 eV compared to the HSE06-D3 calculations, which are computationally very expensive. It has been shown that the HSE06-D3 method requires high computing facility, i.e., computationally very costly, however, it provides more accurate results in terms of electronic band gap and other electronic properties.(*Yu et al., 2023*) We have compared our present finding of the energy band gap with the earlier report by Yu et al.(*Yu et al., 2023*) They used the HSE06 method to calculate the energy band gap of the 2D monolayer WSeTe Janus TMD, and the computed value of the energy band gap is 1.88 eV.(*Bandiello et al., 2023*) The previous report employed the HSE06 method, which is known for its accuracy in predicting electronic properties but is computationally more expensive. Our present calculated value of the energy band gap at the level of B3LYP-D3 theory is 0.51 eV higher than the band gap estimated by the HSE06 method obtained by Yu et al.(*Bandiello et al., 2023; Yu et al., 2023*) Our computed value of the E_g at the HSE06-D3 method overestimates about 0.26 eV obtained by Yu et al. It should be noted here that Yu et al. did not incorporate the Grimmes “-D3” vdW empirical function in their calculations, which causes the large difference in the band gap calculations.

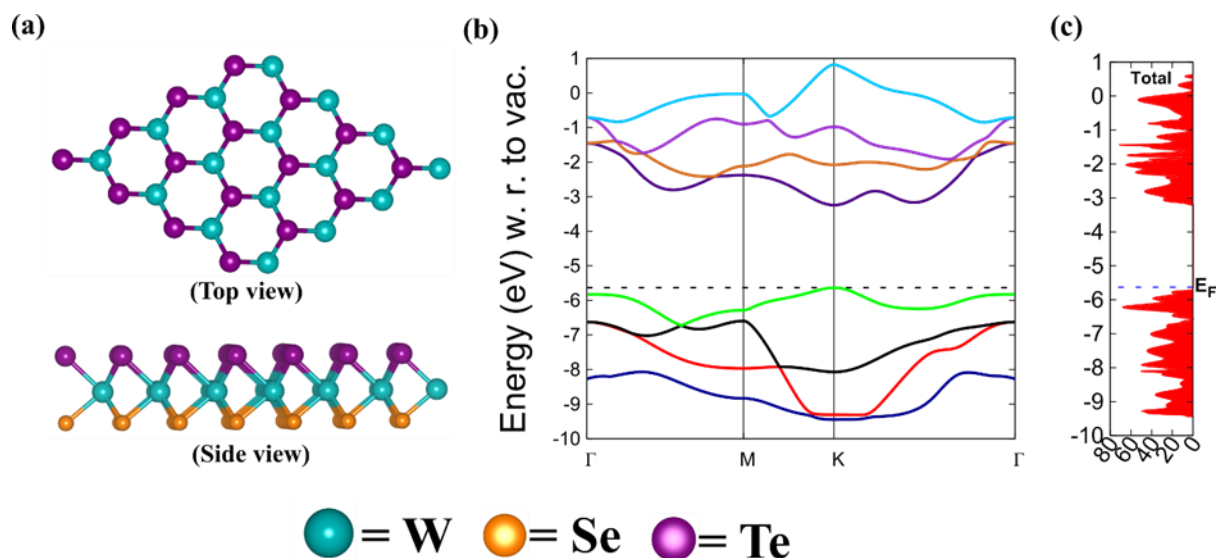


Figure 4.3: (a) Top and side views of the equilibrium structure of the 2D monolayer WSeTe Janus TMD. (b) Band structure and (c) the total density of states (DOS) of the 2D monolayer WSeTe Janus TMD.

The minima of the conduction band (CB) and the maxima of the valence band (VB) are directly located at the K point. Therefore, it is a direct band gap semiconductor in nature. To obtain the fine band structure of the 2D monolayer Janus WSeTe material, a total of eight electronic energy bands have been plotted in specific directions of the irreducible Brillouin zone by selecting the Γ -M-K- Γ high symmetry path, as depicted in Figure 4.3b, which is consistent with the 2D layer group symmetry of the Janus TMD materials. The E_F is at -5.63 eV, which is very close to the top of the valence band (VB), and the direct electronic band gap is located at the K point in the band structure calculation, which was later confirmed by the total DOS calculations. Figure 4.3c represents the total density of states of the pristine 2D monolayer Janus WSeTe. The maximum value of the VB and the minimum value of the CB are -5.63 eV and -3.24 eV, respectively, in the band structure diagram (i.e., E-k diagram) depicted in Figure 4.3b. From the total DOS, we have observed that there is an electron density of states around the E_F with a direct band gap of about 2.39 eV at the K point, which makes 2D monolayer Janus WSeTe semiconducting in nature, and the JTMD may help to enhance the electrocatalytic activity for HER. Janus WSeTe has demonstrated superior electrocatalytic capabilities for the HER compared to WSe₂ and WTe₂ TMDs. Our investigation revealed that Janus WSeTe exhibits a hydrogen adsorption

energy of -2.13 eV, in contrast to -2.59 eV for WSe₂ and -3.71 eV for WTe₂. The more favorable and less negative adsorption energy observed in WSeTe underscores its enhanced performance as an electrocatalyst for HER. The lower hydrogen adsorption energy in Janus WSeTe implies a more efficient facilitation of the hydrogen evolution process, making it a promising candidate for applications requiring efficient electrocatalysis toward HER. Detailed visual representations of the hydrogen adsorption on the Janus WSeTe, WSe₂, and WTe₂ can be found in Figure 4.4, providing valuable insights into their respective adsorption behaviors and characteristics. So, this material, the 2D monolayer Janus WSeTe TMD, can be expected to be a good catalyst toward HER.

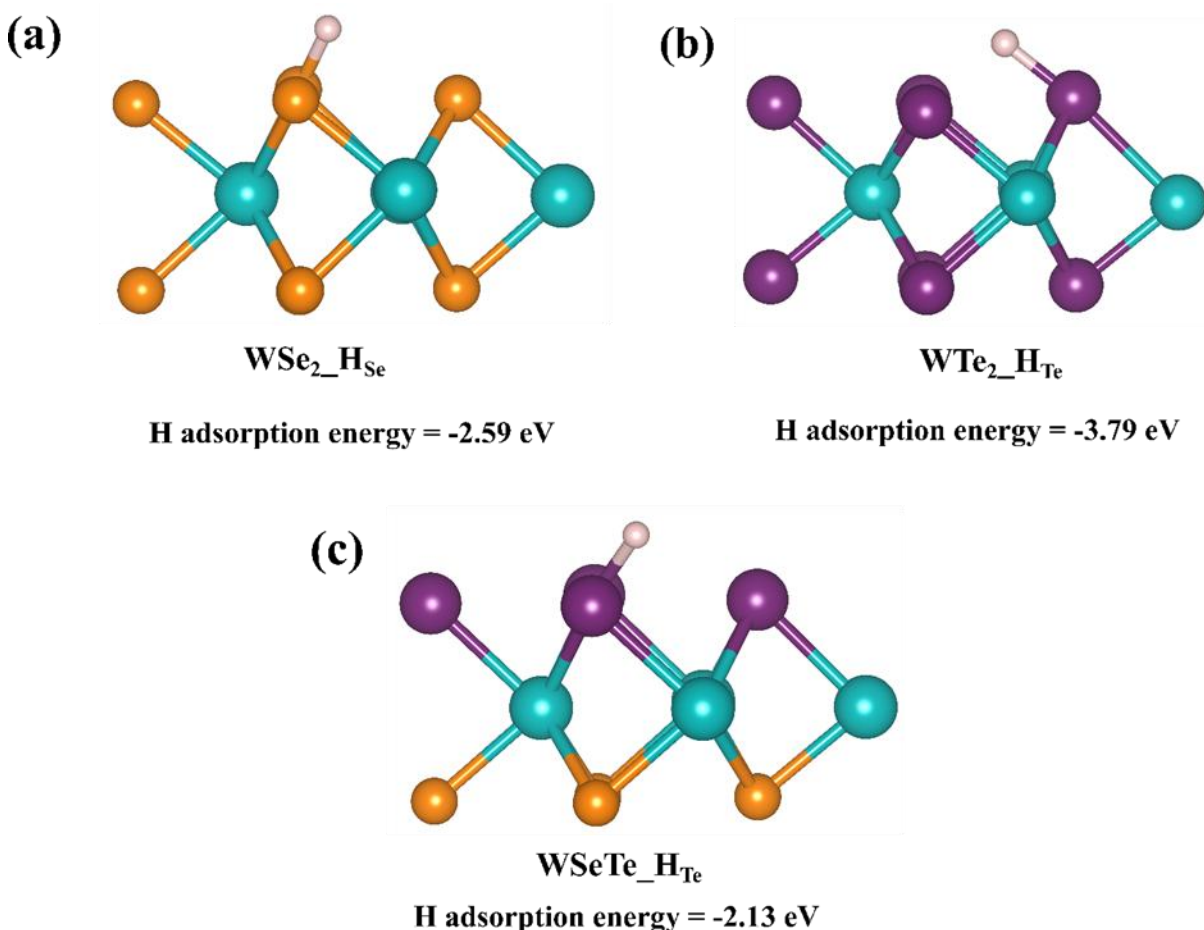
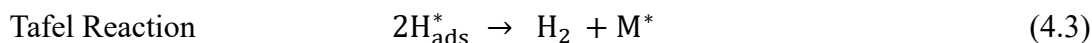
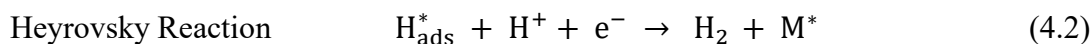
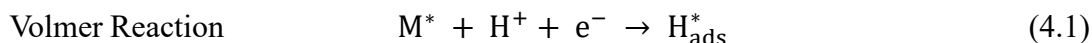


Figure 4.4: (a) The 2D WSe₂ TMD monolayer achieves its equilibrium geometry when hydrogen is adsorbed, with an adsorption energy of -2.59 eV; (b) The 2D WTe₂ TMD monolayer achieves its equilibrium geometry when hydrogen is adsorbed, with an adsorption energy of -3.79 eV; (c) The

2D WSeTe JTMD monolayer achieves its equilibrium geometry when hydrogen is adsorbed, with an adsorption energy of -2.13 eV.

4.3.2 Her Mechanisms

To investigate the catalytic activity of the 2D monolayer WSeTe Janus TMD toward the HER, the relative free energy of hydrogen adsorption (ΔG_H) has been calculated by employing the DFT method. For better catalytic activity, ΔG_H should be almost equal to 0 eV, indicating that the binding energy of hydrogen to the WSeTe JTMD is neither too strong nor too weak, i.e., it should be moderate. (Wang *et al.*, 2017; Li *et al.*, 2019; Ekka *et al.*, 2022) The entire reaction pathway of HER follows either the V–H or V–T mechanism, independent of the medium. These mechanisms are given in the following equations.



The first step is the Volmer reaction, which involves the adsorption of H^* by transferring an electron and proton at the surface-active sites, as shown in equation 4.1. In the next step, the Heyrovsky reaction involves a process on the electrode surface in which adsorbed hydrogen atoms (H_{ads}^*) combine with hydronium ions in an acid solution, and the formation of H_2 occurs, as shown in equation 4.2. One other step of H_2 formation is called the Tafel reaction step, in which two adsorbed hydrogen atoms (H_{ads}^*) combine to form H_2 , as shown in equation 4.3.

To investigate the HER performance of the 2D monolayer WSeTe JTMD, we have computationally designed a finite nonperiodic molecular cluster model system $W_{10}Se_9Te_{12}$ and explored the reaction pathways, mechanisms, thermodynamics, chemical kinetics, transition state (TS) structures, intermediates, and reaction barriers. Here, we have explored both the V–H and V–T HER mechanisms with the pathways shown in Figures 4.5 and 4.6. We have calculated the different intermediates with transition states (TSs) during the HER process. Since the complete HER process may proceed through either the V–H or the V–Treaction mechanism, it is necessary to examine the energy barriers of individual reaction

steps to trace the rate-limiting step. Since the electrocatalytic properties of the 2D monolayer Janus WSeTe materials have been less studied, we have investigated both the reaction pathways proposed for HER followed by the V–H and V–T mechanisms to predict the most prominent mechanism of the subject material.

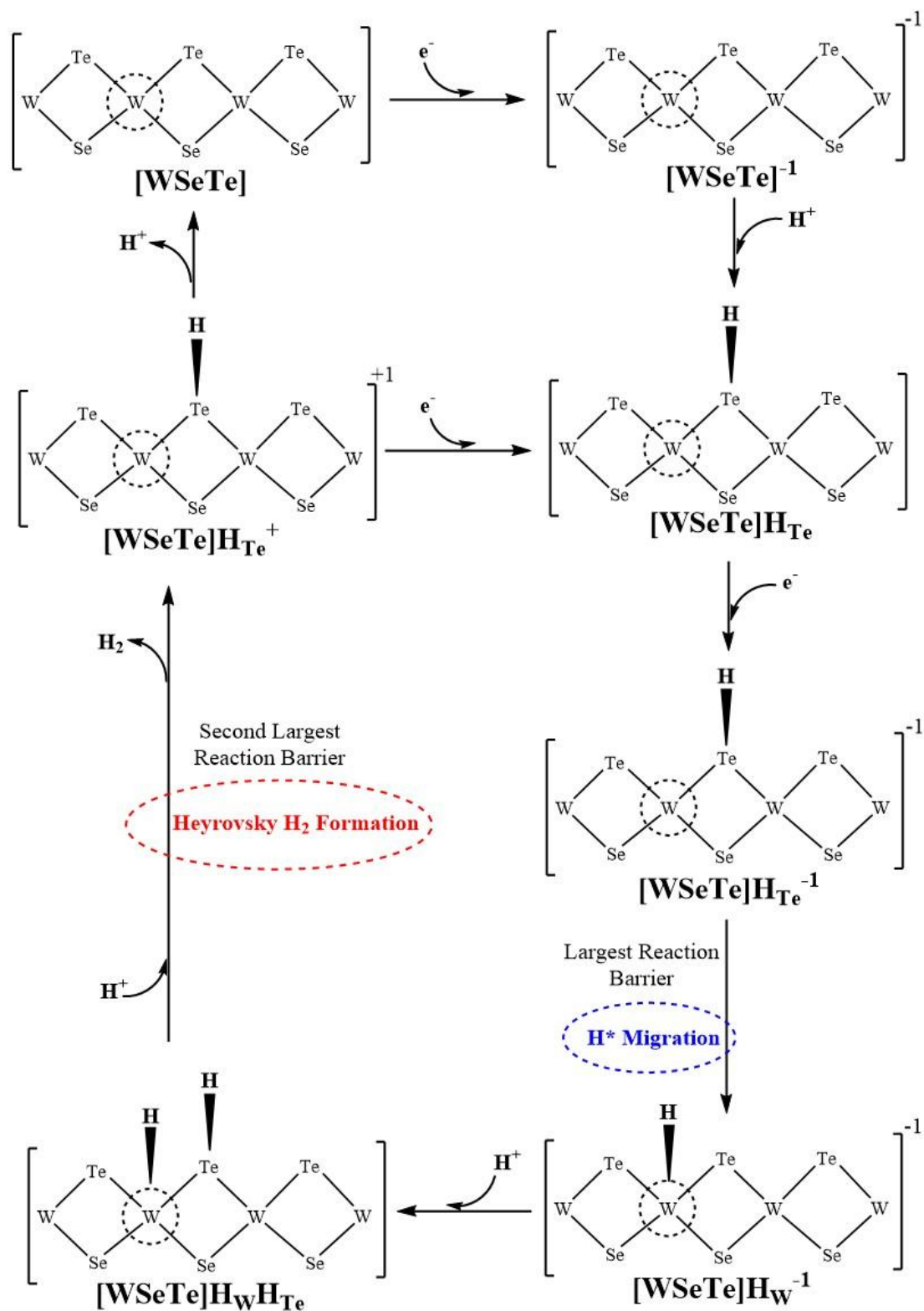


Figure 4.5: Volmer-Heyrovsky hydrogen evolution reaction (HER) mechanism pathway on the 2D monolayer Janus WSeTe TMD surface.

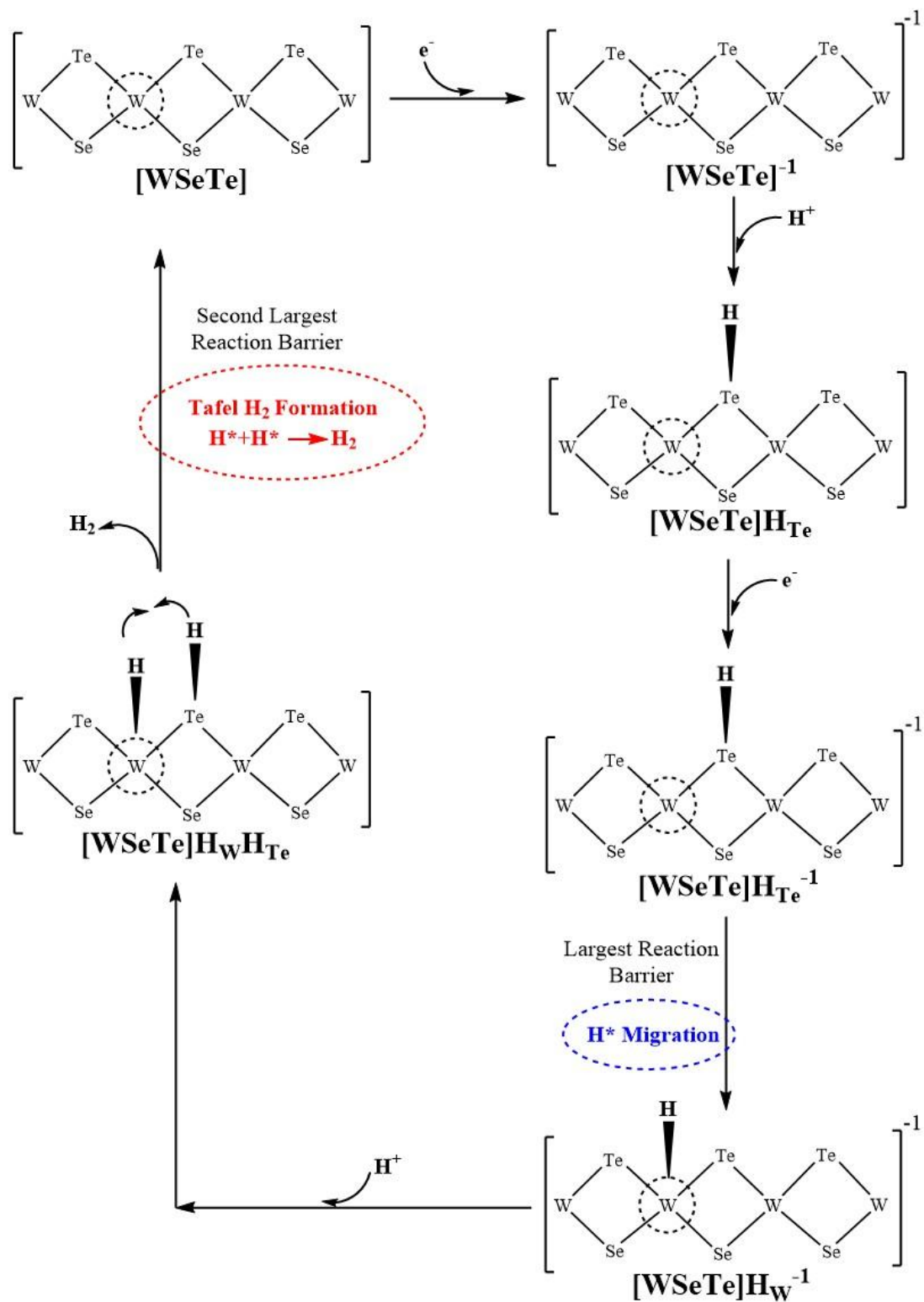


Figure 4.6: Volmer-Tafel hydrogen evolution reaction (HER) mechanism pathway on the 2D monolayer Janus WSeTe TMD surface.

4.3.3 Volmer–Heyrovsky Mechanism

The V–H mechanism goes along with a two-electron ($2e^-$) transfer process, and the whole reaction pathway of this mechanism (when the HER occurs at the W-edge of the 2D monolayer WSeTe nonperiodic molecular cluster model) is shown in Figure 3. This multistep electrode reaction schematic diagram includes possible intermediates and transition states (TSs) formation in the proposed reaction mechanism throughout the HER process. First, we have calculated the free energies of the most probable intermediates to describe thermodynamics, i.e., the kinetics of HER. Then, we examined barriers at individual reaction steps to locate rate-limiting steps. The first reaction step is the Volmer reaction step, where protons (H^+) interact with the electrons, and the hydrogen atoms get adsorbed on the active region of the catalyst (in short, $* + H^+ + e^- \rightarrow H^*_{ads}$, where $*$ represents the active sites of the catalyst). Similarly, in the Heyrovsky reaction step, the formation of H_2 plays a crucial role through the participation of H^* at the transition metal site and the requirement of a proton from the adjacent hydronium ion (H_3O^+). Using the finite molecular cluster model $W_{10}Se_9Te_{12}$, we have combined the number of electrons (e^-) and protons (H^+) independently in discrete steps. The Volmer–Heyrovsky reaction mechanism of the proposed HER on the active edge of the 2D monolayer Janus WSeTe TMD has been thoroughly investigated, and various successive reaction steps with Gibbs free energy changes have been calculated on the same level of the DFT-D method. The relative free energy of each intermediate reaction step has been estimated and is listed in Table 4.2. The detailed reaction steps involved in this proposed HER pathway are as follows.

I. To initiate the HER process, an electron is absorbed into the $W_{10}Se_9Te_{12}$ cluster model system, noted by $[WSeTe]$, resulting in a negatively charged cluster $[WSeTe]^{-1}$ solvated in water with a delocalized electron on its surface. Here, we found that the first reduction potential for introducing a single electron is about -509.09 mV, calculated by the M06-L method. The free energy of the electron $G(e^-)$ is calculated by the expression $G(e^-) = G(1/2 H_2) - G(H^+)$. The free energy $G(H^+)$ of the proton is -274.86 kcal mol $^{-1}$, taken from the value previously reported by Tissandier et al. (*Tissandier et al., 1998*) The equilibrium geometries of both the $[WSeTe]$ and $[WSeTe]^{-1}$ complexes are shown in Figures 4.7a and

4.7b, respectively. The change of free energy between $[\text{WSeTe}]^{-1}$ and $[\text{WSeTe}]$ systems is found to be $11.74 \text{ kcal mol}^{-1}$, which is listed in Table 4.2.

II. The next step involves the addition of an H^+ to the most active Te-edge of the 2D $[\text{WSeTe}]^{-1}$, which results in the formation of the next reaction intermediate, $[\text{WSeTe}]\text{H}_{\text{Te}}$. The equilibrium geometry of the $[\text{WSeTe}]\text{H}_{\text{Te}}$ is shown in Figure 4.7c. The free energy cost (i.e., ΔG , which is the relative free energy) of the first protonation of $[\text{WSeTe}]^{-1}$ to obtain the $[\text{WSeTe}]\text{H}_{\text{Te}}$ intermediate is $2.53 \text{ kcal mol}^{-1}$, as shown in Table 4.2. In short, the HER reaction is initiated by the absorption of a hydride ion on an energetically favorable Te site. This follows a hydride shift to the reactive, neighboring metal (W) site.

III. Further, an electron is added to the $[\text{WSeTe}]\text{H}_{\text{Te}}$, resulting in a second reduction of $[\text{WSeTe}]\text{H}_{\text{Te}}^{-1}$, and the reduction potential of this step is calculated to be approximately -796.17 mV . The energy cost to obtain the $[\text{WSeTe}]\text{H}_{\text{Te}}^{-1}$ intermediate is $\Delta G = 18.67 \text{ kcal mol}^{-1}$, as shown in Table 4.2. After adding another electron, the equilibrium geometry of the $[\text{WSeTe}]\text{H}_{\text{Te}}^{-1}$ is shown in Figure 4.7d.

In the next step, the hydride ion (H^*) adsorbed on the Te atom site migrates to the adjacent W atom site to form the transition state of $[\text{WSeTe}]\text{H}_{\text{W}}^{-1}$, known as the H^* -migration reaction step (TS1). The harmonic vibrational analysis and IRC calculations were performed to confirm the H^* -migration transition state noted by TS1. In the TS1 calculation, where H^* migrates from the Te atom site to the adjacent W atom site, we found an imaginary frequency of around -494.71 cm^{-1} which further confirms the right TS structure during the H^* -migration. The equilibrium geometry of the H^* -migration reaction step (TS1) is shown in Figure 4.7e. The energy cost to obtain the H^* -migration from the Te atom site to the W atom site in the TS1 intermediate is $\Delta G = 3.80 \text{ kcal mol}^{-1}$, as shown in Table 4.2. This study indicates that the barrier of H^* -migration is very low compared to those of other TMDs and JTMDs, which suggests that the 2D monolayer WSeTe JTMD can be a promising electrocatalyst for H_2 evolution.

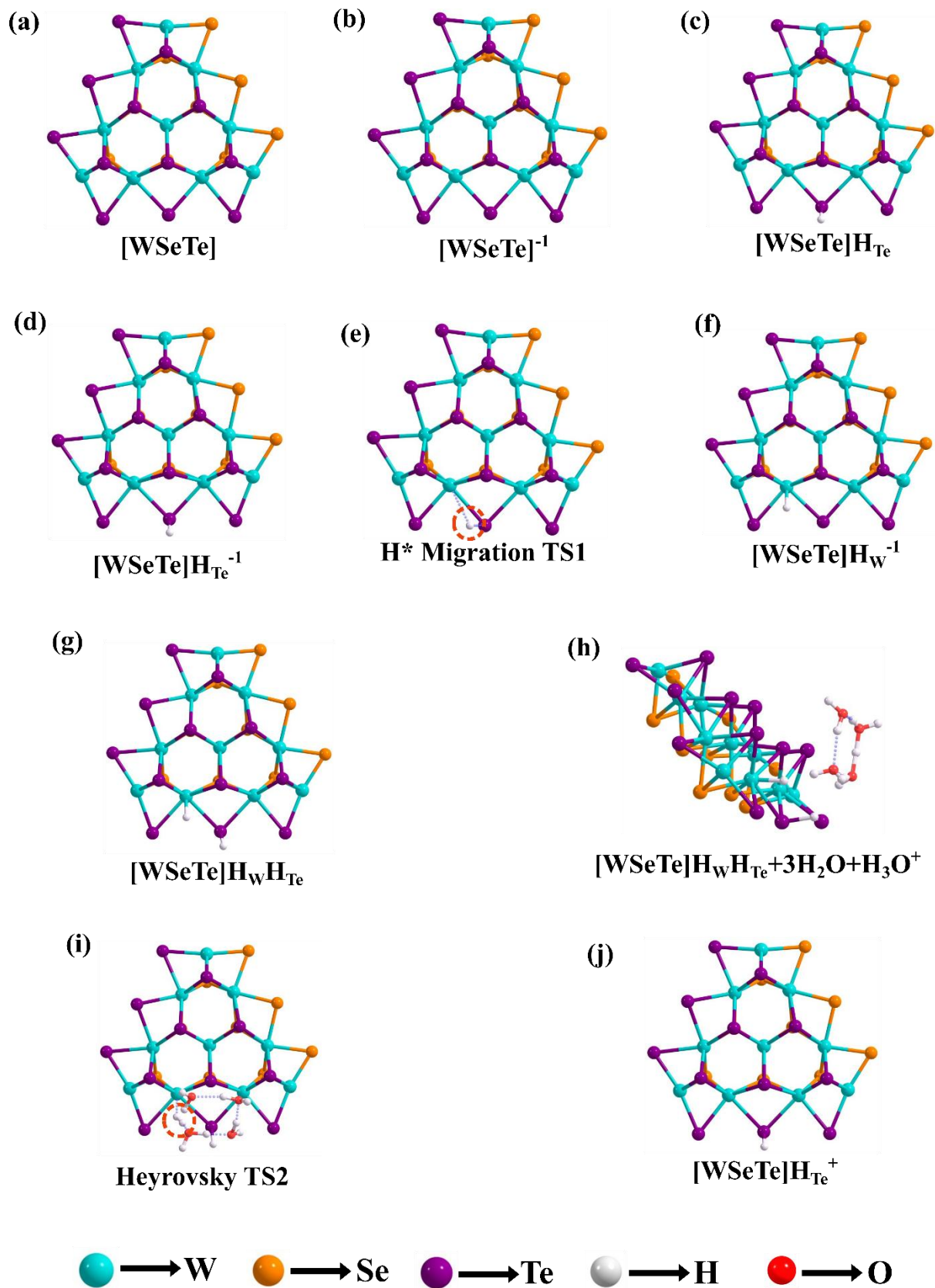


Figure 4.7: Equilibrium structures of various systems appeared during the HER process on the surface of the subject material: (a) [WSeTe], (b) [WSeTe]⁻, (c) [WSeTe]H_{Te}, (d) [WSeTe]H_{Te}⁻, (e) H^{*}-Migration TS1, (f) [WSeTe]H_W⁻, (g) [WSeTe]H_{Te}H_W, (h) [WSeTe]H_{Te}H_W + 3H₂O + H₃O⁺, (i) Heyrovsky TS2, and (j) [WSeTe]H_{Te}⁺ computed by the M06-L DFT method considering a nonperiodic finite molecular cluster model system W₁₀Se₉Te₁₂ to represent the 2D monolayer WSeTe JTMD are displayed here.

IV. In the next step after obtaining the TS1, the energy cost (ΔG) to obtain the intermediate [WSeTe]H_W⁻ from the TS1 is about -24.01 kcal mol⁻¹, as shown in Table 4.2. The equilibrium geometry of this intermediate [WSeTe]H_W⁻ is depicted in Figure 4.7f. Further, the HER proceeds by the addition of a second H⁺ from the medium to the Te site of [WSeTe]H_W⁻, resulting in the formation of the next intermediate, [WSeTe]H_WH_{Te}, with an energy cost (ΔG) of about -0.62 kcal mol⁻¹. The equilibrium geometry of the [WSeTe]H_WH_{Te} is displayed in Figure 4.7g.

V. The next step of the HER is the formation of H₂ by the Heyrovsky mechanism, in which a hydrated hydrogen water cluster (3H₂O+H₃O⁺) is added to the intermediate [WSeTe]H_WH_{Te}. This is a crucial phase of the HER process where the concept of H₂ evolution is involved in the subject reaction. The energy cost of this step to obtain [WSeTe]H_WH_{Te}+3H₂O+H₃O⁺ from the [WSeTe]H_WH_{Te} is $\Delta G = -3.88$ kcal mol⁻¹, as shown in Table 4.2. After adding the water cluster, the equilibrium geometry of the [WSeTe]H_WH_{Te} + 3H₂O+H₃O⁺ reaction intermediate is shown in Figure 4.7h. Subsequently, the H₂ formation would occur preferentially over the W site via the reaction of a W-absorbed hydride ion with a solvated proton from the solution. It should be mentioned here that the Volmer–Heyrovsky mechanism is more complicated in this case because it is necessary to solvate the H₃O⁺ source of the proton along the reaction pathway during the HER process taking place on the surfaces of 2D single layer WSeTe JTMD (as depicted in Figure 4.5 and Figure 4.7h).

VI. Finally, H₂ formation, where one absorbed hydride (H⁻) reacts with a solvated proton of an adjacent explicit water cluster (3H₂O+H₃O⁺), also known as the Heyrovsky reaction mechanism. In the Heyrovsky reaction mechanism, the rate-determining step requires an adjacent hydronium (H₃O⁺), the source of a proton along the reaction pathway involving

adsorbed H^- atoms, to form H_2 by forming a transition state in the reaction pathway. A second transition state, called Heyrovsky's transition state (TS2), as shown in Figure 4.7i, was found by the following imaginary modes. The second TS arises from $[\text{WSeTe}]\text{H}_\text{W}\text{H}_\text{Te}^- + 3\text{H}_2\text{O} + \text{H}_3\text{O}^+$, where H^* from the W site and H^+ from the water group combine, and the formation and evolution of H_2 occur from the surface of the electrocatalyst. The activation energy barrier of Heyrovsky TS2 is calculated to be approximately $5.95 \text{ kcal mol}^{-1}$ in the gas phase, as shown in Table 4.2, which is slightly higher than the value of H^* -migration TS1. During the TS2 formation, we found an imaginary frequency around -839.81 cm^{-1} , confirming this structure to be a transition state structure. Therefore, the activation energy barrier for H_2 evolution following the Heyrovsky reaction mechanism is about $5.95 \text{ kcal mol}^{-1}$ is computed in the gas phase, which is much smaller than the ordinary TMDs. This lower value of the activation energy barriers reveals that the pristine WSeTe JTMD is an excellent electrocatalyst for HER. Therefore, this overall chemical reaction mechanism gives insights into why WSeTe JTMD is a good catalyst for effective H_2 evolution.

Table 4.2. Energy changes (ΔE , ΔH , and ΔG) of various reaction intermediates and transition state structures (TSs) during the Volmer-Heyrovsky reaction mechanism computed by the M06-L DFT method in gas phase calculations are listed here.

HER Reaction Intermediates	ΔE (kcal.mol^{-1}) Gas Phase	ΔH (kcal.mol^{-1}) Gas Phase	ΔG (kcal.mol^{-1}) Gas Phase
$[\text{WSeTe}] \rightarrow [\text{WSeTe}]^-$	13.36	13.29	11.74
$[\text{WSeTe}]^- \rightarrow [\text{WSeTe}]\text{H}_\text{Te}$	-3.17	1.41	2.53
$[\text{WSeTe}]\text{H}_\text{Te} \rightarrow [\text{WSeTe}]\text{H}_\text{Te}^-$	18.80	18.73	18.67
$[\text{WSeTe}]\text{H}_\text{Te}^- \rightarrow \text{H}^*\text{Migration TS1}$	4.21	3.30	3.80
$\text{H}^*\text{Migration TS1} \rightarrow [\text{WSe}]\text{H}_\text{W}^-$	-26.01	-24.56	-24.01
$[\text{WSeTe}]\text{H}_\text{W}^- \rightarrow [\text{WSeTe}]\text{H}_\text{W}\text{H}_\text{Te}$	-5.16	-0.34	-0.62

$[\text{WSeTe}]\text{H}_\text{W}\text{H}_\text{Te} \rightarrow$	-16.27	-16.59	-3.88
$[\text{WSeTe}]\text{H}_\text{W}\text{H}_\text{Te} + 3\text{H}_2\text{O} + \text{H}_3\text{O}^+$			
$[\text{WSeTe}]\text{H}_\text{W}\text{H}_\text{Te} + 3\text{H}_2\text{O} + \text{H}_3\text{O}^+$ \rightarrow Heyrovsky TS2	8.89	6.56	5.95
Heyrovsky TS2 $\rightarrow [\text{WSeTe}]\text{H}_\text{Te}^+$	6.60	6.92	-9.64

VII. After the formation of Heyrovsky TS (which is noted by TS2), the system became $[\text{WSeTe}]\text{H}_\text{Te}^{+1}$. A H₂ molecule and 4H₂O molecules evolved after the reaction, and the free energy consumption is about 9.94 kcal mol⁻¹, as tabulated in Table 4.2. After forming the H₂ molecule, the equilibrium geometry of the $[\text{WSeTe}]\text{H}_\text{Te}^{+1}$ intermediate is displayed in Figure 4.7j.

In short, we have calculated two transition structures, TS1 and TS2 (Volmer TS and Heyrovsky TS). The first one is when H* migrates from the chalcogen (Te) site to a metal site (here, W). The second TS is calculated at the time of formation of the H₂ molecule on the active surface of the 2D monolayer Janus WSeTe material during the Heyrovsky reaction step in the HER process. Both the calculated H*-migration and Heyrovsky reaction barriers in the gas phase are 3.80 kcal mol⁻¹ and 5.95 kcal mol⁻¹, respectively, obtained by the present calculations using the M06-L method. The changes in the electronic energy (ΔE), enthalpy (ΔH), and free energy (ΔG) of the different reaction intermediates involved in HER (in gas phase calculations) are reported in Table 4.2.

The HER mechanism mainly focuses on two reaction steps, according to Figure 4.8. One of them is the H*-migration step when the H* migrates from the Te site to the W site, and the second one is hydrogen molecule formation through the water cluster. In both cases, the activation energy barriers of TS1 and TS2 are essential parameters to test the performance of the electrocatalyst for effective HER. The reaction energy diagram or potential energy surface (PES) of this Volmer–Heyrovsky reaction mechanism is depicted in Figure 4.8. The change in Gibbs free energy (ΔG) relative to the progress of the reaction steps (i.e., reaction coordinates) involved in the V–H reaction is plotted in Figure 4.8.

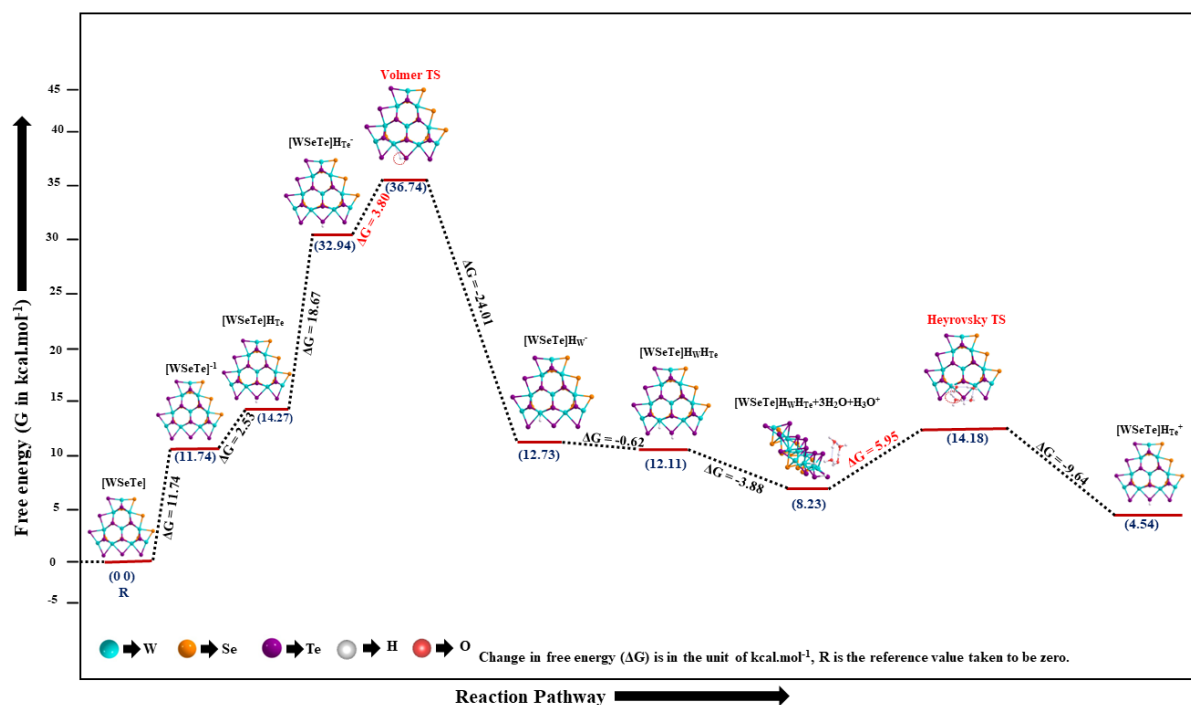


Figure 4.8: Reaction energy diagram or PES of the Volmer–Heyrovsky reaction mechanism during HER on the surface of the 2D monolayer Janus WSeTe material is presented here. Changes in free energy (ΔG) (in the gas phase) are expressed in kcal mol^{-1} .

For industrial applications and commercialization of the electrocatalysts, most of the H_2 evolution reactions are carried out in solution (i.e., in the solvent phase), so solvent-phase calculations are equally required to determine both the activation barriers. (Lei, Pakhira, Fujisawa, Wang, Iyiola, Perea López, et al., 2017; Ekka et al., 2022; Pakhira and Upadhyay, 2022) Therefore, in the present study, solvent phase calculations have also been performed by considering the solvent effects of the universal solvent “water” for the subject reaction, followed by the V–H mechanism. We have used the polarizable continuum model (PCM) method to calculate the energy barriers in the solvent phase. This is the standard method for computational study to calculate the solvent effects. The PCM analysis has been studied at the equilibrium structures of the complexes with the solvent radius of about 1.4 Å and H_2O with a dielectric constant $\epsilon = 78.54$ at 298.15 K temperature to encounter the solvation effects in the present calculations. In other words, we have used water as a solvent for the PCM calculations with a dielectric constant $\epsilon = 78.54$ at 298.15 K. In the finite molecular cluster model system, we have considered three water molecules ($3\text{H}_2\text{O}$) with one hydronium (H_3O^+) explicitly, and the rest of the reaction environment has been

considered implicitly water by employing the PCM analysis during Heyrovsky's reaction mechanism. The present DFT-D calculations have been performed using the M06-L DFT method, and it has been found that the energy barrier of the H*-migration (TS1) during the H*-migration after the Volmer reaction step in the solvent phase is about 3.65 kcal mol⁻¹. The lower energy barrier value of TS1 in the solvent phase calculation shows better hydrogen adsorption on the surface of 2D monolayer WSeTe Janus TMD. This indicates that the barrier of H*-migration is very low compared with other TMDs and JTMDs, which suggests that the 2D monolayer WSeTe JTMD can be a promising electrocatalyst for H₂ evolution. Similarly, the PCM analysis has been performed to compute the activation of the Heyrovsky reaction step, and the energy barrier of TS2 during the H₂ formation is about 8.72 kcal mol⁻¹ computed in the solvent phase. This H₂ evolution barrier during Heyrovsky's reaction step is also small compared to other TMDs and JTMDs, indicating an excellent electrocatalytic performance of the 2D monolayer WSeTe JTMD for H₂ evolution. The changes in electronic energy, enthalpy, and Gibbs free energy of the H*-migration and Heyrovsky reaction barriers in the solvent phase are listed in Table 4.3. It should be mentioned here that the transition state for the H*-migration step is of smaller energy than the Heyrovsky barrier, as depicted in Figure 4.8 and Table 4.2-4.3. Here, we have observed that the 2D Janus WSeTe may be an excellent electrocatalyst for HER.

Table 4.3. Energy changes (ΔE , ΔH , and ΔG) of the transition states (TS) during the Volmer-Heyrovsky reaction mechanism by computed M06-L DFT method in solvent phase calculations are listed here.

Activation barrier	ΔE (kcal.mol ⁻¹) in solvent phase	ΔH (kcal.mol ⁻¹) in solvent phase	ΔG (kcal.mol ⁻¹) in solvent phase
Volmer reaction barrier	4.07	3.16	3.65
Heyrovsky reaction barrier	11.93	9.33	8.72

4.3.4 Volmer–Tafel Reaction Mechanism

H₂ formation can take place via two possible HER mechanisms: V–H and V–T. The Volmer–Heyrovsky reaction mechanism has been discussed in the previous section. Now, we have also studied the V–T reaction mechanism of the proposed HER on the active edge of the 2D monolayer Janus WSeTe TMD. The V–T reaction mechanism has been thoroughly investigated, and various successive reaction steps with the relative Gibbs free energy (i.e., the changes of Gibbs free energy ΔG) have been calculated on the same level of the DFT method. The V–T mechanism is also a two-electron transfer process for the H₂ formation. In the case of the V–T reaction mechanism, two adjacent hydrogens adsorbed on the catalyst surface recombine to form H₂, i.e., $H^* + H^* \rightarrow H_2$, without further solvation of protons as in the case of the V–H mechanism. Figure 4.6 presents the complete reaction process involved in this proposed V–T reaction pathway on the surface of the 2D WSeTe JTMD. In the V–T mechanism, the completion of the HER mechanism occurs with the following steps:

I. This V–T mechanism follows the same path as in the case of the V–H mechanism until the $[WSeTe]H_W H_{Te}$ intermediate is generated from the $[WSeTe]H_W^{-1}$ with the gradual addition of a proton (H^+) at a free energy cost of $-0.62 \text{ kcal mol}^{-1}$, as shown in the V–H mechanism. In the V–T mechanism, two adsorbed hydrogen atoms next to each other, which are noted by H_W and H_{Te} in the $[WSeTe]H_W H_{Te}$ intermediate, react to form a molecular H₂ during this HER process.

II. In the upcoming step, the two adsorbed hydrogen atoms, one at the W atom site (noted by H_W) and the other at the Te atom site (noted by H_{Te}), both hydrogens recombine to form H₂, which is called the Volmer–Tafel mechanism. The activation energy barrier of the Tafel TS3 is calculated to be approximately $2.99 \text{ kcal mol}^{-1}$ in the gas phase, as shown in Table 4.4. During the calculation of TS3, we found an imaginary frequency around -432.30 cm^{-1} , confirming this structure to be a transition state. The third TS arises from $[WSeTe]H_W H_{Te}$, where H^* from the W atom site and H^* from the atom site recombine and finally evolve into H₂ and separate from the system, as shown in Figure 4.9.

III. After the formation of Tafel TS3, the initial step $[WSeTe]$ of the reaction, which is nothing but the original catalyst, is achieved. A H₂ molecule is evolved from the surface of

the catalyst [WSeTe], and the free energy consumption is 15.16 kcal mol⁻¹, as shown in Table 4.4.

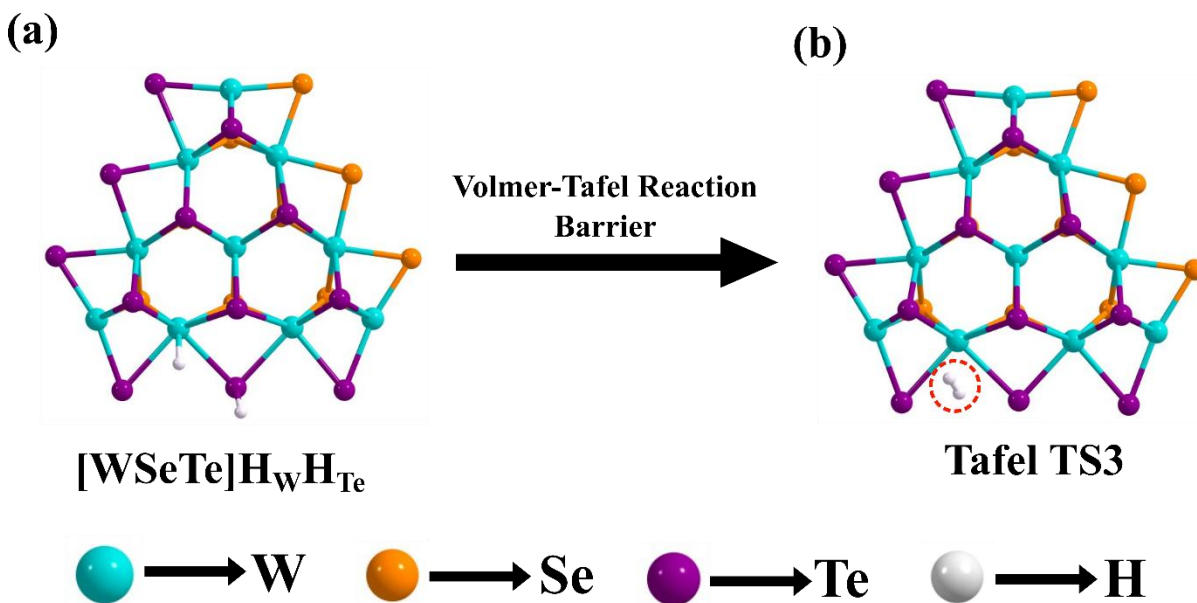


Figure 4.9: Volmer–Tafel reaction mechanism equilibrium geometries of the [WSeTe]H_WH_{Te} and TS3 are shown here.

Table 4.4: Energy changes (ΔE , ΔH , and ΔG) of different intermediates and transition states (TS) during the Volmer-Tafel reaction mechanism computed by the M06-L DFT method in gas phase are listed here.

HER Reaction Intermediates	ΔE (kcal.mol ⁻¹) Gas Phase	ΔH (kcal.mol ⁻¹) Gas Phase	ΔG (kcal.mol ⁻¹) Gas Phase
[WSeTe] → [WSeTe] ⁻	13.36	13.29	11.74
[WSeTe] ⁻ → [WSeTe]H _{Te}	-3.17	1.41	2.53
[WSeTe]H _{Te} → [WSeTe]H _{Te} ⁻	18.80	18.73	18.67
[WSeTe]H _{Te} ⁻ → H* Migration (TS1)	4.21	3.30	3.80

H*Migration (TS1) → [WSe]H_W⁻	-26.01	-24.56	-24.01
[WSeTe]H_W⁻ → [WSeTe]H_WH_{Te}	-5.16	-0.34	-0.62
[WSe]H_WH_{Te} → Tafel TS3	4.14	3.17	2.99
Tafel TS3 → [WSeTe]	-5.32	-5.77	-15.16

In conclusion, we have calculated two transition structures, TS1 and TS3 (H*-migration TS and Tafel TS), during the V–T reaction step, the first of which is when H* migrates from the tellurium (Te) site to a metal site (here, W). The third TS, i.e., TS3, is calculated when the formation of a H₂ molecule occurs on the active surface of the 2D monolayer Janus WSeTe TMD material during the Tafel reaction step in the HER process. The H*-migration and Tafel reaction barriers are 3.80 kcal mol⁻¹ and 2.99 kcal mol⁻¹, respectively, computed in the gas phase. The changes in electronic energy (ΔE), enthalpy (ΔH), and free energy (ΔG) of the different reaction intermediates involved in the subject reaction (obtained in a gas phase study) are reported in Table 4.4.

We have followed the V–T reaction pathway but mainly focused on two points, according to Figure 4.10. One of them was the migration of H* from the Te-site to the W-site, and the second was hydrogen formation through the two adsorbed hydrogens on the W-site and Te-site. The reaction energy diagram or potential energy surface (PES) of this Volmer–Tafel reaction mechanism is shown in Figure 4.10, and it represents the change in Gibbs free energy (ΔG) relative to the progress of the reaction steps involved in the V–T reaction calculated in the gas phase. The solvation effects have been considered during the HER by incorporating the polarization continuum model (PCM) during the TS formation (here, Tafel TS noted by TS3) to compute the reaction barrier in the solvent environment. The free energy barrier of TS3 during the Tafel reaction step for hydrogen evolution is about 3.27 kcal mol⁻¹, obtained in the solvent phase.

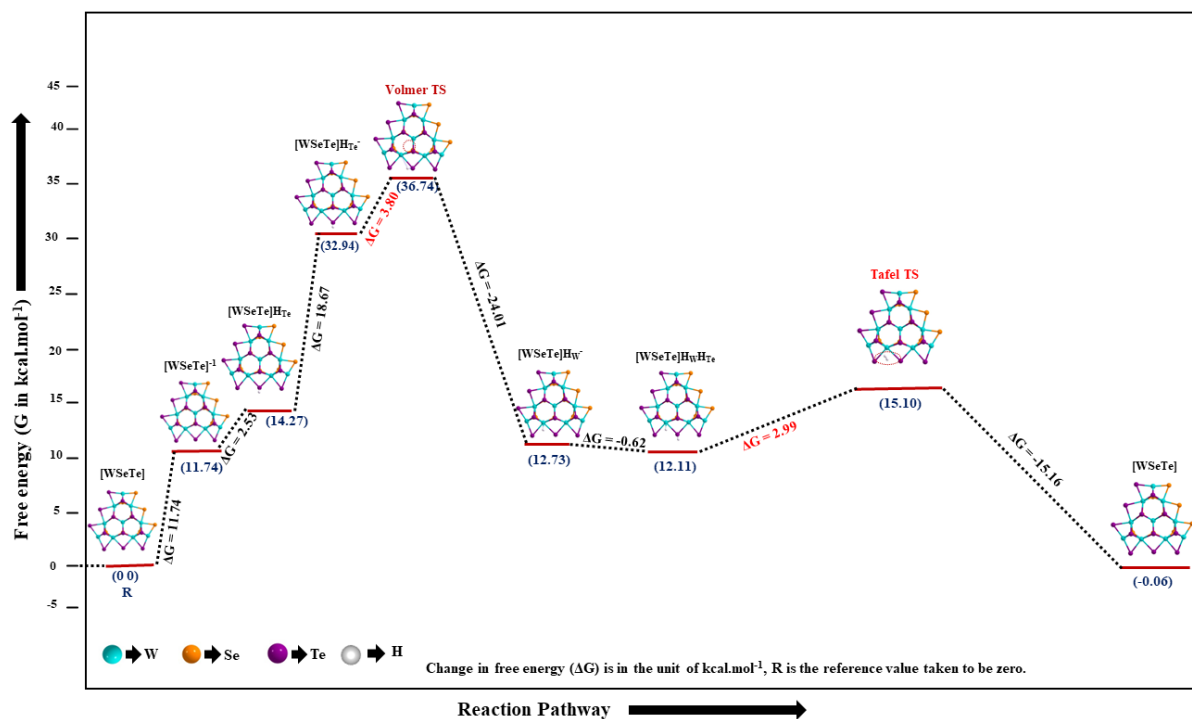


Figure 4.10: Reaction energy diagram or PES of the Volmer–Tafel reaction mechanism during HER on the surface of 2D Janus WSeTe material is depicted here. Changes in the free energy (ΔG) diagram are expressed in kcal mol⁻¹.

It is worth noting here that the reaction barrier of TS3 during the Tafel reaction step in the V–T reaction mechanism is lower than that of the Heyrovsky transition state (TS2) of the V–H reaction mechanism in both the gas and solvent phases. Here, the present study shows that the V–H mechanism is energetically less favorable than the V–T mechanism for the HER on the surface of the 2D monolayer WSeTe Janus TMD electrocatalyst. This lower reaction barrier proposes that the evolution of H₂ can proceed through this V–T pathway with a reaction barrier comparable to that of noble metal-based electrocatalysts.

An electrocatalyst lowers the activation energy of an electrochemical reaction, often lowering the electric potential at which the reaction occurs. In our present work, we have used a nonperiodic cluster model WSeTe for the HER mechanism. For the stability of the molecular cluster model system and all of the reaction intermediates formed during the HER process, we have performed geometry optimization followed by thermodynamic calculations, including electronic energy, enthalpy, and Gibbs free energy. We have also performed frequency calculations for all the structures, which confirm the thermodynamic

stability of the system. Our present calculations presented here found that all the structures have real frequency (positive) except the three transition states (TSs). All three TSs (H^{*}-migration, Tafel, and Heyrovsky TS) have one imaginary frequency, which confirms them to be transition state structures. This information, i.e., electronic energy, enthalpy, Gibbs free energy, frequency, and charges of the various structures, are listed in Table 4.5 and Table 4.6, respectively. All of the energy values are negative, which corresponds to the stability of all of the reaction intermediate structures.

Table 4.5: Energy (E), Enthalpy (H) and Gibbs free energy (G) for different steps and transition states (TSs) during HER mechanism in the gas phase calculations are tabulated here.

Systems	Energy (E) (in Hartree)	Enthalpy (H) (in Hartree)	Gibbs free energy (G) (in Hartree)
[WSeTe]	-859.192899	-859.102491	-859.271739
[WSeTe] ⁻¹	-859.3194096	-859.229114	-859.400824
[WSeTe]H _{Te}	-859.7624692	-859.664884	-859.834801
[WSeTe]H _{Te} ⁻¹	-859.8803034	-859.782831	-859.952849
TS1	-859.8735889	-859.777572	-859.946800
[WSeTe]H _W ⁻¹	-859.9150321	-859.816711	-859.985058
[WSeTe]H _W H _{Te}	-860.3612687	-860.255267	-860.424063
[WSeTe]H _W H _{Te} + 3H ₂ O+H ₃ O ⁺	-1166.467904	-1166.240583	-1166.432420
TS2	-1166.4533095	-1166.230131	-1166.422937
[WSeTe]H _{Te} ⁺¹	-859.5416392	-859.443906	-859.612717
TS3	-860.3546774	-860.250207	-860.419293

Table 4.6: Charge distribution and imaginary frequency count across intermediates and TSs in the HER mechanism.

Systems	Charge	No. of imaginary frequencies
[WSeTe]	0	0
[WSeTe] ⁻¹	-1	0
[WSeTe]H _{Te}	0	0
[WSeTe]H _{Te} ⁻¹	-1	0
TS1	-1	1 (-494.71 cm ⁻¹)
[WSeTe]H _W ⁻¹	-1	0
[WSeTe]H _W H _{Te}	0	0
[WSeTe]H _W H _{Te} + 3H ₂ O+H ₃ O ⁺	+1	0
TS2	+1	1 (-839.81 cm ⁻¹)
[WSeTe]H _{Te} ⁺¹	+1	0
TS3	0	1 (-432.30 cm ⁻¹)

4.3.5 Other Thermodynamic Properties of the HER Mechanism

4.3.5.1 HOMO and LUMO Calculations

The visualization of the highest occupied molecular orbital (HOMO) and the lowest unoccupied molecular orbital (LUMO) provides a deeper understanding of the H^{*}-migration during the H^{*}-migration reaction step, and the role of the electrons in H₂ formation and evolution during Heyrovsky or Tafel reaction steps calculations of their respective TS structures, as shown in Figure 4.11. Here, the energies of the HOMO and the LUMO have been calculated at the equilibrium structure of all transition states (TSs) by using the same DFT method. Figure 4.11a, b represents the H^{*}-migrated HOMO and LUMO of TS1, respectively, where the electron density of H^{*} has shifted from the Te site to the transition metal site (W-site) when the TS1 has been formed during the H^{*}-migration reaction step of the HER. Throughout the H^{*}-migration process, we found the HOMO–LUMO energy gap around 0.145 eV, as shown in Table 4.7. This HOMO–LUMO gap is a valuable tool for predicting the stability of the electrocatalyst and the color of complexes in solution. Both the HOMO and LUMO of TS2 in the Heyrovsky reaction step of H₂ evolution are represented in Figure 4.11c, d, respectively. During the formation of TS2, the

creation of H_2 stabilized due to better overlap between the $5d$ orbital of the W atom and the $1s$ orbital of the H atom. The HOMO–LUMO energy gap of TS2 has been found to be 0.567 eV, as shown in Table 4.7. The HOMO and LUMO of TS3 in the Tafel reaction step of H_2 evolution are represented in Figures 4.11f, respectively. The HOMO–LUMO energy gap of the TS3 has been found to be 0.642 eV, as shown in Table 4.7. The better overlap of atomic orbitals during the H^* -migration in the Volmer reaction step and the formation of H_2 in the Heyrovsky and Tafel reaction steps stabilized the system well, which also revealed the excellent electrocatalytic activity of the 2D monolayer Janus WSeTe for HER.

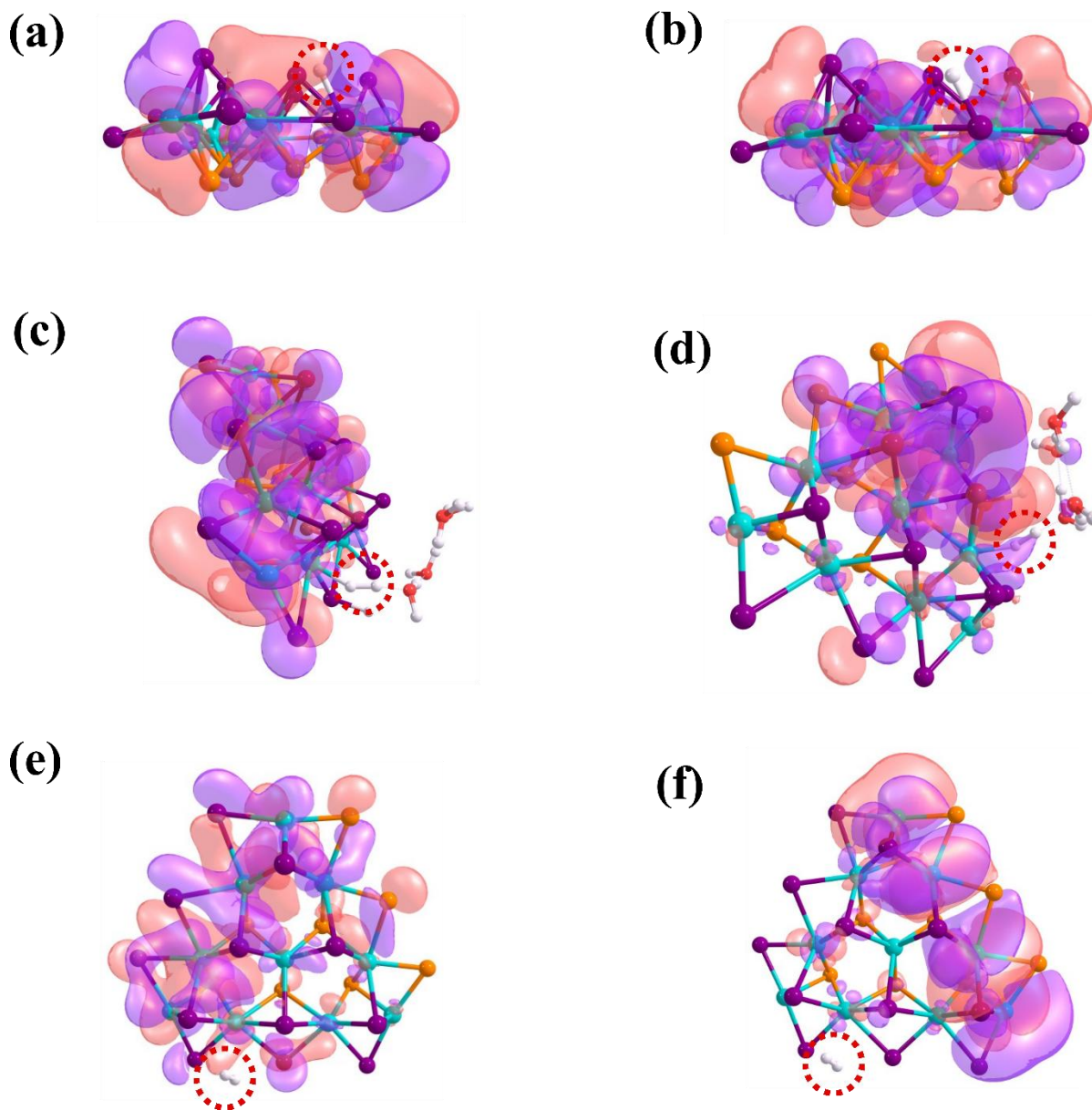


Figure 4.11: (a) HOMO of TS1 during the H*-migration, (b) LUMO of TS1 during the H*-migration, (c) HOMO of TS2 during the Heyrovsky reaction step during H₂ formation, (d) LUMO of TS2 during the Heyrovsky reaction step during H₂ formation, (e) HOMO of TS3 during the Tafel reaction step during H₂ formation, and (f) LUMO of TS3 during the Tafel reaction step during H₂ formation are shown here.

Table 4.7: HOMO and LUMO energy and HOMO-LUMO energy gaps (E_g) of all Transition states (TSs).

Activation energy barrier	HOMO energy (in eV)	LUMO energy (in eV)	HOMO-LUMO energy gap (E _g) (in eV)
H*-migration TS1	-2.195	-2.050	0.145
Heyrovsky TS3	-7.274	-6.707	0.567
Tafel TS3	-5.154	-4.512	0.642

4.3.5.2 Turnover Frequency (TOF) and Tafel Slope Calculation

To understand the activity of an electrocatalyst, the turnover frequency (TOF) is the most important factor that influences the overall catalytic activity of the HER. The better catalytic activity of an electrocatalyst requires a high turnover frequency, so one must focus on catalysts with higher TOF values. With transition state theory (TST),[\(Jordan, 1979\)](#) the TOF at a specific temperature is theoretically given by

$$TOF = \left(\frac{k_B T}{h} \right) e^{\left(\frac{-\Delta G}{RT} \right)}$$

k_B = Boltzmann constant (3.298×10^{-27} kcal.mol⁻¹)

T = Room temprature (here 298.15 K)

h = Planck's constant (1.584×10^{-37} kcal.sec)

R = Universal gas constant (1.987×10^{-3} kcal.K⁻¹.mol⁻¹)

ΔG = Free energy barrier

The present study shows that the TOF at the W-edge of the 2D monolayer Janus WSeTe TMD is about $2.51 \times 10^6 \text{ s}^{-1}$, computed in the solvent phase during the Volmer–Heyrovsky reaction mechanism, corresponding to an activation free energy barrier of $8.72 \text{ kcal mol}^{-1}$. Similarly, the calculated value of the TOF for the solvent phase in the Volmer–Tafel reaction mechanism was found to be $2.48 \times 10^{10} \text{ s}^{-1}$, corresponding to an activation energy barrier of $3.27 \text{ kcal mol}^{-1}$ during the Tafel reaction step. Such a large TOF value indicates the excellent performance of the 2D monolayer Janus WSeTe TMD for competent HER. All the electronic structure calculations have been performed at 0 K, which is already implemented in the CRYSTAL17 and GAUSSIAN16 suite codes by default. It should be mentioned here that all the thermodynamic calculations with the harmonic vibrational analysis have been performed at room temperature (i.e., $T = 298.15 \text{ K}$). It is important to acknowledge here that the temperature can have a significant influence on the observed phenomena in real-world conditions. At higher temperatures, thermal energy can affect the kinetics and energetics of reactions, potentially altering reaction pathways, equilibrium constants, and catalytic activity. Higher temperatures often lead to increase the reaction rates due to greater reactant kinetic energy. This can result in more frequent collisions between reactant molecules and catalytic sites. Elevated temperatures can enhance the mobility of reactant molecules, making them more likely to reach the active sites of the catalyst. This improved accessibility can lead to higher catalytic activity. Some catalysts may exhibit improved activity at higher temperatures due to changes in their surface chemistry or structure. This increased catalytic activity can result in higher TOF values as more active sites become available for catalysis. It is important to note that the relationship between temperature and TOF may not always be straightforward and can depend on many other factors such as the nature of the reaction, the specific catalyst, and the presence of any temperature-dependent kinetic or thermodynamic barriers. Additionally, excessively high temperatures can sometimes lead to catalyst deactivation or undesirable side reactions, which may ultimately decrease TOF. Therefore, optimizing temperature conditions is crucial for maximizing catalytic efficiency and TOF in a given system.

Another important parameter for the HER calculation to compare with the experimental results is the Tafel slope, which is the inverse measure of the response

strength of the reaction rate to a change in potential. (Huang *et al.*, 2015) The following formula has calculated the Tafel slope:

$$m = 2.303 \left(\frac{RT}{nF} \right)$$

R = Universal gas constant ($1.987 \times 10^{-3} \text{ kcal. K}^{-1} \cdot \text{mol}^{-1}$)

T = Room temprature (here 298.15 K)

F = faraday constant ($96485 \text{ C. mol}^{-1}$)

n = number of electrons transferred to the system

The Tafel slope provides information about the catalyst's rate-determining steps, kinetics, and the energy required to obtain the desired activity. For our aperiodic cluster model calculations, the Tafel slope is $29.57 \text{ mV dec}^{-1}$, as $n = 2$ electrons have been transferred into the system to evolve an H₂ molecule.

The present DFT calculations show that the 2D monolayer Janus WSeTe material has a lower reaction energy barrier for all the H*-migration TS in the H*-migration reaction step, and H₂ formation in the Heyrovsky, and Tafel reaction step during the HER mechanism compared to other materials listed in Table 4.8. (Ekka *et al.*, 2022; Pakhira and Upadhyay, 2022) The current DFT studies show that the activation energy barriers of the Volmer reaction during H*-migration across the surface of 2D Janus WSeTe material were around $3.80 \text{ kcal mol}^{-1}$ in the gas phase and $3.65 \text{ kcal mol}^{-1}$ in the solvent phase calculations, respectively. In the same way, considering water as the solvent, the activation energy barriers of the formation of H₂ in the Heyrovsky reaction step are approximately $5.95 \text{ kcal mol}^{-1}$ computed in the gas phase and $8.72 \text{ kcal mol}^{-1}$ computed in the solvent phase, respectively. Furthermore, the activation energy barriers for forming H₂ in the Tafel reaction step are approximately $2.99 \text{ kcal mol}^{-1}$ calculated in the gas phase and $3.27 \text{ kcal mol}^{-1}$ in the solvent phase, respectively. These lowest activation energy barriers and high turnover frequency (TOF) during H*-migration and H₂ formation confirm the superior HER electrocatalytic activity of the 2D monolayer Janus WSeTe compared to the other 2D TMDs, as shown in Table 4.8.

Table 4.8: Reaction barriers in both gas and solvent phases for various 2D TMDs.

Catalysts	H*-migration TS1 barrier		Heyrovsky TS2 barrier		Tafel TS3 barrier		References
	Gas phase (kcal.mol ⁻¹)	Solvent phase (kcal.mol ⁻¹)	Gas phase (kcal.mol ⁻¹)	Solvent phase (kcal.mol ⁻¹)	Gas phase (kcal.mol ⁻¹)	Solvent phase (kcal.mol ⁻¹)	
MoS₂	11.90	17.70	16.0	23.8	-	-	<i>ACS Nano</i> 2017, 11, 5, 5103–5112
WS₂	12.40	18.10	14.4	21.3	-	-	<i>ACS Nano</i> 2017, 11, 5, 5103–5112
W_{0.4}Mo_{0.6}S₂	6.80	11.90	11.50	13.30	-	-	<i>ACS Nano</i> 2017, 11, 5, 5103–5112
WSe₂	2.67	6.11	6.24	8.41	-	-	<i>Adv. Mater. Interfaces</i> 2023, 10, 2202075
Mn-MoS₂	7.23	10.34	10.59	10.79	90.13	93.72	<i>Phys. Chem. Chem. Phys.</i> , 2022,24, 265-280.
MoSSe	3.93	7.10	5.61	4.72	8.52	-	<i>Sustainable Energy Fuels</i> ,

*Electrocatalytic Performance of 2D Monolayer WSeTe Janus Transition Metal
Dichalcogenide for Highly Efficient H₂ Evolution Reaction*

							2022,6, 1733-1752.
MoP	17.5	-	16.3	-	56	60	<i>ACS Catal.</i> 2019, 9, 1, 651–659
MoSP	12.90	14	9.2	12.90	34	-	<i>ACS Catal.</i> 2019, 9, 1, 651–659
Borophene	4.84	-	8.07	-	31.62	-	<i>ACS Appl. Energy Mater.</i> 2023, 6, 8941–8948.
NbCO₂	-	-	31.59	-	43.58		<i>J. Mater. Chem. A</i> , 2018,6, 4271-4278
Epitaxial Graphene	28.59	35.51	-	-	28.74	29.03	<i>ACS Omega</i> 2022, 7, 13221–13227
WSeTe	3.80	3.65	5.95	8.72	2.99	3.27	This work

4.4 Summary

In Summary, we have computationally designed a Janus 2D monolayer slab of WSeTe TMD and investigated its electronic and structural properties using the first principles-based DFT-D3 (here, B3LYP-D3) method. The present study shows that the 2D monolayer Janus WSeTe material acts as an efficient electrocatalyst for effective HER. Compared to the pristine 2D monolayer ordinary TMDs such as MoS₂, WS₂, WSe₂, etc., the Janus structure introduces asymmetry, which helps readily transfer electrons during the reactions. A direct band gap has been found to be 2.39 eV of the 2D Janus WSeTe monolayer, indicating a semiconducting nature. The lower bandgap of 2D monolayer Janus WSeTe suggests that it can be used as an electrocatalyst for HER. The catalytic

performance of 2D monolayer WSeTe JTMD has been studied based on the change in HER intermediates adsorption energy considering the nonperiodic molecular cluster model system of the 2D single layer Janus WSeTe ($\text{W}_{10}\text{Se}_9\text{Te}_{12}$) surface. Each reaction step involved in the V–H and V–T mechanisms has been studied to reveal the HER pathway by employing the M06-L DFT method. The H^* -migration reaction barrier (when H moves from the Te-site to the W-site on the surfaces of the 2D Janus WSeTe material) was about $3.80 \text{ kcal mol}^{-1}$ computed in the gas phase and $3.65 \text{ kcal mol}^{-1}$ in the solvent phase, respectively. The activation energy barrier during the formation of H_2 in the Heyrovsky reaction step is approximately $5.95 \text{ kcal mol}^{-1}$ in the gas phase and $8.72 \text{ kcal mol}^{-1}$ in the solvent phase, respectively. Furthermore, in the V–T HER mechanism, the activation energy barrier of the formation of H_2 during the Tafel reaction step is approximately $2.99 \text{ kcal mol}^{-1}$ calculated in the gas phase and $3.27 \text{ kcal mol}^{-1}$ calculated in the solvent phase, respectively. Here, it can be concluded that the V–H mechanism of HER is less favorable than the V–T mechanism (due to the lower energy barrier of the Tafel TS3 compared to the Heyrovsky TS2) taking place on the surface of 2D monolayer Janus WSeTe TMD.

To support the theoretical results, the HOMO–LUMO calculations have been performed at the equilibrium structures of all the TSs, and it has been found that a better overlap of the atomic orbitals of the W atom of the WSeTe with the H atom during the TSs formation in the HER process stabilized the system in a better way. This calculation explains why the 2D monolayer Janus WSeTe material has excellent HER catalytic activity. The TOF is about $2.51 \times 10^6 \text{ s}^{-1}$ through the solvent phase calculation of the V–H reaction mechanism, and in the V–T reaction mechanism, TOF was found to be $2.48 \times 10^{10} \text{ s}^{-1}$ in the solvent phase. These higher TOF values confirm the effective hydrogen evolution per active site and unit time of the 2D monolayer WSeTe catalyst. The value of the theoretical Tafel slope of our two-electron transfer mechanism is approximately $29.57 \text{ mV dec}^{-1}$. These very low reaction barrier values, low Tafel slope, and very high TOF values confirm the excellent electrocatalytic activity of 2D monolayer Janus WSeTe for HER. It is believed that these results would bring more experimental and theoretical insights to explore the potential of the 2D monolayer Janus TMDs-based materials as a superior electrocatalyst for the HER. In short, the excellent electrocatalytic HER performance and stability suggest that the 2D monolayer Janus WSeTe TMD can be regarded as a promising candidate for

highly efficient electrocatalyst for the HER, which can solve the key problem for hydrogen production from water on a large scale.

Chapter 5

2D Monolayer Molybdenum(IV) Telluride TMD: an Efficient Electrocatalyst for H₂ Evolution

In this chapter, we have used the first principles-based hybrid DFT method, we have computationally designed a pure 2D monolayer MoTe₂ TMD and examined its structural and electronic properties with electrocatalytic efficacy towards HER. A non-periodic finite molecular cluster model Mo₁₀Te₂₁ system has been employed to explore the feasibility of both the V–H and V–T reaction mechanisms for the HER. The solvent-phase calculations demonstrate that this material can effectively undergo either V–H or V–T reaction pathways. This conclusion is supported by our determination of low reaction barriers for the H^{}-migration, Heyrovsky, and Tafel transition states (TSs), which were found to be approximately 9.80, 12.55, and 5.29 kcal mol^{−1}, respectively. These results highlight the potential utility of 2D monolayer MoTe₂ TMD as a promising electrocatalyst for the HER. The unusual electrocatalytic activity of the pristine 2D monolayer MoTe₂ TMD is evidenced by its ability to significantly reduce reaction barriers, achieving impressive TOF values of 3.91×10^3 and 8.22×10^8 s^{−1} during the Heyrovsky and Tafel reaction steps, respectively. Additionally, it demonstrates a remarkably low Tafel slope of 29.58 mV dec^{−1}. These outstanding performance metrics indicate that the pure 2D monolayer MoTe₂ TMD is a highly efficient electrocatalyst for the HER, surpassing the capabilities of traditional platinum group metal-based alternatives. Further exploration of its potential applications in electrocatalysis is warranted. The present work provides valuable insights into the atomic modulation of active sites for enhanced electrocatalytic performance towards the HER, paving the way for designing advanced non-noble metal-free electrocatalysts.*

5.1. Introduction

Recently, two-dimensional (2D) materials have offered numerous advantages, such as a large specific surface area, exceptional mechanical characteristics, and high carrier mobility. Therefore, in recent years, 2D materials have become one of the most promising candidate materials for electrocatalysts. Especially, the 2D layer structure of TMDs has various special characteristics, including excellent stability, electrical tunability, high-density active edges, tunable electronic band gap, high electrical conductivity, and the potential for defect engineering. (Wang *et al.*, 2017; Som and Jha, 2020) These exceptional features have garnered significant attention from the scientific community, particularly in the context of studying H₂ evolution and its numerous practical applications. In recent times, considerable research has been focused on exploring the potential of 2D TMDs monolayers (such as MoSe₂, WSe₂, and MoS₂) as substitutes for Pt catalysts. This is mainly due to their remarkable electronic, magnetic, and chemical properties that make them attractive alternatives to traditional catalysts. (Huang *et al.*, 2015; Lei, Pakhira, Fujisawa, Wang, Iyiola, Perea López, *et al.*, 2017)

Based on research analysis, it has been discovered that the MoTe₂ semiconductor possesses exceptional catalytic activity, particularly in the vicinity of the Fermi energy level (E_F) and exhibits high carrier mobility. These properties make MoTe₂ a promising candidate for use as an electrocatalyst beyond the HER, with potential uses in the ORR and OER in fuel cell technology. (Huang *et al.*, 2016; Xiao and Shen, 2021) Here, we introduce a 2D monolayer MoTe₂ TMD material as a unique and efficient non-noble metal catalyst for the HER. The present research work highlights the various phases of monolayers of molybdenum telluride (MoTe₂) as very efficient HER electrocatalysts. (Bhat and Nagaraja, 2019; McGlynn *et al.*, 2019) A finite molecular cluster model system, Mo₁₀Te₂₁, has been computationally designed to investigate the reaction process and identify the most effective 2D monolayer MoTe₂ phase and HER active sites using quantum mechanical DFT calculations. (Baker, Scheiner and Andzelm, 1993; Beck, 1993; Pakhira, Sen, *et al.*, 2013; Ekka *et al.*, 2022) This DFT approach offers a comprehensive means of exploring the catalytic activity of the 2D single-layer MoTe₂, as well as the potential to enhance its performance in comparison to traditional electrocatalytic materials. The Mo₁₀Te₂₁ cluster

model system has been chosen specifically to represent the edge-specific properties of 2H-MoTe₂, as it captures localized surface interactions that are relevant to the HER. The primary goal of the cluster model is to provide a computationally efficient framework for studying localized reaction pathways and energy barriers with TSs, which is especially important for understanding the HER mechanism in small, edge-specific regions. In this study, we have computationally designed a 2D monolayer MoTe₂ TMD material and investigated its electronic properties, including the electronic band structure, total DOS, Fermi energy level (E_F), and electronic band gap (E_g), to gain insight into its potential for HER applications by employing the periodic DFT method. The density of exposed active edge sites is critical in determining the HER catalytic activity of the 2D monolayer TMDs. The hydrogen adsorption-free energy (ΔG_H) reflects the strength of the interaction between the catalyst and the reactant and is a key indicator of the catalyst's activity. The TOF is the rate of hydrogen evolution per active site and is a measure of the efficiency of an electrocatalyst. We have utilized M06-L, a local meta-generalized gradient approximation (meta-GGA) method to investigate the HER catalytic activity of the pristine 2D monolayer of MoTe₂ by considering the finite molecular model system of the subject material. Our focus is on determining the reaction pathway of the subject reaction (i.e., HER) at the Mo edge ($10\bar{1}0$) of the 2D single-layer MoTe₂ TMD material through theoretical and computational analysis. The exposed Te-edge ($\bar{1}010$) and Mo-edge ($10\bar{1}0$) of the 2D monolayer TMD MoTe₂ have been found to be catalytically active for the HER, while the Te–Mo–Te tri-layer of the MoTe₂ TMD is the exposed surface. To describe the Mo edge of the 2D monolayer MoTe₂, we have used a finite non-periodic molecular cluster model of Mo₁₀Te₂₁ (as shown in Figure 5.1). The polarization continuum model (PCM) was used to account for the solvation effects of water as a solvent, allowing for the exact integration of the M06-L method to compute reaction barriers. (Zhao and Truhlar, 2008; Grimme et al., 2010; Pakhira, Lucht and Mendoza-Cortes, 2017) The first-principles-based M06-L meta-GGA method has been used to investigate the reaction pathways, kinetics, and barrier energies for the HER on the surfaces of the 2D monolayer MoTe₂ TMD by considering the finite cluster model system of the MoTe₂ (Mo₁₀Te₂₁) TMD, as shown in Figure 5.1. It should be noted here that surprisingly, M06-L stands out for its striking accuracy,

outperforming any other investigated functionals and it is very fast, good for transition metals, and inorganic and organometallic chemical reactions.

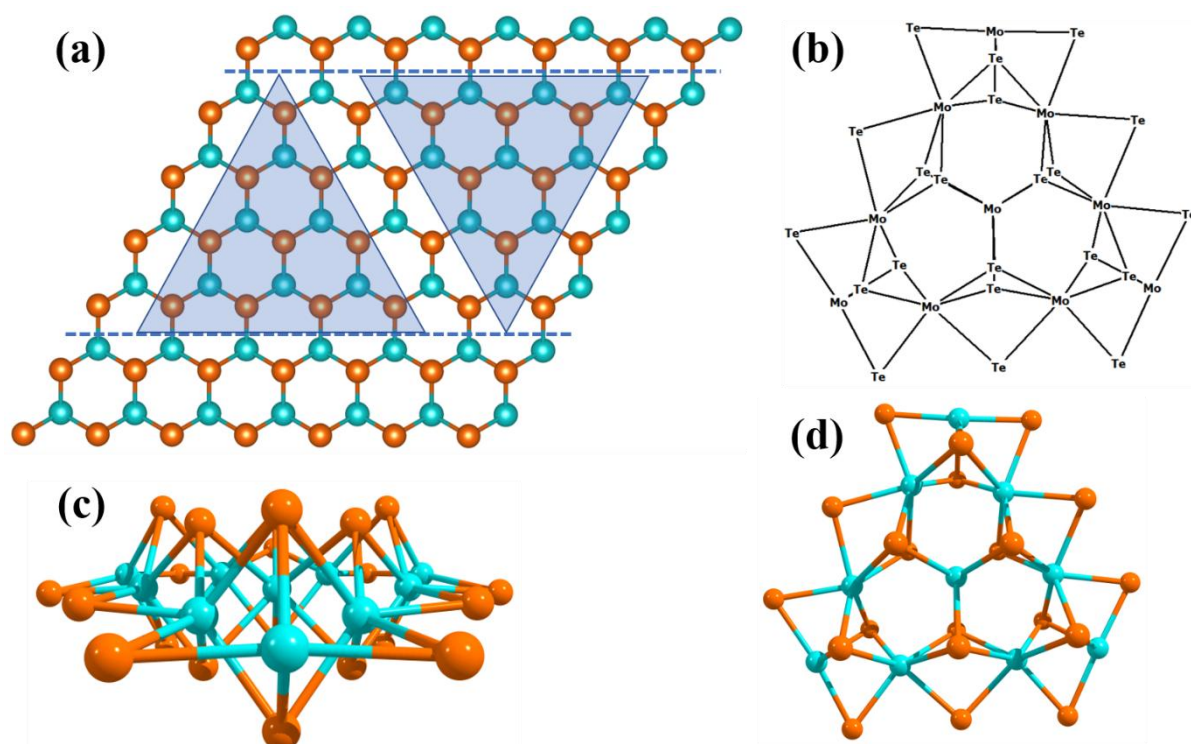


Figure 5.1: (a) The equilibrium 2D monolayer MoTe_2 TMD with a Te–Mo–Te tri-layer structure. The two horizontal blue color dashed lines indicate terminations along the $(10\bar{1}0)$ Mo-edge and $(\bar{1}010)$ Te-edge. The two triangles represent the terminations for Mo-edge and Te-edge clusters. It includes a non-periodic molecular cluster with an active Te-edge and a non-periodic molecular cluster with an active Mo-edge. (b) The molecular cluster model system of the 2D monolayer MoTe_2 TMD represented schematically. (c) A side view of the chosen $\text{Mo}_{10}\text{Te}_{21}$ non-periodic triangular molecular cluster. (d) A top view of the MoTe_2 TMD Mo-edge cluster.

5.2. Computational details

Computational methods are used during the present theoretical studies, and the other parameters play a momentous role in determining the electrocatalytic activity of an efficient HER. Here, a periodic 2D monolayer structure of the MoTe_2 TMD is computationally designed to examine its structural and electronic properties by using the first principles-based hybrid DFT method.^{(Lei, Pakhira, Fujisawa, Wang, Iyiola, Perea}

López, et al., 2017; Liang et al., 2018) The HER mechanism at the active edge has been further investigated by DFT computations using a non-periodic finite molecular cluster model system $Mo_{10}Te_{21}$ corresponding to the pristine 2D monolayer $MoTe_2$. A further discussion of both the periodic and non-periodic systems is explained below.

5.2.1. Periodic structure DFT calculations

For the periodic 2D structure calculations, the monolayer of 2D $MoTe_2$ TMD is bound by Mo-edge ($10\bar{1}0$) and Te-edge ($\bar{1}010$), as shown in Figure 5.1, and the two horizontal blue color dashed lines indicate terminations along the ($10\bar{1}0$) Mo-edge and ($\bar{1}010$) Te-edge. First, we have performed a computational study of 2D monolayer $MoTe_2$ to obtain the equilibrium structure and geometry of the TMD. To determine the equilibrium geometry and electronic properties of the 2D monolayer $MoTe_2$ material, we have utilized the quantum mechanical first-principles-based B3LYP-D3 (in short, DFT-D) method implemented in the CRYSTAL17 suite code. (*Dovesi et al., 2017, 2018; Lei et al., 2021; Patel et al., 2022; Upadhyay et al., 2022*) Due to the layered nature of $MoTe_2$, the edge terminations in the bulk structure are expected to be similar in atomic composition to those of a single $MoTe_2$ layer. However, electronic properties and chemical reactivity at the edges may still differ due to interlayer interactions and surface reconstruction effects. It has been shown that additional layers decrease the current density due to electron hopping across the layers, such that the top layers are not as active as the bottom layers. Spin-polarized calculations have been incorporated into the computation by defining the electron occupancy (i.e., α for up spin and β for down spin). The spin-polarized solution was obtained using the keywords “ATOMSPIN” and “SPINLOCK” when the DFT-D method was executed in the CRYSTAL17 program. (*Baker, Scheiner and Andzelm, 1993; Pakhira, Lucht and Mendoza-Cortes, 2017*) Compared to the HF method, the DFT method (here, B3LYP-D3) suffers from less or no spin contamination, which helps provide excellent geometry, energy, and electron density calculations. To account for non-bonded weak van der Waals (vdW) interactions between atoms and different layers, we incorporate the semi-empirical Grimme's third-order dispersion correction (Grimme's-D3) in our calculations to obtain accurate equilibrium geometries. (*Ehrlich et al., 2011; Caldeweyher, Bannwarth and Grimme, 2017*) In order to accurately capture the electronic and structural properties of the

system under investigation, we have employed the density functional theory with dispersion correction (DFT-D) method, specifically the B3LYP-D3 variant, to account for exchange-correlation effects. (Upadhyay and Pakhira, 2021a; Pakhira, Kumar and Ghosh, 2023)

During calculations in the CRYSTAL17 program, a Gaussian-type of atomic basis set (GTO) has been used for all atoms as this code uses only the Gaussian-types of atomic basis sets for quantum mechanical calculations. This basis set offers a more efficient alternative to the plane-wave basis set for hybrid DFT calculations. Gaussian-type basis sets are widely used in quantum chemistry calculations due to their flexibility in accurately describing the electron density around atomic nuclei. (Lei *et al.*, 2021; Upadhyay and Pakhira, 2022; Pakhira, Kumar and Ghosh, 2023) They are especially useful for hybrid DFT calculations, which incorporate local and non-local exchange-correlation effects, as they compromise computational cost and accuracy. In comparison, plane-wave basis sets require larger cut-off energies and k-point sampling to achieve similar accuracy in hybrid DFT calculations, which can result in higher computational expenses. In the context of hybrid density functionals, localized Gaussian type of basis set-based codes are better suited for solving the HF component of the calculation. Gaussian basis sets can handle a wide range of system sizes and molecular geometries, making them a versatile choice for various computational chemistry studies. In this study, we have employed triple- ζ valence polarized (TZVP) Gaussian-type basis sets for both the Mo and Te atoms. (Laun and Bredow, 2022) We set the value of convergence threshold for evaluating forces, electron density, and energy to 10^{-7} atomic units (a.u.), ensuring accurate and precise results. Gaussian-type basis sets are particularly well-suited for describing the electron density around atomic nuclei, making them a popular choice for quantum solid state chemistry calculations. To prevent any interactions between the slabs and their periodic images, we have implemented a vacuum space of approximately 500 Å in the z-direction of the simulated cells. The standard convention adopted in CRYSTAL17 suite code with a specific keyword “SLAB” considers the reference 500 Å vacuum space for the 2D layer structure calculations. This approach differs from the plane-wave codes (e.g., VASP, Quantum Espresso, etc.); however, both reach similar results. 20 Å or 30 Å vacuum space is generally allowed in the VASP software package, which is completely different from the

CRYSTAL17 code. Moreover, taking the vacuum region of 500 Å provides more accuracy in computations because there is no possibility of any kind of interaction of other layers in the z-direction during the calculations. (Huang et al., 2015; Ekka et al., 2022; Pakhira and Upadhyay, 2022; Kumar and Pakhira, 2023; Pakhira, Kumar and Ghosh, 2023)

Using the same level of theory, we have conducted electronic property calculations at the optimized structure of the 2D monolayer MoTe₂ TMD material. To accurately capture the electronic properties of the system, we have employed Monkhorst k-mesh grids with a size of $20 \times 20 \times 1$ to compute the 2D electronic layer structure, geometry, band structure, and total density of states. (Evarestov and Smirnov, 2004) The use of k-mesh grids allows for a thorough sampling of the Brillouin zone, ensuring accurate results. We calculated eight electronic bands around the Fermi energy level in the high-symmetry Γ – M – K – Γ direction within the first Brillouin zone. To accurately capture the electronic states of the 2D monolayer MoTe₂ TMD material, we have considered all the atomic orbitals of both Mo and Te atoms in calculating the total density of states (DOSs). The electronic band structures and DOS have been estimated with respect to the vacuum to account for the effects of the electrostatic potential. The equilibrium 2D monolayer structure of MoTe₂ TMD has been shown using VESTA, a visualization program. (Momma and Izumi, 2011)

5.2.2. Finite non-periodic molecular cluster modelling

We have computationally designed a Mo₁₀Te₂₁, non-periodic finite molecular cluster model system of the 2D single layer MoTe₂ TMD, as shown in Figure 5.1, to find out the HER mechanisms with equilibrium structures, geometries, molecular properties and reaction barriers. This Mo₁₀Te₂₁ cluster model system consists of 10 Mo atoms and 21 Te atoms representing the parent MoTe₂ periodic slab structure, as shown in Figure 5.1. The right triangle represents non-periodic finite cluster models terminating along the Te-edge ($\bar{1}010$), and the inverted triangle corresponds to non-periodic cluster models terminating along the Mo-edge ($10\bar{1}0$). In the finite molecular cluster model system, which has been considered in the present investigation, each Mo atom in the basal plane (001) has a “+4” oxidation state and each Mo atom forms six bonds with six adjacent Te atoms. Due to this configuration, a stabilized structure results in each Mo–Te bonding having $4/6 = 2/3$ electron contributions in the inert basal plane. The stabilization of the molecular cluster

model also can be understood from the oxidation state of Te atoms in the basal plane. Each Te atom has a “-2” oxidation state and creates bonding with 3 Mo atoms, contributing $2/3$ electrons towards each Mo–Te bonding in the basal plane. Again, the edges of the molecular cluster model are stabilized with the 2 local electron Mo–Te bonds with a single electron contribution towards four Mo–Te bonds in the basal plane, as shown in Figure 5.1. This $14/3$ {i.e., $(2 \times 1) + [4 \times (2/3)]$ } contribution of electrons towards the Mo–Te bonds of the edge Mo atom are satisfied with the d^2 configuration of one Mo atom and the d^1 configuration of two Mo atoms at the edges. With this configuration, a stabilized molecular cluster model with periodicity 3 is achieved that derives the molecular cluster model having three edges without any unsatisfied valency. Thus, we have considered a molecular cluster $\text{Mo}_{10}\text{Te}_{21}$ model system (noted by $[\text{MoTe}_2]$) to represent the Te-terminated Mo-edges on the surfaces of 2D monolayer MoTe_2 TMD, as shown in Figure 5.1, and this $\text{Mo}_{10}\text{Te}_{21}$ molecular cluster model system is good enough to explain the HER process. (Huang *et al.*, 2015)

This molecular cluster model system allows us to investigate the unique properties and potential applications of the 2D monolayer MoTe_2 TMD. The development of the finite molecular cluster model has computationally been built in such a way that it has the same chemical properties as the periodic 2D slab of MoTe_2 TMD. We have used the M06-L DFT method to determine the reaction barriers, kinetics, and bond energies. This method provides more flexibility and accuracy while using molecular clusters and gives very precise results for the HER calculations. It is computationally easy to use a cluster model with net charges, which is not possible to consider in the case of a periodic system using the CRYSTAL17 suite code. Several studies have investigated the performance of the HER of the MoTe_2 TMD using periodic GGA calculations implemented in VASP, typically employing slab models to analyze adsorption energies, reaction barriers, and electronic structure modifications. (Wang *et al.*, 2017; Huang *et al.*, 2025) While these studies provide valuable insights into HER catalysis, they do not explicitly capture the stepwise electron transfer (ET) and proton transfer (PT) processes or their dependence on electrochemical potential and pH. Such mechanistic details are critical for a comprehensive understanding of the reaction pathways. It should be mentioned here that explicitly solvent phase calculations with the reaction barriers and solvation effects have not been studied yet. To

address these limitations, we have employed a finite molecular cluster model system in this study, which offers significant advantages over periodic slab models. One key distinction is that the periodic DFT-D calculations implemented in CRYSTAL or VASP do not support stepwise ET and PT analysis, which is essential for accurately describing the HER mechanism. Instead, we have utilized Gaussian 16, which allows for detailed proton-coupled electron transfer (PCET) calculations, enabling us to track separate ET and PT steps. This approach provides deeper mechanistic insights, as it accurately models reaction intermediates, captures charge redistribution, and allows for the computation of free energy changes as a function of electrochemical potential and pH. Additionally, the cluster model allows explicit treatment of net charges, which is computationally challenging in periodic systems. This capability enables the incorporation of electrons (e^-) and protons (H^+) at various reaction steps, facilitating a more accurate representation of electrochemical conditions. Incorporation of simultaneous electrons (e^-) and protons (H^+) while performing the chemical reaction studies of various steps in the HER becomes very easy when the molecular cluster model is used.

We have used a periodic 2D slab model of the 2D monolayer $MoTe_2$ to study the electronic properties, i.e., electronic band structure, electronic band gap (E_g), the position of the Fermi energy level (E_F) in the electronic band structure and total density of states (DOS), and we have designed a molecular cluster model ($Mo_{10}Te_{21}$) of the 2D monolayer $MoTe_2$ to explore the HER mechanism. This molecular cluster model system allows us to investigate the unique properties and potential applications of the $MoTe_2$ TMD. The development of the finite molecular cluster model was done in such a way that it has the same chemical properties as the periodic 2D slab of $MoTe_2$ TMD. We have used the M06-L DFT method to determine the reaction barriers, kinetics, and bond energies. This method provides more flexibility and accuracy while using molecular clusters and gives very precise results for the HER calculations. It is easy to use a cluster model with net charges, which is not possible to consider in the case of a periodic system using the CRYSTAL17 suite code. Incorporation of simultaneous electrons (e^-) and protons (H^+) while performing the chemical reaction studies of various steps in the HER becomes very easy when the molecular cluster model is used. The molecular cluster model system has computationally been designed in such a way so that it consists of properties similar to those of the periodic

2D monolayer MoTe₂ TMD. For the validation of the molecular cluster model system Mo₁₀Te₂₁, which has the same chemical properties as the 2D monolayer periodic slab Mo-edges of the MoTe₂ TMD, we have calculated the hydrogen adsorption energies for the molecular cluster model system and periodic 2D monolayer slab both under vacuum conditions. The calculated values of hydrogen adsorption energies for both systems are almost equal. Figure 5.2 shows that the hydrogen binding energies are calculated by using both the finite molecular cluster model system and the periodic 2D slab structure of the subject material. Thus, it can be mentioned here that the molecular cluster model system has the same chemical properties as the periodic 2D MoTe₂ TMD. A similar cluster model system for other TMDs or Janus TMDs, such as MoS₂, WS₂, MoSSe, WSSe, W_xMo_{1-x}S₂, etc., has been considered in previous theoretical and experimental studies.*(Huang et al., 2015; Lei, Pakhira, Fujisawa, Wang, Iyiola, Perea López, et al., 2017; Liang et al., 2018; Pakhira and Upadhyay, 2022; Kumar and Pakhira, 2023)* The DFT-M06-L method was used to study the HER mechanism on the active surface of MoTe₂ through the Mo₁₀Te₂₁ finite molecular model. A previously reported report says that the DFT-M06-L method gives authentic energy barriers for reaction mechanisms of transition metal-based catalysts.*(Zhao and Truhlar, 2006, 2008; Garza et al., 2018; Niu et al., 2018)* For all the calculations, we have used 6-31+G** (double- ζ Pople-type) basis sets for O*(Warren J Hehre, Ditchfield and Pople, 1972)* and H*(Ditchfield, Hehre and Pople, 1971)* atoms and LANL2DZ basis sets for Mo*(P. Jeffrey Hay and Wadt, 1985)* and Te*(Wadt and Hay, 1985)* atoms with effective core potentials (ECPs) and include the solvent effect of water by utilizing the polarizable continuum model (PCM).*(Lipparini and Mennucci, 2016)* For the PCM calculations, water has been taken as a solvent with a dielectric constant of 80.13.*(Uematsu and Frank, 1980)* PCM is one of the best models to consider the solvation effects, and it is a commonly used method in computational quantum chemistry to model solvation effects.

All periodic DFT calculations, including geometry optimizations and electronic structure calculations, are performed at 0 K within the framework of DFT-D methods. However, the thermodynamic analysis, based on the non-periodic finite molecular cluster model, has been conducted at room temperature (298.15 K) to incorporate thermal energy contributions into the reaction energetics. To account for temperature effects, we have

performed a harmonic vibrational analysis at 298.15 K using the Gaussian 16 software package. This approach allows us to include zero-point vibrational energy (ZPE), enthalpic, and entropic contributions in our free energy calculations, which are crucial for understanding reaction thermodynamics under experimental conditions. By incorporating these thermal effects, we ensure that key parameters such as adsorption energies, reaction barriers, and transition states (TSs) accurately represent the material's behavior at room temperature rather than at absolute zero. Thus, while our periodic DFT simulations provide fundamental electronic and structural insights at 0 K, our thermodynamic calculations at 298.15 K bridge the gap between theoretical predictions and practical experimental conditions. This approach enhances the reliability of our findings for real-world applications.

The ZPE and frequencies are calculated using the same methods and basis sets at the optimized geometry of all the intermediates. TSs have been observed and confirmed by obtaining only one imaginary frequency (negative value) in the modes of vibrations. All the computations are performed with the general-purpose electronic structure quantum chemistry program Gaussian16 to obtain the optimized geometries and TSs to explain the HER mechanism.*(Frisch, Trucks, Schlegel, Scuseria, Ma, Robb, et al., 2016)* All the TS structures are computed using the optimized geometries, and ChemCraft software is used to visualize them.*(Andrienko, 2010)* In this study, all the transition states have been verified by analyzing the vibrational frequencies and the intrinsic reaction coordinates (IRCs).*(Pakhira et al., 2016)*

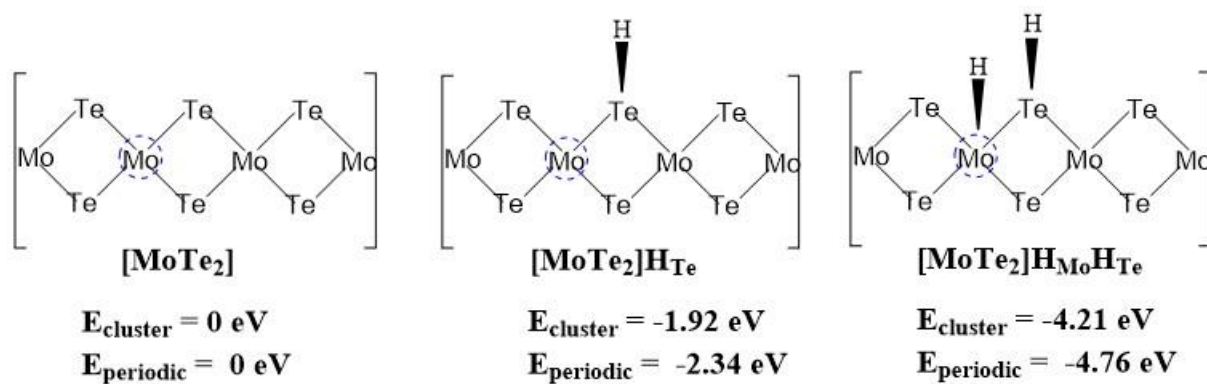


Figure 5.2: Hydrogen adsorption energies on the 2D monolayer $MoTe_2$ TMD. $E_{cluster}$ represents the relative electronic energy during hydrogen adsorption considering the molecular cluster model system and $E_{periodic}$ is the relative electronic energy obtained from the periodic 2D layer calculations.

5.3. Results and Discussion

5.3.1. Structural and electronic properties

The main objective of this work is to find the equilibrium 2D monolayer structure of $MoTe_2$ TMD belonging to the 2H phase and find the electrocatalytic activity of the same TMD. The equilibrium 2D monolayer structure of 2H- $MoTe_2$ TMD is shown in Figure 5.3, obtained by the DFT-D method. By using VESTA software, a 2D monolayer $MoTe_2$ primitive cell was developed, and its structure was optimized by using the first principles-based periodic dispersion-correction hybrid DFT (DFT-D3) method, as displayed in Figure 5.3. The layer slab structure of the 2D monolayer $MoTe_2$ TMD material belongs to the trigonal symmetry with a $P\bar{6}m_2$ layer group number in the symmetry table. The unit cell of the material is defined by the lattice parameters $a = b = 3.40 \text{ \AA}$, which is in excellent agreement with previously reported values. (Dawson and Bullett, 1987) Each unit cell consists of one Mo and one Te atom, as shown in Figure 5.3. The equilibrium bond length between Mo and Te atoms has been found to be 2.66 \AA . The electronic characteristics have been examined by calculating and examining the electronic band structure and density of states (DOS) of the 2D single-layer $MoTe_2$ TMD. Analysis of the electronic properties can be useful in obtaining information about electron distribution on the catalytic surface, which is useful for fully understanding the electrocatalytic performance of the TMD.

We have used the DFT-D technique to calculate the equilibrium electronic properties of the 2D single-layer MoTe₂ TMDs at equilibrium geometries. The electronic band structure, energy gap (E_g), Fermi level (E_F), and DOS are all computed using the same level of DFT method and are one of the main subjects of our investigation in the present work. This made it possible for us to explore and comprehend the electronic characteristics of the 2D monolayer pristine MoTe₂ TMD consistently. We have computed the electronic band structures of 2D monolayer MoTe₂ along the Γ – M – K – Γ band pathway (which is the high symmetric k-path direction consisting of the original symmetry of the 2D slab MoTe₂ TMD) with respect to the vacuum, taking into account the initial symmetry of the subject material. The corresponding results are presented in Figure 5.3b. This approach enabled us to gain valuable insights into the electronic properties of the 2D single-layer MoTe₂ TMD systematically and accurately. In our electronic band structure calculations around the E_F of the 2D monolayer MoTe₂, we took into account the number of four valence bands (VBs) and four conduction bands (CBs), as depicted in Figure 5.3b. Our computations revealed that the E_F of MoTe₂ is located at –4.50 eV, and the material exhibits a direct band gap of approximately 1.65 eV at the K point, which is much lower than the pristine monolayer MoS₂ 2D TMD. Notably, this finding is consistent with earlier reported data, confirming the accuracy and reliability of our calculations. (Kanoun, 2019) We have estimated the DOS of the monolayer MoTe₂ using the same theoretical framework in order to further study its electrical characteristics. The resultant DOS, which corresponds to the electronic band structures of the pure 2D monolayer MoTe₂, has been displayed in Figure 5.3c. The electronic bandgap E_g of the 2D monolayer MoTe₂ TMD has been determined by our DOS calculations to be around 1.65 eV, which is consistent with the direct band gap found at the K point in the band structure calculations. Thus, it is abundantly clear from our calculations of the electronic properties that the pure 2D monolayer MoTe₂ is a semiconductor with a recognizable bandgap, which may be useful for electrocatalytic activities toward H₂ evolution. The same DFT-D method obtained the intrinsic electronic and structural properties at the equilibrium geometries. After obtaining the equilibrium structure (see Table 5.1), we have computed the electronic properties of the 2D slab structure of the monolayer MoTe₂ TMD by employing the B3LYP-D3 method. These findings are crucial for understanding the catalytic performance of the catalyst and

finding a suitable electrocatalyst for the hydrogen evolution reaction. The stability of the material has been confirmed by computing the thermodynamic potentials, and the computations are consistent with the previously reported values. The results provide valuable insights into the electronic properties of 2D MoTe_2 and its potential applications in electrocatalysis.

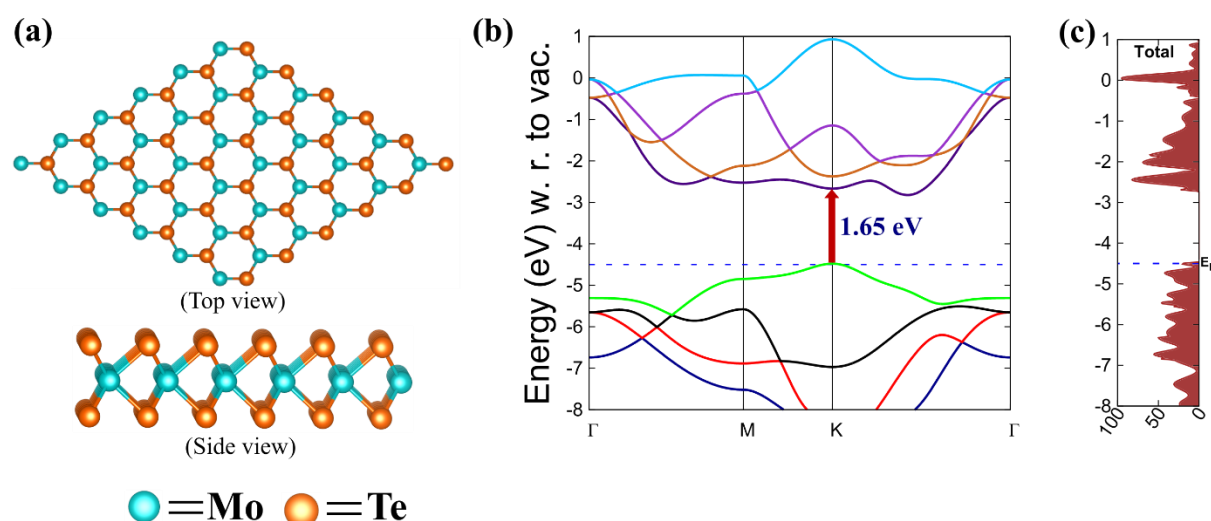


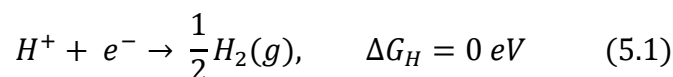
Figure 5.3: (a) The top view and side view of the 2D monolayer MoTe_2 TMD; (b) electronic band structure and (c) total density of states (DOSs) of the 2D monolayer MoTe_2 TMD, obtained by the B3LYP-D3 DFT method.

Table 5.1: The average equilibrium bond length of the 2D monolayer MoTe_2 with optimal equilibrium lattice parameters obtained by the DFT-D method.

Materials	Lattice parameter (in Å)	Bond angles (in °)	Bond distance Mo-Te (in Å)	Thickness (in Å)	Band Gap (in eV)	References
MoTe_2 (Previously reported)	$a = b = 3.51$	$\alpha = \beta = 90$ $\gamma = 120$	2.71	3.60	1.15	(Dawson and Bullett, 1987)(Kanon, 2019)
MoTe_2	$a = b = 3.40$	$\alpha = \beta = 90$ $\gamma = 120$	2.66	3.59	1.65	This work

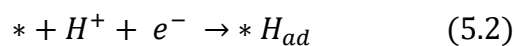
5.3.2. HER Pathway

The HER, which takes place at the cathode of an electrolyzer, is a half-reaction in which protons (in an acidic environment) are reduced, followed by the generation of gaseous hydrogen via the water-splitting process. The overall HER pathway can be described by equation (5.1) (Gao, O'Mullane and Du, 2017)

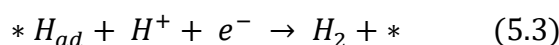


V–H or V–T are two possible methods to take place in the HER. For the purpose of providing an intermediate state (adsorbed H*) of the processes, it occurs at an electrode in an acidic medium:

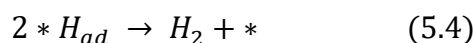
- (i) The Volmer reaction occurs when a proton and an electron combine on the electrode surface to form a hydrogen atom (proton discharge):



- (ii) Electrochemical desorption occurs when the adsorbed hydrogen atom interacts with a proton and an electron, and finally it forms H₂. The Heyrovsky reaction is as follows:



- (iii) The Tafel reaction results from the coupling of the two hydrogen atoms that have been adsorbed:



The aforementioned fundamental processes result in the V–H and V–T mechanisms. Volmer, Heyrovsky, and Tafel are three rate-determining steps (RDS) that can be used with the aforementioned two reaction mechanisms or methods. Equation (5.1) can be used to explain the overall HER route during standard conditions. It includes the beginning state, H⁺ + e[−], the intermediate, adsorbed H*, and the ultimate result, 1/2H₂ (g). The sum of the energies of 1/2H₂ (g) and H⁺ + e[−] is the same. As a result, the change of Gibbs free energy

of the intermediate hydrogen adsorption on a catalyst (ΔG_H^*), which can be calculated using Equation (5.5), is a crucial indicator of the HER activity of the catalyst.

$$\Delta G_H = \Delta E_H + \Delta E_{ZPE} - T\Delta S_H \quad (5.5)$$

where ΔE_{ZPE} and ΔS_H stand for the disparity between the zero-point energy of atomic hydrogen adsorption and hydrogen in the gas phase, respectively, and entropy. ΔE_H is the electronic energy of H upon adsorption. Both the values of ΔE_{ZPE} and ΔS_H are negligible and underappreciated catalytic contributions. Equation (5.5) can finally be condensed into Equation (5.6): (Gao, O'Mullane and Du, 2017)

$$\Delta G_H = \Delta E_H + 0.30 \text{ eV} \quad (5.6)$$

In this work, we have systematically applied ZPE corrections across all calculations to capture the vibrational contributions of adsorbed hydrogen species and reaction intermediates. These corrections are essential for providing a realistic representation of HER thermodynamics, particularly at room temperature (298.15 K). The adsorption stage will restrict the rate of the overall reaction if the hydrogen-to-surface connection is too weak. The reaction-desorption stage will cap the rate of the total reaction if the hydrogen-to-surface connection is too strong. Hydrogen adsorption energies of ideal HER catalysts are near $\Delta G_H = 0$, binding hydrogen neither too weakly nor too strongly.

We have used a finite non-periodic cluster model $\text{Mo}_{10}\text{Te}_{21}$ system for the present work to explore the HER. In this cluster, we have calculated the adsorption energy of hydrogen on the surface of the catalyst. The site which is more active for hydrogen adsorption will favor the adsorption of hydrogen easily. We have calculated hydrogen adsorption at both the sites, Te and Mo. First, we calculated hydrogen adsorption free energy at the Te site, which resulted in the formation of $[\text{MoTe}_2]\text{H}_{\text{Te}}$ as an intermediate (where the subscript Te indicates that the hydrogen is bound to the Te atom) with free energy change (ΔG) of -1.92 eV . The equilibrium bond length of the Te–H in the equilibrium structure of the intermediate $[\text{MoTe}_2]\text{H}_{\text{Te}}$ is 1.67 \AA . Here, we found a negative change in free energy, meaning hydrogen strongly bonds with the Te atom. Now, we also calculated hydrogen adsorption at the Mo site and found that the change in free energy (ΔG) is -1.78 eV . The equilibrium bond length of the Mo–H in the intermediate

[MoTe₂]H_{Mo} is 1.72 Å. At both sites Te and Mo changes in free energy are negative. But at the Te site, the change in free energy is slightly more negative compared to the Mo site. So, the first H energetically prefers to form a bond with the Te atom, as the direct hydrogen adsorption at the Mo-edge site is not thermodynamically favorable in the early stage of the HER.

Inspired by previous works on 2D TMDs towards the HER, 2D single-layer MoTe₂ is highly expected to enhance the electrochemical HER performance and stability of the system by the overlapping of d-orbitals of the Mo and p-orbitals from Te and provide an alternate way to tune and control the electronic and material properties of the subject material. The purpose of this paper is to suggest the synthesis and predict the properties of 2D single-layer MoTe₂ as this 2D material studied here has not been synthesized experimentally and has not been experimented with for the HER and electrochemical performances. However, the calculated vibrational frequencies and binding energies predict that the subject material is thermodynamically stable. The harmonic frequency analysis and binding energy have been shown to be enough to demonstrate material stability and a posteriori synthesis in previous works on 2D TMDs followed by our published research works. (Lei, Pakhira, Fujisawa, Wang, Iyiola, Perea López, *et al.*, 2017; Liang *et al.*, 2018; Pakhira and Upadhyay, 2022; Kumar and Pakhira, 2023) Thus, we expect this 2D single layer MoTe₂ to be readily fabricated experimentally and it can be used as an efficient electrocatalyst towards the HER.

In our study, we calculated the hydrogen adsorption energy on MoTe₂ to be -1.92 eV, which contrasts with the previously reported value of 2.15 eV. (Wang *et al.*, 2017) The discrepancies between our results and previously reported values can be attributed to several factors. First, our study has utilized a finite cluster model (Mo₁₀Te₂₁) to represent edge-specific properties, which differ inherently from the periodic models used in other studies. This difference in model choice affects the adsorption characteristics due to the localized nature of edge-specific interactions in the cluster model.

The optimal performance of a catalyst toward the HER is governed by its ability to adhere to the Sabatier principle. A good catalyst should not bind too strongly to reagents and intermediates, as this would inhibit desorption and impede the catalytic cycle.

Simultaneously, it should bind moderately enough to facilitate effective adsorption and subsequent reaction of the reagents on its surface. According to the Sabatier principle, the ideal catalyst achieves a delicate balance between adsorption and desorption energies. (Laursen *et al.*, 2012) Our theoretical study supports this principle by demonstrating a moderate binding energy that ensures efficient adsorption of hydrogen while allowing easy desorption of the products. To study the HER performance of 2D monolayer MoTe₂ materials, we created a finite non-periodic cluster model system of Mo₁₀Te₂₁. The HER process is being studied from several angles, including reaction pathways, thermodynamics, chemical kinetics, transition state structures, and reaction barriers. Figure 5.4 and 5.7 show the V–H and V–T mechanisms that we looked at in order to assess the HER pathways. We can determine the rate-limiting steps by calculating the intermediates and transition states during the production of H₂ and by looking at the energy barriers of particular reaction steps. The electrocatalytic properties of the 2D monolayer MoTe₂ material have been underexplored, which motivated our study to predict the most dominant HER mechanisms for these kinds of TMD materials by analyzing the proposed reaction pathway for both the V–H and V–T mechanisms.

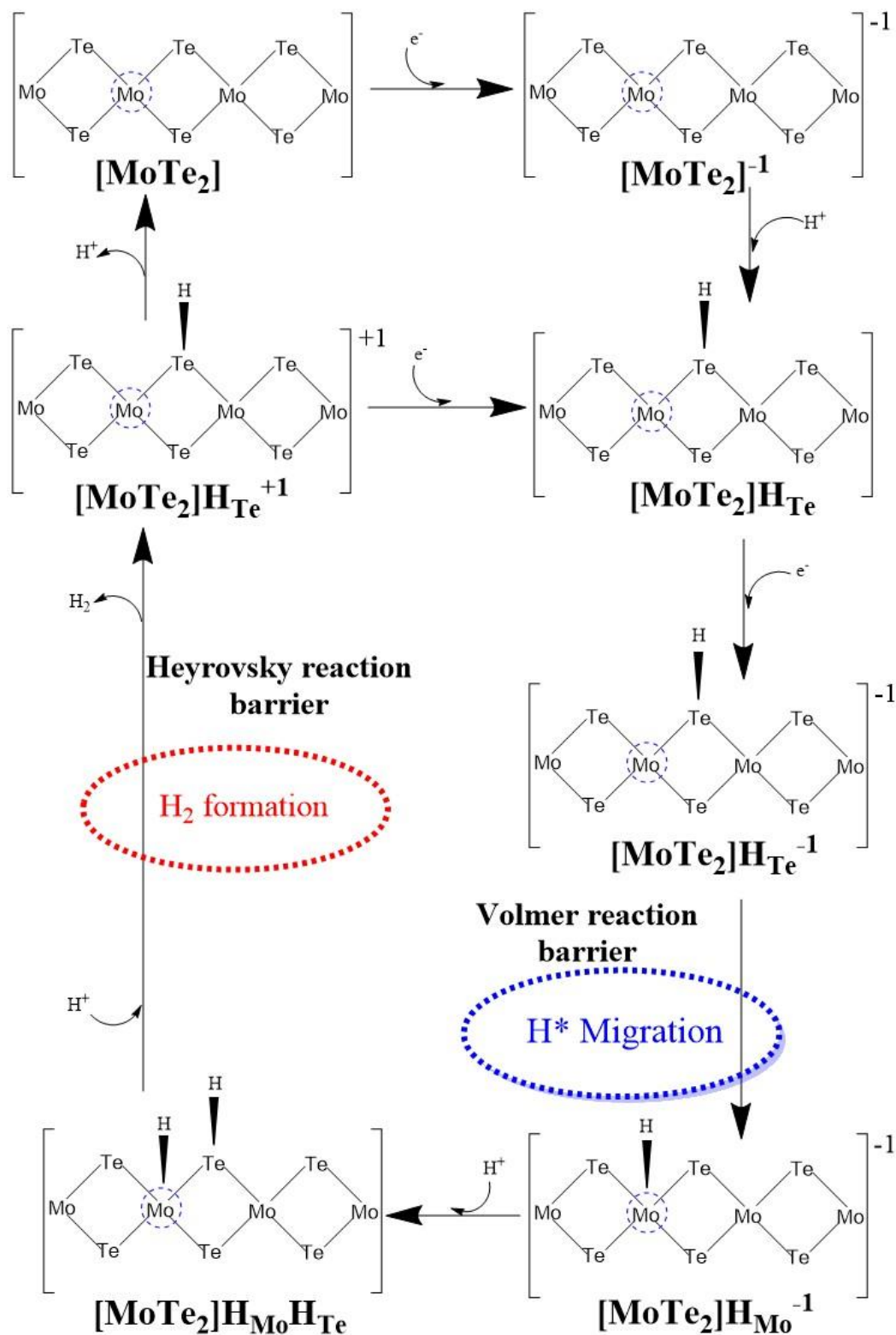


Figure 5.4: Volmer–Heyrovsky HER mechanism of the detailed two electron transfer reaction pathways on the surface of the 2D MoTe₂ material.

5.3.2.1. Volmer–Heyrovsky reaction mechanism

The HER process on the 2D MoTe₂ TMD material follows the V–H mechanism, which involves a multistep electrode reaction with several intermediate and transition states formed along the reaction pathway. Figure 5.4 provides a schematic representation of this process, depicting the possible intermediate and transition states formed during the reaction. In this mechanism, the electrocatalyst simultaneously absorbs protons (H⁺) and electrons (e[−]) during the Volmer reaction. Then, during the Heyrovsky reaction step, H₂ is formed with one proton from the nearby hydronium ion (H₃O⁺) and H* at the transition metal site in the MoTe₂ TMD. To facilitate the whole H₂ development process, individual electrons and protons are introduced throughout the HER process. We looked at the stable structures of the non-periodic finite cluster model of the 2D monolayer MoTe₂ TMD (Mo₁₀Te₂₁) with sequential additions of each extra electron (e[−]) and proton (H⁺) in order to comprehend the fluctuation of free energy between intermediates and identify the pathway with the lowest reaction barrier. The following describes the precise chemical reactions that make up this suggested HER route:

- (1) The [MoTe₂] material can be found in its most stable state with a neutral Mo-edge under typical circumstances of the standard hydrogen electrode (SHE) at pH = 0, which serves as the starting point for our estimates of the thermodynamic potential. [MoTe₂] represents the abbreviation for the finite molecular cluster Mo₁₀Te₂₁. Figure 5.5a shows the equilibrium structure of the [MoTe₂] material.
- (2) The [MoTe₂] material absorbs an electron onto its surface to start the HER process, which produces a negatively charged cluster of [MoTe₂]^{−1} that is solvated in water and has a delocalized electron on its surface. The DFT technique yielded a value of roughly −424.97 mV for the first reduction potential of the suggested chemical pathway, which entails generating [MoTe₂]^{−1} from the pure [MoTe₂] by introducing a single electron. Figure 5.5b shows the equilibrium geometry of [MoTe₂]^{−1}.

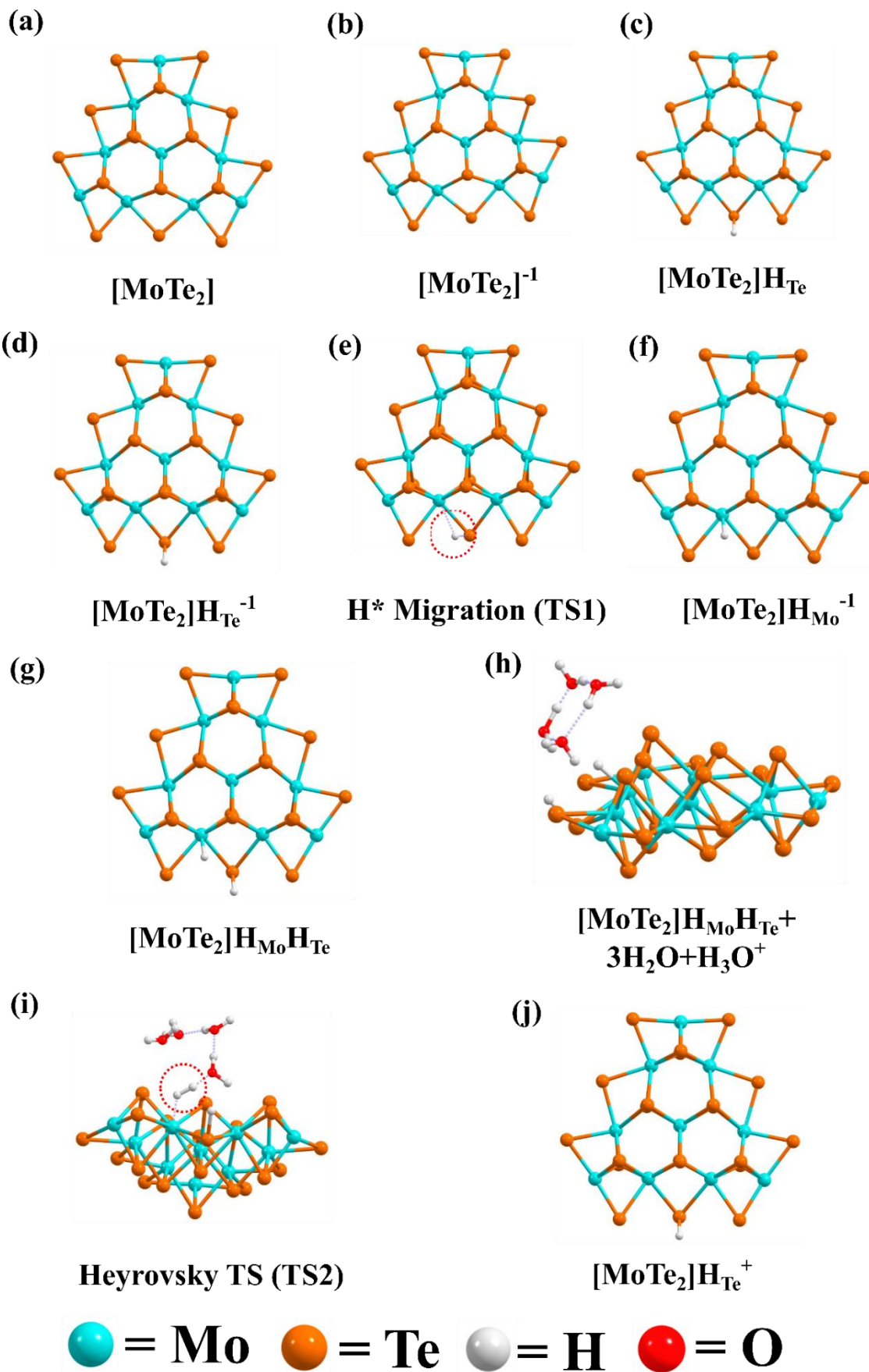


Figure 5.5: The equilibrium geometry of important reaction intermediates and TSs: (a) $[\text{MoTe}_2]$, (b) $[\text{MoTe}_2]^{-1}$, (c) $[\text{MoTe}_2]\text{H}_{\text{Te}}$, (d) $[\text{MoTe}_2]\text{H}_{\text{Te}}^{-1}$, (e) H^* -Migration TS (TS1), (f) $[\text{MoTe}_2]\text{H}_{\text{Mo}}^{-1}$, (g) $[\text{MoTe}_2]\text{H}_{\text{Te}}\text{H}_{\text{Mo}}$, (h) $[\text{MoTe}_2]\text{HTeHMo}+3\text{H}_2\text{O}+\text{H}_3\text{O}^+$, (i) Heyrovsky TS (TS2) and (j) $[\text{MoTe}_2]\text{H}_{\text{Te}}^{+1}$ by M06-L calculation shows the DFT method considering the molecular cluster model system $\text{Mo}_{10}\text{Te}_{21}$ to represent the 2D monolayer of MoTe_2 .

- (3) According to a study, [\(Huang et al., 2015\)](#) the first hydrogen atom has a strong preference for binding to the Te-edge rather than the Mo atom. As a result, an intermediate molecule called $[\text{MoTe}_2]\text{H}_{\text{Te}}$ is created when a proton (H^+) is added to the Te-edge, which has an additional electron. The subscript Te denotes the hydrogen atom's bond to the Te atom. The formation of this intermediate incurs an energy cost of approximately $1.93 \text{ kcal mol}^{-1}$. The Te–H equilibrium bond length in the $[\text{MoTe}_2]\text{H}_{\text{Te}}$ intermediate's equilibrium structure is 1.67 \AA . The equilibrium geometry of the complex is depicted in Figure 5.5c.
- (4) A second reduction happens after adding one more electron to the $[\text{MoTe}_2]\text{H}_{\text{Te}}$ intermediate, producing $[\text{MoTe}_2]\text{H}_{\text{Te}}^{-1}$ (as shown in Figure 5.5d). The second reduction potential is roughly equal to -766.68 mV .
- (5) The hydride ion (H^*) moves from the Se-site to the neighboring Mo-site in the following process, creating a TS of $[\text{MoTe}_2]\text{H}_{\text{Te}}^{-1}$. It is the first transition state to arise during the HER process and is known as the H^* -migration reaction or Volmer TS1. In order to locate the TS, a harmonic vibrational frequency analysis was carried out, and IRC calculations were done in order to confirm the existence of TS1. [\(Sahu et al., 2013; Pakhira et al., 2015\)](#) During the transfer of H^* from the Te-site to the Mo-site, it was discovered that this TS1 had a single hypothetical vibrational frequency, i.e., one imaginary frequency. The equilibrium geometry of TS1 is shown in Figure 5.5e. It is interesting to note that the current DFT work found that, when computed in the gas phase, the activation energy barrier for the H^* -migration reaction to create TS1 in the pure 2D monolayer MoTe_2 is about $G = 8.47 \text{ kcal mol}^{-1}$.
- (6) Using the DFT approach, it was found that the energy needed to create the $[\text{MoTe}_2]\text{H}_{\text{Mo}}^{-1}$ complex from TS1 was around $G = -18.69 \text{ kcal mol}^{-1}$. The equilibrium geometry of the system is shown in Figure 5.5f. The Mo–H equilibrium

bond length in the $[\text{MoTe}_2]\text{H}_{\text{Mo}}^{-1}$ intermediate equilibrium structure is about 1.73 Å. The M06-L DFT method was used to calculate the changes in electronic energy (ΔE), relative enthalpy (ΔH), and Gibbs free energy (ΔG) that occurred during the HER process in each of the several reaction stages and are shown in Table 5.2.

Table 5.2: Relative electronic energy (ΔE), enthalpy (ΔH), and free energy (ΔG) for various intermediates and transition states (TSs) during the HER process followed by the Volmer–Heyrovsky reaction mechanism are computed in the gas phase

	HER Reaction Intermediates	ΔE (kcal.mol ⁻¹) Gas Phase	ΔH (kcal.mol ⁻¹) Gas Phase	ΔG (kcal.mol ⁻¹) Gas Phase
1	$[\text{MoTe}_2] \rightarrow [\text{MoTe}_2]^{-1}$	10.63	10.57	9.80
2	$[\text{MoTe}_2]^{-1} \rightarrow [\text{MoTe}_2]\text{H}_{\text{Te}}$	-2.04	2.51	1.93
3	$[\text{MoTe}_2]\text{H}_{\text{Te}} \rightarrow [\text{MoTe}_2]\text{H}_{\text{Te}}^{-1}$	17.18	17.05	17.68
4	$[\text{MoTe}_2]\text{H}_{\text{Te}}^{-1} \rightarrow \text{Volmer TS1}$	9.50	8.18	8.47
5	$\text{Volmer TS} \rightarrow [\text{MoTe}_2]\text{H}_{\text{Mo}}^{-1}$	-20.89	-19.14	-18.69
6	$[\text{MoTe}_2]\text{H}_{\text{Mo}}^{-1} \rightarrow [\text{MoTe}_2]\text{H}_{\text{Mo}}\text{H}_{\text{Te}}$	-6.01	-1.25	-1.97
7	$[\text{MoTe}_2]\text{H}_{\text{Mo}}\text{H}_{\text{Te}} \rightarrow$ $[\text{MoTe}_2]\text{H}_{\text{Mo}}\text{H}_{\text{Te}} + 3\text{H}_2\text{O} + \text{H}_3\text{O}^+$	-21.60	-20.82	-6.08
8	$[\text{MoTe}_2]\text{H}_{\text{Mo}}\text{H}_{\text{Te}} + 3\text{H}_2\text{O} + \text{H}_3\text{O}^+ \rightarrow \text{Heyrovsky TS2}$	11.13	9.32	8.85
9	$\text{Heyrovsky TS} \rightarrow [\text{MoTe}_2]\text{H}_{\text{Te}}^{+1}$	-0.95	0.63	-15.34

(7) To form the $[\text{MoTe}_2]\text{H}_{\text{Mo}}\text{H}_{\text{Te}}$ complex, an additional H⁺ from the solvent medium was added to the Te-site of the $[\text{MoTe}_2]\text{H}_{\text{Mo}}^{-1}$ complex, resulting in a complex where one hydrogen is bound to the Mo atom, and the other hydrogen is bound to the Te atom, as shown in Figure 5.5g. According to Table 5.2, the DFT calculation showed that this step cost energy around $-1.97 \text{ kcal mol}^{-1}$. Using the same DFT technique, the equilibrium structure of the $[\text{MoTe}_2]\text{H}_{\text{Mo}}\text{H}_{\text{Te}}$ complex was found to have equilibrium bond lengths of Mo–H around 1.72 Å and Te–H approximately

1.67 Å, respectively. The optimized equilibrium structures of all the intermediates and transition states involved in the HER process are displayed in Figure 5.5.

- (8) For H₂ evolution, the [MoTe₂]H_{Mo}H_{Te} complex can proceed through the Heyrovsky or Tafel reactions. We added a hydronium water cluster (3H₂O + H₃O⁺) close to the active site of the Mo₁₀Te₂₁ non-periodic molecular cluster to aid the Heyrovsky reaction process. The cluster forms the [MoTe₂]H_{Mo}H_{Te} + 3H₂O + H₃O⁺ complex as an intermediate with an energy cost of $\Delta G = -6.08 \text{ kcal mol}^{-1}$ because it has one H at the transition metal Mo site and another H at the Te site. Figure 5.5h depicts the equilibrium structure of the [MoTe₂]H_{Mo}H_{Te} + 3H₂O + H₃O⁺ complex as a reaction intermediate formed during the Heyrovsky reaction step.
- (9) In order to continue with the HER, we formed the second TS known as Heyrovsky's TS2, as depicted in Figure 5.5i. The [MoTe₂]H_{Mo}H_{Te} + 3H₂O + H₃O⁺ intermediate, where the H* from the Mo-site and the H⁺ from the hydronium water cluster combine to produce H₂, which separates from the system, is where the Heyrovsky TS2 is obtained. A red circle with a dot in it appears in Figure 5.5i to represent the generation of H₂ during the reaction in TS2. According to the present calculations accomplished in the gas phase, the activation energy barrier of the Heyrovsky TS2 is approximately $8.85 \text{ kcal mol}^{-1}$.
- (10) After the formation of the Heyrovsky TS2, the system changes into [MoTe₂]H_{Te}⁺, and one H₂ molecule and four H₂O molecules are released with an energy cost of $-15.34 \text{ kcal mol}^{-1}$. As depicted in Figure 5.4, this is where the H₂ molecule emerges through the catalyst's surface, and the reaction process resumes from the beginning by either absorbing one electron or releasing a proton.

As already mentioned, a very promising route for efficient HER of the catalysts containing transition metals is the V–H mechanism.^(Huang *et al.*, 2015) As a result, we concentrated primarily on determining the activation energy barriers for two important saddle points, the H*-migration TS (noted by TS1) and Heyrovsky TS (noted by TS2). According to gas phase calculations, Table 5.2 lists the variations in relative electronic energy (ΔE), enthalpy (ΔH), and free energy (ΔG) that occur during the numerous reaction intermediates and TSs involved in the HER via the Volmer–Heyrovsky reaction route.

A reaction barrier of approximately $\Delta G = 8.47 \text{ kcal mol}^{-1}$ was found in the current investigation for the H^* -migration process or TS1 formation, which was obtained in the gas phase. Corresponding to this, a reaction barrier of $8.85 \text{ kcal mol}^{-1}$ was obtained (in gas phase calculation) during the TS2 formation in the Heyrovsky reaction process at the Mo-edges of the pure 2D monolayer MoTe_2 material. In the case of the pure 2D monolayer MoTe_2 TMD, the Heyrovsky reaction step is likely to be the rate-determining step in the V–H reaction mechanism of the HER process given that the Heyrovsky TS2 has a slightly higher value of reaction barrier than the H^* -migration transition state TS1. The HER pathway followed by the V–H reaction mechanism is shown in Figure 5.6, which shows the fluctuations of relative Gibbs free energies (ΔG) with regard to the reaction coordinates involved in the V–H reaction. The activation energy barriers must also be calculated in the solvent phase because the reactions in commercial fields are typically conducted in solutions. In order to account for the solvent effect of water, the solvent phase calculation was performed using the PCM analysis, and the corresponding reaction barriers were noted down, as described in the Volmer–Heyrovsky mechanism steps above.

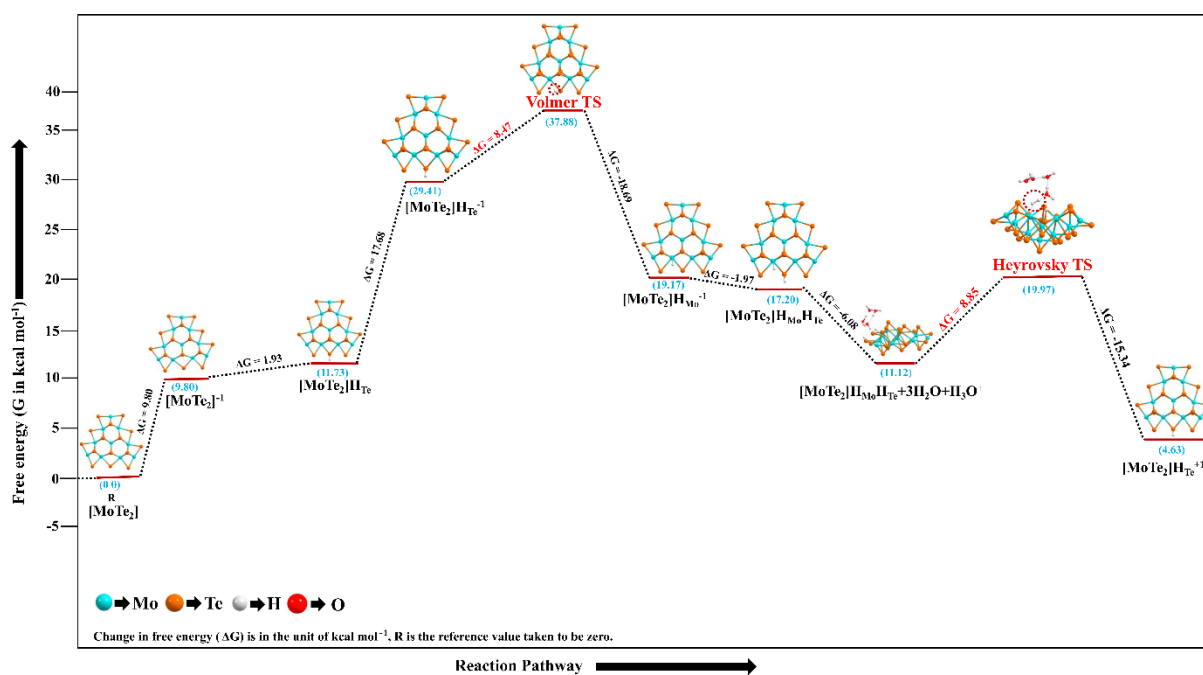


Figure 5.6: The HER pathway followed by the Volmer–Heyrovsky reaction mechanism is shown here as it occurs during the HER process at the surface of the 2D monolayer MoTe_2 material.

We used the PCM analysis in our study to take into account the solvation impact during the HER process. Our DFT-D calculations showed that the energy barrier for the H^* -migration during the formation of TS1 in a water environment was about 9.80 kcal mol⁻¹. In comparison to other pristine TMDs, this 2D MoTe₂ TMD exhibits better hydrogen migration/adsorption capabilities due to its low energy barrier value in both the solvent and gas phases. We estimated the energy barrier of the TS2 to be about 12.55 kcal mol⁻¹ in the solvent phase during the Heyrovsky reaction step for H₂ production and evolution. It is significant to note that this number exceeds the relevant energy barrier determined by calculations in the gas phase. We first investigated the reaction in the gas phase and then carried out solvent phase calculations utilizing the equilibrium geometries of all the reaction intermediates/TSs estimated in the gas phase because, in reality, the HER happens in a solvent phase. The equilibrium geometries of the systems involved in the reaction, which were estimated in the gas phase, were used for the PCM calculations. Usually, the solvent phase has higher reaction barriers than the gas phase. Significant energy changes result from the explicit consideration of the solvent–reactant interaction by the addition of solvent characteristics. Both the gas and solvent phases are two separate phases with totally different characteristics. Several other kinds of chemical bonds and interactions, including hydrogen bonds, ion–dipole interactions, and weak van der Waals (vdW) forces, are created during the solvation process.

5.3.2.2. *Volmer–Tafel reaction mechanism*

In comparison to the V–H reaction mechanism, the V–T reaction mechanism is a simpler two-electron transfer process for the HER. To create molecular hydrogen, two hydrogen atoms that were adsorbed on the catalyst surface must recombine. Due to the lack of additional solvated protons, this reaction pathway is simpler than the V–H reaction mechanism. According to this mechanism, two neighboring adsorbed hydrogen atoms on the catalyst surface combine to generate H₂ without a solvated proton, as demonstrated by the reaction $H^* + H^* \rightarrow H_2$. The catalyst surface, where this reaction occurs, gets the energy from the room temperature (298.15 K) which is required to break through the activation energy barrier by forming TS noted by Tafel TS. Ultimately, the V–T reaction mechanism is a straightforward but significant process that takes place on a catalyst surface. It must be

understood and optimized to create effective and long-lasting electrochemical processes. Figure 5.7 shows the general reaction steps of the V–T reaction mechanism involved in this indicated process.

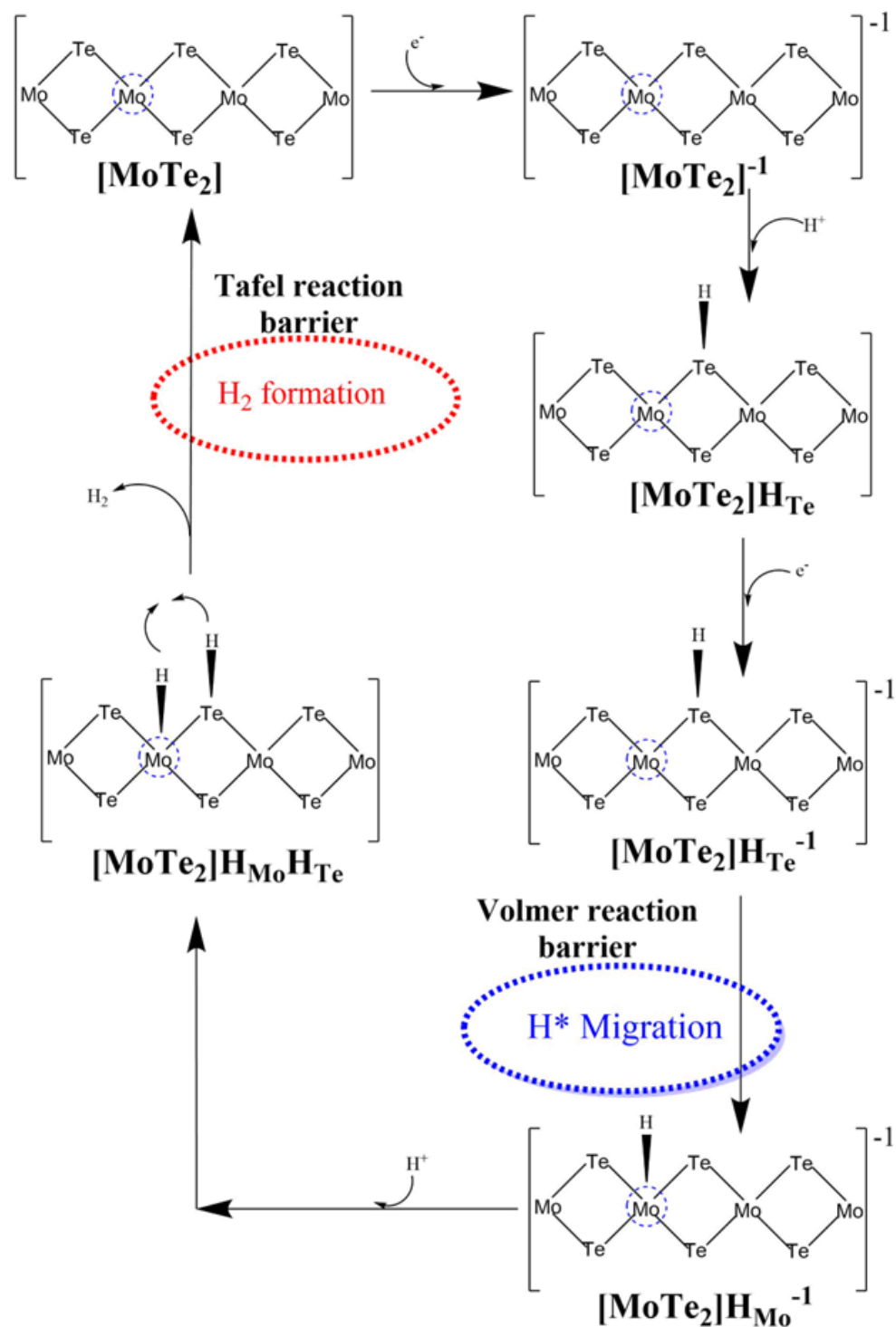


Figure 5.7: Volmer–Tafel HER mechanism with the detailed two-electron transfer reaction pathway on the surface of the 2D MoTe₂ material.

- (1) The $[\text{MoTe}_2]\text{H}_{\text{Mo}}^{-1}$ intermediate turns into an $[\text{MoTe}_2]\text{H}_{\text{Mo}}\text{H}_{\text{Te}}$ intermediate by taking an additional proton (H^+), and here is the place of H_2 evolution where the Volmer–Tafel process diverges from the V–H mechanism. This phase has a -1.97 kcal mol⁻¹ energy cost, which is consistent with the V–H mechanism pathway. This intermediate, which acts as the starting point for the creation of molecular hydrogen, is essential to the overall reaction mechanism.
- (2) The interaction of two adsorbed hydrogen atoms, one at the Mo-site and the other at the Te-site, during the HER, leads to the formation of H_2 , which is a result of the Tafel reaction. A TS3 is created as a result of this reaction, and it has a single imaginary frequency, an equilibrium Mo–H bond length of 1.73 Å, an equilibrium Te–H bond length of 1.68 Å, and a final H–H bond length of roughly 1.74 Å. Using the M06-L DFT approach, it was discovered that the energy barrier of TS3 in the gas phase is 6.07 kcal mol⁻¹. Figure 5.8 illustrates the TS3's equilibrium geometry and schematic representation. Additionally, using the same level of theory, it was determined that the energy barrier of TS3 for H_2 evolution during the Tafel reaction step is approximately 5.29 kcal mol⁻¹ obtained in the solvent phase calculations (water). These findings suggest that the energetics and kinetics of the Tafel reaction are strongly influenced by the solvent environment.
- (3) The last stage of the V–T mechanism, $[\text{MoTe}_2]$, is reached once Tafel TS3 is generated. As indicated in Table 5.3, one H_2 molecule is produced from the catalyst's surface in this step, requiring -23.34 kcal mol⁻¹ of free energy. The HER process is finished with the development of H_2 , giving it an ideal avenue for the creation of clean and sustainable energy.

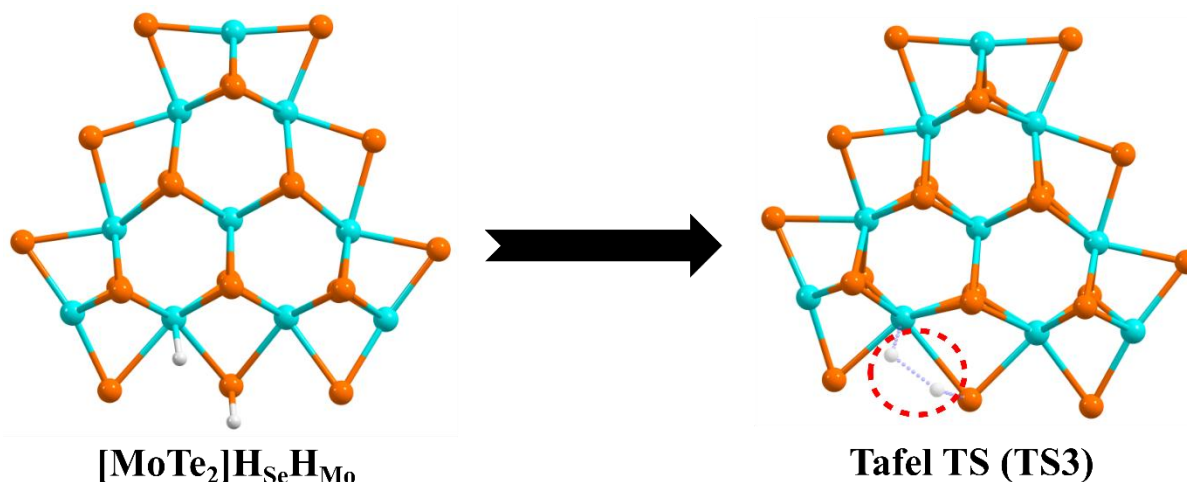


Figure 5.8: The Volmer–Tafel reaction mechanism equilibrium geometries of [MoTe₂]H_{Mo}H_{Te} and TS3 are shown here.

Table 5.3: Below are tabulated energy changes (ΔE , ΔH , and ΔG) for various intermediates and transition states (TSs) during calculations of the Volmer-Tafel reaction mechanism in the gas phase.

	HER Reaction Intermediates	ΔE (kcal.mol ⁻¹) Gas Phase	ΔH (kcal.mol ⁻¹) Gas Phase	ΔG (kcal.mol ⁻¹) Gas Phase
1	[MoTe ₂] → [MoTe ₂] ⁻¹	10.63	10.57	9.80
2	[MoTe ₂] ⁻¹ → [MoTe ₂]H _{Te}	-2.04	2.51	1.93
3	[MoTe ₂]H _{Te} → [MoTe ₂]H _{Te} ⁻¹	17.18	17.05	17.68
4	[MoTe ₂]H _{Te} ⁻¹ → Volmer TS1	9.50	8.18	8.47
5	Volmer TS → [MoTe ₂]H _{Mo} ⁻¹	-20.89	-19.14	-18.69
6	[MoTe ₂]H _{Mo} ⁻¹ → [MoTe ₂]H _{Mo} H _{Te}	-6.01	-1.25	-1.97
7	[MoTe ₂]H _{Mo} H _{Te} → Tafel TS3	6.93	5.84	6.07
8	Tafel TS3 → [MoTe ₂]	-14.45	-14.54	-23.34

In the present calculations for both the gas and the solvent phases, the energy barrier for the Tafel reaction step (TS3) is lower than the energy barrier for the Heyrovsky reaction step (TS2) for H₂ evolution. According to gas phase calculations, the H^{*}-migration step in the TS1 of the V–T reaction pathway of the HER has a reaction barrier of around $\Delta G =$

8.47 kcal mol⁻¹, while the Tafel reaction step in the TS3 has a substantially lower reaction barrier of roughly 6.07 kcal mol⁻¹. Figure 5.9 shows how the Gibbs free energies, also known as the HER pathway, diverge relatively with respect to the various reaction steps in the V–T reaction mechanism. The values of relative changes in various energies during the V–T reaction pathway of the HER are reported in Table 5.3.

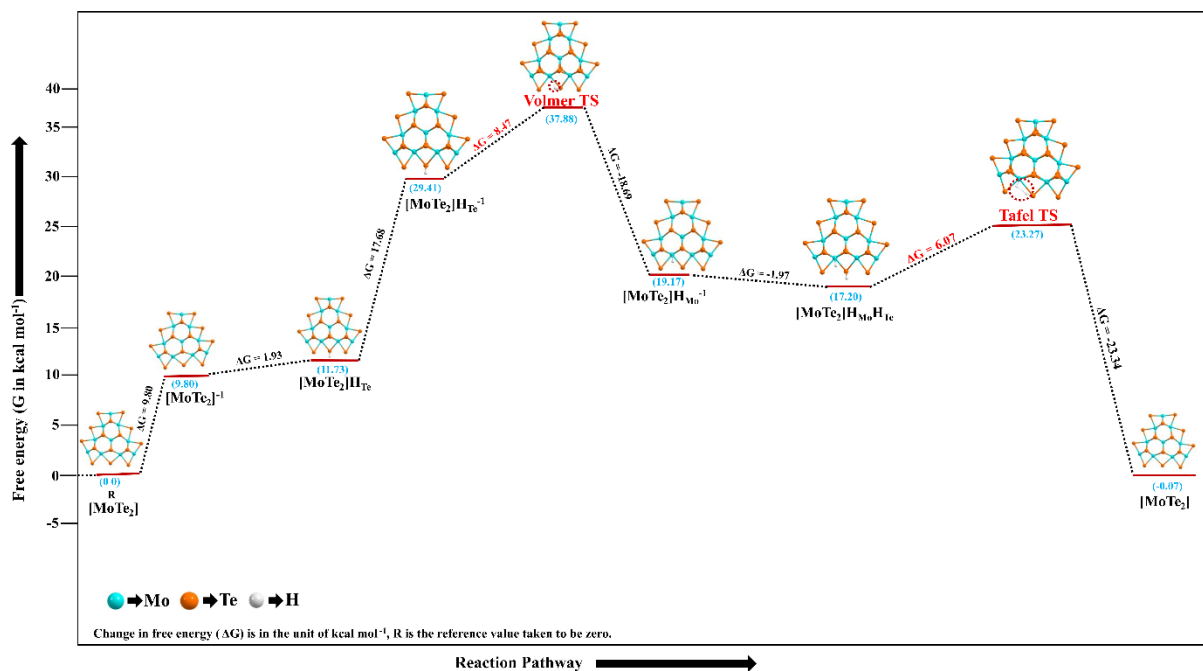


Figure 5.9: The PES of the Volmer–Tafel reaction mechanism is shown here as it occurs during the HER process at the surface of the MoTe₂ material.

The Mo₁₀Te₂₁ non-periodic finite molecular cluster model system of the pure 2D monolayer MoTe₂ was the subject of this DFT investigation, which looked into the HER on its surfaces. According to the calculations in both the gas and the solvent phases, the activation reaction barrier of the TS3 in the Tafel reaction step ranges from 6.07 to 5.29 kcal mol⁻¹ computed by the DFT method. It is important to note that the reaction energy barrier (ΔG) of the Heyrovsky transition state, TS2, in the V–H reaction mechanism, computed in both the gas and solvent phases, is about 8.85–12.55 kcal mol⁻¹ higher than the barrier of TS3, which is the Tafel reaction step. These numbers are within the DFT accuracy range, indicating that both the HER pathways have comparable low energy barriers and can enhance the HER catalytic performance of the 2D monolayer MoTe₂ TMD material. With comparable reaction barriers to the noble metal-based catalysts, these decreased reaction barriers suggest that the H₂ evolution can occur through either pathway.

The current DFT calculations demonstrate that, in comparison to the other materials listed in Table 5.4, the 2D monolayer MoTe₂ material has a lower reaction energy barrier for both the H^{*}-migration TS in the Volmer reaction step and H₂ formation in the Heyrovsky and Tafel reaction steps for the HER mechanism.

Table 5.4: Reaction barriers in both gas and solvent phases for various 2D TMDs.

Catalysts	H [*] migration TS1 barrier		Heyrovsky TS2 barrier		Tafel TS3 barrier		References
	Gas phase (kcal.m ol ⁻¹)	Solvent phase (kcal.m ol ⁻¹)	Gas phase (kcal.m ol ⁻¹)	Solvent phase (kcal.m ol ⁻¹)	Gas phase (kcal.m ol ⁻¹)	Solvent phase (kcal.m ol ⁻¹)	
Mn-MoS₂	7.23	10.34	10.59	10.79	90.13	93.72	(Ekka <i>et al.</i> , 2022)
MoSSe	3.93	7.10	5.61	4.72	8.52	-	(Pakhira and Upadhyay, 2022)
MoTe₂	8.47	9.80	8.85	12.55	6.07	5.29	This work

5.3.2.3. Turnover Frequencies and Tafel slope calculations:

Different types of technologies correspond to load quality and thus have many differences. Therefore, improved HER performance by turnover frequency (TOF) is an important parameter to evaluate to address such difficulties.(Huang *et al.*, 2015) The TOF employs the number of catalytic cycles that actually happen per unit of time to determine the catalyst's activity under the reaction circumstances. The higher the TOF value, the better the performance of the electrocatalysts. We have used the following formula for the TOF theoretical calculation:

$$rate = \frac{(k_B T)}{h} \times \exp\left(-\frac{\Delta G}{RT}\right)$$

Here k_B means Boltzmann constant (3.298x10⁻²⁷ kcal mol⁻¹), T is the absolute temperature (298.15 K), h is plank's constant (1.584x10⁻³⁷ kcal s⁻¹), R is the universal ideal gas constant (1.987x10⁻³ kcal K⁻¹ mol⁻¹), and ΔG is the energy barrier of the intermediate steps of HER.

Using transition state theory (TST)(*Jordan, 1979*), including DFT calculations, we calculated the TOF for both reaction mechanisms (V-H and V-T) for H₂ formation at the edge of the Mo atom.

Another parameter, the Tafel slope is also important for HER calculation to compare with experimental results.(*Huang et al., 2015*) The Tafel slope (*m*) demonstrates the effectiveness with which an electrode can generate current in response to a change in applied potential. In other words, if the Tafel slope (mV/decade) is lower, less overpotential is required to get a high current, assuming that the catalyst's reaction rate does not limit the electron transfer from the support to the catalyst. Tafel slope is a theoretical calculation based on the number of electron transfers during the HER steps. The following formula calculates the Tafel slope:

$$m = 2.303 \left(\frac{RT}{nF} \right)$$

Here R= the universal gas constant, T = absolute temperature, F = Faraday constant (96485 C mol⁻¹), and n = the number of electrons in the HER mechanism.(*Huang et al., 2015*) This Tafel slope provides information regarding the rate-determining step, kinetics, and energy required to obtain the required activity of the catalyst. Earlier, we discussed two-electron transfer mechanisms in the HER system as in Figure 5.4, so the value of n should be taken as 2 for the evolution of one H₂ molecule. So, the Tafel slope calculated for 2D single-layer MoTe₂ is found to be 29.58 mV dec⁻¹ at T=298.15 K.

Here we calculated the TOF for the solvent phase energy barrier of the Heyrovsky reaction barrier. We have calculated the TOF of the evolution of H₂ at the edge of each Mo atom in a 2D monolayer MoTe₂ catalyst. The turnover frequency is calculated according to the formula mentioned earlier. The TOF of the 2D monolayer MoTe₂ obtained from the reaction barrier (ΔG) formed by H₂ in the Heyrovsky TS and Tafel TS in the solvent phase, is about $3.91 \times 10^3 \text{ sec}^{-1}$ and $8.22 \times 10^8 \text{ sec}^{-1}$, respectively. The higher the TOF value, the more efficient the development of H₂ during HER. The TOF values of other catalysts, such as 2D monolayer MoS₂, WS₂, W_{0.4}Mo_{0.6}S₂, and Mn-MoS₂, are mentioned in Table 5.5 for comparison with 2D monolayer MoTe₂ catalysts. The 2D MoTe₂ catalyst material shows a

reasonably high TOF value, which helps the catalyst material to exhibit significantly superior and efficient performance during HER.

Table 5.5: The reaction barrier (ΔG) of the comparasion with 2D monolayer TMD and other 2D materials in the solvent phase are listed here.

Catalysts	H*-migration TS1 barrier		Heyrovsky TS2 barrier		Tafel TS3 barrier		References
	Gas phase (kcal.mol ⁻¹)	Solvent phase (kcal.mol ⁻¹)	Gas phase (kcal.mol ⁻¹)	Solvent phase (kcal.mol ⁻¹)	Gas phase (kcal.mol ⁻¹)	Solvent phase (kcal.mol ⁻¹)	
MoS₂	11.90	17.70	16.0	23.8	-	-	<i>ACS Nano</i> 2017, 11, 5, 5103–5112
WS₂	12.40	18.10	14.4	21.3	-	-	<i>ACS Nano</i> 2017, 11, 5, 5103–5112
W_{0.4}Mo_{0.6}S₂	6.80	11.90	11.50	13.30	-	-	<i>ACS Nano</i> 2017, 11, 5, 5103–5112
WSe₂	2.67	6.11	6.24	8.41	-	-	<i>Adv. Mater. Interfaces</i> 2023, 10, 2202075
Mn-MoS₂	7.23	10.34	10.59	10.79	90.13	93.72	<i>Phys. Chem. Chem. Phys.</i> , 2022,24, 265-280.
MoSSe	3.93	7.10	5.61	4.72	8.52	-	<i>Sustainable Energy Fuels</i> , 2022,6, 1733-1752.
MoP	17.5	-	16.3	-	56	60	<i>ACS Catal.</i> 2019, 9, 1, 651–659
MoSP	12.90	14	9.2	12.90	34	-	<i>ACS Catal.</i> 2019, 9, 1, 651–659
Borophene	4.84	-	8.07	-	31.62	-	<i>ACS Appl. Energy Mater.</i> 2023, 6, 8941–8948.

NbCO₂	-	-	31.59	-	43.58		<i>J. Mater. Chem. A</i> , 2018,6, 4271-4278
Epitaxial Graphene	28.59	35.51	-	-	28.74	29.03	<i>ACS Omega</i> 2022, 7, 13221–13227
MoTe₂	8.47	9.80	8.85	12.55	6.07	5.29	This work

5.3.2.4. HOMO-LUMO Calculations

Our present calculations using 2D single-layer MoTe₂ reveal the low energy barriers of the Vollmer-Heyrovsky phases in HER, which are expected to be a good candidate as electrocatalysts in HER. To further support the development of our MoTe₂ molecular cluster model system, we apply natural bond orbital (NBO), HOMO, and LUMO calculations by the same DFT analysis. HOMO-LUMO energy is the most famous quantum mechanics parameter, and it plays an essential role in controlling a wide range of chemical interactions. NBO calculations can detect the structure with the largest electron charge in the Lewis orbital. This NBO study explains the wave function's density of interaction or overlaps. The wave function calculated from the NBO is a linear combination of the atomic orbitals of the Te, Mo, and H atoms of the Volmer energy barrier and the atomic orbitals of the Te, Mo, H, and O atoms of the Heyrovsky energy barrier. Understanding the Highest Occupied Molecular Orbitals (HOMO) and Lowest Unoccupied Molecular Orbitals (LUMO) computation for the Vollmer and Heyrovsky transition state has been performed using the same DFT method as shown in Figure 5.10, where the red color indicates the in-phase bonding and blue color represents the out-of-phase bonding of the orbital. These calculations of the Heyrovsky transition TS2 can better explain the Heyrovsky mechanism of effective HER from the perspective of the charge cloud and molecular orbital overlap during the formation of H₂.

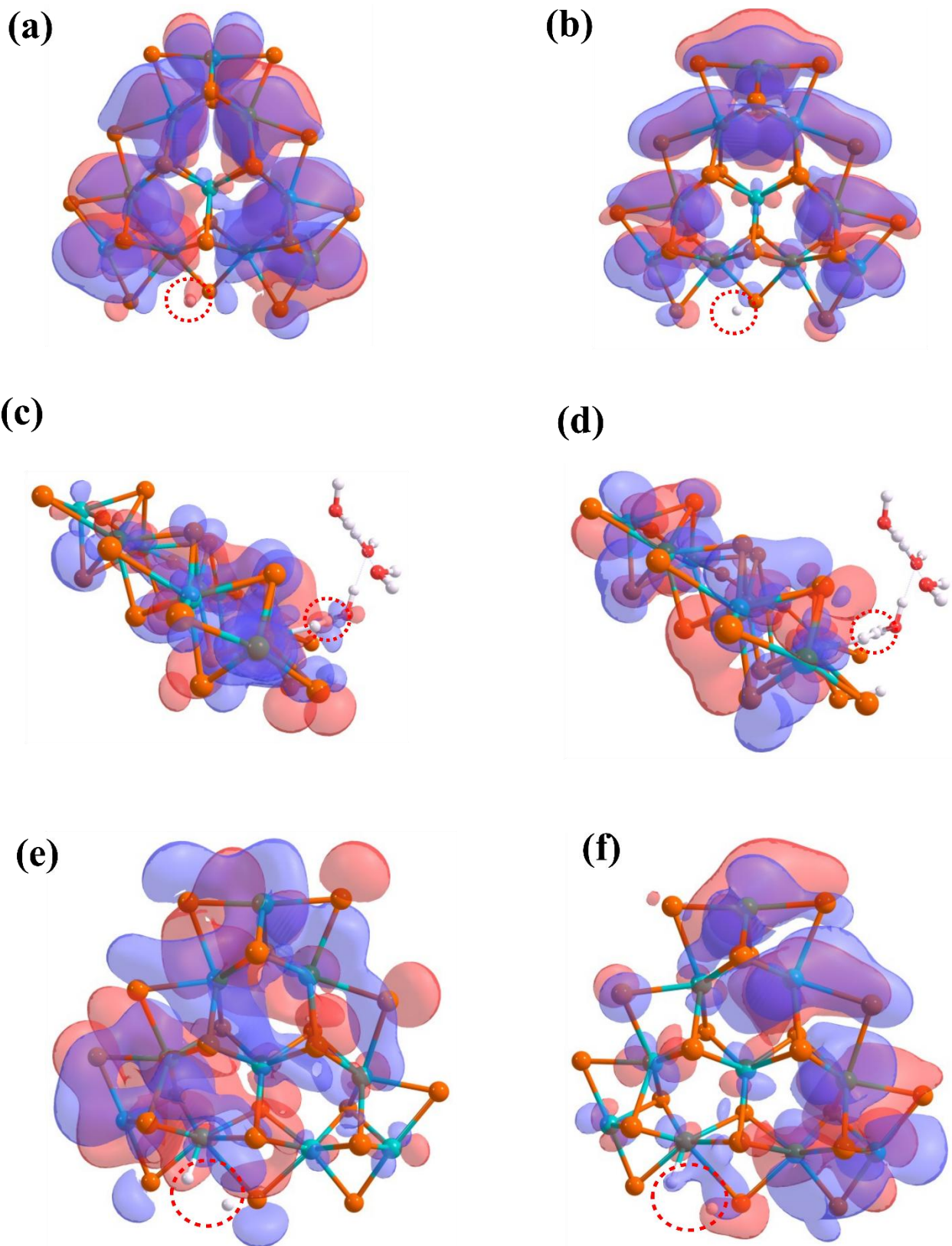


Figure 5.10: The equilibrium structure of MoTe₂ (a) The HOMO of Volmer TS; (b) The LUMO of Volmer TS; (c) The HOMO of Heyrovsky TS; (d) The LUMO of Heyrovsky TS; (e) The HOMO of Tafel TS; (f) The LUMO of Tafel TS is shown here.

The energy difference between the HOMO and LUMO studies provides stability to the molecule. The potentials of the electron donor and acceptor units are explained by the HOMO energy and the LUMO energy, respectively. This study found that TS1 and TS2 in the case of 2D MoTe₂ are reduced by the overlap of *s* orbitals of H and *d* orbitals of Mo metal atoms, as shown in Figure 5.10(a-d). Figure 5.10(a-b) indicates the HOMO and LUMO of the Volmer transition state of 2D MoTe₂, respectively. The electron cloud between the H atom and Mo metal atom in the Volmer transition state structure highlighted by the red dotted circle is the 2D MoTe₂ TMD structure in the Volmer step of H* migration. The electron cloud between the H atom and Mo metal atom in the Volmer transition state structure highlighted by the red dotted circle is the 2D MoTe₂ TMD structure in the Volmer step of H* migration. The energy values of HOMO and LUMO of Volmer TS are found to be $E_{\text{HOMO}} = -2.18$ eV and $E_{\text{LUMO}} = -2.10$ eV, respectively. So, the energy difference between HOMO and LUMO of Volmer TS is found to be $E_{\text{GAP}} = E_{\text{LUMO}} - E_{\text{HOMO}} = 0.075$ eV, so it means this is the energy required for an electron to transition from HOMO to LUMO. The electron cloud between two H atoms in the Heyrovsky transition state structure highlighted by the red dotted circle is the 2D MoTe₂ TMD structure in the presence of four water molecules in the Heyrovsky step of H₂ evolution, as shown in Figures 5.10 c and d. So, the Heyrovsky reaction is performed by overlapping the atomic orbitals of two H atoms with adjacent hydrated hydrogen (H₃O⁺) in the water cluster to form H₂ molecules during the HER process. Figure 5.10 c-d indicates the HOMO and LUMO of the Heyrovsky transition state of 2D MoTe₂, respectively. The energy difference between HOMO and LUMO, also known as the HOMO–LUMO gap, is used to predict the HER's stability of transition metal-based electrocatalysts. The energy values of HOMO and LUMO of Heyrovsky TS are found to be $E_{\text{HOMO}} = -6.90$ eV and $E_{\text{LUMO}} = -6.74$ eV, respectively. So, the energy difference between HOMO and LUMO of Heyrovsky TS is found to be $E_{\text{GAP}} = E_{\text{LUMO}} - E_{\text{HOMO}} = 0.16$ eV, so it means this is the energy required for an electron to transition from HOMO to LUMO. This is also another reason why the 2D monolayer MoTe₂ shows excellent HER activity. To better visualize the Tafel reaction mechanism, a HOMO-LUMO calculation

was also performed, shown in Figures 5.10(b) and 5.10(c). The electron cloud uses red and blue to represent the positive and negative parts of the wave function. A red dotted circle highlights the electron cloud around hydrogen in the HOMO-LUMO. The phase or orbit is the direct result of the wave-like characteristics of electrons. Usually, in-phase mixing indicates a low energy state, and out-of-phase mixing indicates an anti-bonding orbital or higher energy state. The HOMO and LUMO of Heyrovsky TS energy values are $E_{\text{HOMO}} = -4.80$ eV and $E_{\text{LUMO}} = -4.66$ eV, respectively. So, the energy difference between HOMO and LUMO of Tafel TS is found to be $E_{\text{GAP}} = E_{\text{LUMO}} - E_{\text{HOMO}} = 0.14$ eV, so it means this is the energy required for an electron to transition from HOMO to LUMO. The gentle orbital overlaps of the molecular orbitals during the H migration in the H*-migration reaction step and the H₂ formation in the Heyrovsky and Tafel reaction steps reveal the excellent electrocatalytic activity of the 2D monolayer MoTe₂ TMD for HER.

5.4. Summary

We have used first principles-based DFT-D3 computations (more particularly, the B3LYP-D3 method) to analyze the electronic and structural features of a 2D monolayer slab of the MoTe₂ TMD. The present study has found that the 2D MoTe₂ monolayer TMD has a direct band gap of about 1.65 eV. Furthermore, we have studied that the 2D monolayer MoTe₂ is a good candidate as an efficient electrocatalyst towards the HER because of its lower bandgap and lower activation energy barrier during the HER. We have looked at the variation in the adsorption energy of the HER intermediates taking place on the MoTe₂ (Mo₁₀Te₂₁) surface to examine the catalytic performance of the TMD. Using the M06-L DFT approach, we have carried out each reaction step of both the V-H and V-T reaction pathways to comprehend the HER mechanism route. According to our findings, the Volmer reaction during H*-migration across the 2D MoTe₂ TMD material surface, when H* transfers from the Te-site to the Mo-site was around 8.47 kcal mol⁻¹ in the gas phase and 9.80 kcal mol⁻¹ in the solvent phase calculations. In the Heyrovsky reaction step, the activation energy barriers for the production of H₂ are about 8.85 kcal mol⁻¹ obtained in the gas phase and 12.55 kcal mol⁻¹ computed in the solvent phase analysis. Also, the activation energy barriers of the V-T HER mechanism are about 6.07 kcal mol⁻¹ in the gas phase and 5.29 kcal mol⁻¹ in the solvent phase during the production of H₂ in the Tafel

reaction step. Due to the lower energy barrier of the Tafel TS3 compared to the Heyrovsky TS2, we have understood that the V–H mechanism is less advantageous or favorable than the V–T mechanism for the HER.

The HOMO and LUMO calculations show that the H*-migration happens during the Volmer steps, whereas H₂ evolution happens during Heyrovsky or Tafel stages. The extraordinary HER catalytic activity of the 2D monolayer MoTe₂ material is explained by this computation. In the solvent phase, the predicted TOF of the V–H reaction mechanism is about $3.91 \times 10^3 \text{ s}^{-1}$, whereas that of the V–T reaction mechanism is $8.22 \times 10^8 \text{ s}^{-1}$. The catalyst's efficient hydrogen evolution per active site per unit time is confirmed by these increased TOF values. Also, the theoretical Tafel slope is around $29.58 \text{ mV dec}^{-1}$. This exceptional electrocatalytic activity of the 2D monolayer MoTe₂ for the HER is demonstrated by the extremely low reaction barrier values, low Tafel slope, and extremely high TOF values. These results imply the need for additional experimental and theoretical research into the potential of 2D monolayer TMD-based materials as HER catalysts.

Chapter 6

Conclusions and Future Perspectives

In this chapter, we have highlighted the significant conclusions drawn from the research work reported in this Thesis. Scopes for further research on these novel 2D TMDs and Janus TMDs have been suggested in this section.

6.1 Major Conclusion

In conclusion, this thesis work extensively examines the crucial domains of 2D monolayer calaysts degin, electrocatalysis, particularly investigating the HER occurring on the surfaces of 2D TMDs and Janus TMDs. The present study has explored the structural and electronic properties of these 2D TMDs and has evaluated their electrocatalytic activity towards HER.

In the first part of the Thesis, we have computationally designed a 2D Janus monolayer WSSe (JTMD) using first-principles periodic hybrid B3LYP-D3 method. We have thoroughly investigated its electronic structure, equilibrium geometry, band gap (~ 2.64 eV), and density of states (DOS). The Se-/S- and W-edge sites have been identified as electrocatalytically active for the HER. A non-periodic $W_{10}S_{12}Se_9$ molecular cluster model system has been used to explore the HER mechanism, and detailed V–H pathways have been studied via the M06-L DFT method. The activation barriers for H^* -migration and the Heyrovsky step in solvent have been computed to be 2.88 and 7.52 kcal mol⁻¹, respectively. A high theoretical turnover frequency (1.91×10^7 s⁻¹) and a low Tafel slope (29.54 mV dec⁻¹) support the superior HER activity of JTMD. HOMO–LUMO analysis has indicated that efficient orbital overlap facilitates H_2 formation. These findings have established Janus WSSe as a promising and efficient HER electrocatalyst.

In the second part, we have included a computationally designed 2D Janus WSeTe monolayer and have explored its electronic and catalytic properties using first-principles

DFT-D3 (B3LYP-D3) and M06-L methods. The asymmetric Janus structure yields a direct band gap of 2.39 eV, supporting efficient charge transfer and HER activity. Using a $\text{W}_{10}\text{Se}_9\text{Te}_{12}$ cluster model, both V–H and V–T mechanisms have been examined to explore the most suitable reaction pathway. The Tafel pathway has been found to be thermodynamically favored due to a lower activation barrier ($3.27 \text{ kcal mol}^{-1}$) compared to Heyrovsky ($8.72 \text{ kcal mol}^{-1}$). HOMO–LUMO analyses indicate strong orbital overlap between W and H atoms, enhancing catalytic performance. The calculated TOFs for Heyrovsky and Tafel TSs were $2.51 \times 10^6 \text{ s}^{-1}$ and $2.48 \times 10^{10} \text{ s}^{-1}$, respectively, with a Tafel slope of $29.57 \text{ mV dec}^{-1}$, confirming high HER efficiency. These outcomes have demonstrated that Janus WSeTe is a highly promising HER electrocatalyst with low energy barriers and rapid hydrogen evolution kinetics.

In the third part of the thesis work, we have employed first-principles DFT-D3 (B3LYP-D3) calculations to investigate the electronic and catalytic properties of a 2D MoTe_2 monolayer. The material exhibits a direct band gap of 1.65 eV, indicating semiconducting behavior and potential HER activity. We have used a non-periodic $\text{Mo}_{10}\text{Te}_{21}$ cluster to evaluate its electrocatalytic performance and studied HER intermediates via the M06-L DFT method. In the Heyrovsky reaction step, the activation energy barriers for the production of H_2 have been calculated as $8.85 \text{ kcal mol}^{-1}$ in the gas phase and $12.55 \text{ kcal mol}^{-1}$ in the solvent phase analysis. Also, the activation energy barriers of the V–T HER mechanism have been $6.07 \text{ kcal mol}^{-1}$ in the gas phase and $5.29 \text{ kcal mol}^{-1}$ in the solvent phase during the production of H_2 in the Tafel reaction step. Due to the lower energy barrier of the Tafel TS3 compared to the Heyrovsky TS2, we understood that the V–H mechanism is less advantageous or favorable than the V–T mechanism for the HER. HOMO–LUMO analysis confirms effective orbital interactions during hydrogen evolution. The TOF calculated for the HER pathways indicates that the 2D monolayer MoTe_2 exhibits remarkable catalytic performance. Specifically, the TOF for the Volmer–Heyrovsky mechanism is $3.91 \times 10^3 \text{ s}^{-1}$, while the significantly higher TOF of $8.22 \times 10^8 \text{ s}^{-1}$ is observed for the V–T mechanism, indicating a faster rate of hydrogen generation per active site via the Tafel pathway. In addition, the theoretical Tafel slope, determined to be approximately $29.58 \text{ mV dec}^{-1}$, reflects the efficient electrochemical kinetics and high catalytic responsiveness of the material. These findings underscore the

superior electrocatalytic activity of the 2D monolayer MoTe₂, characterized by low activation energy barriers and rapid hydrogen evolution dynamics. Consequently, this study establishes 2D MoTe₂ TMD as a promising candidate for practical applications in HER electrocatalysis and encourages further in-depth experimental and computational investigations to explore its potential in large-scale hydrogen production systems.

6.2 Future Perspective

The present Thesis has made significant strides in understanding and advancing the electrocatalytic behavior of 2D TMDs towards the hydrogen evolution reactions and catalysts design. Future research can focus on extending the study to a broader class of Janus TMDs and conventional TMDs to identify promising candidates with optimal HER activity. This includes investigating underexplored compositions and structural configurations that may exhibit favorable electronic and surface characteristics.

- A promising direction involves the rational tuning of electronic and geometric properties through strategies such as heteroatom doping, vacancy and defect engineering, and surface functionalization. These modifications can tailor the adsorption energies of intermediates, lower activation energy barriers, and enhance overall catalytic performance. In particular, introducing strain or combining TMDs with conductive supports may synergistically improve charge transfer kinetics.
- Another critical area of focus is the systematic design and computational screening of novel Janus TMD structures, such as MoSTe, WSSe, and WSTe, which may provide inherent asymmetric and built-in electric fields conducive to faster electron transport and favorable HER kinetics. Investigating the HER mechanisms on these asymmetric surfaces using advanced theoretical approaches will offer deeper mechanistic insights and guide the development of highly efficient catalysts.
- Further studies can also aim at identifying and optimizing low-cost, non-noble-metal-based TMD catalysts that exhibit catalytic properties comparable to or superior to those of conventional noble metal-based systems. This is particularly relevant for practical and scalable hydrogen production technologies.

- In addition, exploring 2D TMD heterostructures, layered composites, and hybrid materials with tailored interfaces could open new possibilities for improving catalytic selectivity, stability, and turnover frequency. Integrating experimental validation with computational design will be crucial in translating theoretical predictions into practical applications.

Overall, the future direction of this work lies in the comprehensive discovery, design, and mechanistic understanding of novel 2D TMD-based materials for HER. These efforts are expected to accelerate the development of efficient, cost-effective, and scalable electrocatalysts for clean hydrogen generation, contributing meaningfully to the global transition toward sustainable energy systems.

Bibliography

Allouche, A. (2012) ‘Software News and Updates Gabedit — A Graphical User Interface for Computational Chemistry Softwares’, *Journal of computational chemistry*, 32(1), pp. 174–182. doi: 10.1002/jcc.

Anantharaj, S. *et al.* (2018) ‘Precision and correctness in the evaluation of electrocatalytic water splitting: revisiting activity parameters with a critical assessment’, *Energy & Environmental Science*, 11(4), pp. 744–771. doi: 10.1039/C7EE03457A

Andrienko, G. A. (2010) ‘Chemcraft-graphical software for visualization of quantum chemistry computations’. Google Scholar There is no corresponding record for this reference.

Andrienko, G. A. (2015) ‘Chemcraft version 1.8’, URL: [www http://www. chemcraftprog. com](http://www.chemcraftprog.com).

Ao, K. L. *et al.* (2020) ‘Design of novel pentagonal 2D transitional-metal sulphide monolayers for hydrogen evolution reaction’, *International Journal of Hydrogen Energy*, 45(32), pp. 16201–16209. doi: 10.1016/j.ijhydene.2020.04.092.

Armaroli, N. and Balzani, V. (2007) ‘The future of energy supply: challenges and opportunities’, *Angewandte Chemie International Edition*, 46(1–2), pp. 52–66. doi: 10.1002/anie.200602373

Baker, J., Scheiner, A. and Andzelm, J. (1993) ‘Spin contamination in density functional theory’, *Chemical physics letters*, 216(3–6), pp. 380–388. doi: 10.1016/0009-2614(93)90113-F

Bandiello, E. *et al.* (2023) ‘Structural, vibrational, and electronic behavior of two GaGeTe polytypes under compression’, *Materials Today Advances*, 19. doi: 10.1016/j.mtadv.2023.100403.

Baseden, K. A. and Tye, J. W. (2014) ‘Introduction to density functional theory: calculations by hand on the helium atom’, *Journal of Chemical Education*, 91(12), pp. 2116–2123. doi: 10.1021/ed5004788

Beck, A. D. (1993) ‘Density-functional thermochemistry. III. The role of exact exchange’, *J. Chem. Phys.*, 98(7), pp. 5646–5648. doi: 10.1063/1.464913

Becke, A. D. (1993) ‘Density-functional thermochemistry. III. The role of exact exchange’, *The Journal of Chemical Physics*, 98(7), pp. 5648–5652. doi: 10.1063/1.464913.

Becke, A. D. (2005) ‘Density - functional thermochemistry . III . The role of exact exchange Density-functional thermochemistry . III . The role of exact exchange’, *J. Chern. Phys.*, 98(7), pp. 5648–5652. doi: 10.1063/1.464913

Bera, J., Betal, A. and Sahu, S. (2020) ‘Ultralow lattice thermal conductivity and high thermoelectric performance near room temperature of Janus monolayer HfSSe’, pp. 268–

279. Available at: <http://arxiv.org/abs/2003.02439>.

Berezin, F. A. and Shubin, M. (2012) *The Schrödinger Equation*. Springer Science & Business Media.vol(66)

Bergner, A. *et al.* (1993) ‘Ab initio energy-adjusted pseudopotentials for elements of groups 13--17’, *Molecular Physics*, 80(6), pp. 1431–1441.doi: 10.1080/00268979300103121

Bhat, K. S. and Nagaraja, H. S. (2019) ‘Performance evaluation of molybdenum dichalcogenide (MoX_2 ; X= S, Se, Te) nanostructures for hydrogen evolution reaction’, *International Journal of Hydrogen Energy*, 44(33), pp. 17878–17886.doi: 10.1016/j.ijhydene.2019.05.179

Bhowmik, T., Kundu, M. K. and Barman, S. (2016) ‘Palladium nanoparticle--graphitic carbon nitride porous synergistic catalyst for hydrogen evolution/oxidation reactions over a broad range of pH and correlation of its catalytic activity with measured hydrogen binding energy’, *Acs Catalysis*, 6(3), pp. 1929–1941.doi: 10.1021/acscatal.5b02485

Bickelhaupt, F. M. and Baerends, E. J. (2000) ‘Kohn-Sham density functional theory: predicting and understanding chemistry’, *Reviews in computational chemistry*, pp. 1–86.doi: 10.1002/9780470125922

Bockris, J. O. M. (2013) ‘The hydrogen economy: Its history’, *International Journal of Hydrogen Energy*, 38(6), pp. 2579–2588.doi: 10.1016/j.ijhydene.2012.12.026

Caldeweyher, E., Bannwarth, C. and Grimme, S. (2017) ‘Extension of the D3 dispersion coefficient model’, *Journal of Chemical Physics*, 147(3). doi: 10.1063/1.4993215.

Capurso, T. *et al.* (2022) ‘Perspective of the role of hydrogen in the 21st century energy transition’, *Energy Conversion and Management*, 251, p. 114898.doi: 10.1016/j.enconman.2021.114898

Cardoso, G. L., Piquini, P. C. and Ahuja, R. (2021) ‘From Monolayers to Nanotubes: Toward Catalytic Transition-Metal Dichalcogenides for Hydrogen Evolution Reaction’, *Energy and Fuels*, 35(7), pp. 6282–6288. doi: 10.1021/acs.energyfuels.1c00462.

Chaurasiya, R., Gupta, G. K. and Dixit, A. (2019) ‘Ultrathin Janus WSe buffer layer for $\text{W}(\text{S}/\text{Se})_2$ absorber based solar cells: A hybrid, DFT and macroscopic, simulation studies’, *Sol. Energy Mater. Sol. Cells*, 201, p. 110076.doi: 10.1016/j.solmat.2019.110076

Chen, J. G., Menning, C. A. and Zellner, M. B. (2008) ‘Monolayer bimetallic surfaces: Experimental and theoretical studies of trends in electronic and chemical properties’, *Surface Science Reports*, 63(5), pp. 201–254.doi: 10.1016/j.surfrep.2008.02.001

Cheng, Y. C. *et al.* (2013) ‘Spin-orbit--induced spin splittings in polar transition metal dichalcogenide monolayers’, *EPL (Europhysics Letters)*, 102(5), p. 57001.doi: 10.1209/0295-5075/102/57001

Chia, X. *et al.* (2018) ‘Morphological Effects and Stabilization of the Metallic 1T Phase in Layered V-, Nb-, and Ta-Doped WSe_2 for Electrocatalysis’, *Chem. Eur. J.*, 24, pp. 3199–

3208.doi: 10.1002/chem.201704158

Corà, F. *et al.* (1996) ‘An ab initio Hartree-Fock study of the cubic and tetragonal phases of bulk tungsten trioxide’, *Journal of the American Chemical Society*, 118(48), pp. 12174–12182. doi: 10.1021/ja961514u.

Davidson, E. R. (1988) ‘Basis Set Selection for Molecular Calculations’, *Chemical Reviews*, 86, pp. 681–96.doi: 10.1021/cr00074a002

Dawson, W. G. and Bullett, D. W. (1987) ‘Electronic structure and crystallography of MoTe₂ and WTe₂’, *Journal of Physics C: Solid State Physics*, 20(36), p. 6159.doi: 10.1088/0022-3719/20/36/017

Debe, M. K. (2012) ‘Electrocatalyst approaches and challenges for automotive fuel cells’, *Nature*, 486(7401), pp. 43–51. doi: 10.1038/nature11115.

Deng, S., Li, L. and Li, M. (2018) ‘Stability of direct band gap under mechanical strains for monolayer MoS₂, MoSe₂, WS₂ and WSe₂’, *Physica E: Low-dimensional Systems and Nanostructures*, 101, pp. 44–49.doi: 10.1016/j.physe.2018.03.016

Ditchfield, R., Hehre, W. J. and Pople, J. A. (1971) ‘Self-Consistent Molecular-Orbital Methods. IX. An Extended Gaussian-Type Basis for Molecular-Orbital Studies of Organic Molecules’, *J. Chem. Phys.*, 54, pp. 724–728. doi: 10.1063/1.1674902.

Dong, L., Lou, J. and Shenoy, V. B. (2017) ‘Large in-plane and vertical piezoelectricity in Janus transition metal dichalcogenides’, *ACS nano*, 11(8), pp. 8242–8248.doi: 10.1021/acsnano.7b03313

Dovesi, R. *et al.* (2017) ‘CRYSTAL17’.

Dovesi, R. *et al.* (2018) ‘Quantum-mechanical condensed matter simulations with CRYSTAL’, *Wiley Interdisciplinary Reviews: Computational Molecular Science*, 8(4), p. e1360.

Echenique, P. and Alonso, J. L. (2007) ‘A mathematical and computational review of Hartree–Fock SCF methods in quantum chemistry’, *Molecular Physics*, 105(23–24), pp. 3057–3098.doi: 10.1080/00268970701757875

Ehrlich, S. *et al.* (2011) ‘System-dependent dispersion coefficients for the DFT-D3 treatment of adsorption processes on ionic surfaces’, *ChemPhysChem*, 12(17), pp. 3414–3420.doi: 10.1002/cphc.201100521

Ekka, J. *et al.* (2022) ‘Unveiling the role of 2D monolayer Mn-doped MoS₂ material: toward an efficient electrocatalyst for H₂ evolution reaction’, *Physical Chemistry Chemical Physics*, 24(1), pp. 265–280. doi: 10.1039/d1cp04344g.

Engel, E. (2011) *Density functional theory*. Springer.

Er, D. *et al.* (2018) ‘Prediction of Enhanced Catalytic Activity for Hydrogen Evolution Reaction in Janus Transition Metal Dichalcogenides’, *Nano Letters*, 18(6), pp. 3943–3949. doi: 10.1021/acs.nanolett.8b01335.

Evarestov, R. A. and Smirnov, V. P. (2004) ‘Modification of the Monkhorst-Pack special points meshes in the Brillouin zone for density functional theory and Hartree-Fock calculations’, *Physical Review B - Condensed Matter and Materials Physics*, 70(23), pp. 1–4. doi: 10.1103/PhysRevB.70.233101.

Frisch, E., Hratchian, H.P., Dennington, R.D., Keith, T.A., Millam, J., Nielsen, A.B., Holder, A.J. and Hiscoks, J. (2009) ‘GaussView 5 Reference’, *Gaussian, Inc, Wallingford*.

Frisch, M. J.; Trucks, G. W.; Schlegel, H. B.; Scuseria, G. E.; Robb, M. A.; Cheeseman, J. R.; Scalmani, G.; Barone, V.; Petersson, G. A.; Nakatsuji, H. . (2016) ‘Gaussian 16, Revision C. 01; GaussianNo Title’, *Inc.: Wallingford CT*.

Frisch, M. J., Trucks, G. W., Schlegel, H. B., Scuseria, G. E., Robb, Ma., *et al.* (2016) ‘Gaussian 16, Revision A. 03, Gaussian’, *Inc., Wallingford CT*, 3.

Frisch, M. J., Trucks, G. W., Schlegel, H. B., Scuseria, G. E., Robb, M. A., *et al.* (2016) ‘Gaussian 16’. Gaussian, Inc. Wallingford, CT.

Frisch, M. J., Pople, J. A. and Binkley, J. S. (1984) ‘Self-consistent molecular orbital methods 25. Supplementary functions for Gaussian basis sets’, *The Journal of Chemical Physics*, 80(7), pp. 3265–3269. doi: 10.1063/1.447079.

Frost, A. A. and Musulin, B. (1953) ‘Density-functional thermochemistry. III. The role of exact exchange’, *Hydrocarbons The Journal of Chemical Physics*, 21(October 1992), p. 5648. Available at: <https://doi.org/10.1063/1.1698970>.

Gao, G., O’Mullane, A. P. and Du, A. (2017) ‘2D MXenes: a new family of promising catalysts for the hydrogen evolution reaction’, *Acs Catalysis*, 7(1), pp. 494–500. doi: 10.1021/acscatal.6b02754

Garza, A. J. *et al.* (2018) ‘Reaction mechanism of the selective reduction of CO₂ to CO by a tetraaza [Co^{II}N₄H]²⁺ complex in the presence of protons’, *Physical Chemistry Chemical Physics*, 20(37), pp. 24058–24064. doi: 10.1039/C8CP01963K

Ghosh, S. and Basu, R. N. (2018) ‘Multifunctional nanostructured electrocatalysts for energy conversion and storage: current status and perspectives’, *Nanoscale*, 10(24), pp. 11241–11280. doi: 10.1039/C8NR01032C

Giustino, F. (2014) *Materials modelling using density functional theory: properties and predictions*. Oxford University Press.

Greeley, J. *et al.* (2006) ‘Computational high-throughput screening of electrocatalytic materials for hydrogen evolution’, *Nature Materials*, 5(11), pp. 909–913. doi: 10.1038/nmat1752.

Grimme, S. *et al.* (2010) ‘A consistent and accurate ab initio parametrization of density functional dispersion correction (DFT-D) for the 94 elements H-Pu’, *Journal of Chemical Physics*, 132(15). doi: 10.1063/1.3382344.

Gupta, S. *et al.* (2020) ‘Metal boride-based catalysts for electrochemical water-splitting: a

review', *Advanced Functional Materials*, 30(1), p. 1906481. doi: 10.1002/adfm.201906481

Hay, P. Jeffrey and Wadt, W. R. (1985) 'Ab initio effective core potentials for molecular calculations. Potentials for K to Au including the outermost core orbitals', *The Journal of Chemical Physics*, 82(1), pp. 299–310. doi: 10.1063/1.448975.

Hay, P. Jeffrey and Wadt, W. R. (1985) 'Ab initio effective core potentials for molecular calculations. Potentials for the transition metal atoms Sc to Hg', *The Journal of chemical physics*, 82(1), pp. 270–283. doi: 10.1063/1.448799

Hehre, Warren J, Ditchfield, R. and Pople, J. A. (1972) 'Self—consistent molecular orbital methods. XII. Further extensions of Gaussian—type basis sets for use in molecular orbital studies of organic molecules', *The Journal of Chemical Physics*, 56(5), pp. 2257–2261. doi: 10.1063/1.1677527

Hehre, W J, Ditchfield, R. and Pople, J. A. (1972) 'Self — Consistent Molecular Orbital Methods . XII . Further Extensions of Gaussian — Type Basis Sets for Use in Molecular Orbital Studies of Organic Molecules Published by the AIP Publishing Articles you may be interested in Selfconsistent molecular orbit', *J. Chem. Phys.*, 56(1985), pp. 2257–2261. doi: 10.1063/1.1677527

Hinnemann, B. *et al.* (2005) 'Biomimetic hydrogen evolution: MoS₂ nanoparticles as catalyst for hydrogen evolution', *Journal of the American Chemical Society*, 127(15), pp. 5308–5309. doi: 10.1021/ja0504690.

Hu, G., Wu, Z. and Jiang, D. E. (2018) 'Stronger-than-Pt hydrogen adsorption in a Au₂₂ nanocluster for the hydrogen evolution reaction', *Journal of Materials Chemistry A*, 6(17), pp. 7532–7537. doi: 10.1039/c8ta00461g.

Huang, H. H. *et al.* (2016) 'Controlling phase transition for single-layer MTe₂ (M= Mo and W): modulation of the potential barrier under strain', *Physical Chemistry Chemical Physics*, 18(5), pp. 4086–4094. doi: 10.1039/C5CP06706E

Huang, Y. *et al.* (2015) 'The reaction mechanism with free energy barriers for electrochemical dihydrogen evolution on MoS₂', *Journal of the American Chemical Society*, 137(20), pp. 6692–6698. doi: 10.1021/jacs.5b03329

Huang, Y. *et al.* (2025) 'Transition-metal atoms embedded MoTe₂ single-atom catalyst for efficient electrocatalytic hydrogen evolution reaction', *Applied Surface Science*, 680, p. 161335. doi: 10.1016/j.apsusc.2024.161335

Huang, Y., Nielsen, R. J. and Goddard III, W. A. (2018) 'Reaction mechanism for the hydrogen evolution reaction on the basal plane sulfur vacancy site of MoS₂ using grand canonical potential kinetics', *Journal of the American Chemical Society*, 140(48), pp. 16773–16782. doi: 10.1021/jacs.8b10016

Hui, J., Schorr, N. B., *et al.* (2018) 'Achieving fast and efficient K⁺ intercalation on ultrathin graphene electrodes modified by a Li⁺ based solid-electrolyte interphase', *Journal of the American Chemical Society*, 140(42), pp. 13599–13603. doi: 10.1021/jacs.8b08907

Hui, J., Pakhira, S., *et al.* (2018) 'Modulating Electrocatalysis on Graphene

Heterostructures: Physically Impermeable Yet Electronically Transparent Electrodes', *ACS Nano*, 12(3), pp. 2980–2990. doi: 10.1021/acsnano.8b00702.

International Energy Institute (IEI) (2023) 'Statistical Review of World Energy 2023', *BP Energy Outlook 2023*, 70, pp. 8–20.

Jensen, F. (2013) 'Atomic orbital basis sets', *Wiley Interdisciplinary Reviews: Computational Molecular Science*, 3(3), pp. 273–295. doi: 10.1002/wcms.1123.

Ji, Y. *et al.* (2018) 'Janus Structures of Transition Metal Dichalcogenides as the Heterojunction Photocatalysts for Water Splitting', *Journal of Physical Chemistry C*, 122(5), pp. 3123–3129. doi: 10.1021/acs.jpcc.7b11584.

Jin, H. *et al.* (2018) 'Emerging Two-Dimensional Nanomaterials for Electrocatalysis', *Chemical Reviews*, 118(13), pp. 6337–6408. doi: 10.1021/acs.chemrev.7b00689.

Jones, R. O. (2015) 'Density functional theory: Its origins, rise to prominence, and future', *Reviews of modern physics*, 87(3), pp. 897–923.

Jordan, P. (2012) *Chemical kinetics and transport*. Springer Science & Business Media.

Jordan, P. C. (1979) 'Theories of Reaction Rates', in *Chemical Kinetics and Transport*. Springer, pp. 269–323.

Ju, L. *et al.* (2020) 'Janus WSe monolayer: an excellent photocatalyst for overall water splitting', *ACS Applied Materials & Interfaces*, 12(26), pp. 29335–29343.

Kanoun, M. B. (2019) 'Modeling of Nanosheets Based on Transition-Metal Dichalcogenides for Spintronic Applications: Insights From First-Principles', in *Nano-Sized Multifunctional Materials*. Elsevier, pp. 207–218.

Katsounaros, I. and Koper, M. T. M. (2017) 'Electrocatalysis for the hydrogen economy', *Electrochemical Science for a Sustainable Society: A Tribute to John O'M Bockris*, pp. 23–50.

Kellie, J. L. and Kellie, J. L. (2013) 'COMPUTATIONAL INVESTIGATION OF THE MECHANISM OF ACTION OF DNA GLYCOSYLASES'.

Khan, K. *et al.* (2019) *Recent advances in two-dimensional materials and their nanocomposites in sustainable energy conversion applications*, *Nanoscale*. Royal Society of Chemistry. doi: 10.1039/c9nr05919a.

Krstajic, N. (2014) 'Hydrogen Evolution Reaction', *Encyclopedia of Applied Electrochemistry*, 815, pp. 1039–1044. doi: 10.1007/978-1-4419-6996-5_403.

Kumar, V. *et al.* (2024) 'Electrocatalytic Performance of 2D Monolayer WSeTe Janus Transition Metal Dichalcogenide for Highly Efficient H₂ Evolution Reaction', *Langmuir*, 40(29), pp. 14872–14887. doi: 10.1021/acs.langmuir.4c00867.

Kumar, V. and Pakhira, S. (2023) 'Mechanistic understanding of efficient electrocatalytic

hydrogen evolution reaction on a 2D monolayer WS₂ Janus transition metal dichalcogenide', *Molecular Systems Design and Engineering*, 8(8), pp. 1060–1074. doi: 10.1039/d3me00037k.

Kumar, V. and Pakhira, S. (2025) '2D monolayer molybdenum(iv) telluride TMD: an efficient electrocatalyst for the hydrogen evolution reaction', *Materials Advances*. doi: 10.1039/d4ma00892h.

Laun, J. and Bredow, T. (2021) 'BSSE-corrected consistent Gaussian basis sets of triple-zeta valence with polarization quality of the sixth period for solid-state calculations', *Journal of Computational Chemistry*, 42(15), pp. 1064–1072.

Laun, J. and Bredow, T. (2022) 'BSSE-corrected consistent Gaussian basis sets of triple-zeta valence with polarization quality of the fifth period for solid-state calculations', *Journal of Computational Chemistry*, 43(12), pp. 839–846.

Laursen, A. B. *et al.* (2012) 'Electrochemical hydrogen evolution: Sabatiers principle and the volcano plot', *Journal of Chemical Education*, 89(12), pp. 1595–1599. doi: 10.1021/ed200818t.

Lee, J. *et al.* (2018) 'Hydrogen Evolution Reaction at Anion Vacancy of Two-Dimensional Transition-Metal Dichalcogenides: Ab Initio Computational Screening', *Journal of Physical Chemistry Letters*, 9(8), pp. 2049–2055. doi: 10.1021/acs.jpclett.8b00712.

Lei, Y., Pakhira, S., Fujisawa, K., Wang, X., Iyiola, O. O., Perea López, N., *et al.* (2017) 'Low-temperature synthesis of heterostructures of transition metal dichalcogenide alloys (W_xMo_{1-x}S₂) and graphene with superior catalytic performance for hydrogen evolution', *ACS nano*, 11(5), pp. 5103–5112.

Lei, Y., Pakhira, S., Fujisawa, K., Wang, X., Iyiola, O. O., Perea López, N., *et al.* (2017) 'Low-temperature Synthesis of Heterostructures of Transition Metal Dichalcogenide Alloys (W_xMo_{1-x}S₂) and Graphene with Superior Catalytic Performance for Hydrogen Evolution', *ACS Nano*, 11(5), pp. 5103–5112. doi: 10.1021/acsnano.7b02060.

Lei, Y. *et al.* (2021) 'Low temperature activation of inert hexagonal boron nitride for metal deposition and single atom catalysis', *Materials Today*. doi: <https://doi.org/10.1016/j.mattod.2021.09.017>.

LeValley, T. L., Richard, A. R. and Fan, M. (2014) 'The progress in water gas shift and steam reforming hydrogen production technologies--A review', *International Journal of Hydrogen Energy*, 39(30), pp. 16983–17000.

Li, C. *et al.* (2019) 'Mechanisms for hydrogen evolution on transition metal phosphide catalysts and a comparison to Pt(111)', *Physical Chemistry Chemical Physics*, 21(44), pp. 24489–24498. doi: 10.1039/c9cp05094a.

Li, F. *et al.* (2017) 'Electronic and optical properties of pristine and vertical and lateral heterostructures of Janus MoSSe and WS₂', *The journal of physical chemistry letters*, 8(23), pp. 5959–5965.

Li, G. *et al.* (2016) 'All the Catalytic Active Sites of MoS₂ for Hydrogen Evolution',

Journal of the American Chemical Society, 138(51), pp. 16632–16638. doi: 10.1021/jacs.6b05940.

Li, R., Cheng, Y. and Huang, W. (2018) ‘Recent progress of Janus 2D transition metal chalcogenides: from theory to experiments’, *Small*, 14(45), p. 1802091.

Liang, K. *et al.* (2018) ‘S-doped MoP nanoporous layer toward high-efficiency hydrogen evolution in pH-universal electrolyte’, *ACS Catalysis*, 9(1), pp. 651–659.

Liang, K. *et al.* (2019) ‘S-Doped MoP Nanoporous Layer Toward High-Efficiency Hydrogen Evolution in pH-Universal Electrolyte’, *ACS Catalysis*, 9(1), pp. 651–659. doi: 10.1021/acscatal.8b04291.

Lipparini, F. and Mennucci, B. (2016) ‘Perspective: Polarizable continuum models for quantum-mechanical descriptions’, *Journal of Chemical Physics*, 144(16). doi: 10.1063/1.4947236.

Liu, Z. (2015) ‘Clean Energy Replacement and Electricity Replacement’, *Global Energy Interconnection*, pp. 65–90. doi: 10.1016/b978-0-12-804405-6.00002-6.

Loo, A. H. *et al.* (2015) ‘Exfoliated transition metal dichalcogenides (MoS₂, MoSe₂, WS₂, WSe₂): An electrochemical impedance spectroscopic investigation’, *Electrochemistry Communications*, 50, pp. 39–42. doi: 10.1016/j.elecom.2014.10.018.

Lu, A.-Y. *et al.* (2017) ‘Janus monolayers of transition metal dichalcogenides’, *Nature nanotechnology*, 12(8), pp. 744–749.

Lu, A. Y. *et al.* (2017) ‘Janus monolayers of transition metal dichalcogenides’, *Nature Nanotechnology*, 12(8), pp. 744–749. doi: 10.1038/nnano.2017.100.

Maghirang, A. B. *et al.* (2019) ‘Predicting two-dimensional topological phases in Janus materials by substitutional doping in transition metal dichalcogenide monolayers’, *npj 2D Materials and Applications*, 3(1), pp. 1–8.

Martin, J. M. L. and Sundermann, A. (2001) ‘Correlation consistent valence basis sets for use with the Stuttgart--Dresden--Bonn relativistic effective core potentials: The atoms Ga--Kr and In--Xe’, *The Journal of Chemical Physics*, 114(8), pp. 3408–3420.

McGlynn, J. C. *et al.* (2019) ‘The rapid electrochemical activation of MoTe₂ for the hydrogen evolution reaction’, *Nature communications*, 10(1), p. 4916.

Michalsky, R., Zhang, Y.-J. and Peterson, A. A. (2014) ‘Trends in the hydrogen evolution activity of metal carbide catalysts’, *Acs Catalysis*, 4(5), pp. 1274–1278.

Miles, M. H. and Thomason, M. A. (1976) ‘Periodic variations of overvoltages for water electrolysis in acid solutions from cyclic voltammetric studies’, *Journal of the Electrochemical Society*, 123(10), p. 1459.

Mir, S. H. *et al.* (2017) ‘A comparative study of hydrogen evolution reaction on pseudo-monolayer WS₂ and PtS₂: Insights based on the density functional theory’, *Catalysis Science and Technology*, 7(3), pp. 687–692. doi: 10.1039/c6cy02426b.

Mohammadi, A. and Mehrpooya, M. (2018) ‘A comprehensive review on coupling different types of electrolyzer to renewable energy sources’, *Energy*, 158, pp. 632–655.

Momma, K. and Izumi, F. (2011) ‘VESTA 3 for three-dimensional visualization of crystal, volumetric and morphology data’, *Journal of applied crystallography*, 44(6), pp. 1272–1276.

Montoya, A., Truong, T. N. and Sarofim, A. F. (2000) ‘Spin contamination in Hartree-Fock and density functional theory wavefunctions in modeling of adsorption on graphite’, *Journal of Physical Chemistry A*, 104(26), pp. 6108–6110. doi: 10.1021/jp000534m.

Morales-Guio, C. G., Stern, L.-A. and Hu, X. (2014) ‘Nanostructured hydrotreating catalysts for electrochemical hydrogen evolution’, *Chemical Society Reviews*, 43(18), pp. 6555–6569.

Nagaraj, R. *et al.* (2020) ‘Catalyzing the Intercalation Storage Capacity of Aqueous Zinc-Ion Battery Constructed with Zn (II) Preinserted Organo-Vanadyl Hybrid Cathode’, *ACS Applied Energy Materials*, 3(4), pp. 3425–3434.

Nagy, B. and Jensen, F. (2017) ‘Basis sets in quantum chemistry’, *Reviews in computational chemistry*, 30, pp. 93–149.

Nasser, M. *et al.* (2022) ‘A review of water electrolysis--based systems for hydrogen production using hybrid/solar/wind energy systems’, *Environmental Science and Pollution Research*, 29(58), pp. 86994–87018.

Nazari, M. and Ghaemmaghami, M. (2023) ‘Approach to evaluation of electrocatalytic water splitting parameters, reflecting intrinsic activity: toward the right pathway’, *ChemSusChem*, 16(11), p. e202202126.

Niu, W. *et al.* (2018) ‘Apically Dominant Mechanism for Improving Catalytic Activities of N-Doped Carbon Nanotube Arrays in Rechargeable Zinc–Air Battery’, *Advanced Energy Materials*, 8(20). doi: 10.1002/aenm.201800480.

Ortmann, F., Bechstedt, F. and Schmidt, W. G. (2006) ‘Semiempirical van der Waals correction to the density functional description of solids and molecular structures’, *Physical Review B—Condensed Matter and Materials Physics*, 73(20), p. 205101.

Owusu, P. A. and Asumadu-Sarkodie, S. (2016) ‘A review of renewable energy sources, sustainability issues and climate change mitigation’, *Cogent Engineering*, 3(1). doi: 10.1080/23311916.2016.1167990.

Pakhira, S. *et al.* (2012) ‘Theoretical study of spectroscopy, interaction, and dissociation of linear and T-shaped isomers of RgClF (Rg= He, Ne, and Ar) van der Waals complexes’, *Structural Chemistry*, 23(3), pp. 681–692.

Pakhira, S., Sahu, C., *et al.* (2013) ‘Dispersion corrected double high-hybrid and gradient-corrected density functional theory study of light cation-dihydrogen (M^+-H_2 , where M = Li, Na, B and Al) van der Waals complexes’, *Structural Chemistry*, 24(2), pp. 549–558.

doi: 10.1007/s11224-012-0107-y.

Pakhira, S., Sen, K., *et al.* (2013) ‘Performance of dispersion-corrected double hybrid density functional theory: A computational study of OCS-hydrocarbon van der Waals complexes’, *The Journal of chemical physics*, 138(16), p. 164319.

Pakhira, S. *et al.* (2015) ‘A quantum monte carlo study of the reactions of CH with acrolein’, *Journal of Physical Chemistry A*, 119(18), pp. 4214–4223. doi: 10.1021/acs.jpca.5b00919.

Pakhira, S. *et al.* (2016) ‘Quantum Monte Carlo Study of the Reactions of CH with Acrolein: Major and Minor Channels’, *J. Phys. Chem. A*, 120, pp. 3602–3612.

Pakhira, S. (2019) ‘Rotational dynamics of the organic bridging linkers in metal--organic frameworks and their substituent effects on the rotational energy barrier’, *RSC Advances*, 9(65), pp. 38137–38147.

Pakhira, S., Bera, N. C. and Das, A. K. (2011) ‘Coupled cluster study of structural properties of RgI and RgI-(Rg= He, Ne, Ar) weakly bound molecules’, *Structural Chemistry*, 22(4), pp. 893–900.

Pakhira, S. and Das, A. K. (2011) ‘Spectroscopy and dissociation of I₂-Rg (Rg= Kr and Xe) van der Waals complexes’, *Theoretical Chemistry Accounts*, 130(1), pp. 95–101.

Pakhira, S. and Das, A. K. (2012) ‘Spectroscopic properties, potential energy surfaces and interaction energies of RgClF (Rg = Kr and Xe) van der Waals complexes’, *The European Physical Journal D*, 66(5), p. 144. doi: 10.1140/epjd/e2012-30110-9.

Pakhira, S., Kumar, V. and Ghosh, S. (2023) ‘Revealing the Superior Electrocatalytic Performance of 2D Monolayer WSe₂ Transition Metal Dichalcogenide for Efficient H₂ Evolution Reaction’, *Advanced Materials Interfaces*, 10(8), p. 2202075. doi: 10.1002/admi.202202075.

Pakhira, S., Lucht, K. P. and Mendoza-Cortes, J. L. (2016) ‘An Alternative Strategy to Control the Electronic Properties of Bilayer Graphene: Semi-metal to Metal Transition and a 2D Material with Dirac Cone’. Available at: <http://arxiv.org/abs/1610.04777>.

Pakhira, S., Lucht, K. P. and Mendoza-Cortes, J. L. (2017) ‘Iron intercalation in covalent-organic frameworks: A promising approach for semiconductors’, *Journal of Physical Chemistry C*, 121(39), pp. 21160–21170. doi: 10.1021/acs.jpcc.7b06617.

Pakhira, S. and Mendoza-Cortes, J. L. (2020) ‘Quantum Nature in the Interaction of Molecular Hydrogen with Porous Materials: Implications for Practical Hydrogen Storage’, *The Journal of Physical Chemistry C*, 124(11), pp. 6454–6460.

Pakhira, S., Mondal, B. and Das, A. K. (2011) ‘Spectroscopic properties of I₂-Rg (Rg= He, Ne, Ar) van der Waals complexes’, *Chemical Physics Letters*, 505(4–6), pp. 81–86.

Pakhira, S., Takayanagi, M. and Nagaoka, M. (2015) ‘Diverse Rotational Flexibility of Substituted Dicarboxylate Ligands in Functional Porous Coordination Polymers’, *Journal of Physical Chemistry C*, 119(52), pp. 28789–28799. doi: 10.1021/acs.jpcc.5b10393.

Pakhira, S. and Upadhyay, S. N. (2022) 'Efficient electrocatalytic H₂ evolution mediated by 2D Janus MoSSe transition metal dichalcogenide', *Sustainable Energy and Fuels*, 6(7), pp. 1733–1752. doi: 10.1039/d1se02040d.

Pan, Y. *et al.* (2016) 'Metal doping effect of the M-Co₂P/Nitrogen-Doped carbon nanotubes (M= Fe, Ni, Cu) hydrogen evolution hybrid catalysts', *ACS applied materials & interfaces*, 8(22), pp. 13890–13901.

Patel, C. *et al.* (2022) 'Large and Uniform Single Crystals of MoS₂ Monolayers for ppb-Level NO₂ Sensing', *ACS Applied Nano Materials*. doi: 10.1021/acsanm.2c01701.

Peintinger, M. F., Oliveira, D. V. and Bredow, T. (2013) 'Consistent Gaussian basis sets of triple-zeta valence with polarization quality for solid-state calculations', *Journal of Computational Chemistry*, 34(6), pp. 451–459. doi: 10.1002/jcc.23153.

Perdew, J. P., Burke, K. and Wang, Y. (1996) 'Generalized gradient approximation for the exchange-correlation hole of a many-electron system', *Physical review B*, 54(23), p. 16533.

Phys, J. C. (2008) 'A new local density functional for main- group thermochemistry , transition metal bonding , thermochemical kinetics , and noncovalent interactions', 194101(2006). doi: 10.1063/1.2370993.

Puttaswamy, R. *et al.* (2021) 'Constructing a High-Performance Aqueous Rechargeable Zinc-Ion Battery Cathode with Self-Assembled Mat-like Packing of Intertwined Ag (I) Pre-Inserted V₃O₇·H₂O Microbelts with Reduced Graphene Oxide Core', *ACS Sustainable Chemistry & Engineering*, 9(11), pp. 3985–3995.

Ramasubramaniam, A. (2012) 'Large excitonic effects in monolayers of molybdenum and tungsten dichalcogenides', *Physical Review B*, 86(11), p. 115409.

Sahu, C. *et al.* (2013) 'A computational study of detoxification of lewisite warfare agents by british anti-lewisite: Catalytic effects of water and ammonia on reaction mechanism and kinetics', *J. Phys. Chem. A*, 117, pp. 3496–3506.

Salustro, S. *et al.* (2017) 'Comparison between cluster and supercell approaches: the case of defects in diamond', *Theoretical Chemistry Accounts*, 136(4), pp. 1–13. doi: 10.1007/s00214-017-2071-5.

Shi, W. and Wang, Z. (2018) 'Mechanical and electronic properties of Janus monolayer transition metal dichalcogenides', *Journal of Physics Condensed Matter*, 30(21), p. 215301. doi: 10.1088/1361-648X/aabd59.

Shilpa, R. *et al.* (2023) 'Electrocatalysts for Hydrogen Evolution Reaction', *Materials for Hydrogen Production, Conversion, and Storage*, 42(16), pp. 115–146. doi: 10.1002/9781119829584.ch5.

Sinha, N., Deshpande, I. and Pakhira, S. (2019) 'Substituents Effects of Organic Linkers on Rotational Energy Barriers in Metal-Organic Frameworks', *ChemistrySelect*, 4(29), pp. 8584–8592.

Sinha, N. and Pakhira, S. (2021) ‘Tunability of the Electronic Properties of Covalent Organic Frameworks’, *ACS Applied Electronic Materials*, 3(2), pp. 720–732. doi: 10.1021/acsaelm.0c00867.

Som, N. N. and Jha, P. K. (2020) ‘Hydrogen evolution reaction of metal di-chalcogenides: ZrS₂, ZrSe₂ and Janus ZrSSe’, *International Journal of Hydrogen Energy*, 45(44), pp. 23920–23927. doi: 10.1016/j.ijhydene.2019.09.033.

Som, N. N., Mankad, V. and Jha, P. K. (2018) ‘Hydrogen evolution reaction: The role of arsenene nanosheet and dopant’, *International Journal of Hydrogen Energy*, 43(47), pp. 21634–21641. doi: 10.1016/j.ijhydene.2018.03.066.

Staffell, I. *et al.* (2019) ‘The role of hydrogen and fuel cells in the global energy system’, *Energy & Environmental Science*, 12(2), pp. 463–491.

Tang, Q. and Jiang, D. E. (2016) ‘Mechanism of hydrogen evolution reaction on 1T-MoS₂ from first principles’, *ACS Catalysis*, 6(8), pp. 4953–4961. doi: 10.1021/acscatal.6b01211.

Tirado-Rives, J. and Jorgensen, W. L. (2008) ‘Performance of B3LYP density functional methods for a large set of organic molecules’, *Journal of chemical theory and computation*, 4(2), pp. 297–306.

Tissandier, M. D. *et al.* (1998) ‘The proton’s absolute aqueous enthalpy and Gibbs free energy of solvation from cluster-ion solvation data’, *Journal of Physical Chemistry A*, 102(40), pp. 7787–7794. doi: 10.1021/jp982638r.

Uematsu, M. and Frank, E. U. (1980) ‘Static Dielectric Constant of Water and Steam’, *J. Phys. Chem. Ref. Data*, 9, pp. 1291–1306.

Upadhyay, S. N. *et al.* (2022) ‘Elucidating the oxygen reduction reaction mechanism on the surfaces of 2D monolayer CsPbBr₃ perovskite’, *Physical Chemistry Chemical Physics*, 24(46), pp. 28283–28294.

Upadhyay, S. N. and Pakhira, S. (2021a) ‘Mechanism of electrochemical oxygen reduction reaction at two-dimensional Pt-doped MoSe₂ material: an efficient electrocatalyst’, *Journal of Materials Chemistry C*, 9(34), pp. 11331–11342.

Upadhyay, S. N. and Pakhira, S. (2021b) ‘Mechanism of electrochemical oxygen reduction reaction at two-dimensional Pt-doped MoSe₂ material: an efficient electrocatalyst’, *J. Mater. Chem. C*, 9(34), pp. 11331–11342. doi: 10.1039/D1TC02193A.

Upadhyay, S. N. and Pakhira, S. (2022) ‘Nanostructured Pt-doped 2D MoSe₂: an efficient bifunctional electrocatalyst for both hydrogen evolution and oxygen reduction reactions’, *Physical Chemistry Chemical Physics*, 24(37), pp. 22823–22844.

Vesborg, P. C. K., Seger, B. and Chorkendorff, I. (2015) ‘Recent development in hydrogen evolution reaction catalysts and their practical implementation’, *Journal of Physical Chemistry Letters*, 6(6), pp. 951–957. doi: 10.1021/acs.jpclett.5b00306.

Vilela Oliveira, D. *et al.* (2019) ‘BSSE-correction scheme for consistent gaussian basis sets of double-and triple-zeta valence with polarization quality for solid-state calculations’, *Journal of computational chemistry*, 40(27), pp. 2364–2376.

Vu, T. V *et al.* (2020) ‘Graphene/WSeTe van der Waals heterostructure: Controllable electronic properties and Schottky barrier via interlayer coupling and electric field’, *Applied Surface Science*, 507, p. 145036.

Wadt, W. R. and Hay, P. J. (1985) ‘Ab initio effective core potentials for molecular calculations. Potentials for main group elements Na to Bi’, *J. Chem. Phys.*, 82, pp. 284–298. doi: 10.1063/1.448800.

Wang, H. *et al.* (2015) ‘Transition-metal doped edge sites in vertically aligned MoS₂ catalysts for enhanced hydrogen evolution’, *Nano Research*, 8(2), pp. 566–575. doi: 10.1007/s12274-014-0677-7.

Wang, J. *et al.* (2017) ‘The mechanism of hydrogen adsorption on transition metal dichalcogenides as hydrogen evolution reaction catalyst’, *Physical Chemistry Chemical Physics*, 19(15), pp. 10125–10132. doi: 10.1039/c7cp00636e.

Wang, J. *et al.* (2018) ‘Intriguing electronic and optical properties of two-dimensional Janus transition metal dichalcogenides’, *Physical Chemistry Chemical Physics*, 20(27), pp. 18571–18578.

Wu, L. *et al.* (2018) ‘Multiscale modeling for high-performance concrete: A review’, *International Journal for Multiscale Computational Engineering*, 16(3), pp. 267–283. doi: 10.1615/IntJMultCompEng.2018022827.

Xia, C. *et al.* (2018) ‘Universality of electronic characteristics and photocatalyst applications in the two-dimensional Janus transition metal dichalcogenides’, *Physical Review B*, 98(16), pp. 1–8. doi: 10.1103/PhysRevB.98.165424.

Xiao, C. *et al.* (2021) ‘High-throughput screening of transition metal single-atom catalyst anchored on Janus MoSSe basal plane for hydrogen evolution reaction’, *International Journal of Hydrogen Energy*, 46(17), pp. 10337–10345. doi: 10.1016/j.ijhydene.2020.12.148.

Xiao, Y. and Shen, C. (2021) ‘Predicted electrocatalyst properties on metal insulator MoTe₂ for hydrogen evolution reaction and oxygen reduction reaction application in fuel cells’, *Energy & Fuels*, 35(9), pp. 8275–8285.

Yang, J. and Shin, H. S. (2014) ‘Recent advances in layered transition metal dichalcogenides for hydrogen evolution reaction’, *Journal of Materials Chemistry A*, 2(17), pp. 5979–5985.

Yang, Y. *et al.* (2019) ‘Structural and electronic properties of 2H phase Janus transition metal dichalcogenide bilayers’, *Superlattices and Microstructures*, 131, pp. 8–14.

Yu, Y. *et al.* (2023) ‘Tunable electronic and photodiode characteristics of Janus WSeTe:

A first-principles study', *Surfaces and Interfaces*, 37(August 2022), p. 102572. doi: 10.1016/j.surfin.2022.102572.

Yuan, J., Shan, Y. and Li, T. (2020) 'Electronic structure and hydrogen evolution reaction in Janus monolayer MoSSe regulated by strain engineering', *Journal of Physics D: Applied Physics*, 53(12). doi: 10.1088/1361-6463/ab622e.

Zhang, H. M. *et al.* (2022) 'Review on Intrinsic Electrocatalytic Activity of Transition Metal Nitrides on HER', *Energy Material Advances*, 2022, p. 6. doi: 10.34133/ENERGYMATADV.0006.

Zhang, J. *et al.* (2017) 'Janus Monolayer Transition-Metal Dichalcogenides', *ACS Nano*, 11(8), pp. 8192–8198. doi: 10.1021/acsnano.7b03186.

Zhao, Y. and Truhlar, D. G. (2006) 'A new local density functional for main-group thermochemistry, transition metal bonding, thermochemical kinetics, and noncovalent interactions', *The Journal of chemical physics*, 125(19), p. 194101.

Zhao, Y. and Truhlar, D. G. (2008) 'The M06 suite of density functionals for main group thermochemistry, thermochemical kinetics, noncovalent interactions, excited states, and transition elements: two new functionals and systematic testing of four M06-class functionals and 12 other fun', pp. 215–241. doi: 10.1007/s00214-007-0310-x.

Zhu, J. *et al.* (2019) 'Recent advances in electrocatalytic hydrogen evolution using nanoparticles', *Chemical reviews*, 120(2), pp. 851–918.